

**Improved Sampled Grating DBR
Widely-Tunable 1.55 μ m Lasers**

Final Technical Report
9/20/96-2/29/00

PI - L.A. Coldren

ECE Technical Report #00-02

Naval Research Laboratory
Contract No. N00014-96-1-G014

DISTRIBUTION STATEMENT A
Approved for Public Release
Distribution Unlimited

University of California
Department of Electrical & Computer Engineering
Santa Barbara, CA 93106-9560

20000310 043

Improved Sampled Grating DBR Widely-Tunable 1.55 μ m Lasers

T. G. B. Mason, J. Barton, L. A. Coldren

Final Report

Abstract

Over the last three years, a number of improvements have been made in the design of SGDBR lasers with integrated componentry. Device design has improved the output power and tuning range due to an increase in the number of quantum wells in the active region from four to six. Devices with up to 8 mW of output power with integrated amplifiers and buried heterostructure devices with 72 nm tuning ranges were realized. Current laser results indicate that leakage current in buried heterostructure lasers is a major factor in limiting the device performance. To eliminate the parasitic leakage paths we have begun to investigate Fe doped blocking junctions for the device. Work on the wavelength monitor has focused on an external approach, which uses a wavelength dependent coupler in conjunction with a pair of photodetectors. Initial results show better than 1 nm sensitivity over a 30 nm range. The most recent work on the laser has focussed on integrating additional components for increased functionality. We have developed a curved waveguide semiconductor optical amplifier that can be integrated with the laser to increase the output power to greater than 6 mW. We have also investigated SGDBR lasers with integrated electro-absorption modulators. Using a 300 μ m long bulk EA modulator we have demonstrated error free data transmission at 2.5 GBit/s with a 2^{31} -1 pattern length at received powers of -32.5 dBm.

Subject terms

Semiconductor lasers, photonic integrated circuits, wavelength monitors, WDM devices, semiconductor optical amplifiers, electro-absorption modulators

Introduction

The goal of this program was to develop a widely tunable semiconductor laser diode with an integrated wavelength monitor. The widely tunable laser is a four section device with a pair of sampled grating distributed Bragg reflector mirrors as shown in figure 1.

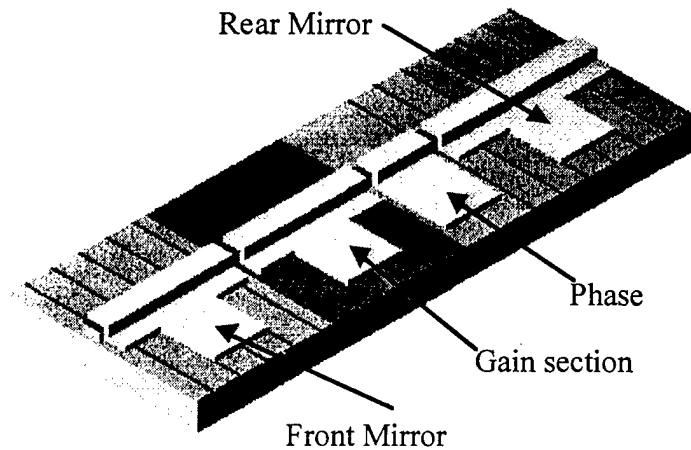


Figure 1 SGDBR Laser schematic

These devices use a Vernier effect tuning mechanism to provide widely tunable wavelength ranges. Because of the simple offset waveguide design, SGDBR lasers are easily integrated with other optoelectronic devices such as wavelength monitors, optical amplifiers, and modulators to form photonic integrated circuits. They employ periodically sampled grating mirrors which have multiple reflection peaks spaced approximately 5-7 nm apart. The duty cycle and sampling periods have been optimized for the desired wavelength coverage. A phase control section is included to enable alignment of the cavity mode with the mirror reflection peaks. Devices were fabricated using both ridge and buried ridge waveguide processes with passive regions formed by a combination of etching and MOCVD regrowth.

This work is discussed in detail in Dr. T.G.B Mason's dissertation – which is included as Appendix I. Supplementary material outlining work on semiconductor optical amplifiers (SOAs) and Electro-absorption modulators (EAM) is also included in the report.

Thesis summary

First we will briefly summarize the key results from Dr. Mason's dissertation. In appendix I, Dr. Mason discusses the design and development of photonic circuits - in particular the monolithic integration of a widely tunable laser with an on-chip wavelength monitor.

Chapter 1

This chapter describes an overview of photonic devices and systems. It discusses the need for wavelength monitoring and other integrated photonic circuits. With the growth of wavelength division multiplexing (WDM) systems, widely tunable lasers have become highly desirable.

Chapter 2

This chapter touches on the motivation for the development of widely tunable devices and discusses design parameters for the waveguide structure, grating patterns, and tuning characteristics. Some of the key points are outlined below:

- Improved active region design with higher peak gain and lower leakage current is demonstrated. The active region consists of six 0.8% compressive strained quaternary quantum wells grown on top of the waveguide.

- Wet and dry etch processes for fabricating the gratings were investigated. The dry etch process enables an InP surface to be maintained over the waveguide for the regrowth. This will improve the quality of the regrowth interface and reduce the contribution to leakage current from non-radiative recombination at the interface.
- Previous SGDBR structures employed quaternary waveguides with a band gap wavelength of 1.3 μm (1.3Q). The amount of index shift that can be achieved by carrier injection into the waveguide increases as bandgap of the material is reduced. The loss associated with the waveguide will also increase as the bandgap is reduced. Both of these effects are highly nonlinear and depend on the wavelength of the laser. The optimum composition for the highest ratio of index change to absorption increase for light at 1.55 μm is a quaternary material with a band gap wavelength around 1.4 μm .
- Buried heterostructure devices have been fabricated – demonstrating record tuning ranges (72nm) with full wavelength coverage. The device structure and results are discussed in section 2.6. Using a buried heterostructure will improve the carrier confinement, however leakage paths need to be minimized and work has progressed using Fe doping of the regrowth material.

Chapter 3. Wavelength Monitoring

As elaborated in section 3.1-3.3 a number of wavelength monitors have been fabricated for ridge and buried heterostructure devices. This area of the project evolved out of the requirement for simple “two knob” operation of the SGDBR one for amplitude and the other for wavelength. The complexity of the tuning mechanism in these types of lasers makes it desirable to have an integrated method for providing wavelength monitoring. This would operate in much the same way that the backside photodetector provides output power monitoring in a conventional laser diode. There are many different methods for achieving a wavelength dependent signal in an integrated photonic circuit. We focused on a design that would provide a compact, robust wavelength monitor that could easily be integrated with the existing device process. The design is based on a two mode interference waveguide. Using the difference in the propagation velocity for the lowest order odd and even modes in an asymmetrically excited waveguide, a wavelength dependent output signal can be generated. The design was simulated and refined using the beam propagation method. This design can be integrated with the existing laser process and provides a monotonic varying output signal over a wide wavelength range. Ultimately, the sensitivity of the structure will be limited by the signal to noise ratio of the detectors. Since the waveguide is integrated directly with the laser, it is expected that the high optical signal levels will provide a clean output signal.

Light is launched off-axis into the TMI waveguide and propagates along it. At the output, the splitting ratio into the two guides is governed by the phase difference between the excited waveguide modes which is wavelength dependent. The output range is governed by the device length. For a 100 nm range the device length is ~ 2 mm which is large compared to conventional laser diodes, but much smaller than an AWG or Mach-Zehnder based device would be.

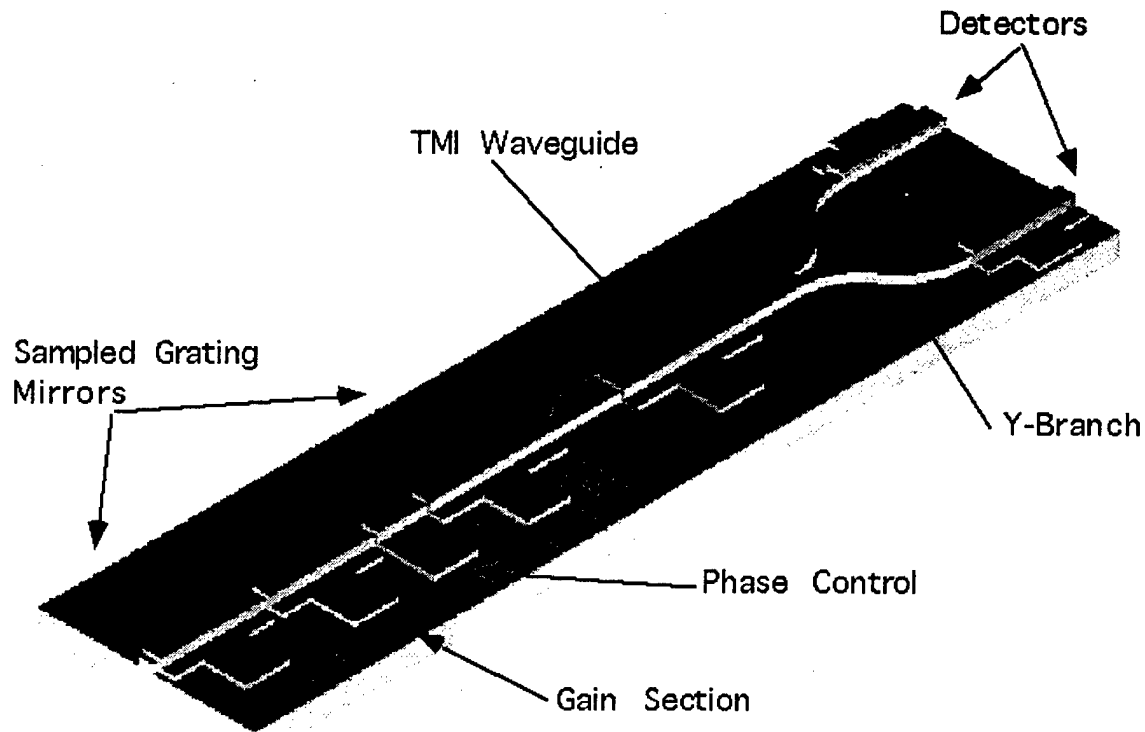


Figure 2. Integrated SGDBR and TMI wavelength Monitor

Chapter 4. Growth and Characterization

This chapter delves into the growth and characterization of photonic integrated circuits with MOCVD. This chapter overviews the sources and reactor that was used to grow the material and the types of characterization tools that are used to evaluate the material.

Chapter 5. Device packaging and testing

This chapter examines the device packaging and testing of SGDBR lasers. packaging provides far more stable electrical and optical properties and facilitates for testing efforts and the development of feedback circuits with wavelength monitoring and/or other control circuitry. The lasers packaged in a modified butterfly package with an SMA integrated on the back end to provide for a high speed connection. Small thin film heater stages have been used to solder a metalized lensed fiber in place once it has been aligned to the laser chip.

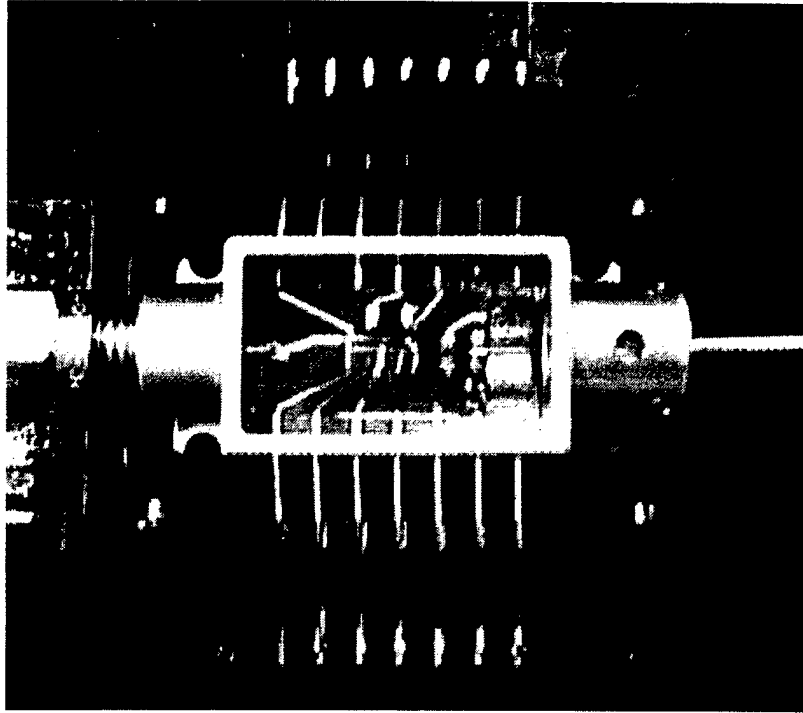


Figure 3. Laser Diode Package

Recent Results

To achieve very wide range tuning from the SGDBR laser requires a carefully optimized mirror design and a high quality gain section with a wide spectral bandwidth. The goal in the mirror design is to optimize the tuning enhancement factor so that the largest wavelength range can be covered with the minimum amount of index tuning. Ultimately the tuning range is limited by the repeat mode spacing in the mirrors. Which is equal to the product of the peak spacings in the mirrors divided by the difference in the peak spacing. To maximize the repeat mode spacing $\Delta\lambda_{RMS}$ and minimize the maximum index tuning, which is equal to the front mirror peak spacing $\Delta\lambda_F$, we must use the minimum possible value for the difference in the mirror peak spacing $\delta\lambda_S$.

$$\Delta\lambda_{RMS} = \frac{\Delta\lambda_F \Delta\lambda_B}{\delta\lambda_S}, \quad \delta\lambda_S = \Delta\lambda_F - \Delta\lambda_B$$

The minimum value for $\delta\lambda_S$ is set by the side mode suppression ratio which is required for the device. In order to maintain a high SMSR it is essential that the 3 dB bandwidth for the mirror reflection peaks be less than double difference in the mirror peak spacing. The bandwidth of the mirror peaks is determined by the number of sampling periods. For a mirror with a grating κ of 300 cm^{-1} and a $3 \mu\text{m}$ grating burst length at least 10 sampling periods are required to achieve a reflection peak bandwidth below 1 nm. However since the peak width tends to broaden somewhat during tuning we chose a minimum of 12 sampling periods for the front mirror and 17 for the back. The front mirror sampling period was $46 \mu\text{m}$ giving a peak spacing of $\sim 7 \text{ nm}$ and the back mirror sampling period was $43 \mu\text{m}$ giving a peak spacing of $\sim 7.5 \text{ nm}$. This gave the device a tuning enhancement factor of 14 with a repeat mode spacing of 105 nm. The relatively short burst length of $3 \mu\text{m}$ was chosen to give an

overall reflection envelope of 90 nm. This limited the tuning range to about 15 nm less than the tuning enhancement factor enabled. The number of quantum wells in the active section was increased to 6 to provide more gain and a wider gain bandwidth. The laser was capable of tuning quasi-continuously over 72 nm. The tuning curves are shown in Figure 4a and 4b.

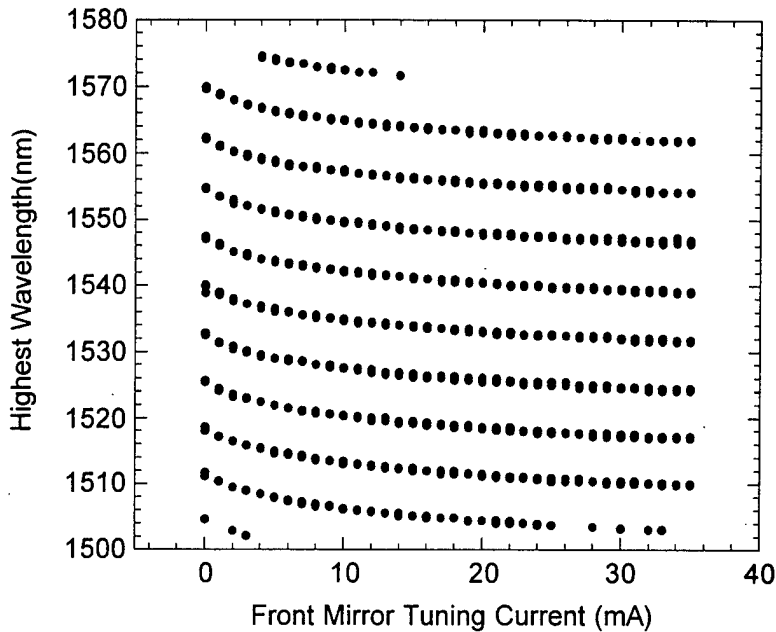


Figure 4a. Front mirror tuning curves for 72 nm quasi-continuous tuning range tested at 0.5 mA intervals from 0 to 35 mA. All points > 30 dB SMSR

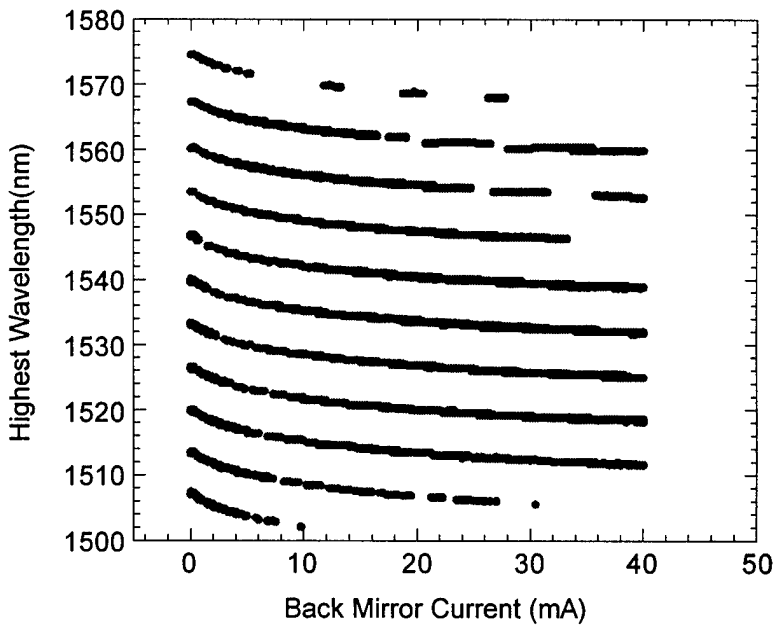


Figure 4b. Back mirror tuning curves for 72 nm quasi-continuous tuning range tested at 0.1 mA intervals from 0 to 40 mA. All points > 30 dB SMSR.

Fe DOPED BLOCKING JUNCTIONS

The light versus current curves for the new lasers had a tendency to roll over at fairly low current densities indicating a strong leakage path. The key to preventing leakage in the buried ridge stripe design is to use high doping levels at the parasitic P-N junction. The doping levels must be high enough that the turn on voltage for the homo-junction is significantly greater than the bandgap of the active region. The problem with the SGDBR laser is that the high doping levels cause high propagation loss in the waveguide due to inter-valence band absorption. Another drawback to the buried ridge stripe design is that the large parasitic P-N junction has a high capacitance which limits the modulation bandwidth of the device. Iron doped blocking junctions have the potential to provide a low leakage low capacitance structure due to their semi-insulating nature. This would enable significant improvements in both the output power and the tuning efficiency for the SGDBR. It would also increase the modulation bandwidth for the device. We have begun to investigate the conditions for growing these structures using a Biscyclopentadienyl-iron source to dope InP. The resistivity and critical voltage for a variety of Fe doping levels in 1 μm thick n-Fe-n structures are shown in Figure 5.

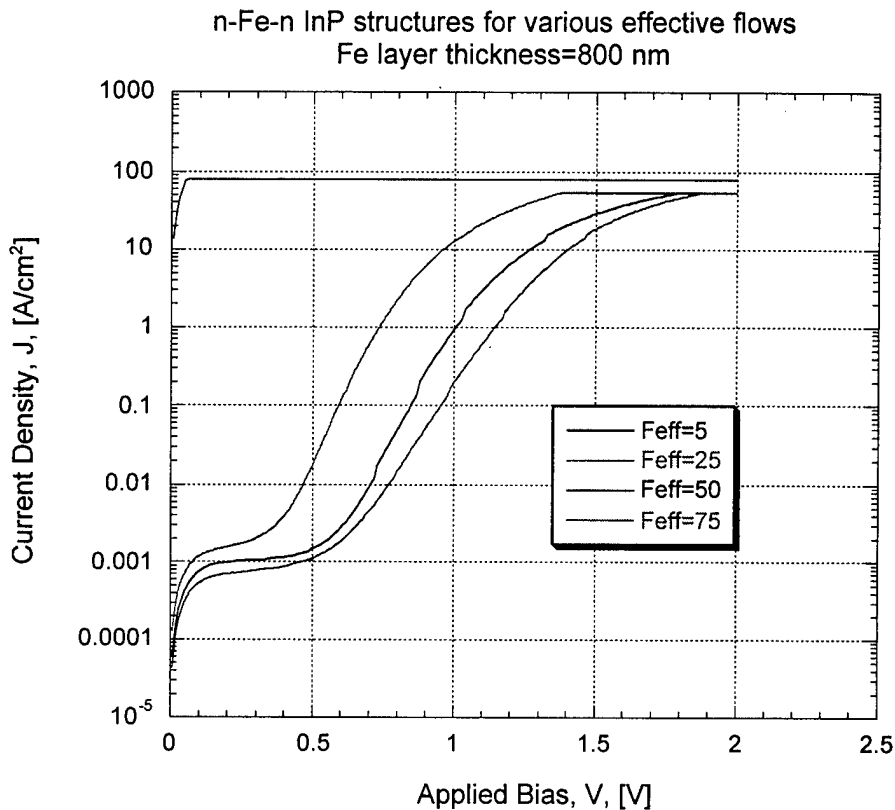


Figure 5. Resistivity for n-Fe-n InP structures grown with a variety of effective dopant flow rates. (3000Å n-type/10000Å Fe-SI/5000Å n-type).

The maximum effective flow rate which we can achieve with the current mass flow controllers is 100. It is clear from this plot that much higher effective flows will be required to make the material semi-insulating. The current critical voltage is around 0.5V. This will have to be increased to more than 2V for effective blocking. The intended growth structure for the semi-insulating device is shown in Figure 6 with a scanning electron micrograph of the device cross section in Figure 7. This structure requires a masked regrowth for the blocking junction followed by an additional capping regrowth for the upper contact layer.

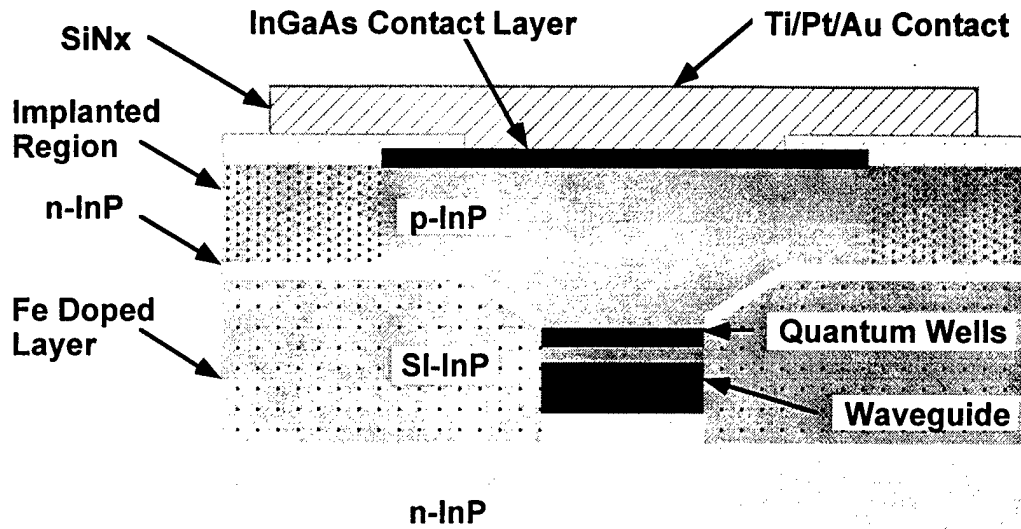


Figure 6. Buried heterostructure laser with Fe doped semi-insulating blocking junction.



Figure 7. Scanning Electron Microscope cross section of SI-BRS laser.

So far we have developed the conditions for good selective regrowth without any mask overgrowth but more work remains to be done to optimize the doping profiles in order to obtain functional devices.

SGDBR LASERS WITH INTEGRATED AMPLIFIERS

A principle advantage of the sampled grating DBR over other widely tunable lasers is that it can be monolithically integrated with different devices such as semiconductor optical amplifiers (SOA's) and electro-absorption modulators to create complex photonic integrated circuits. Integration with an SOA can be difficult because of the need to achieve very high suppression of the facet reflections. To do this we have developed a SGDBR with an integrated SOA that has a curved passive output waveguide. A schematic of the device is shown in Figure 8. The principle advantage of the integrated SOA is that it can compensate for increased absorption loss in the mirrors at high tuning currents, and increase the output power from the device. Placing the power control outside of the laser cavity is highly advantageous since it decouples the output power control from the wavelength tuning characteristics.

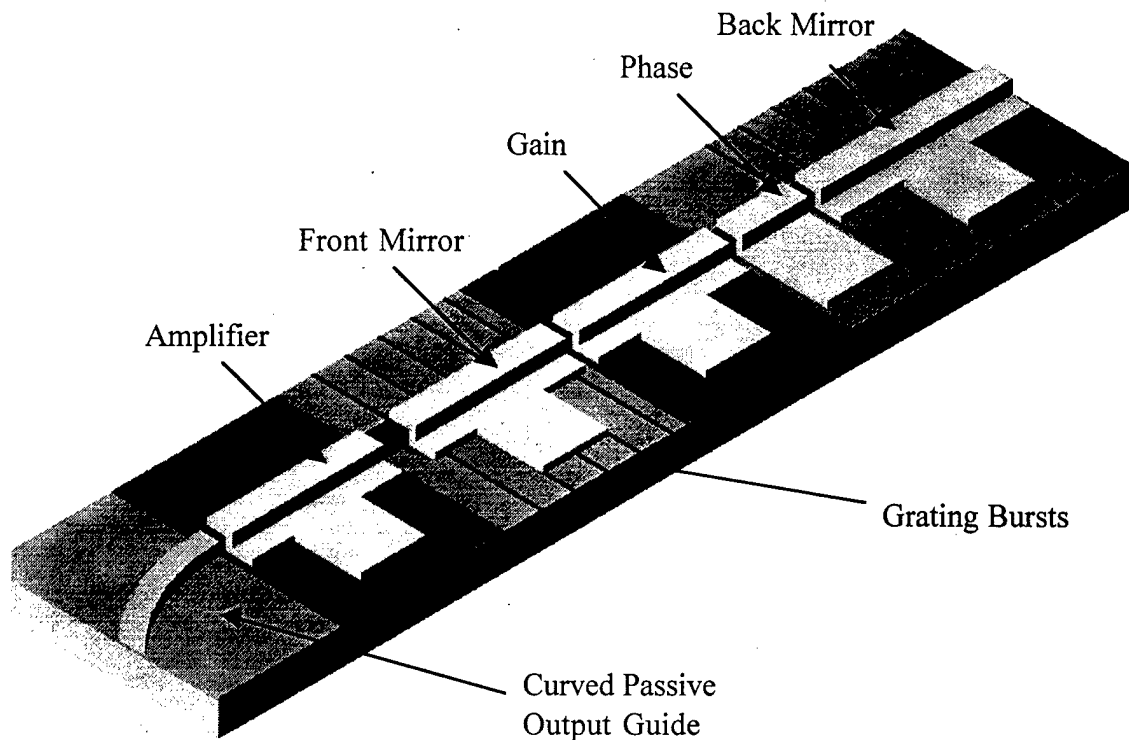


Figure 8. SGDBR laser with integrated semiconductor optical amplifier.

The key to successful integration of the amplifier is to suppress the output facet reflectivity to less than $1E-4$. This is very difficult to achieve, especially over the entire 50 nm tuning range of the laser, even with the best multi-layer antireflection (AR) coatings. It is however relatively easy to achieve this by using an angled facet and a simple single layer AR coating. To avoid the difficulties associated with placing the entire device at an angle we use a curved passive waveguide at the output of the amplifier to create an angled facet. This gives a calculated facet reflectivity of less than $2.5E-5$ over the entire 50 nm tuning range of the device when combined with a 1% antireflection coating. This low residual facet reflectivity enables the device to maintain a high side-mode suppression ratio even at relatively high amplifier gains. Better than 46 dB of SMSR was obtained at an amplifier gain of 8.5 dB.

The tuning performance for the front and back mirror are excellent for this device. Full wavelength coverage over 50 nm can be achieved with tuning currents as low as 15 mA for the rear SGDBR mirror and 14 mA for the front SGDBR mirror. These low tuning currents are achieved by optimum selection of the mirror design parameters. In this case a nominal peak spacing of 5.5 nm was used in the front mirror and 5.0 nm in the back mirror giving a repeat mode spacing of 55 nm. Despite the small difference in the mirror peak spacing between the front and the back mirror careful control of the grating kappa allowed better than 35dB SMSR to be maintained over the entire tuning range.

The saturation power for the integrated amplifier is greater than 6 mW for a bias of 150 mA. For all bias levels we begin to see gain compression once the input power exceeds 0.6 mW. The material transparency current density for the amplifier varied from 5.2 mA at 1570 nm to 14.3 mA at 1510 nm. Taking into account the waveguide losses we calculated the unity gain current at 1550 nm to be 14 mA and the peak gain to be 8.5 dB at 100 mA. Increasing the amplifier bias beyond this point increased the output saturation power but did not increase the gain. Varying the amplifier current from 0 to 150 mA enabled the output power to be varied over a 40 dB range without perturbing the laser wavelength. A similar change can not be achieved by varying the laser gain current without also adjusting the tuning currents to maintain the wavelength. This demonstrates the utility of the integrated amplifier, which provides both increased output power and improved wavelength stability.

SGDBR With Integrated EA Modulator

Widely tunable SGDBR lasers have potential applications in a wide variety of communications networks. Unfortunately the large optical cavities in these devices limit their direct modulation bandwidth to between 3 and 4 GHz. For data transmission applications these lasers must typically be operated with an extinction ratio penalty in order to ensure wavelength stability. They can also have fairly large chirp parameters for wavelengths which are detuned significantly from the band edge of the active region. External modulators have the potential to provide a higher bandwidth and lower chirp for data transmission applications. However external modulators increase the cost and complexity of a transmitter and can have significant insertion losses. To overcome this we have developed a monolithically integrated modulator for use with a SGDBR. The modulator section has the same waveguide structure as the passive and tuning sections in the laser. The same thick low bandgap waveguide that provides good index tuning makes an effective electroabsorption modulator. A cross section of the device is shown in Figure 6.

We fabricated a buried ridge stripe device with an integrated modulator. Electrical isolation between the different laser sections and between the laser and the modulator is achieved by removing the InGaAs contact layer and proton implanting. This implant is also used for lateral current confinement in the buried ridge stripe. The laser sections are separated by 10 μm long implants and the modulator is isolated from the laser with a 50 μm long implanted section. After implantation the sample is annealed at 410°C for 45 seconds to reduce the optical loss from the implant. It is important to keep the annealing temperature below 430°C to maintain the electrical isolation between the sections. The threshold current for the laser was 20 mA and the output power was 1.2 mW at 75 mA. The laser had a tuning range of 47 nm.

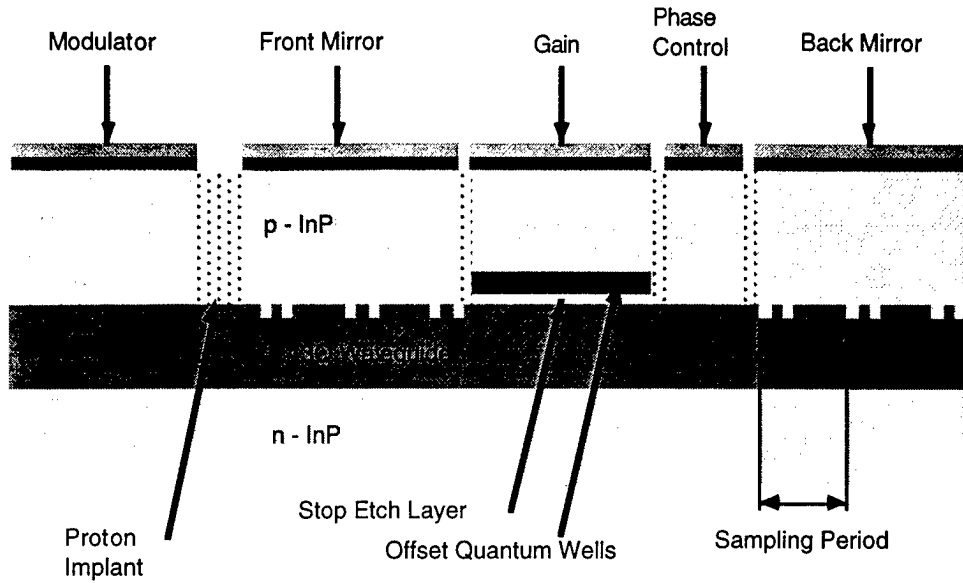


Figure 9. Cross Section of the Integrated Laser Modulator Device

The extinction ratio of the modulator as a function of reverse bias voltage is shown in Figure 10 for four different wavelengths that span the tuning range of the laser. The absorption increases monotonically for all four channels from 0.0 to -4.0V. The maximum extinction was 41.5 dB for 1525 nm at -4.0 V and the minimum was 22.3 dB at 1565.5 nm. There was no observable change in the wavelength of the output light over the entire range of bias voltages indicating sufficient electrical isolation of the laser and modulator sections.

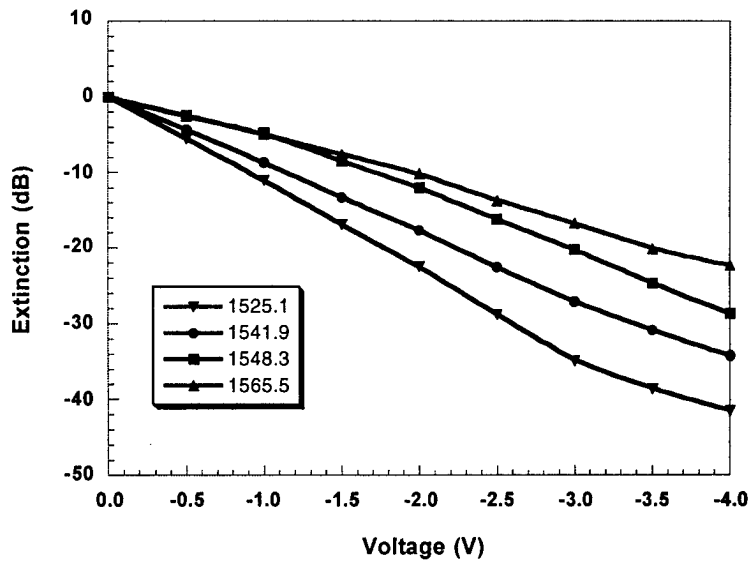


Figure 10. Extinction ratio vs. applied voltage for four different wavelengths.

Unfortunately the modulation bandwidth for the buried device was limited by the parasitic junction capacitance so no data transmission experiments were possible with this device. We also fabricated a ridge waveguide SGDBR with an integrated modulator. This device had a larger detuning between the laser wavelength and the modulator bandgap. The DC extinction curves is shown in Figure 11. A much higher voltage is required to achieve the same on off ratio with this device.

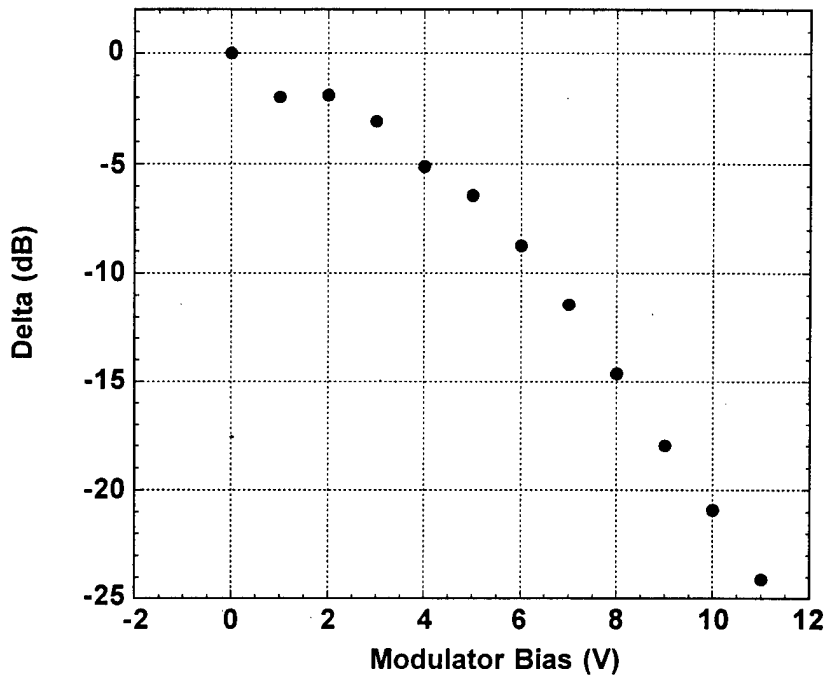


Figure 11. DC extinction curves for EA modulator at 1535 nm

The modulator was tested in back to back transmission using a -5.3V bias and a peak to peak drive amplitude of 5V . This produced an extinction ratio of 13 dB at 2.5 Gbit/s . Error free operation was achieved at a receiver power of -32 dBm using a pattern length of $2^{31}-1$. The sensitivity at a bit error ratio of $1\text{E}-9$ was -33.5 dBm (Figure 12). This was partially limited by spontaneous-signal beat noise from the erbium preamplifier. The optical filter bandwidth at the receiver was 1.3 nm which allowed excess noise to reach the receiver. There is also a small pattern dependent effect since the sensitivity was 1 dB better at a shorter pattern length of $2^{15}-1$. Despite this, these results are significantly better than has been achieved with directly modulated SGDBR lasers. The eye diagram for a bit error ratio of $1\text{E}-9$ is shown in Figure 13. This diagram shows symmetrical open eyes which are visible after the limiting amplifier. Future work will concentrate on reducing the drive voltage for the modulator by reducing the bandgap of the waveguide layer.

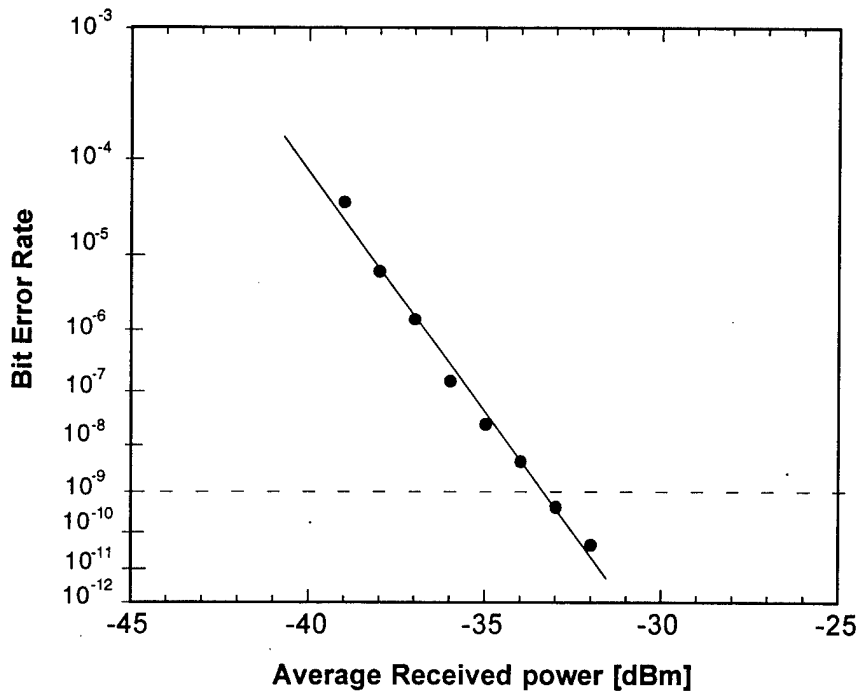


Figure 12. Back to Back Bit Error Rate Curves at 2.5 Gbit/s and $2^{31}-1$ Pattern Length

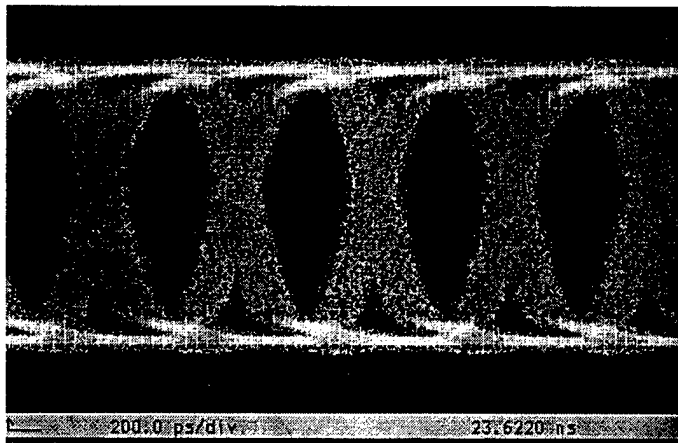


Figure 13. Eye Diagram at 2.488 Gbit/s Data Rate, $2^{31}-1$ Pattern Length and $1E-9$ Error Ratio

FUTURE WORK

Future work will focus on a number of projects. New control systems are required both to lock the laser to a desired operating wavelength and to lock the different sections of the laser to each other in order to ensure that the mirror peaks and the cavity mode are aligned. Mode transformers will be included for better coupling and easier alignment to optical fibers. SGDBR characteristics will involve more waveguide optimization for EA modulators and improvements in the SOA device gain.

In addition, heterodyned devices will be explored as shown in figure 14. This configuration allows two signals to be transmitted with very similar wavelengths so that they can be mixed at the receiver for FR-LO generation. The overall tunability allows the use of wavelength routers to direct the signal to a given destination.

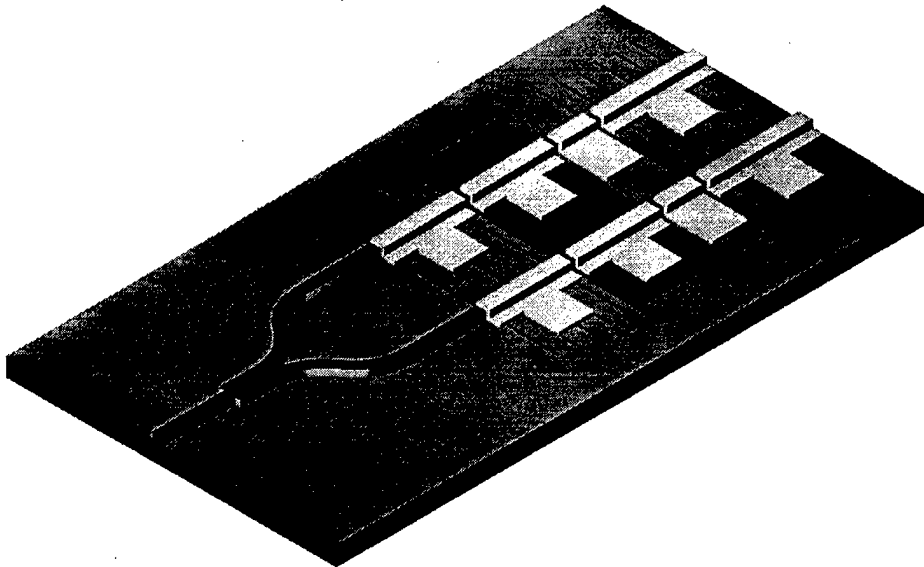


Figure 14. Hetrodyned SGDBR lasers

CONCLUSION

Over the span of this project, we have improved significantly the design of SGDBR lasers with integrated wavelength monitors, modulators and optical amplifiers. Output powers and tuning ranges have increased due to an increase in the number of quantum wells in the active region from four to six. Devices with up to 8 mW of output power with integrated amplifiers and buried hetrostructure devices with 72 nm tuning ranges were realized. To eliminate the parasitic leakage paths we have begun to investigate Fe doped blocking junctions for the device. Work on the wavelength monitor has focused on an external approach, which uses a wavelength dependent coupler in conjunction with a pair of photodetectors. Initial results show better than 0.4 nm sensitivity over a 30 nm range. The most recent work on the laser has focussed on integrating additional components for

increased functionality. We have developed a curved waveguide semiconductor optical amplifier that can be integrated with the laser to increase the output power to greater than 6 mW. We have also investigated SGDBR lasers with integrated electro-absorption modulators. Using a 300 μm long bulk EA modulator we have demonstrated error free data transmission at 2.5 GBit/s with a $2^{31}-1$ pattern length at received powers of -32.5 dBm.

REFERENCES

Mason, B.; Fish, G.A.; DenBaars, S.P.; Coldren, L.A., "Ridge waveguide sampled grating DBR lasers with 22-nm quasi-continuous tuning range." IEEE Photonics Technol. Lett. (USA), vol.10, (no.9), Sept. 1998. p.1211-13.

Mason, B.; DenBaars, S.P.; Coldren, L.A., "Tunable sampled-grating DBR lasers with integrated wavelength monitors.", IEEE Photonics Technol. Lett. (USA), vol.10, (no.8), IEEE, Aug. 1998.

"Widely Tunable Sampled Grating DBR Laser with Integrated Electroabsorption Modulator," B. Mason, G.A. Fish, S.P. DenBaars, and L.A. Coldren, *Photon. Tech. Letts.*, 11, (6), 638-640, (June 1999).

Conferences

Mason, B.; Fish, G.A.; DenBaars, S.P.; Coldren, L.A., "Sampled Grating DBR Lasers with 22 nm Quasi-Continuous Tuning and Monolithically Integrated Wavelength Monitors", 16th IEEE International Semiconductor Laser Conference, Nara Japan, Oct. 4, 1998

"Monolithic Integration of a Widely Tunable Laser and an Electroabsorption Modulator," B. Mason, G.A. Fish, S.P. DenBaars, and L.A. Coldren, *Integrated Photonics Research '99*, Santa Barbara, CA, paper no. RME2, 53-55, (July 19-21, 1999).

"Design of Sampled Grating DBR Lasers with Integrated Semiconductor Optical Amplifiers," B. Mason, G.A. Fish, J. Barton, L.A. Coldren, and S.P. DenBaars, submitted to OFC 2000.

InP Based Photonic Integrated Circuits

© by Thomas Gordon Beck Mason
June, 1999

Electrical and Computer Engineering Department
University of California at Santa Barbara
Santa Barbara, CA 93106

Acknowledgements

None of the work in this dissertation would have been possible without the help and support of a great many people. I am extremely grateful for having had the opportunity to complete my dissertation at UCSB. The excellent facilities and many brilliant people that I have encountered here have made it the most enjoyable experience in my life.

I wish to thank my advisor, Professor Larry Coldren, for the advice and support he has generously provided me during my five years of working with him. I have learned a great deal and I appreciate both the direction and perspective he provided as well as his technical insights. I would like to thank Professor Steve DenBaars for giving me the opportunity to work on MOCVD growth and for his knowledge and support in this area. I am also grateful to the other members of my committee Professor John Bowers and Professor DanBlumenthal for their interest and support of my research.

It is not possible to individually thank all of the different researchers who contributed to this work both in advice and assistance. The cooperative atmosphere that has been fostered at UCSB enabled me to work with a large number of researchers from many different groups. I am deeply grateful for the invaluable assistance they have provided.

I am indebted to Greg Fish whom I have worked closely with for the past four years. Greg has provided many insights and ideas about growth, processing and device design. I am also grateful for having had the opportunity to work with Amber Abare and Ola Sjolund who have always been generous both with their time and their knowledge.

I must also acknowledge the members of the support staff who keep the labs running and provide the excellent facilities at UCSB: Jack Whaley, Bob Hill, Gerry Robinson, and Brian Carrelejo. Included in this is the superb

administrative team of Giulia, Kerri, and Joan, that keeps OTC and Larry's group together.

The research funding for this work was provided by a grant from the Office of Naval Research. It would not have been possible without the help and support of Ron Esman from the U.S. Naval Research Labs.

Last and most importantly I would like to thank my wife Traci for her three years of support and sacrifice. She has been my partner and my best friend helping me and supporting me through many late nights and long hours. My time here at UCSB has taught me to be a better scientist, my time with Traci has taught me to be a better person.

*This dissertation is dedicated
To my wife Traci*

VITA

April 29, 1967	Born in Barnet, United Kingdom
June, 1989	B.A.Sc. Mechanical Engineering, University of Waterloo
December, 1989	M.A.Sc. Aerospace Engineering, University of Toronto
April, 1997	M.S. Electrical and Computer Engineering, University of California, Santa Barbara
June, 1999	Ph.D., Electrical and Computer Engineering University of California, Santa Barbara

Patents

US05469265 Issued Nov. 21, 1995
"Method and apparatus for an optoelectronic smart structure interface with wavelength demodulation of laser sensors."

U.S. Patent Pending
"Tunable Laser Source with Integrated Wavelength Monitor"

Publications

B. Mason, G.A. Fish, S.P. DenBaars, L.A. Coldren, "Monolithic Integration of a Bulk Electro-Absorption Modulator with a Widely Tunable SGDBR Laser.", *IEEE Photonics Technology Letters*, vol.10, (no.9), IEEE, Sept. 1998. p.1256-8.

B. Mason, G.A. Fish, S.P. DenBaars, L.A. Coldren, "Monolithic Integration of a Bulk Electro-Absorption Modulator with a Widely Tunable SGDBR Laser.", *To be presented at IPR '99*

B. Mason, G.A. Fish, S.P. DenBaars, L.A. Coldren, "Sampled Grating DBR Lasers With 22 nm Quasi-Continuous Tuning and Monolithically Integrated Wavelength Monitors," IEEE 16th International Semiconductor Laser Conference, Nara, Japan, 4-8 Oct. 1998

B. Mason, G.A. Fish, S.P. DenBaars, L.A. Coldren, "Ridge Waveguide Sampled Grating DBR Lasers With 22-nm Quasi-Continuous Tuning Range", *IEEE Photonics Technology Letters*, vol.10, (no.9), Sept. 1998. p.1211-13.

G.A. Fish, **B. Mason**, L.A. Coldren, S.P. DenBaars, "Compact, 4*4 InGaAsP-InP Optical Crossconnect With a Scaleable Architecture," *IEEE Photonics Technology Letters*, vol.10, (no.9), Sept. 1998. p.1256-8.

B. Mason, S.P. DenBaars, L.A. Coldren, "Tunable Sampled-Grating DBR Lasers with Integrated Wavelength Monitors," *IEEE Photonics Technology Letters*, vol.10, (no.8), Aug. 1998. p.1085-7.

G.A. Fish, **B. Mason**, L.A. Coldren, S.P. DenBaars, "Improved Compositional Uniformity of InGaAsP Grown by MOCVD Through Modification of the Susceptor Temperature Profile," *Journal of Crystal Growth*, vol.186, (no.1-2), Elsevier, March 1998. p.1-7.

L.A. Coldren, Y.H. Jan, **B. Mason**, M.E. Heimbuch, S.P. DenBaars, "Properties of Widely-Tunable Integrated WDM Sources and Receivers", *Conference Proceedings 10th Annual Meeting IEEE Lasers and Electro-Optics Society, San Francisco, CA, USA, Nov. 1997.*

B. Mason, S.L. Lee, M.E. Heimbuch, and L.A. Coldren, 'Directly Modulated Sampled Grating DBR Lasers for Long Haul Communication Systems', *IEEE Photonics Technology Letters*, vol. 9, (no. 3), March 1997, pp. 377-9

B. Mason, S.L. Lee, M.E. Heimbuch, and L.A. Coldren, "Widely Tunable Lasers for Wavelength Division Multiplexed Communications," *OSA OFC*, Dallas, Feb. 1997

B. Mason, "A Decision Process Used for FPGA Selection in Digital Signal Processing for Fiber Optic Sensors", *Third Annual PLD Design Conference & Exhibit*, San Jose, EE Times proceedings pp. 2.2.2.C, March 1993.

B. Mason, T. Valis and D. Hogg, "Parallel Multiplexing and Demodulation of Fiber-Optic Strain Gauges," *Smart Sensing, Processing and Instrumentation*, SPIE vol. 1918, Albuquerque, February 1993.

B. Mason, T. Valis and D. Hogg, "Commercialization of Fiber-Optic Strain Gauge Systems", *Fiber Optic and Laser Sensors X*, SPIE vol. 1795, Boston, pp. 215-222, September 1992.

B. Mason, D. Hogg, T. Valis, T. Alavie, and R.M. Measures, "Fiber Optic Strain Sensor Signal Processing", *Fiber Optic Sensor-Based Smart Materials and Structures Workshop*, pp. 159-167, April 1992.

D. Hogg, **B. Mason**, T. Valis, and R.M. Measures, "Temperature Compensated Strain Measurement Using Fabry-Perot (FFP) Strain Gauges", *Fiber Optic Sensor-Based Smart Materials and Structures Workshop*, pp. 31-38, April 1992.

D. Hogg, **B. Mason**, T. Valis, and R.M. Measures, "Development of a Fiber Fabry-Perot (FFP) Strain Gauge System", *Active Materials & Adaptive Structures*, Alexandria, VA, pp. 667-672, Nov. 1991.

ABSTRACT

InP Based Photonic Integrated Circuits

By

Thomas Gordon Beck Mason

The continued advancement of growth and processing technology in compound semiconductor materials has opened up new possibilities for the creation of complex photonic devices and circuits. This dissertation discusses the design and development of a photonic circuit based on the monolithic integration of a widely tunable laser with an on chip wavelength monitor. The widely tunable laser is a four-section device with a pair of sampled grating distributed Bragg reflector mirrors. This enables it to use a Vernier effect tuning mechanism to overcome the $\Delta n/n$ characteristic which limits the wavelength range of conventional injection tuned semiconductor lasers. Index tuning in the laser is improved by using a thick low band gap waveguide with an optimized grating etch and regrowth technique. A record 22 nm quasi-continuous tuning range has been demonstrated for a ridge waveguide device. For even greater tuning range, a buried heterostructure device was developed that is capable of tuning over more than 47 nm, enabling it to cover almost 60 DWDM wavelength channels. The complexity of the tuning mechanism in these devices makes it desirable to have a wavelength monitor to provide feedback for control of the laser. In this work, we have developed a compact integrated wavelength monitor that can be fabricated on chip with the tunable sampled grating DBR laser. The wavelength monitor takes advantage of two-mode interference in a semiconductor waveguide to create a wavelength dependent splitter. Monitors based on this principle have been successfully integrated with both ridge waveguide and buried heterostructure sampled grating DBR lasers. This dissertation reviews all of the aspects of the design, growth, processing and packaging of these devices.

Table of Contents

CHAPTER 1 INTRODUCTION.....	1
1.1 PHOTONIC DEVICES AND SYSTEMS	1
1.2 WDM COMMUNICATION	2
1.3 SEMICONDUCTOR LASERS	3
1.4 WAVELENGTH MONITORING AND CONTROL	8
1.5 PHOTONIC INTEGRATED CIRCUITS	10
CHAPTER 2 TUNABLE LASERS.....	13
2.1 INTRODUCTION	13
2.1.1 Motivation for development of widely tunable lasers	13
2.1.2 Types of widely tunable lasers	18
2.1.3 SGDBR lasers advantages and disadvantages	26
2.2 DESIGN CONSIDERATIONS FOR WIDELY TUNABLE SGDBR LASERS	29
2.2.1 Waveguide Structure	30
2.2.2 Mirror Design.....	35
2.2.3 Cavity Structure.....	40
2.2.4 Optimization of Ridge Width.....	43
2.3 INDEX TUNING IN SEMICONDUCTOR WAVEGUIDES	45
2.3.1 Model of Index tuning mechanisms	46
2.3.2 Theoretical and practical tuning performance	52
2.4 GRATING ETCHING PROCESS.....	61
2.4.1 Holographic Patterning	62
2.4.2 Wet etched gratings.....	64
2.4.3 Dry etched gratings.....	65
2.5 CONTINUOUSLY TUNABLE RIDGE SGDBR LASERS.....	68
2.5.1 Device structure	68
2.5.2 Tuning Characteristics.....	69
2.5.3 Dynamic Characteristics	73
2.6 BURIED HETEROSTRUCTURE DEVICES.....	76
2.6.1 Device Structure	76
2.6.2 Tuning Characteristics.....	79
2.7 SUMMARY	83
CHAPTER 3 WAVELENGTH MONITORING.....	87
3.1 INTRODUCTION	87
3.1.1 Importance of wavelength monitoring	88

3.1.2	<i>Types of wavelength monitors</i>	90
3.1.3	<i>Advantages of integrated wavelength monitoring</i>	93
3.1.4	<i>Methods for Integrated Wavelength Monitoring</i>	95
3.2	TMI WAVELENGTH MONITORS	97
3.2.1	<i>Two mode interference in waveguides</i>	97
3.2.2	<i>BPM simulations of wavelength monitor</i>	105
3.2.3	<i>Ridge TMI Wavelength Monitor Test Results</i>	109
3.3	INTEGRATION OF WAVELENGTH MONITORS WITH TUNABLE LASERS	111
3.3.1	<i>Ridge waveguide laser with integrated wavelength monitor</i>	112
3.3.2	<i>Buried Heterostructure Laser with Integrated Wavelength Monitor</i>	115
3.3.3	<i>Sources of Spurious Signals</i>	124
3.4	SUMMARY	127

CHAPTER 4 MOCVD GROWTH FOR INP PIC'S 131

4.1	INTRODUCTION	131
4.1.1	<i>MOCVD Growth Fundamentals</i>	131
4.1.2	<i>Source Materials</i>	132
4.1.3	<i>Reactor Design</i>	135
4.2	BASE STRUCTURE GROWTH AND CHARACTERIZATION	136
4.2.1	<i>Characterization Tools</i>	136
4.2.2	<i>Determination of Material Parameters</i>	143
4.2.3	<i>MOCVD Growth Conditions</i>	148
4.2.4	<i>Quantum Well Design</i>	150
4.2.5	<i>Growth Structure and Doping</i>	154
4.3	GRATING REGROWTH	156
4.3.1	<i>Surface Preparation</i>	156
4.3.2	<i>Regrowth Interface</i>	157
4.4	BURIED HETEROSTRUCTURE LASER REGROWTH	162
4.5	SUMMARY	170

CHAPTER 5 DEVICE PACKAGING AND SYSTEM TESTING..... 175

5.1	INTRODUCTION	175
5.2	DEVICE PACKAGING	176
5.2.1	<i>SGDBR Laser Butterfly Package Design</i>	176
5.2.2	<i>Fiber attachment</i>	177
5.3	DEVICE CHARACTERIZATION AND SYSTEM TESTING	183
5.3.1	<i>Dynamic Tuning Characteristics</i>	183
5.3.2	<i>BERT results and analysis</i>	185
5.4	SUMMARY	190

CHAPTER 6	SUMMARY AND SUGGESTIONS FOR FUTURE WORK	193
6.1	SUMMARY OF THESIS	193
6.1.1	<i>Tunable Lasers</i>	193
6.1.2	<i>Wavelength Monitoring</i>	194
6.1.3	<i>Growth and Fabrication</i>	195
6.1.4	<i>Packaging</i>	196
6.2	SUGGESTIONS FOR FUTURE WORK	197
6.2.1	<i>Tunable Laser with Integrated Modulator</i>	197
6.2.2	<i>Integrated wavelength converters</i>	199
APPENDIX A	BURIED RIDGE SGDBR FABRICATION PROCESS.....	201
APPENDIX B	SUBMOUNT FABRICATION PROCESSES.....	211
APPENDIX C	DEVICE PACKAGING PROCESS	217

Chapter 1

Introduction

1.1 Photonic Devices and Systems

The development of optoelectronic component technology is proceeding along a path that in many ways mirrors the developments that occurred in electronics almost two decades earlier. Increasingly complex and more highly integrated devices are being developed using both hybrid and monolithic integration techniques. This rapid advancement in technology is both fueling and being driven by an explosive growth in the telecommunications industry. In much the same way as the advent of personal computers led to an explosion in integrated circuit technology. The new field of photonics which deals with devices or systems that emit, detect, or transport light is enabling a revolution in the communications industry. This revolution is fundamentally changing the way that society interacts with and uses information.

Currently we are at the very nascent stages of the development of photonic technology. Discrete components predominate as they did in the early stages of electronic technology. In the field of fiber optic communications the most widely used photonic devices are the semiconductor laser and the PIN photodiode. These devices perform two of the most basic functions for photonic components emitting and detecting light. The challenges inherent in the development of photonic integrated circuits (PIC's) are much greater than for electronic IC's. The available technology is much more diverse and the fundamental components are more complex.

For current and next generation fiber optic communication systems photonic devices are being used for transmitters and receivers, amplifiers, routers, switches, filters, and multiplexers. The majority of these tasks are currently

performed by interconnected discrete components or by hybrid devices. The main driver towards developing PIC's with increased functionality is reduced cost. For a typical InP based laser or receiver used in a long haul network up to 80% of the cost is in the packaging. Of this a significant amount is related to the pigtailling of the optical fiber. Increasing the functions that can be performed within the device through the integration of multiple photonic elements on chip can therefore significantly reduce the cost. The other area where cost is a driver for PIC technology is in the development of the all optical network which can route and switch data entirely within the optical layer. A simple example of this is selectively adding or dropping an optical channel in a wavelength division multiplexed (WDM) link. Achieving this requires a substantial increase in the complexity and functionality of the photonic components but results in a tremendous reduction in the overall cost of the system when compared to a conventional SONET based electrical add drop multiplexer [1, 2].

1.2 WDM Communication

The ability to expand the capacity of existing fiber links has been one of the main drivers behind the implementation of WDM technology. For many long haul carriers it is the most cost effective way to cope with the exploding bandwidth demands that have been created by the Internet. Current dense WDM technology uses arrays of fixed wavelength laser transmitters with wavelengths that are equally spaced at 100 GHz intervals. As channel counts increase to 80 or more the problems associated with supplying and inventorying multiple fixed wavelength lasers become more and more difficult. This has created a strong desire in the industry for reconfigurable or tunable semiconductor lasers. These could be used to simplify the ordering of spares and also as direct replacements for fixed wavelength devices. Using tunable or wavelength settable lasers opens up new opportunities for network reconfiguration and dynamic bandwidth allocation in current DWDM system architectures. For next generation fiber optic networks WDM packet

switching and wavelength routing technologies will enable dramatic increases in flexibility and capacity [3]. Wavelength tunable sources and receivers are enabling components for these technologies. There are numerous examples of proposed network architectures that rely on tunable or wavelength settable sources. These include WDM passive optical networks (PON's) which use a single tunable laser at the head end office to route data to distributed remote optical networking units (Figure 1-1)[4]. This is one proposed strategy for providing low cost fiber to the home (FTTH) or fiber to the curb (FTTC) service.

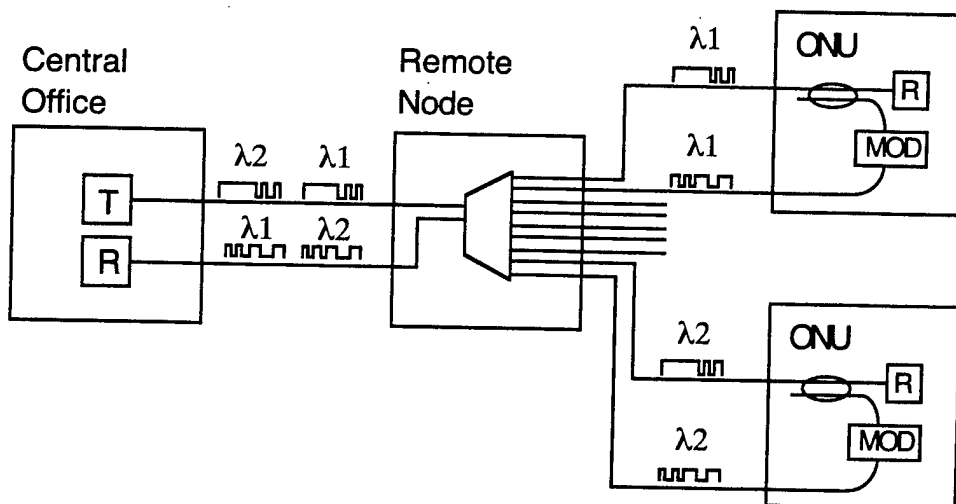


Figure 1-1 Wavelength Routed Passive Optical Network

1.3 Semiconductor Lasers

There has been a gradual progression in the complexity and capability of laser sources for telecommunications. Early systems employed simple Fabry-Perot laser diodes with no wavelength control and multiple longitudinal modes (Figure 1-2)[5].

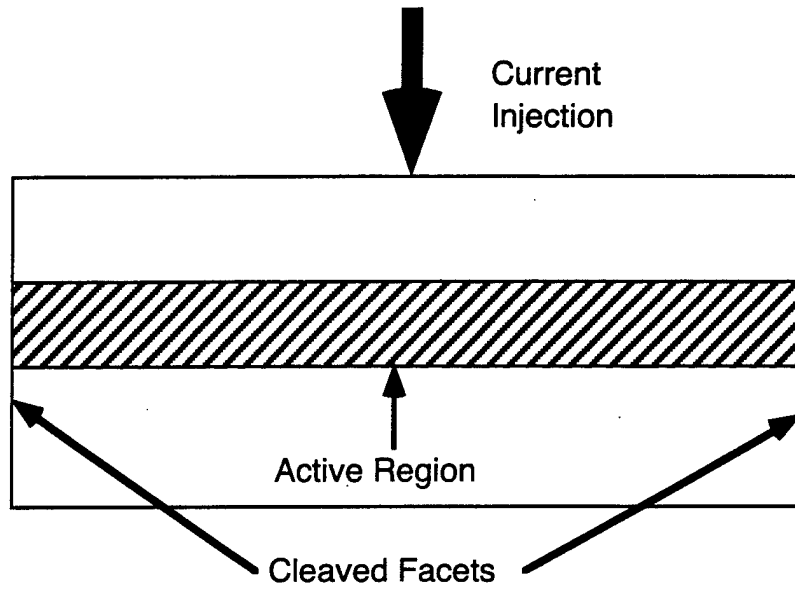


Figure 1-2 Fabry-Perot Laser Diode

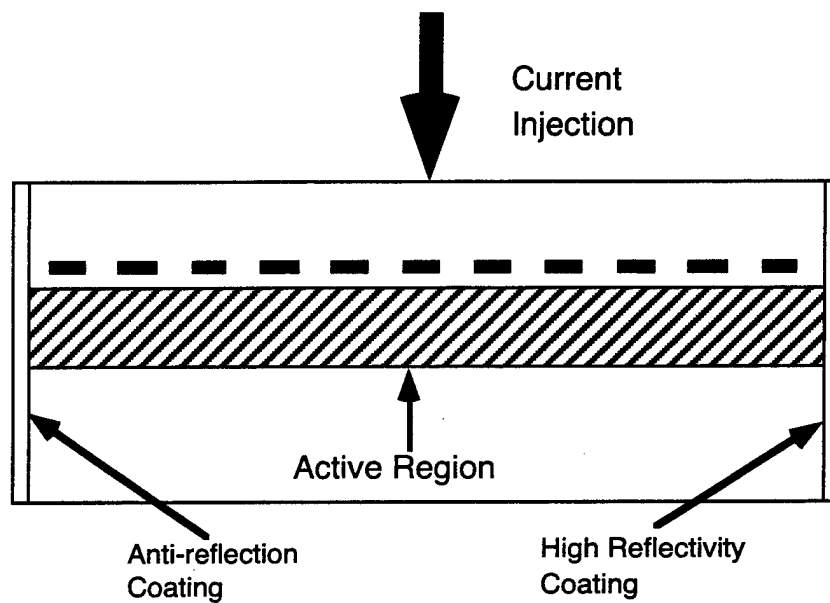


Figure 1-3 Distributed Feedback Laser Diode

As bit rates increased and transmission spans became longer single mode distributed feedback (DFB) lasers were developed to provide fixed wavelength sources with a narrow spectrum to reduce dispersion induced pulse broadening [6]. These lasers incorporated a Bragg grating in the laser cavity to stabilize the wavelength (Figure 1-3). For WDM systems DFB lasers could be fabricated with different grating periods to provide lasers for the different wavelength channels. Fine tuning of the lasing wavelength could be realized by adjusting the temperature of the device. These lasers can be directly modulated in transmission systems operating at Bit rates up to 2.488 Gbit/s and they currently dominate the market for telecommunications applications

When a laser is intensity modulated its output light also undergoes some frequency modulation. This frequency modulation is called chirp and its magnitude is governed by the linewidth enhancement factor for the laser. This frequency chirp limits the maximum distance bit rate product for transmission systems. For very long haul transmission or higher bandwidth applications such as OC-192 systems, which operate at 10 Gbit/s, direct modulation is unsuitable. For these systems external modulators based on lithium niobate Mach-Zehnder interferometers are commonly used. External modulators are expensive, have high insertion loss and require a fixed input polarization. These drawbacks led to the development of the electro-absorption modulator laser or EML (Figure 1-4)[7]. This device is one of the first commercially successful photonic integrated circuits. It consists of a standard DFB laser with an integrated EA modulator. Putting the modulator on chip with the laser gives a dramatic cost reduction over external lithium niobate modulators with better performance than is possible in direct modulated devices. The commercial success of these devices is a strong indicator of the future benefits that can be realized through continued development of PIC's.

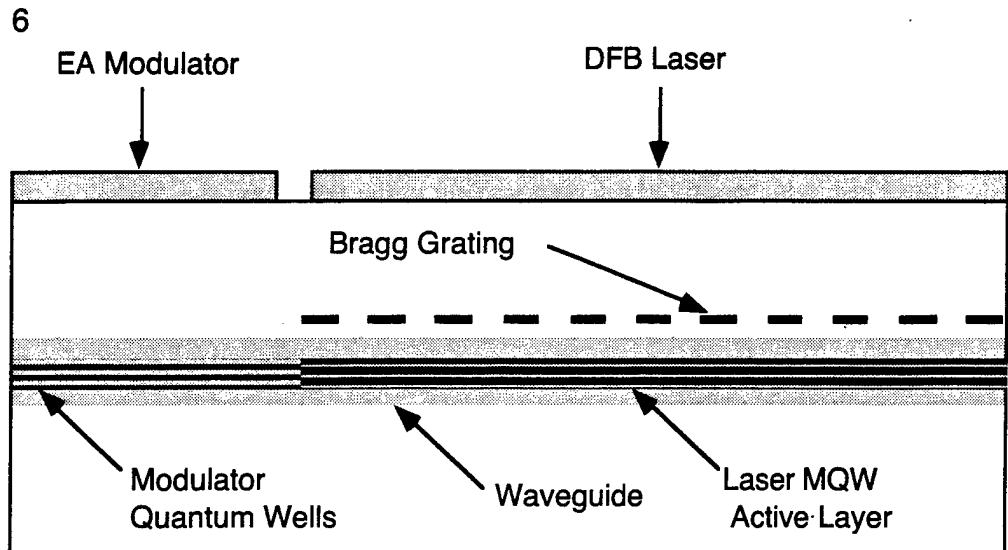


Figure 1-4 DFB Laser with integrated electro-absorption modulator

The next phase in transmitter development will likely involve the use of tunable laser sources that can rapidly switch between multiple WDM channels. These more advanced tunable lasers typically are multi-section devices that require complicated control systems with wavelength feedback. Long term stability and wavelength control are two critical issues that may delay but will not ultimately prevent these devices from becoming widely used in data and telecommunications networks. Early attempts at making multi-wavelength sources have included DFB lasers that are temperature tuned (Figure 1-5), arrays of fixed wavelength lasers with integrated combiners and modulators [8] and electrically tuned distributed Bragg reflector (DBR) lasers (Figure 1-6) [9]. New multi-element widely tunable lasers with the capability of tuning over hundreds of channels represent the current state of the art in semiconductor laser development. Chapter 2 of this thesis discusses in detail the design and development of a widely tunable Sampled Grating Distributed Bragg Reflector (SGDBR) laser.

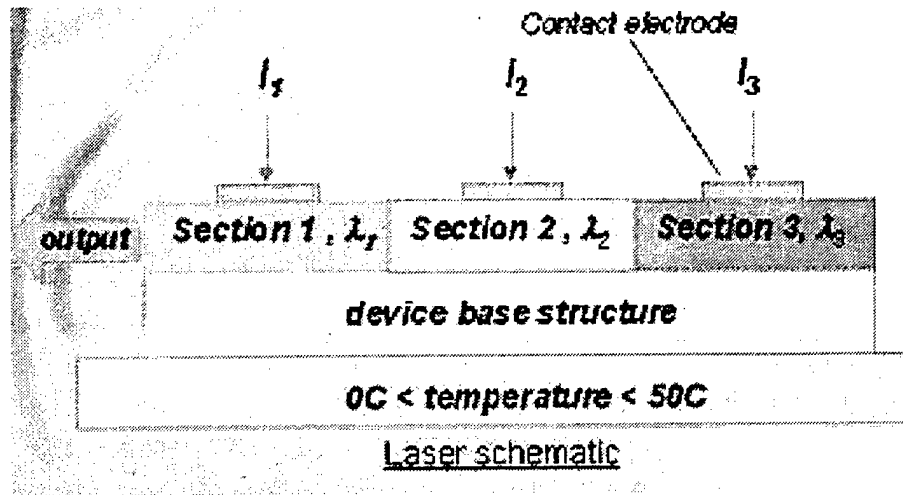


Figure 1-5 Temperature Tuned Multi-Section DFB Laser

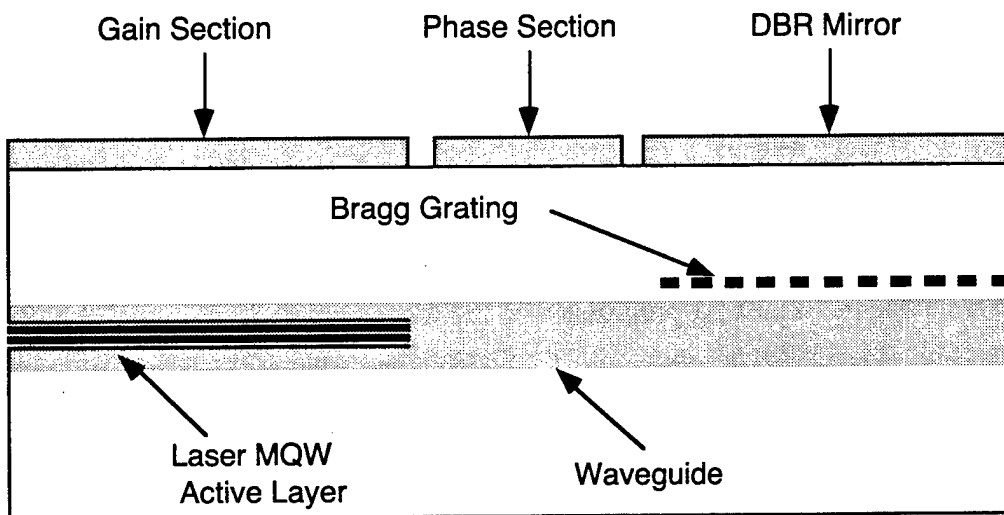


Figure 1-6 Tunable three section distributed Bragg reflector laser

1.4 Wavelength Monitoring and Control

For both tunable and fixed wavelength lasers in WDM systems wavelength stability and control is an important issue. Current dense WDM systems use a 100 GHz channel spacing and can have over 96 different channels. Next generation systems will move to an even tighter frequency spacing of 50 GHz or about 0.4 nm. Over time aging of a laser can lead to degradation in its characteristics. For fixed wavelength lasers this can result in a shift in the operating wavelength and for tunable lasers it can change the entire tuning curve. To compensate for this current systems employ wavelength lockers. These lockers use an etalon or a differential filter to monitor the laser wavelength. A control system uses this feedback to keep the laser at the desired wavelength for its channel. For DFB lasers this is accomplished by adjusting the device temperature or fine tuning the drive current. In tunable lasers a more complicated wavelength monitor is required that can enable the device to lock to many different channels [10].

Etalon or differential filter based wavelength lockers can be integrated directly into the laser package to monitor the back facet output (Figure 1-7)[11]. They can also be used as external components with a coupler to tap off a portion of the laser light for monitoring (Figure 1-8). Integrating the monitor in the same package with the laser is a more compact lower cost option than using an external locker. The next progression in this development is to monolithically integrate the wavelength monitor with the device. This will yield even more dramatic cost reductions by simplifying the packaging procedure and eliminating multiple components. Chapter 3 of this thesis investigates the design and development of an integrated semiconductor wavelength monitor.

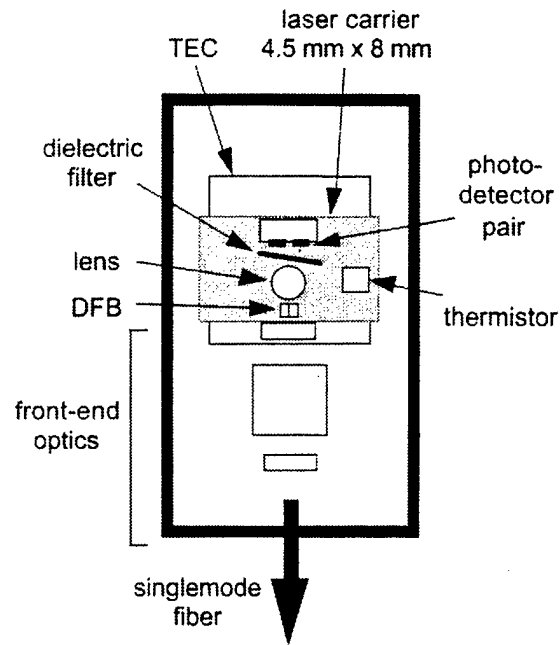


Figure 1-7 Laser with integrated wavelength monitor.



Figure 1-8 Commercial packaged wavelength locker

1.5 Photonic Integrated Circuits

The design and fabrication of photonic integrated circuits relies on the development of compatible building block elements that can be interconnected to form a more advanced functional element. By using standard elements and interconnecting them in different ways we can create components with a variety of different functions. A complicated multi-element photonic device is not by definition a PIC. It is only by using a design process that relies on the integration of standardized building block elements that a PIC is formed. The advantages of this approach are tremendous. Since the same basic elements are re-used multiple times PIC designs can benefit from a well developed device design that is fully characterized. In CMOS IC technology these building blocks are at the most basic level the n-mos and p-mos transistors. PIC's can be differentiated from IC's in two ways. The first is that there is generally a much larger variety of basic building block elements in a PIC and the second is that the interconnection of these elements is frequently the most difficult problem in the design. For a PIC the basic building blocks must share a common fabrication procedure, and base structure. These building blocks can be divided into three main categories. One category contains active elements that perform a direct optical to electrical conversion like emitters, detectors, amplifiers and modulators. These elements contain material with a bandgap that is smaller than or close to the wavelength of light in the circuit. Another category contains active elements that are tuned with carrier injection or reverse bias, this includes phase shifters, grating mirrors and switches. The third category contains passive components that are used to interconnect the various active elements. These include straight and curved waveguide sections, splitters, combiners and couplers. Integrating an active section with a phase shifter and a pair of sampled grating mirrors creates a tunable laser. Using the same platform we can also create an interferometric wavelength converter using simple MMI based y-branch splitter elements and a pair of gain sections. Since these devices were created using a common platform they can be easily

integrated to form a tunable wavelength converter with an integrated source
Figure 1-9.

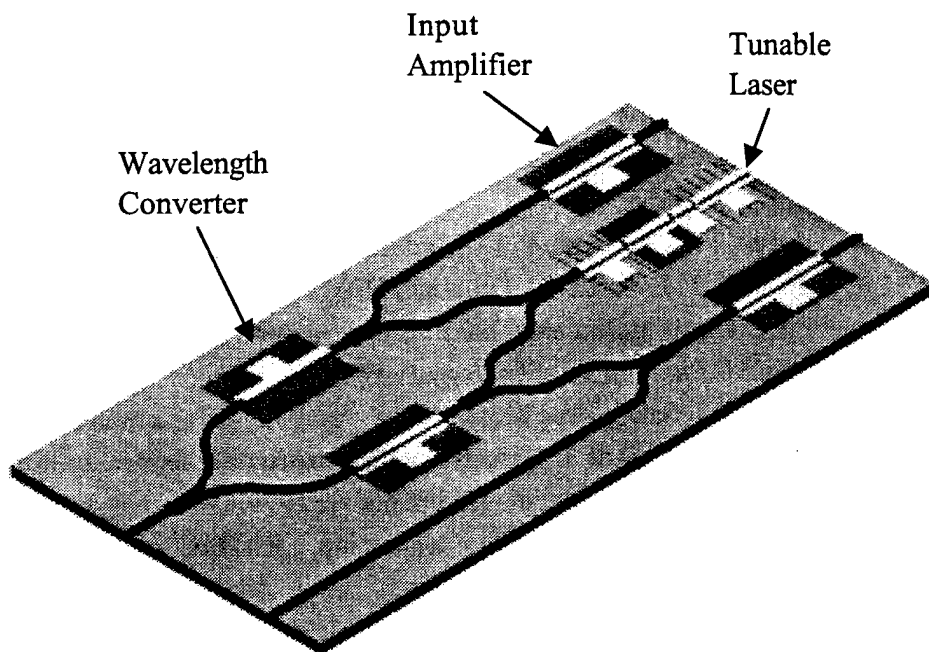


Figure 1-9 Interferometric wavelength converter with integrated tunable laser source.

The key to the PIC technology is having an established set of building block elements and the appropriate fabrication technology to integrate them together on a common substrate. In this thesis we discuss the design, fabrication, and testing of a simple PIC which incorporates a tunable semiconductor laser and an integrated wavelength monitor.

References

- [1] S. L. Borthick, "Fire sale in the fibersphere? [optical communication]," *Business Communications Review*, vol. 27, pp. 30-4, 1997.
- [2] K. Sato, "Recent advances in photonic transport network technologies," , 1996.
- [3] D. J. Blumenthal, P. R. Prucnal, and J. R. Sauer, "Photonic packet switches: architectures and experimental implementations," *Proceedings of the IEEE*, vol. 82, pp. 1650-67, 1994.
- [4] N. J. Frigo, P. P. Iannone, P. D. Magill, T. E. Darcie, M. M. Downs, B. N. Desai, U. Koren, T. L. Koch, C. Dragone, H. M. Presby, and G. E. Bodeep, "A wavelength-division multiplexed passive optical network with cost-shared components," *IEEE Photonics Technology Letters*, vol. 6, pp. 1365-7, 1994.
- [5] S. Skiba, K. Sakai, Y. Matsushima, and T. Yamamoto, "Room temperature CW operation of InGaAsP/InP heterostructure lasers emitting at 1.56 μm ," *Electronics Letters*, vol. 15, pp. 606-7, 1979.
- [6] A. Doi, T. Fukuzawa, M. Nakamura, R. Ito, and K. Aiki, "InGaAsP/InP distributed-feedback injection lasers fabricated by one-step liquid phase epitaxy," *Applied Physics Letters*, vol. 35, pp. 441-3, 1979.
- [7] A. Ramdane, P. Krauz, E. V. K. Rao, A. Hamoudi, A. Ougazzaden, D. Robein, A. Gloukhian, J. Landreau, M. Carre, and A. Mircea, "Monolithic integration of strained layer multi-quantum well distributed feedback laser and external modulator by selective disordering," , 1994.
- [8] C. E. Zah, M. R. Amersfoort, B. N. Pathak, F. J. Favire, P. S. D. Lin, N. C. Andreadakis, A. W. Rajhel, R. Bhat, C. Caneau, M. A. Koza, and J. Gamelin, "Multiwavelength DFB laser arrays with integrated combiner and optical amplifier for WDM optical networks," *Ieee Journal of Selected Topics in Quantum Electronics*, vol. 3, pp. 584-597, 1997.
- [9] S. L. Woodward, I. M. I. Habbab, T. L. Koch, and U. Koren, "The Side-Mode-Suppression Ratio of a Tunable Dbr Laser," *Ieee Photonics Technology Letters*, vol. 2, pp. 854-856, 1990.
- [10] H. Ishii, F. Kano, and Y. Yoshikuni, "Wavelength stabilization of a superstructure-grating DBR laser for WDM networks," , 1997.
- [11] B. Villeneuve, M. Cyr, and H. B. Kim, "High-stability wavelength-controlled DFB laser sources for dense WDM applications," , 1998.

Chapter 2

Tunable Lasers

2.1 Introduction

This chapter will cover the design, growth and fabrication issues related to the development of widely tunable semiconductor lasers based on the sampled grating distributed Bragg reflector design (SGDBR). These devices are the fundamental building block for all of the photonic integrated circuits that are discussed in this thesis.

2.1.1 *Motivation for development of widely tunable lasers*

Widely tunable lasers are essential components for a wide variety of wavelength division multiplexing (WDM) and packet switching network architectures. They can be used as replacement sources in long haul dense WDM communication systems or for wavelength routing in access networks[1]. They are also important devices for next generation phased array radar systems that use fiber-optic control for true-time delay beam steering[2, 3].

The three most successful types of widely tunable lasers are the super structure grating distributed Bragg reflector laser (SSGDBR)[4, 5], the grating assisted co-directional coupler with sampled grating reflector laser (GCSR)[6], and the sampled grating DBR laser (SGDBR)[7, 8]. All of these devices are capable of continuous tuning ranges greater than 40 nm, and high-speed data transmission under direct modulation. However SGDBR lasers and other widely tunable designs have fairly large optical cavities which limit their direct modulation bandwidth to between 3 and 4 GHz[9, 10]. This enables them to be used in OC-48 data transmission systems under direct modulation.

However it is insufficient for use in most phased array radar systems or in OC-192 data transmission networks operating at 10 Gbit/s. In these applications external modulators are frequently used to apply the r.f. signal or data to the optical carrier.

Of the three different laser types the SGDBR and the SSGDBR are best suited for use in photonic integrated circuits. Devices such as modulators and wavelength converters can be integrated onto the front output waveguide and wavelength-monitoring elements can be integrated onto the back. This is not possible with the GCSR because it uses the front facet of the laser chip as a mirror. It is also difficult due to the dual vertically integrated waveguide structure.

Phased array radar beam steering

Phased array antenna systems provide great flexibility for radar beam formation, steering and detection. The use of multiple transmitters results in a diversity of beam shapes permitting various radar functions to be performed simultaneously. Electronic steering is much faster and more robust than mechanical steering, and higher powers can be generated from the multiple transmission elements than is possible with a single element transmitter. Unfortunately electronic phase shifters provide only a few fixed phase shifts, tend to have high side lobes due to phase errors, and only operate at fixed frequencies. The use of fiber optic control for phased array radar promises to reduce or eliminate many of the traditional problems associated with these systems such as excessive weight and size, and susceptibility to electromagnetic interference. Optical control techniques enable the use of true time-delay beam steering, which allows for a wide instantaneous bandwidth and squint-free operation. In this type of system an optical carrier is used for the r.f. signal feed to the antenna array. The signal is split and fed to the array elements using a combination of non-dispersive and highly dispersive fiber of varying lengths such that the time delay is matched for all of the elements at a particular wavelength. Tuning the wavelength of the laser away from this nominal value changes the relative delay between the microwave signals fed to the array. This delay is used to steer the beam[11]. Using tunable lasers with a

wide tuning range enables greater control over the beam. Currently however most widely tunable lasers are external cavity devices that use mechanical tuning. Integrated semiconductor lasers, which use current injection for tuning, have the capability to provide much faster beam steering. They are also smaller, more mechanically robust and lower cost. However until recently these integrated tunable lasers had tuning ranges that were limited to 15 nm [12] as compared to more than 50 nm for external cavity devices. The tuning range in conventional tunable lasers such as distributed Bragg reflector (DBR) types is limited by the maximum index change that can be achieved in the semiconductor waveguide.

Recently there has been a great deal of research on new widely tunable semiconductor lasers which use Vernier effect tuning mechanisms to enable them to tune over more than 60 nm [13]. An example of these is the sampled grating DBR laser. This device is similar in basic structure to a conventional fixed wavelength DFB laser except that it has four separate sections, one for gain, one for phase control and two mirrors (Figure 2-1). The gratings in the mirrors are periodically sampled. This creates multiple peaks in the mirror reflection spectrum. The spacing between the peaks is slightly shifted for the front and back mirror allowing only a single pair to be aligned concurrently. The laser operates at the wavelength where the two mirror peaks are aligned and the cavity loss is at a minimum. The laser wavelength can be tuned over a much wider range by using different pairs of mirror peaks. It is possible to tune the laser continuously over the entire gain spectrum of the active material by controlling both mirrors and the phase and gain sections independently.

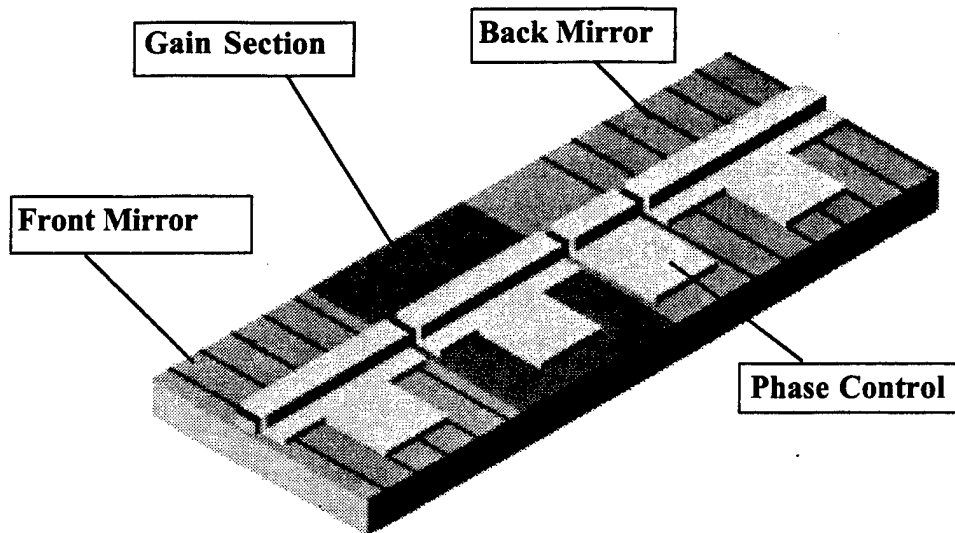


Figure 2-1 Widely tunable SGDBR Laser

One important problem for lasers of this type is the issue of control. Unlike DBR lasers there is no simple monotonic relationship between the tuning current and the output wavelength. To achieve rapid reconfiguration of the laser to any desired wavelength requires a complex control system with four rapidly adjustable current sources. The other important issue which affects all tunable lasers that employ carrier injection tuning is wavelength stability. Over time semiconductor lasers are subject to aging which causes their wavelength to drift. Typically the effect is due to an increase in leakage current at the parasitic junction for buried heterostructure lasers and or a reduction of the carrier lifetime in the waveguide [14]. This wavelength drift can be disastrous in commercial dense wavelength division multiplexed communications systems where channels are typically spaced only 100 GHz (0.8 nm) apart. It can also lead to a significant degradation in the performance of a phased array radar system. Sampled grating DBR lasers are particularly susceptible to this type of degradation since a small change in the index-tuning characteristic for one of

the mirrors can lead to a large change in the laser wavelength. In commercial DWDM systems the most common approach is to use an external wavelength locker in conjunction with a temperature controller to thermally tune the device and lock it at the correct wavelength. These wavelength lockers have a differential output that is matched at the desired wavelength making them suitable for use with fixed wavelength lasers.

Widely tunable lasers require a wavelength monitor that can track the laser wavelength over its entire tuning range. The monitor must be insensitive to the optical power level over a wide dynamic range and sufficiently accurate to guarantee better than 0.01 nm wavelength stability.

DWDM Communication Systems

The proliferation of multi-channel dense wavelength division multiplexed transmission systems has led to an increased demand for widely tunable lasers. Current DWDM systems on the market offer as many as 80 wavelength channels typically spaced at 100 GHz but in some systems as tightly as 50 GHz apart. In SONET systems which use a redundant ring architecture there are two lasers for every channel. Since most commercially available DFB lasers can only be temperature tuned to one or two channels systems designers must specify 40 to 80 different laser types. They also must stock spares for each channel. With tunable lasers a single laser type can be used for every channel and configured when installed to operate at the correct wavelength. This means that only a single laser must be specified and purchased. All of the components in the system are now identical and the number of spares that must be kept is drastically reduced. A further benefit from this is that wavelengths can now be dynamically re-allocated as traffic demands fluctuate throughout the network. In next generation systems the fast tuning of these lasers will enable data routing at the packet level[15]. This will result in a dramatic increase in network capacity and a significant reduction in the cost of the routing and switching equipment due to the high efficiency and low cost at which data can be routed at the optical level. Wavelength accuracy and stability are critical in these types of systems particularly as the channel density is increased with the migration towards the theoretical capacity limit of

1 (bit/s)/Hertz. Wavelength monitoring and control will be required for tunable lasers used in these applications.

Next generation access networks based on WDM passive optical networks (PON's) also represent a significant potential application for widely tunable lasers. The critical issue for current PON's is one of reducing the cost yet providing a scaleable architecture to enable the system installer to upgrade as capacity demands increase. AT&T Bell Laboratories has developed a network architecture that uses a tunable laser and a remote wavelength router to provide a time shared WDM network. In this system the tunable laser routes data to an optical networking unit (ONU) by tuning to the wavelength that corresponds to that unit's port on the wavelength router[16]. Data is transmitted downstream through the router to the ONU where it is split by a passive tap with a portion of the light detected by a receiver. The remaining light is looped back to the central office through a modulator. After the downstream message is transmitted the laser sends a signal with no data on it. This signal is modulated by the ONU to send back the upstream data. Sharing the cost of the tunable laser and the wavelength router between multiple ONU's dramatically lowers the cost of the network. A tunable laser is essential since it must be able to track the drift in the wavelength router which is remotely located. This system is scaleable since additional tunable lasers with other services can be added to simultaneously transmit to more than one ONU. Wavelength control is important in this system but it is inherent in the tracking function for the laser and the ONU so absolute wavelength accuracy is not essential.

2.1.2 *Types of widely tunable lasers*

There are a wide variety of tunable laser designs and they all have a number of common characteristics. They have active sections for gain integrated with passive waveguide elements that are used for wavelength control, they employ some form of grating architecture for wavelength discrimination, and in all but

the MFL case which is not really a tunable laser they use carrier injection for tuning.

Distributed Bragg Reflector (DBR)

One of the earliest types of tunable lasers is the distributed Bragg reflector laser (Figure 2-2). In this device a waveguide Bragg grating is used to provide a narrow band reflector for one half of the laser resonator. The cleaved front facet of the device acts as the second mirror. The grating is formed by etching a periodic corrugation into the waveguide in the mirror section. This results in a periodic index variation for the guided mode. This periodic index variation provides coupling between the forward and backward travelling waveguide modes. The reflection spectrum of a Bragg grating can be determined analytically using coupled mode theory or numerically using a transmission matrix analysis. In either case there is a reflection maxima at what is known as the Bragg wavelength. The Bragg wavelength λ_B for a grating with a period Λ is given by (2-1). Where \bar{n} is the effective index of the waveguide mode.

$$\lambda_B = 2\bar{n}\Lambda \quad (2-1)$$

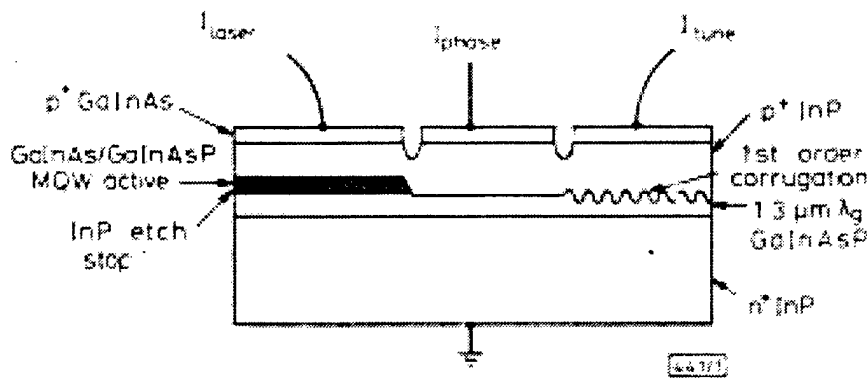


Figure 2-2 Structure of three section DBR laser.

Injecting carriers into the waveguide lowers its index of refraction which reduces the effective index of the mode. This causes the Bragg peak to tune to shorter wavelengths. In this type of tuning the maximum change in the laser wavelength is directly proportional to the maximum change in the effective index the so called $\Delta n/\bar{n}$ limit. DBR lasers use a long grating with a weak coupling coefficient or κ . This gives the mirror a high reflectivity and a narrow reflection spectrum. Since the laser operates at the wavelength corresponding to the minimum threshold gain it will tend to lase at the wavelength corresponding to the longitudinal cavity mode, which is nearest to the Bragg wavelength. Providing the grating peak is within the gain spectrum of the quantum wells. To achieve continuous wavelength coverage a phase control section is typically added to these lasers. This is an additional passive waveguide section, which can be tuned to lock the cavity mode to the Bragg peak. This not only allows continuous tuning of the laser, it also increases the side mode suppression ratio and reduces the threshold current for a given wavelength.

Fabrication of a DBR laser requires the integration of an active gain section, comprised of either quantum wells or bulk material having a band gap wavelength around 1550 nm, with passive waveguide regions for the mirror and phase sections. The waveguide for the passive sections must have a bandgap energy, which is greater than the wavelength of the laser to minimize loss in these sections. However to optimize tuning response a low bandgap material is desirable. The best tradeoff between index tuning increased loss with injected current is found with a waveguide having a band gap wavelength around 1400 nm.

DBR lasers are still not widely available commercially predominantly due to the increased fabrication complexity associated with the formation of active and passive sections within a single laser cavity. This is a difficulty that affects all tunable lasers. The best DBR lasers that have been demonstrated to date have tuning ranges of 17 nm with output powers of greater than 10 mW. The simple structure and monotonic tuning characteristic of these devices makes them

attractive despite the fact that their tuning range is much lower than is possible with other designs.

Sampled Grating DBR (SGDBR)

The sampled grating DBR is similar in structure to a DBR laser except that it employs a Vernier tuning mechanism to increase its' tuning range. The SGDBR uses a pair of grating mirrors at either end of the cavity (Figure 2-3). The gratings in the mirrors are periodically sampled or blanked out. This results in a sequence of equally spaced short grating bursts. These give the mirrors a comb like reflection spectrum with multiple equally spaced peaks. The peak spacing is inversely proportional to the sampling period. Different sampling periods are used in the front and back mirror to give them different peak spacing. This allows only a single pair of peaks to be aligned concurrently. The laser operates at the wavelength where the peaks from the front and back mirrors are aligned (Figure 2-4).

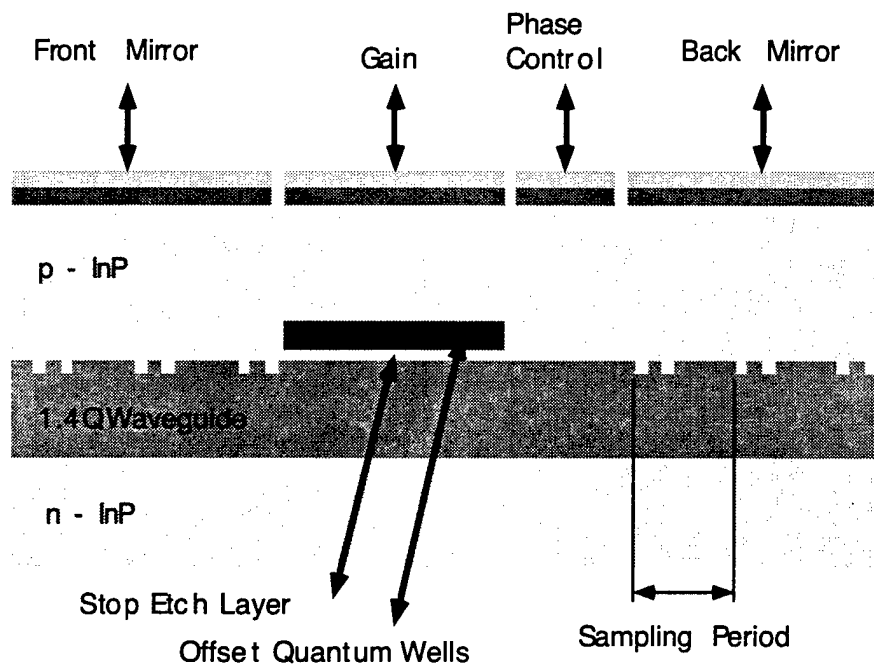


Figure 2-3 Cross section of SGDBR laser

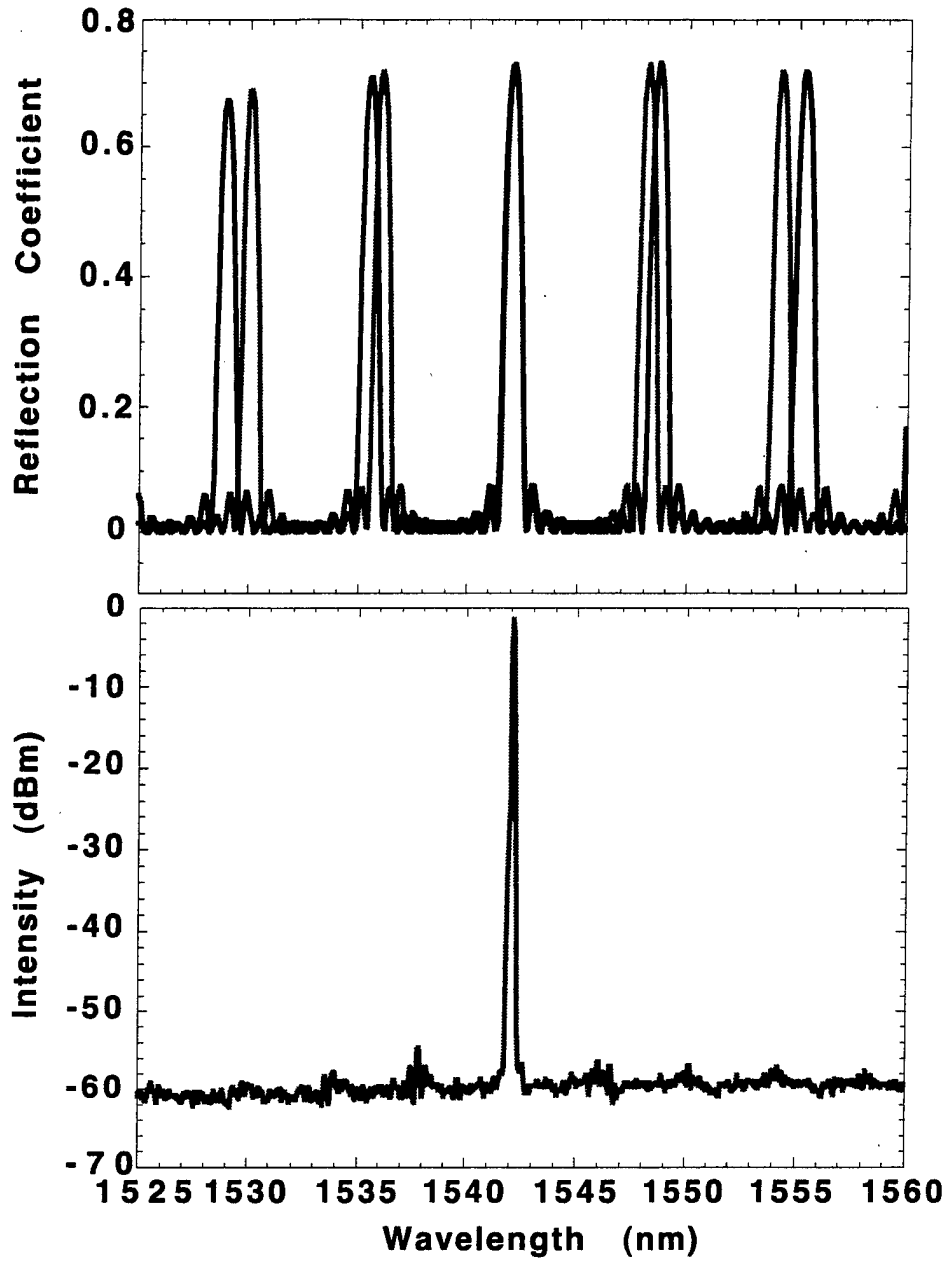


Figure 2-4 Superimposed sampled grating mirror reflection spectra and corresponding laser spectrum.

Just as in the DBR laser the mirrors can be tuned by carrier injection. This causes all of the peaks to shift together. Tuning the front and back mirrors in Tandem enables the laser wavelength to be continuously tuned over a narrow range. By differentially tuning the mirrors a new set of peaks can be brought into alignment allowing the laser wavelength to be tuned over a new range. Taking advantage of this Vernier tuning mechanism allows the laser to be tuned over a range of $M \cdot \Delta n/\bar{n}$ where M is the number of peaks used. This gives it a much wider tuning range than is possible with the simple DBR laser. The theoretical limit on the number of peaks that can be used and thus the tuning range is determined by the repeat mode spacing. The maximum number of peaks is given by (2-2), where λ_p is the peak spacing and $\Delta\lambda_s$ is the difference in peak spacing between the front and back mirrors.

$$M = \frac{\lambda_p}{\Delta\lambda_s} \quad (2-2)$$

The practical limit for $\Delta\lambda_s$ is determined by the minimum side-mode suppression ratio. Using a value less than 0.5 nm results in a side mode suppression ratio that is less than 35 dB.

Super Structure Grating DBR (SSGDBR)

The super structure grating DBR is a modification of the sampled grating DBR design. The two are functionally identical except for the design of the mirrors. In the SSGDBR the gratings in the mirrors are periodically chirped instead of sampled (Figure 2-5). Like in the sampled grating DBR the period of the chirp determines the peak spacing. The advantage of this approach is that the grating occupies the entire length of the mirror so that a much higher reflectivity can be achieved with a lower κ in the grating. The other main advantage is that the reflectivity of the individual peaks can be tailored such that all of the reflection peaks have the same magnitude.

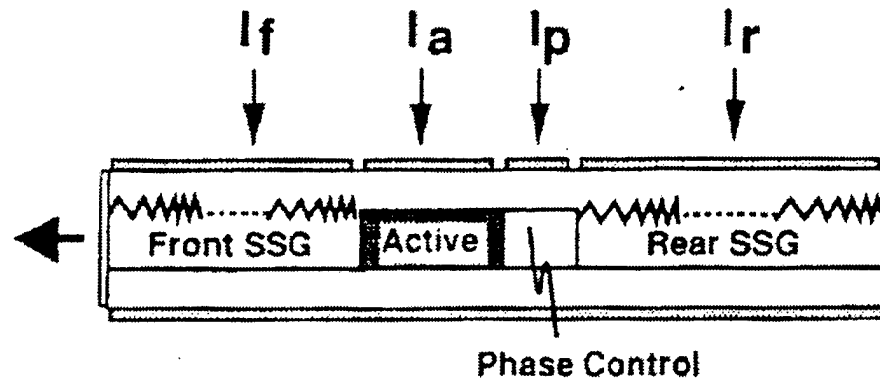


Figure 2-5 SSGDBR schematic cross section.

Grating assisted co-directional Coupler with Sampled Reflector (GCSR)

This device as the name indicates uses a grating assisted co-directional coupler within the laser as a frequency discriminator (Figure 2-6). The device is fabricated with two vertically stacked waveguides having a difference in their modal propagation constants. A long period grating is fabricated on top of the upper waveguide which provides coupling between these two guides for wavelengths at the Bragg frequency given by (2-3)

$$\lambda_B = \Delta\bar{n}\Lambda \quad (2-3)$$

Injecting carriers into one of the guides changes the index difference and tunes the coupling wavelength of the device. Because the Bragg wavelength is now dependant on the difference in index between the two guides a much greater tuning range can be achieved with a given amount of index shift. This coupler has a poor mode selection capability so it is used in conjunction with a sampled grating mirror on the back side of the laser.

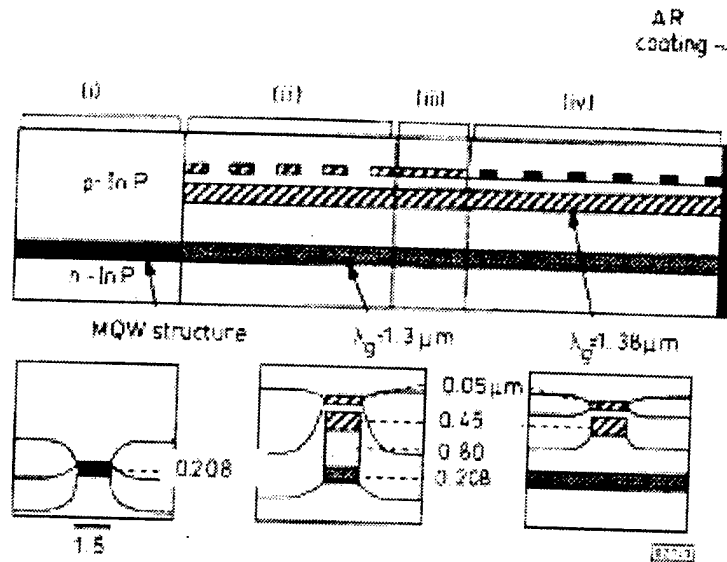


Fig. 1 Schematic diagram of GCSR laser

- (i) gain 250 μm
- (ii) coupler 500 μm
- (iii) phase tuning 150 μm
- (iv) reflector 900 μm

Figure 2-6 Schematic of GCSR laser.

Multi-Frequency Laser (MFL)

The multi-frequency laser is not really a tunable laser but it is included here because it offers many of the same capabilities of a tunable laser. This device is based on an arrayed waveguide grating router. The router acts as a dispersive element in much the same manner as a grating. Active sections in the input arms are pumped and the light is coupled through the router to a common output only light within the pass band of the router for a given arm is coupled back to the input guide. This acts as a narrow band spectral filter for light in the cavity resulting in a minimum loss at the peak of the router passband. Selecting the wavelength of the MFL is accomplished by pumping the input waveguide that corresponds to a given frequency[17].

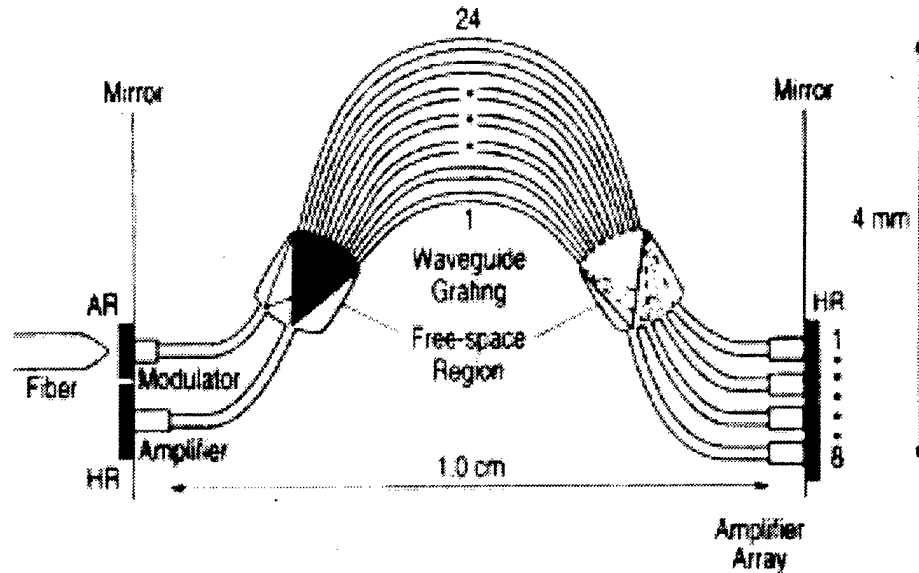


Figure 2-7 Arrayed waveguide grating based multi-frequency laser

2.1.3 SGDBR lasers advantages and disadvantages

Tuning Range

The sampled grating DBR has a number of advantages and disadvantages when compared to the other types of tunable lasers. A key advantage of the SGDBR over the DBR is the extended tuning range. DBR's are limited to only 15 nm of continuous tuning whereas SGDBR's have been demonstrated with more than 40 nm. This increased tuning range comes at the cost of increased tuning complexity and this is true for all of the widely tunable laser designs.

Tuning Efficiency

The SSGDBR is the most similar to the SGDBR. It has an advantage in that it's mirror reflection spectrum can be adjusted to make the reflectivity of all the peaks equal. However there are two key drawbacks with this laser design. The first is the added complexity that is inherent in it's fabrication process. The

SSGDBR requires a high precision direct write e-beam process step to pattern the chirped gratings in the mirror sections. The sampled grating mirrors can be patterned in a simple holographic exposure sequence. This results in a much lower cost process that is more easily scaled up for manufacturing. The other drawback of the SSGDBR design is that they have higher tuning currents due to increased non-radiative recombination in the mirror sections. The tuning efficiency of a waveguide with a grating etched into it is lower than for a simple passive waveguide. This degradation is caused by recombination centers at the grating regrowth interface. Since the gratings cover the entire mirror section in the SSGDBR and only about ten per cent in the SGDBR the tuning efficiency is much higher in the SGDBR. Results have shown that for a SSGDBR with a tuning range of 40 nm the maximum tuning current was 80 mA [5] while for a SGDBR with a tuning range of 41 nm the maximum tuning current was only 23.5 mA .

Fabrication Complexity

The GCSR laser uses a sampled grating for the rear reflector and a grating assisted co-directional coupler for an intra-cavity filter. Fabrication of this device requires five separate epitaxial growth steps and the index of refraction and thickness' of the waveguide layers have to be precisely controlled. The integration with the active section requires a complicated butt joint regrowth which adds considerable difficulty to the process. In general epitaxial growths steps are the most expensive and lowest yield steps in a fabrication process and it is desirable to minimize these. The SGDBR by contrast can be fabricated in a buried heterostructure design with only two growth steps. One of these is the base structure growth and the other is a simple p-type InP regrowth. This simplicity is a major advantage especially when you consider the added difficulty of integrating these devices into complicated photonic integrated circuits.

Output Power and SMSR

Another key advantage of the SGDBR over the GCSR is in it's side mode suppression ratio. The SGDBR has two mirrors with very narrow high reflectivity peaks which must be aligned to determine the lasing mode. This

results in a very high side-mode suppression ratio for these devices. SMSR's of greater than 48 dB have been demonstrated over the entire tuning range. The grating assisted co-directional coupler (GACC) filter element in the GCSR has a very poor mode selection ratio which is the reason that these devices use a sampled grating reflector as the back mirror. Despite this they still suffer from a poor MSR typically on the order of 25 to 30 dB. The only way to improve this is to increase the length of the GACC. However this makes the optical cavity much larger which can adversely effect the modulation bandwidth of the device. One advantage of the GCSR is that it uses the facet of the chip for the front cavity mirror of the laser. This eliminates the mirror losses that are experienced in the SGDBR and SSGDBR designs and gives it the potential for greater output powers. However it also makes it more susceptible to back reflection requiring greater care in the design of the fiber coupling optics.

Modulation Bandwidth

There are a number of factors which can limit the modulation bandwidth of a laser. In widely tunable lasers typically the active regions are selected for wide optical bandwidth and a flat gain profile not for high speed modulation. Also the waveguide structures are designed to enhance the index tuning characteristics. The direct modulation bandwidth of the SGDBR, SSGDBR and GCSR devices is on the order of 4 GHz. Which makes them suitable for use in data transmission systems operating at OC-48 rates under direct modulation. The bandwidth of these devices is limited by a number of factors including the size of the optical cavity and the device capacitance. In practice direct modulation is never used for data rates above OC-48 since the dispersion penalty associated with the modulation chirp is too high. Higher data rates transmission systems use external modulators so the direct modulation bandwidth of these widely tunable lasers is adequate for data transmission requirements. The only device this is not true for is the MFL. For MFL devices the modulation bandwidth is much lower about 500 MHz and in this case it is primarily limited by the size of the optical cavity. These devices are quite large and have cavity lengths on the order of 1 cm so they can only be practically used for direct modulation at rates on the order 622 MBit/s.

Integration

The growing complexity of optical networks particularly in the dense wavelength division multiplexing area has created a need for ever more complicated optical devices. As in electronic circuits cost is the major factor which drives the increasing integration of photonic devices. All optical wavelength routing, conversion, and switching are all tasks that are requiring more complicated integrated photonic devices. Lasers are being integrated on chip with modulators, wavelength monitors and even wavelength converters. A major advantage for the SGDBR and SSGDBR designs is their suitability for integration. Lasers such as the DBR, GCSR, and even the MFL which use cleaved facet mirrors are more limited in their potential for integration.

The combination of wide range tuning, high side mode suppression ratio, large modulation bandwidth, along with a simple low cost fabrication process and a design that enables it to be easily integrated with other components makes the SGDBR laser an ideal choice for use in photonic integrated circuits.

2.2 Design Considerations for Widely Tunable SGDBR Lasers

The design process for a tunable sampled grating DBR laser is extremely complicated and involves a large number of parameters that must be selected. The two most important performance characteristics for the laser are the output power and the tuning range. Other requirements that may be considered in the design are the modulation bandwidth, the fraction of the total output power emitted from the front facet, the mode spacing, and the overall size of the device. The goal of the design process is to select the most efficient structure possible to meet the performance requirements. For photonic integrated circuits efficiency usually pertains to the device size and power dissipation.

The design parameters for the laser fall into two major categories. The first category is for growth dependant parameters and the second is for process

dependant parameters. For the SGDBR laser the growth dependant parameters which can be varied include the band gap, thickness, and doping of the waveguide layer, and the number of quantum wells in the active layer. The key process dependant parameters which can be varied for the laser are the mirror design, and the length of the active and phase control sections.

2.2.1 *Waveguide Structure*

The design of the waveguide structure for the SGDBR laser is complicated by the use of the offset quantum wells. In butt joint fabrication techniques the waveguide structure for the active and passive sections can each be optimized independently for its particular purpose either gain or index tuning. However in the offset quantum well design a compromise must be made between carrier transport through the waveguide and into the quantum wells for the active section and carrier confinement in the tuning sections. A heavily n-doped high bandgap waveguide will allow efficient transport of electrons through the waveguide and into the quantum wells but for optimum carrier confinement we need a low bandgap undoped waveguide. There is also a tradeoff between the quantum well overlap and the tuning efficiency. Using a thicker lower bandgap waveguide will increase the amount of index tuning that can be achieved however this will reduce the quantum well overlap and lower the available modal gain. Increasing the number of quantum wells to compensate for this increases the coupling loss between the active and passive sections due to the mode mismatch. The practical limit for adding quantum wells occurs when the incremental change in modal loss exceeds the increase in modal gain. A typical active and passive structure for an offset quantum well SGDBR are shown in Figure 2-8.

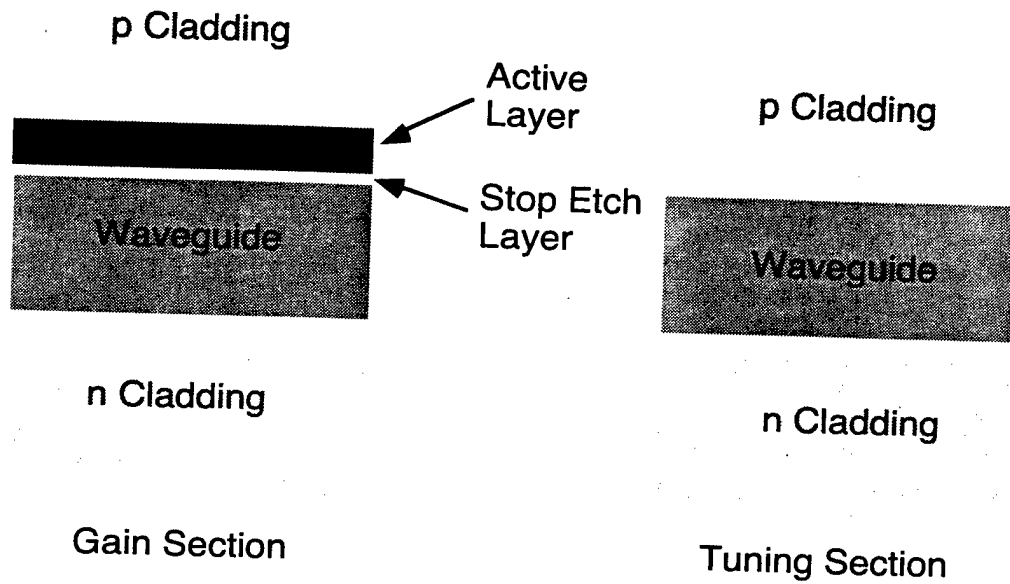


Figure 2-8 Waveguide Structure for Gain and Tuning Sections

Quantum Well Overlap

The modal gain in the quantum well active region is equal to the material gain times the confinement factor (Γ) for the optical mode. This depends strongly on the thickness and bandgap of the waveguide. Increasing the number of wells will increase the confinement factor for the active layer however it will also increase the coupling loss at the active and passive junctions. This junction loss can be reduced by using a thicker lower bandgap waveguide however this will reduce the modal overlap with the active region thereby lowering Γ . The confinement factor vs. waveguide thickness is plotted in Figure 2-9 for three different active regions having 4, 6, and 8 quantum wells. The waveguide bandgap is $1.4 \mu\text{m}$. This plot clearly shows the tradeoff between waveguide thickness and confinement factor.

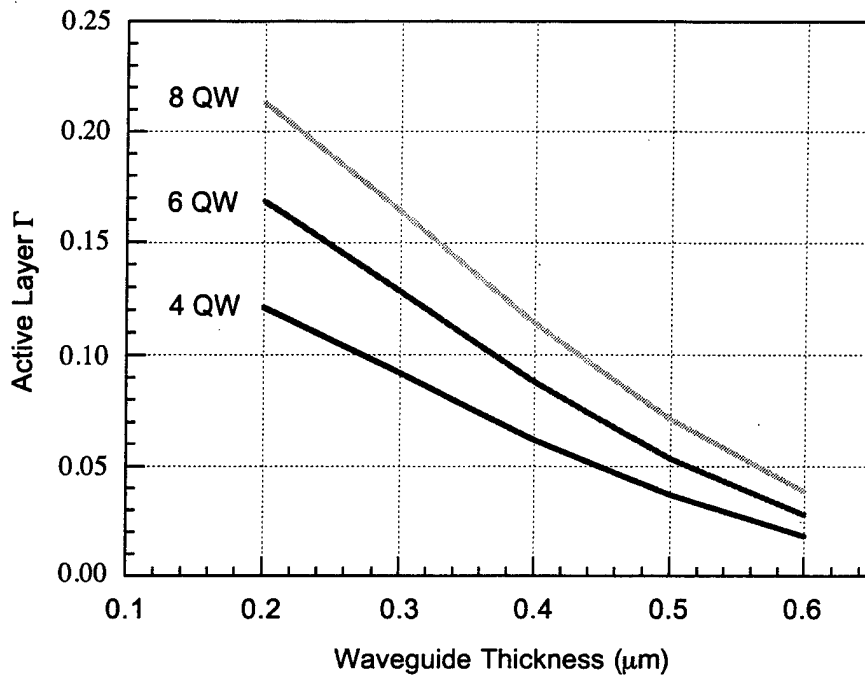


Figure 2-9 Confinement factor vs. waveguide thickness for active layers with 4, 6 and 8 quantum wells.

For a 4000\AA thick 1.4Q waveguide with four offset quantum wells the coupling efficiency between the active and passive sections is better than 98%. This gives an equivalent cavity loss of only 0.3 cm^{-1} for a 1.4 mm effective cavity length. If we increase the number of wells from 4 to 6 the coupling loss increases by 0.28 cm^{-1} . Assuming a $500\text{ }\mu\text{m}$ long gain section the increased gain required to compensate this is only 0.8 cm^{-1} . The four quantum well device has a modal gain Γg_0 of about 26 cm^{-1} . If we increase the number of wells from 4 to 6 then based on the confinement factor the modal gain will increase by more than 40% or 10 cm^{-1} . Based on these calculations it is clear that increasing the number of quantum wells in the active region will give a significant increase in the modal gain. We should therefore use the maximum number of wells in the active region that can be efficiently electrically pumped. With the current

quantum well design which uses 0.8% compressive strain in the well and -0.03% tensile strain in the barriers up to 8 wells can be grown before the critical thickness is reached and the material relaxes.

Carrier Transport

Lightly n doping the waveguide will significantly improve the carrier transport and lower the resistance in the device. The band structure for the active section of the laser at a 1.2 V bias is shown in Figure 2-10.

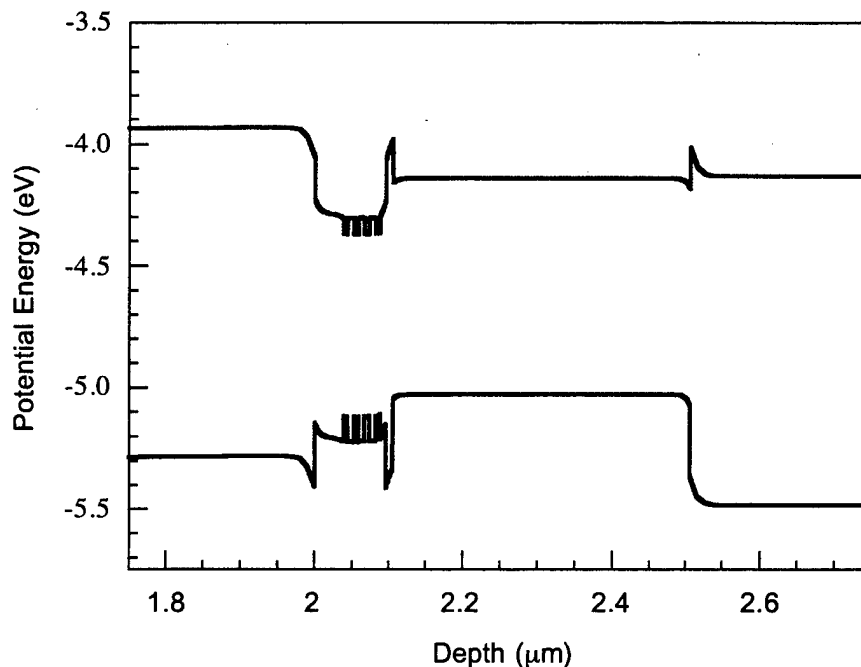


Figure 2-10 Active region band diagram at a bias of 1.2 V.

In this plot we can see that n doping the waveguide and the stop etch layer flattens the bands and improves the carrier injection into the quantum wells. The corresponding band structure for the tuning section is shown in Figure 2-11. The 200 Å thick n doped stop etch layer on top of the waveguide remains after the quantum wells have been etched off and the cap is regrown.

This layer causes the dip in the conduction band immediately above the waveguide. This dip lowers the barrier for electron leakage.

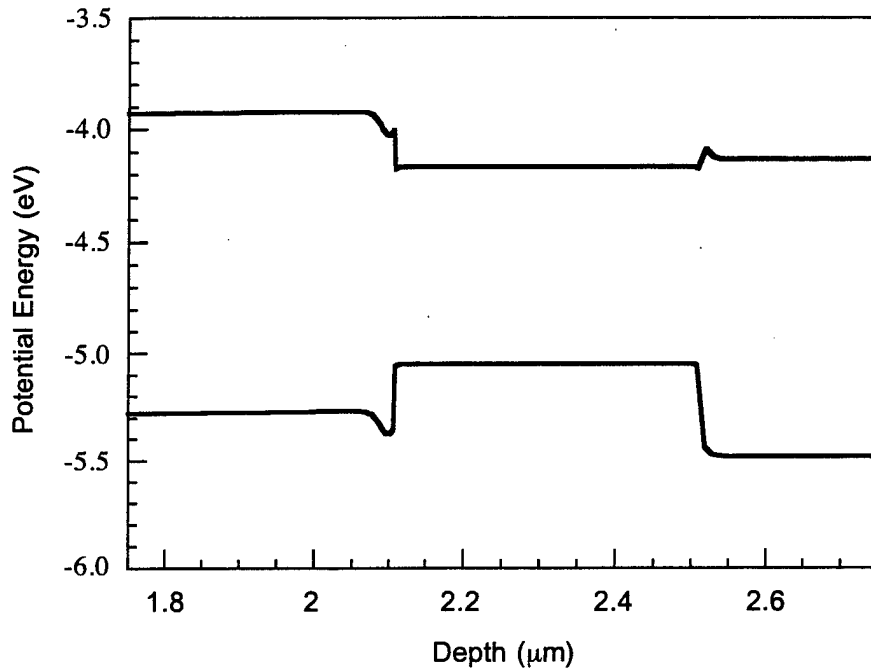


Figure 2-11 Passive section band diagram at a bias of 1.2 V.

Waveguide Doping for Improved Carrier Confinement

Leaving the stop etch layer undoped will enable Zn diffusion during the regrowth to convert it to p-type. This increases the barrier significantly and reduces the calculated electron leakage current by a factor of 6 at a bias of 1.2 V. The difference in the barrier height for electron leakage from the waveguide is shown in Figure 2-12. A 40 meV difference in the barrier height is evident at the p-cladding interface.

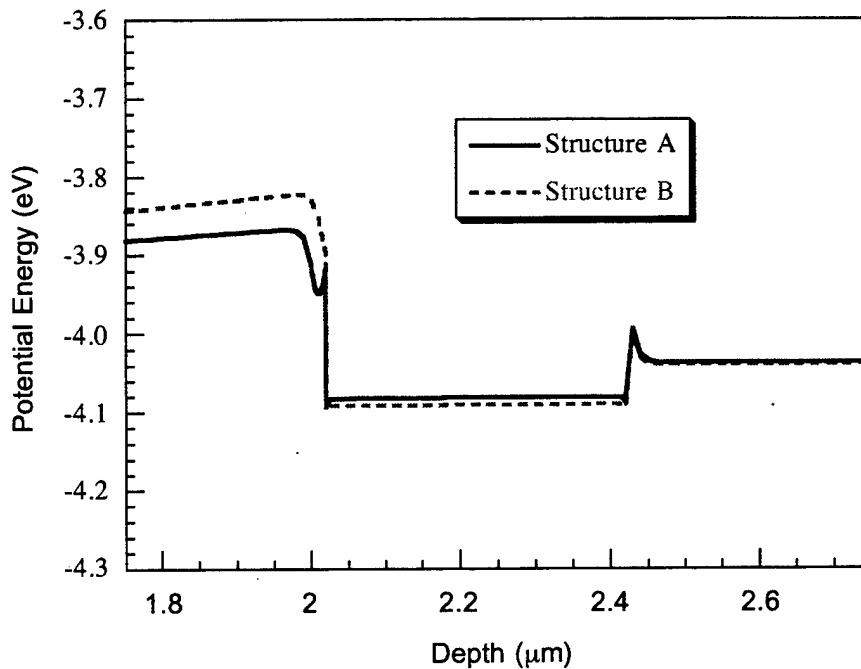


Figure 2-12 Conduction band edge showing barrier height for Structure A with an n doped stop etch layer and Structure B with an undoped stop etch layer.

2.2.2 Mirror Design

The mirror design is a crucial part of the SGDBR laser. There is a wide variety of possible designs for any given tuning range. However the most efficient design can be derived with a few simple rules. The best performance for a given tuning range will be achieved by using a mirror structure which yields the lowest total tuning current, since the loss increases with increased carrier injection into the passive regions. The key design parameters for the mirrors are the grating burst length d , the sampling interval Λ_s and the number of sampling periods M (Figure 2-13).

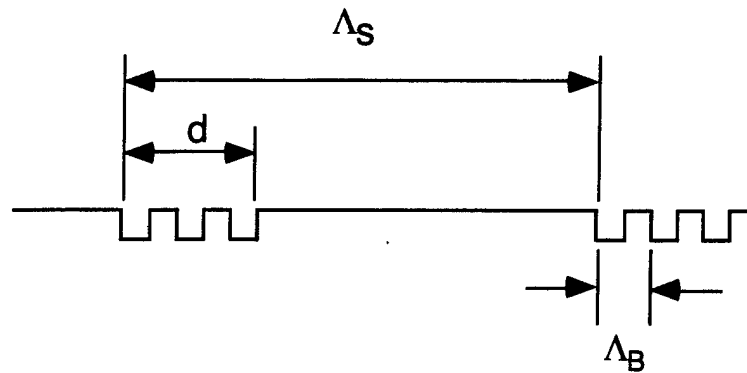


Figure 2-13 Sampled Grating Mirror Layout

Grating Burst Length

The mirror reflectivity increases with increased depth of the Bragg grating etch. It is always desirable to etch the gratings to the maximum depth at which high quality regrowth is possible. For MOCVD regrowth this depth is between 500 and 750 Å which gives a grating coupling coefficient between 400 and 450 cm^{-1} for a 4000 Å thick 1.4Q waveguide. The reflection spectrum of a SGDBR laser is the convolution of the reflection of a continuous grating with a periodic sampling function. Every element of the mirror spectrum has a corresponding element in physical space which follows a reciprocal relationship. The real space sampling of the grating leads to multiple reflection peaks with a spacing that is inversely proportional to the sampling interval. The width of the reflection envelope for the mirror peaks is likewise inversely proportional to the burst length. As the burst length is increased the reflectivity of the central peak increases however the roll off in the strength of the side peaks also increases.

The normalized envelope of the sampled grating reflection spectrum depends only on the effective κl which is equal to the length of the grating burst d times the grating kappa κ and the number of sampling periods M . We can determine

the optimum grating burst length for a given tuning range by selecting the length d to maximize the reflectivity of the outermost peaks. For a waveguide with 9 cm^{-1} of loss and a grating coupling coefficient of 450 cm^{-1} the optimum burst length is plotted in Figure 2-14 as a function of tuning range. For wider tuning ranges shorter grating bursts are required to obtain a wide reflection bandwidth. This reduces the effective κ which can be compensated for by using an increased number of mirror periods. If we require a tuning range of 40 nm then the optimum burst length d will be $7.6 \text{ }\mu\text{m}$.

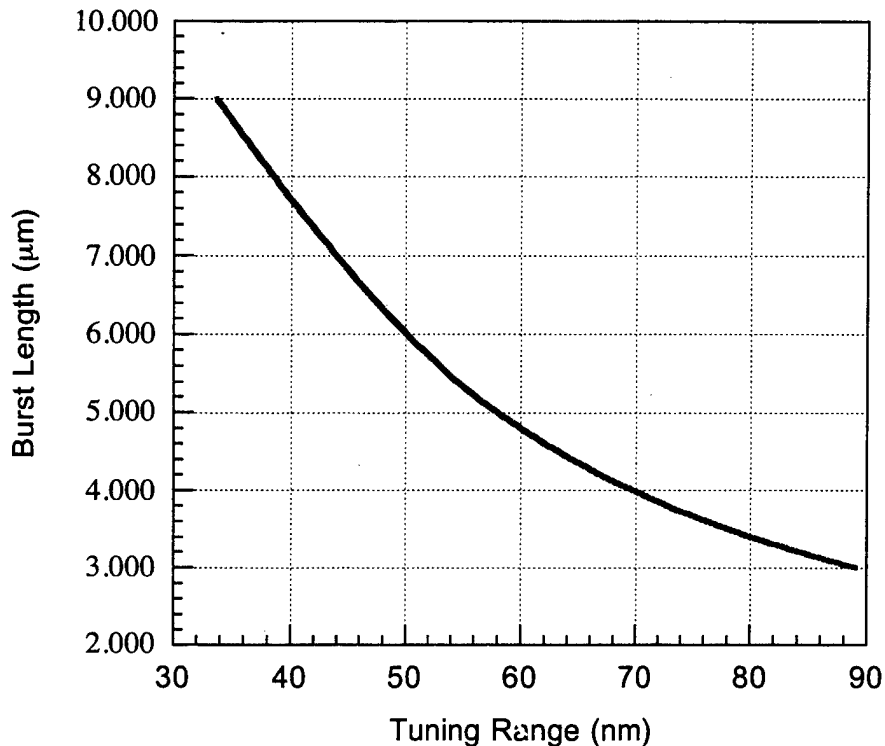


Figure 2-14 Optimum grating burst length vs. tuning range for a mirror with 9 cm^{-1} of loss and a coupling coefficient of 450 cm^{-1} .

Sampling Period

Wide range wavelength tuning in the SGDBR laser is accomplished by using a set of evenly spaced mirror peaks in the front and back sampled grating mirrors. The sampling period in the front mirror is slightly smaller than in the back mirror giving the two mirrors different peak spacing. This enables a single pair of reflection peaks to be aligned within the gain spectrum to select the lasing wavelength. Since the peak spacing in the mirrors is periodic the peaks will come into alignment periodically. The separation between these alignments is called the repeat mode spacing λ_{RMS} . The maximum tuning range for a given set of mirror designs is limited by the repeat mode spacing given by (2-4). Where $\Delta\lambda_F$ is the spacing between the front mirror peaks, $\Delta\lambda_B$ is the spacing between the back mirror peaks and $\delta\lambda_S$ is the difference between them.

$$\lambda_{RMS} = \frac{\Delta\lambda_F \Delta\lambda_B}{\delta\lambda_S} \quad (2-4)$$

A key question in the design of a SGDBR laser is what mirror peak spacing should be used for a given tuning range. The total mirror reflectivity bandwidth is independent of the sampling interval and depends only on the effective κl . Assuming that we have a fixed κl , which implies a fixed number of sampling intervals, we can optimize the sampling period Λ_S independently. To minimize the tuning current we simply choose the smallest peak spacing that will satisfy the repeat mode spacing limit. This can be done by solving (2-4) for $\Delta\lambda_B$ and recognizing that $\Delta\lambda_F = \Delta\lambda_B + \delta\lambda_S$ which gives (2-5)

$$\Delta\lambda_B = \frac{-\delta\lambda_S + \sqrt{\delta\lambda_S(\delta\lambda_S + 4\lambda_{RMS})}}{2} \approx \sqrt{\delta\lambda_S \lambda_{RMS}} \quad (2-5)$$

An alternative is to solve for the shortest mirror length by simply selecting $\Delta\lambda_F$ to be equal to the maximum tuning range for the mirror and calculating Λ_S from (2-6).

$$\Lambda_s = \frac{\lambda^2}{2n_g \Delta\lambda} \quad (2-6)$$

For a tuning range of 40 nm the mirror peak spacing for the front and back mirrors will be 4.5 and 5.0 nm respectively assuming a $\delta\lambda_s$ of 0.5 nm and using the minimum tuning current criterion. This gives a sampling period of 71 μm for the front mirror and 64 μm for the back.

Once the sampling period and the grating burst length have been chosen the number of sampling periods can be selected based on the required reflectivity. Longer mirrors have two advantages, increased reflectivity and a narrower bandwidth for the mirror peaks which gives higher side mode suppression. The peak reflectivity and the bandwidth for the central peak are plotted in Figure 2-15 for increasing numbers of sampling periods.

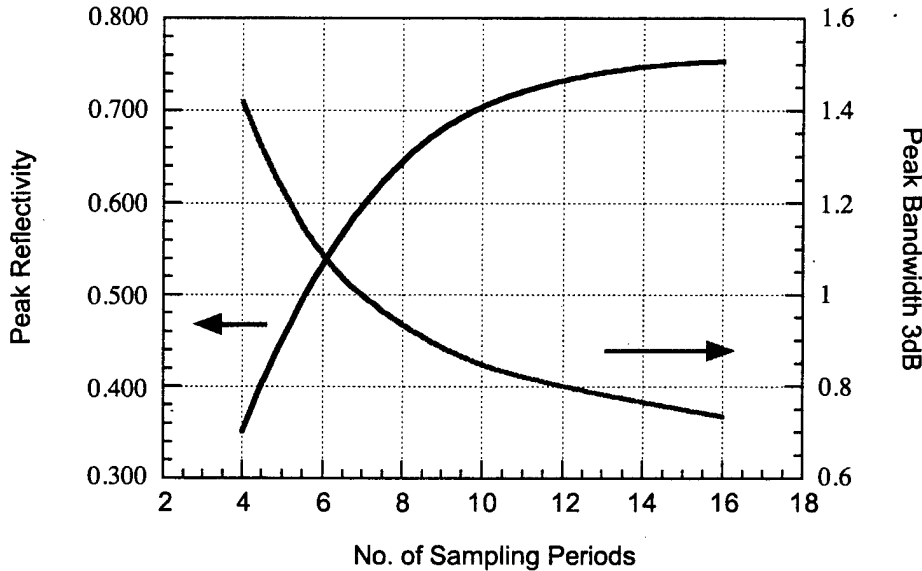


Figure 2-15 Reflectivity and bandwidth for the central peak of a sampled grating mirror vs. number of mirror periods.

These calculations are for a mirror with 6 μm long grating bursts. The grating κ was chosen to be 450 cm^{-1} and the waveguide loss was 9 cm^{-1} . Under these conditions the reflectivity begins to saturate at about 10 periods and the maximum reflectivity does not exceed 75% even for 16 periods due to the waveguide loss. For the back mirror the maximum reflectivity is desired however the total tuning current increases linearly with the number of sampling periods. A good compromise for this structure would be to use ten mirror periods. For the front mirror reflectivity there is a tradeoff between the threshold current and the differential efficiency. A reflection coefficient of 35% which can be achieved with only four mirror periods would make the fraction of power F emitted from the front facet about 75% (2-7). However to achieve a narrower bandwidth for the reflection peaks and thus better SMSR at least 7 sampling periods should be used. The minimum value for the difference in the peak spacing $\delta\lambda_S$ is one half of the 3 dB bandwidth of the widest mirror peak. So for 7 sampling periods in the front mirror $\delta\lambda_S$ must be greater than or equal to 0.5 nm.

$$F = \frac{1 - R_1}{1 - R_1 + (1 - R_2) \sqrt{\frac{R_1}{R_2}}} \quad (2-7)$$

The length of a mirror is equal to the number of sampling intervals M times the sampling period Λ_S however we can cheat slightly and improve the reflectivity by placing an extra grating burst at the beginning of the mirror to make it effectively $M+1$ sampling periods long.

2.2.3 Cavity Structure

The key issues in the design of the cavity structure are the length of the gain section, the length of the phase control section, and the active passive junction design.

Active/Passive Junction

The passive tuning sections of the laser are fabricated by etching off the quantum well active layer. This creates a mode mismatch and an impedance discontinuity at the active passive junction. For a typical laser structure with 6 offset quantum wells, and a 3500 Å thick 1.4Q waveguide layer the coupling efficiency, determined by the modal overlap, between the active and passive sections is better than 95%. This represents a negligible loss for the cavity which is equivalent to 2 cm^{-1} for a 500 μm long gain region. A potentially more significant problem is the small amount of light which is reflected due to the impedance discontinuity. Even though the reflection is typically less than 0.1% it can result in a significant resonance that perturbs the tuning characteristics for the device. To eliminate any resonance's caused by this effect the junction is angled at 10° . This prevents any reflected light from coupling into the cavity mode.

Phase Control

The phase control section is used to align the cavity mode with the mirror reflection peaks at the desired operating wavelength. It's length must be sufficient to enable the cavity mode to be tuned over at least 1 full mode spacing. For practical considerations a minimum of 3 times this tuning range is desirable. The length of the phase section required is completely independent of the laser cavity length. This seems counter intuitive since the mode spacing in a laser varies inversely with the cavity length. However regardless of the cavity dimensions the phase section must be capable of increasing it's round trip phase shift by 2π to tune the cavity over one full mode spacing. So the length of the phase section depends only on the amount of achievable index shift and the desired phase shift according to (2-8).

$$L_p = \frac{1}{2} \left(\frac{\lambda}{2\pi\Delta n} \right) \Delta\phi \quad (2-8)$$

From this we can quickly calculate the required phase section length to be 116 μm for a phase shift of 6π and a maximum index change of 0.02. From Figure 2-22 we see that this corresponds to a current density of 5 kA/cm².

This means the maximum tuning current required in the phase section will only be 3.9 mA for 1 mode spacing.

Optimization of Gain Section Length

For a fixed passive section length it is possible to calculate the optimum active section length using only a few simple parameters (2-9)[18]. The loss in the active and passive sections can be measured experimentally by fabricating ridge lasers with varying active and passive lengths. In this case we have values of 9 cm^{-1} in the passive sections and 12 cm^{-1} in the active section. The gain curve can also be calculated in this manner giving us a value for Γg_o of 6.5 cm^{-1} per well. The mirror reflectivity's r_1 and r_2 for the front and back mirrors were calculated in the previous section to be 0.7 and 0.84 respectively. The length of the passive section includes the phase section and the effective penetration depth of the two mirrors.

$$L_a = \frac{\alpha_p L_p + \ln(1/r_1 r_2)}{\Gamma g_o - \alpha_{ia}} \quad (2-9)$$

The penetration depth for any given peak n numbered from the central peak in the sampled grating reflection spectrum is given by (2-10). Where the parameter $\kappa(n)$ is the effective coupling coefficient for the peak of order n given by (2-11)[19].

$$L_p(n) = \frac{1}{2\kappa(n)} \tanh(\kappa(n)L_m) \quad (2-10)$$

$$\kappa(n) = \kappa \frac{d}{\Lambda_s} \frac{\sin\left(\frac{\pi n d}{\Lambda_s}\right)}{\frac{\pi n d}{\Lambda_s}} e^{-j \frac{\pi n d}{\Lambda_s}} \quad (2-11)$$

For the $n=0$ case this gives us an effective penetration depth for the front and back mirrors of $120 \text{ }\mu\text{m}$ and $128 \text{ }\mu\text{m}$ respectively making the total passive length in the cavity $350 \text{ }\mu\text{m}$. Using these values in (2-9) gives us an optimum

active region length of 604 μm for a four quantum well active region and 313 μm for a six quantum well active region.

2.2.4 Optimization of Ridge Width

For ridge waveguide semiconductor lasers reducing the ridge width increases the optical loss in the cavity due to increased scattering from sidewall roughness. This will increase the threshold current density in the laser. However the total threshold current will be reduced due to the reduction in the active volume. When the ridge becomes too narrow the rate of increase in threshold current density due to increased internal loss will exceed the rate of decrease in active region volume and the threshold current will begin to increase rapidly. Increasing internal loss should also result in a decrease in the differential efficiency for the device. Some compromise between minimizing the threshold current and maximizing the differential efficiency is required when selecting the desired ridge width.

To characterize these effects for the SGDBR laser we fabricated lasers with three different ridge widths to measure the variation in the $L-I$ characteristics. Devices were made with 4, 5 and 6 μm ridge widths. The lasers had active regions that were 550 μm long, with 150 μm long phase control sections and front and back mirrors that were 500 and 750 μm in length respectively. The asymmetric mirror lengths are used to increase the fraction of light emitted from the front facet.

The $L-I$ characteristics were measured for 25 devices at each of the different ridge widths. Using this data the average threshold current was calculated for each size. This is shown in

Figure 2-16. The threshold current reduces by about 20% as the ridge width is decreased from 6 to 4 μm . The corresponding threshold current density increases from 1583 A/cm^2 to 1880 A/cm^2 .

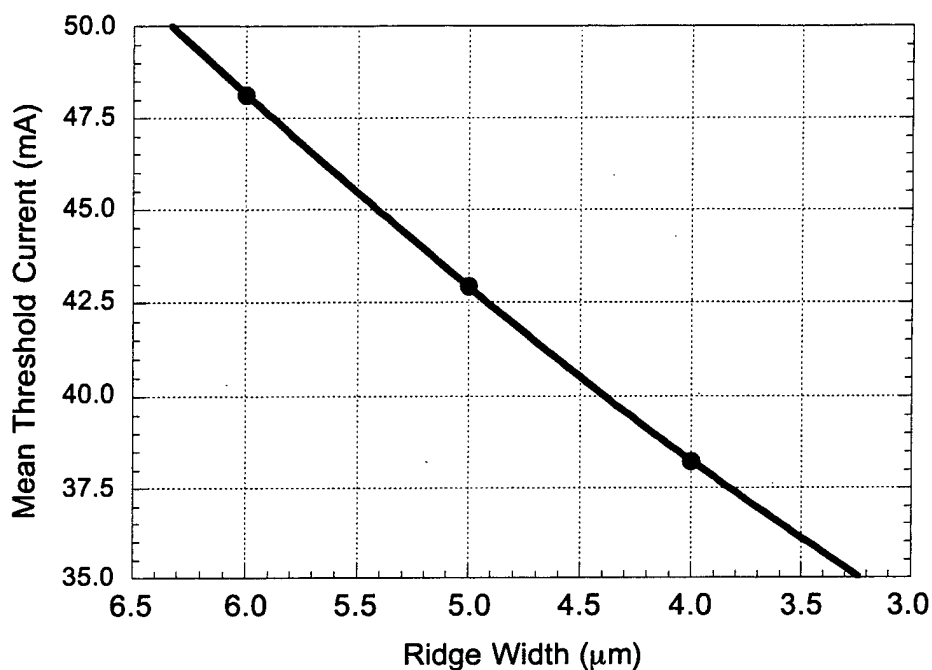


Figure 2-16 Threshold current dependence for SGDBR lasers with 4, 5 and 6 μm ridge widths.

The differential efficiency as a function of ridge width is plotted in Figure 2-17. This indicates a slight increase in η_d as we move to narrower ridges. This is unexpected since the increase in internal loss should result in a reduction in the differential efficiency. However the change is very small and can be attributed to variations in mirror reflectivity across the sample. Tuning tests on devices of all three dimensions showed a weak correlation between ridge width and tuning current. The smaller devices had slightly higher tuning efficiencies than the wider ones. This can be explained if we consider the fact that the index change is proportional to carrier density which will be roughly proportional to current density for the widths considered in this study. So to first order the tuning current should scale with ridge width. However the thermal impedance will be essentially the same for all three widths. Since the

total tuning current is reduced the self heating effects are also reduced for narrower ridge widths which increases the tuning efficiency slightly. Based on these results, a ridge width of 3 μm was chosen for the design of the ridge waveguide SGDBR.

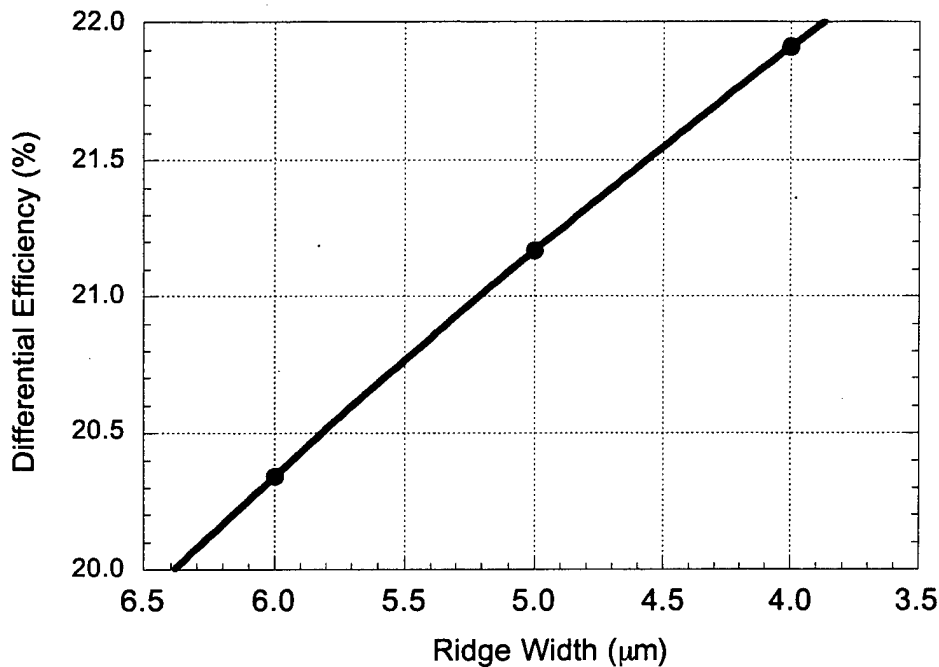


Figure 2-17 η_d dependence for SGDBR lasers with 4, 5 and 6 μm ridge widths.

2.3 Index Tuning in Semiconductor Waveguides

There are two classes of effects that can be used for index tuning in semiconductors; field effects, and carrier effects. The field effects include the linear electro-optic or Pockels effect and the quadratic electro-optic or Kerr effect. Both of these mechanisms produce a change in effective index with an

applied field. This makes them more suitable for use in reverse biased devices which require small index shifts. The field effects are not limited by carrier lifetime or carrier transport effects and thus can be used in applications requiring high speed but relatively low index shifts.

Carrier injection changes the absorption characteristics of the material which changes the index. There are four different components to carrier effect tuning. These include the contributions from free electrons, free holes, bandgap shrinkage and bandfilling. The index shift can be calculated by first calculating the change in absorption and then using the Kramers-Kronig relation between the absorption change and the index change. The free electron and free hole contributions can be calculated independently and then simply added in but the band gap shrinkage and bandfilling effects are interdependent and must be considered together.

2.3.1 *Model of Index tuning mechanisms*

Field Effect Mechanisms

The Pockels effect is anisotropic and gives a positive index shift for TE polarized light propagating along the $\langle 01\bar{1} \rangle$ direction and a negative index shift for light propagating along the $\langle 011 \rangle$. The TM polarization is unaffected by the Pockels effect. The index shift is proportional to the intensity of the electric field and is given by (2-12).

$$\Delta n_p = \frac{1}{2} n^3 r_{41} E \quad (2-12)$$

Where E is the applied field, n is the index of refraction and r_{41} is the Pockels coefficient for InGaAsP/InP materials. The best measured value for this coefficient is $1.4 \cdot 10^{-10}$ cm/V. For forward biased tuning the change in the electric field E is very low and the index shift due to the Pockels effect can be neglected.

The Kerr effect is independent of the polarization of the light and produces an index shift which is proportional to the square of the electric field (2-13).

$$\Delta n_K = \frac{1}{2} n^3 R_{Kerr} E^2 \quad (2-13)$$

The Kerr coefficient is dependant on the difference between the bandgap energy of the material and the photon energy of the guided light ΔE . It has been found to obey the empirical relation in (2-14).

$$R_{Kerr} = 1.5 \cdot 10^{-15} \exp(-8.85\Delta E) \text{ cm}^2/V \quad (2-14)$$

Carrier Induced Index Tuning

The carrier induced change in the index of refraction for a material can be calculated from the change in absorption using (2-15) derived from the Kramers-Kronig relation. Where P denotes the principle value of the integral.

$$\Delta n_r = \frac{\hbar c}{\pi} P \int_0^{\infty} \frac{\Delta \alpha(E')}{E'^2 - E^2} dE' \quad (2-15)$$

The contributions from the free electron and free hole plasma effect can be calculated separately and then added to the index shift due to bandfilling and bandgap shrinkage. Throughout this section n_r will be used for the index of refraction and N will be used for the electron density.

Free-Carrier Absorption

Free carriers can absorb photons and move to a higher energy state within a band. This intra-band free-carrier absorption, also known as the plasma effect, can be modeled as being directly proportional to the concentration of electrons and holes and to the square of the wavelength. The corresponding change in refractive index is given by (2-16). This equation uses the fact that the concentrations of the heavy and light holes are proportional to their effective masses raised to the three-halves power[20].

$$\Delta n = -\left(\frac{e^2 \lambda^2}{8\pi^2 c^2 \epsilon_o n_r}\right) \left[\frac{N}{m_e} + P \left(\frac{m_{hh}^{1/2} + m_{lh}^{1/2}}{m_{hh}^{3/2} + m_{lh}^{3/2}} \right) \right] \quad (2-16)$$

This formula gives the index of refraction change for the free holes and free electrons for all semiconductor materials lattice matched to InP. In general the free carrier effects are small compared to the band filling and bandgap shrinkage effects however they can make a significant contribution for optical wavelengths which are far from the band edge of the material.

Band Filling and Bandgap Shrinkage

The index shift due to the free electrons and free holes can be considered independently and simply added to the total shift. However the bandgap shrinkage and band filling effects combine when carriers are injected into the semiconductor. The bands are filled as the bandgap shrinks so these two effects must be treated together. For a direct bandgap semiconductor with parabolic bands the absorption spectrum is given by (2-17) neglecting the Urbach tail[21].

$$\alpha_o(E) = \frac{C(y)}{E} \sqrt{E - E_g(y)} \quad \text{for } E > E_g \quad (2-17)$$

The absorption constant C depends on the material and can be estimated for $\text{In}_{1-x}\text{Ga}_x\text{As}_y\text{P}_{1-y}$ materials lattice matched to InP ($x \approx 0.47y$) using (2-18).

$$C(y) = (1.004 - 1.318y + 0.517y^2) \times 10^5 \quad [\text{cm}^{-1} \text{eV}^{1/2}] \quad (2-18)$$

The absorption coefficient for a semiconductor with carrier injection is given by (2-19).

$$\alpha(N, P, E) = \alpha_o(E) [f_v(E_v) - f_c(E_c)] \quad (2-19)$$

If we consider the contributions from the light holes and heavy holes separately the change in absorption can be given by (2-20).

$$\begin{aligned} \Delta\alpha(N, P, E) = & \frac{C_{hh}}{E} \sqrt{E - E_g - \Delta E_g} [f_v(E_{vh}) - f_c(E_{ch})] \\ & + \frac{C_{lh}}{E} \sqrt{E - E_g - \Delta E_g} [f_v(E_{vl}) - f_c(E_{cl})] \end{aligned} \quad (2-20)$$

The ΔE_g term has been included to account for the band gap shrinkage effect. Which can be modeled using (2-21).

$$\Delta E_g(N) = -\frac{0.13}{\epsilon_s} \left(\frac{N}{N_{cr}} - 1 \right)^{1/3} \quad (2-21)$$

Where ϵ_s is the relative static dielectric constant of the material (in units of ϵ_0 , the vacuum permittivity) and N_{cr} is a critical carrier density below which there is no shrinkage its value is given by (2-22) where m_c^* is the conduction band effective mass (in units of m_0).

$$N_{cr} = 1.6 \times 10^{30} \left(\frac{m_c^*}{1.4\epsilon_s} \right)^3 [m^{-3}] \quad (2-22)$$

The heavy hole and light hole absorption constants can be determined from the experimental absorption constant $C(y)$ and the density of states effective masses.

$$\begin{aligned} C_{hh} &= \left(\frac{\mu_h^{3/2}}{\mu_h^{3/2} + \mu_l^{3/2}} \right) C(y) & \mu_h &= \left(\frac{1}{m_c} + \frac{1}{m_{hh}} \right)^{-1} \\ C_{lh} &= \left(\frac{\mu_l^{3/2}}{\mu_h^{3/2} + \mu_l^{3/2}} \right) C(y) & \mu_l &= \left(\frac{1}{m_c} + \frac{1}{m_{lh}} \right)^{-1} \end{aligned} \quad (2-23)$$

The probabilities f_c and f_v are given by the Fermi-Dirac distribution functions where F_c and F_v are the quasi-Fermi levels for the conduction band and valence band respectively.

$$f_c(E) = \left(1 + \exp \left[\frac{E - F_c}{k_B T} \right] \right)^{-1}$$

$$f_v(E) = \left(1 + \exp \left[\frac{E - F_v}{k_B T} \right] \right)^{-1}$$
(2-24)

The Fermi levels can be obtained from the carrier densities by solving (2-25) where E_c and E_v are the potential energies of the conduction and valence band edges.

$$N = \frac{1}{2\pi^2} \left(\frac{2m_c}{\hbar^2} \right)^{3/2} \int_{F_c}^{\infty} \frac{\sqrt{E - E_c}}{1 + e^{(E - F_c)/k_B T}} dE$$

$$P = \frac{1}{2\pi^2} (m_{lh}^{3/2} + m_{hh}^{3/2}) \left(\frac{2}{\hbar^2} \right)^{3/2} \int_{F_c}^{\infty} \frac{\sqrt{E - E_v}}{1 + e^{(E - F_v)/k_B T}} dE$$
(2-25)

The four transition energies used in (2-20) can be determined by momentum conservation and are given by (2-26). The conduction band and valence band energies are given relative to the respective band edges.

$$E_{ch} = (E - E_g - \Delta E_g) \left(\frac{m_{hh}}{m_{hh} + m_c} \right)$$

$$E_{cl} = (E - E_g - \Delta E_g) \left(\frac{m_{lh}}{m_{lh} + m_c} \right)$$

$$E_{vh} = (E - E_g - \Delta E_g) \left(\frac{m_c}{m_{hh} + m_c} \right)$$

$$E_{vl} = (E - E_g - \Delta E_g) \left(\frac{m_c}{m_{lh} + m_c} \right)$$
(2-26)

The Fermi-Dirac integrals in (2-25) can be difficult to solve for the Fermi levels. However an excellent global approximation developed by Nilsson exists which can be used to quickly calculate the Fermi level from the carrier density

(2-27)[18]. It is complicated but has less than 0.06% error over the entire range of carrier densities.

$$\left(\frac{F_c - E_c}{k_B T}\right) = \frac{\ln(N/N_c)}{1 - (N/N_c)^2} + \frac{f_H}{1 + (0.24 + 1.08 f_H)^{-2}} \quad (2-27)$$

$$N_c = 2 \left(\frac{m^* k_B T}{2\pi \hbar^2}\right)^{3/2}, \quad f_H = \left(\frac{3\sqrt{\pi}}{4} \left(\frac{N}{N_c}\right)\right)^{2/3}$$

Using the set of relations defined in this section the change in the absorption spectrum can be calculated for a given change in the carrier density. Then by inserting (2-20) into the Kramers-Kronig relation (2-15) and integrating numerically we can determine the corresponding refractive index change

Thermal Compensation

The carrier induced index change in a semiconductor waveguide can be partially compensated by the temperature change that occurs due to device self heating. The temperature dependence of the index of refraction can be modeled for InGaAsP based materials using (2-28). Where the high frequency dielectric constant is given by (2-29) as a function of the y parameter and its variation with temperature is given by (2-30)[21]

$$\Delta n_r = \left(\frac{1}{\epsilon_o} \frac{\partial \epsilon_\infty}{\partial T} (T - 300)\right) \quad (2-28)$$

$$\epsilon_\infty = (9.55 + 2.2y)\epsilon_o \quad (2-29)$$

$$\frac{\partial \epsilon_\infty}{\partial T} = 5.16 \times 10^{-4} \epsilon_o \quad [K^{-1}] \quad (2-30)$$

Estimation of the temperature change in the device as a function of current density can be done by first calculating the power dissipation using (2-31) where V_D is the ideal diode voltage and V_s is a current independent series

voltage. The optical output power from the tuning sections is neglected. This result is then multiplied by the thermal impedance which can be modeled using the simple analytic approximation in (2-32) for a laser of width w and length l having a total substrate thickness of h [18]. For InP the thermal conductivity ζ is about 0.6 W/(cm·K). The series resistance for a typical buried heterostructure device with a width of 2 μm , a length of 350 μm , and a substrate thickness of 100 μm is around 5 Ω .

$$P_D = I^2 R_s + IV_D + IV_s \quad (2-31)$$

$$Z_T \approx \frac{\ln(4h/w)}{\pi\zeta l} \quad (2-32)$$

2.3.2 *Theoretical and practical tuning performance*

Bandgap dependence of index tuning

Using the analysis developed in the previous section it is possible to calculate the tuning efficiency for materials of different bandgap. These are plotted in Figure 2-18 for an optical wavelength of 1.56 μm . As would be expected there is a considerable increase in the index tuning for materials which have bandgap energies that are closer to the photon energy. It is therefore desirable to use a fairly low bandgap material for the waveguide to enhance the tuning efficiency. However it can not be too close to the photon energy because there is a significant increase in the absorption. The best ratio of index tuning to absorption increase for the 1.55 μm wavelength range is achieved by using a material with a 1.42 μm bandgap. For optimum device design it is preferable to use the highest bandgap waveguide which can provide sufficient index shift to meet the requirements since this will minimize the absorption loss.

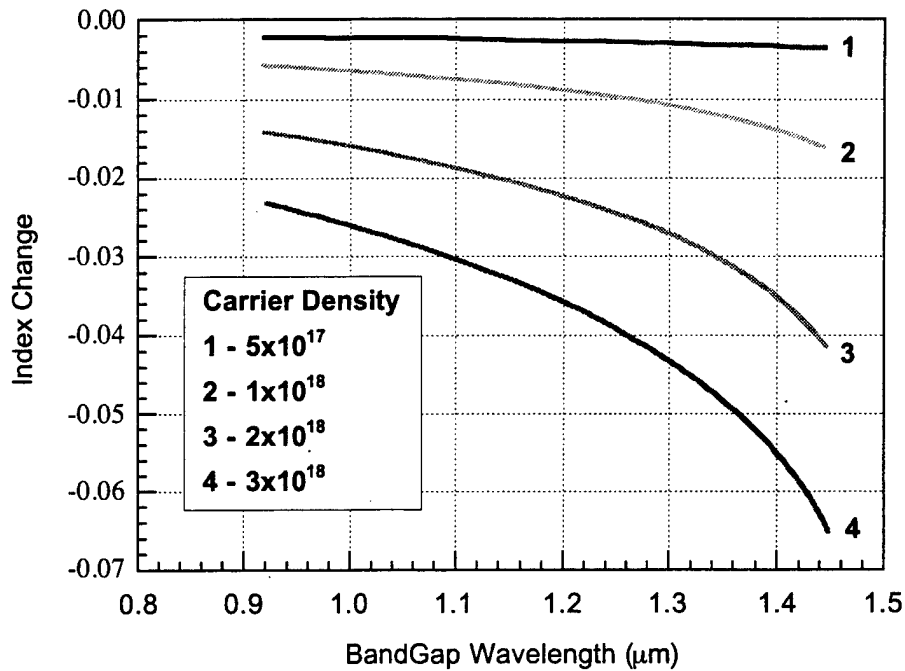


Figure 2-18 Index tuning as a function of bandgap wavelength for four different carrier densities at a wavelength of 1.56 μm .

Recombination

The carrier density in the tuning waveguide is a function of the current density and the recombination rate $R(N)$ which is given by (2-33). This equation includes the contributions from nonradiative recombination AN , bimolecular recombination BN^2 and Auger recombination CN^3 .

$$R(N) = AN + BN^2 + CN^3 \quad (2-33)$$

Current estimates for the coefficients in materials lattice matched to InP are given below.

$$A \approx 1 \times 10^8 [s^{-1}] \quad B \approx 2 \times 10^{-10} [cm^3/s]$$

$$C \approx 2 \times 10^{-29} [cm^6/s] \quad @ 1.3 \mu m$$

$$C \approx 5 \times 10^{-29} [cm^6/s] \quad @ 1.4 \mu m$$

$$C \approx 7.5 \times 10^{-29} [cm^6/s] \quad @ 1.55 \mu m$$

Waveguide Structure With Grating Layer

As shown in Section 2.2.1 the waveguide structure significantly effects the carrier transport properties for the laser both in the tuning sections and in the gain section. The difficulty in designing this structure results from the need to fulfill two contradictory roles. In the active section it is important to have efficient carrier transport into the quantum wells and to minimize the number of carriers trapped in the waveguide. However in the passive sections it is necessary to trap carriers in the waveguide and minimize the electron leakage for maximum index tuning.

Early SGDBR lasers fabricated at UCSB used a wet etching method to transfer the grating layer directly into the waveguide. This left about two thirds of the surface of the sample with exposed quaternary material for the regrowth. This structure was modified to include a separate grating layer between the waveguide and the quantum wells. The gratings were then formed by dry etching through this layer and stopping on an InP layer above the waveguide. The advantage of this approach is that it enables a very precise control over the coupling coefficient or kappa of the grating and it leaves the entire surface covered in InP which improves the quality of the regrowth. The structure had a 3000 Å 1.4Q waveguide layer, a 1000 Å thick 1.4Q grating layer, and four 1% compressively strained quantum wells in the active region. The waveguide and grating layers were separated by a 200 Å InP stop etch layer and another 200 Å InP layer separated the grating layer from the quantum wells (Figure 2-19). The waveguide and grating layers were Si doped at a concentration of 1E17 and

the stop etch layers were doped at $5E17$ to improve the electron transport into the quantum wells.

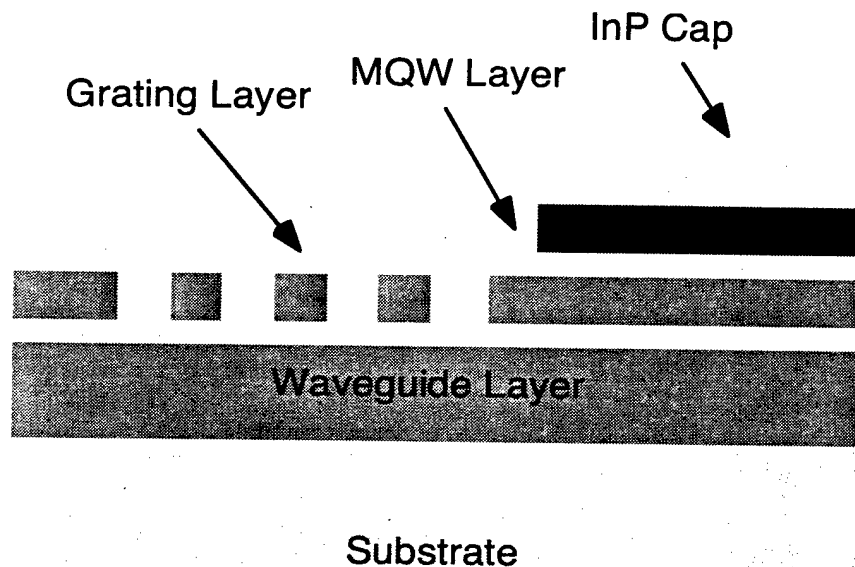


Figure 2-19 Waveguide structure with offset grating layer.

Ridge waveguide SGDBR and DBR lasers were fabricated with this structure using a dry etching technique for the DBR mirrors which left the grating layer intact in the phase control sections and in the sampling periods of the SGDBR mirrors. The DBR lasers had threshold currents of 40 mA for a 500 μm long active region and a 3 μm wide ridge. The front differential efficiencies were typically 11%. The tuning range for the DBR lasers was 5.8 nm which is the best number ever reported for a ridge waveguide DBR laser. Previous results from British Telecom showed tuning ranges on the order of 2.5 nm which is comparable to the values we achieved for DBR lasers with wet etched gratings fabricated with the same waveguide structure. One problem with the laser was that the phase sections for the DBR's displayed almost no forward tuning. The effective index shift for the DBR mirror and phase sections is shown in Figure 2-20.

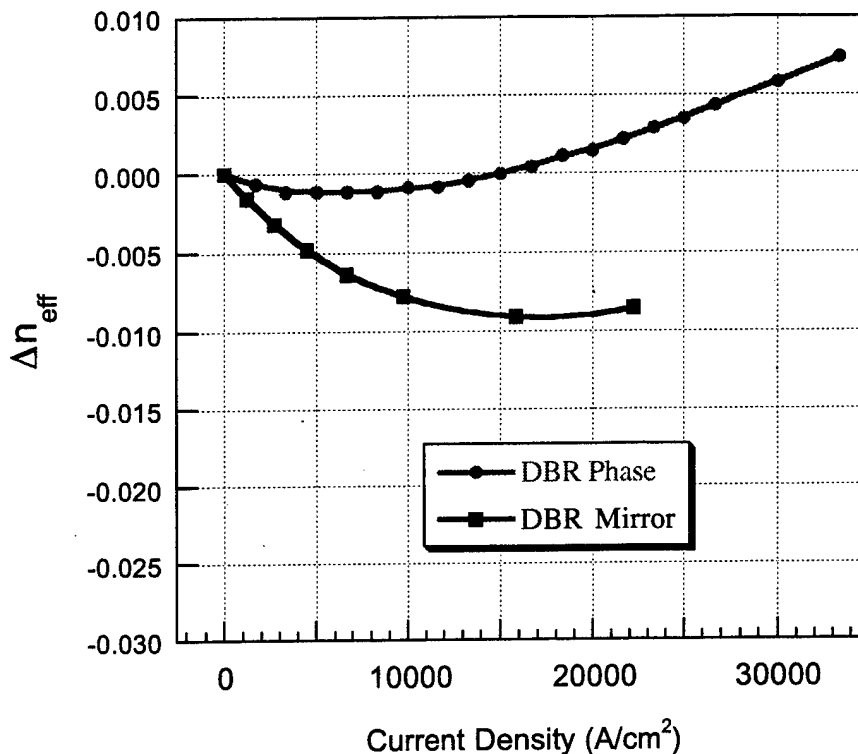


Figure 2-20 Comparison of the tuning efficiency for DBR phase sections and DBR mirror sections.

The sampled grating DBR's also showed almost no forward tuning. Current injection into the mirrors produced only reverse tuning from thermal effects. The cause of this problem was the grating layer in the passive sections. The stop etch between the grating layer and the waveguide blocked hole diffusion trapping the majority of the carriers in the grating layer which was immediately adjacent to the regrowth interface. In the DBR sections the grating etch penetrated through this layer enabling injection of carriers into the waveguide for good tuning. In the rest of the mirror the stop etch layer trapped the carriers in the grating layer which produced two problems. It limited the index

tuning to the thin grating layer which reduced the optical mode overlap and the maximum effective index change. The second is it trapped the carriers close to the regrowth interface where defects tend to reduce the carrier lifetime. After the quantum wells are removed in the passive sections the highly doped n-type InP stop etch layer remains on top of the grating layer. This lowers the barrier for electron confinement which results in increased carrier leakage that further reduces the tuning efficiency.

This problem can be solved in two ways. One is to remove the grating layer in the passive tuning sections and the other is to eliminate it altogether and simply etch the gratings into the top of the waveguide. We chose the latter approach since it results in less active-passive waveguide mode mismatch. The new structure is shown in Figure 2-21. It has a 4000 Å thick 1.4Q waveguide with the same offset quantum well active structure. The stop etch between the waveguide and the quantum wells was thinned from 200 to 100 Å and left undoped. This allows the zinc to diffuse into it during the regrowth and make it p-type. Having p-type InP at the top interface of the waveguide can reduce the electron leakage current by as much as 15%. Thinning the layer down to 100 Å keeps the resistance in the gain section at the same level as for a 200 Å thick n-doped layer.

Ridge waveguide SGDBR and DBR lasers were fabricated with the new base structure design and there was a significant improvement in the tuning efficiency. The DBR lasers had a threshold current of 20 mA for a 500 μm long device and the front differential efficiency improved to 30%. The tuning range for the DBR mirror was 6 nm which is comparable to the results from the previous structure. The major difference was in the tuning of the phase section. The index change vs. carrier density is plotted in Figure 2-22 and shows that the phase tuning is nearly twice as efficient as the DBR tuning.

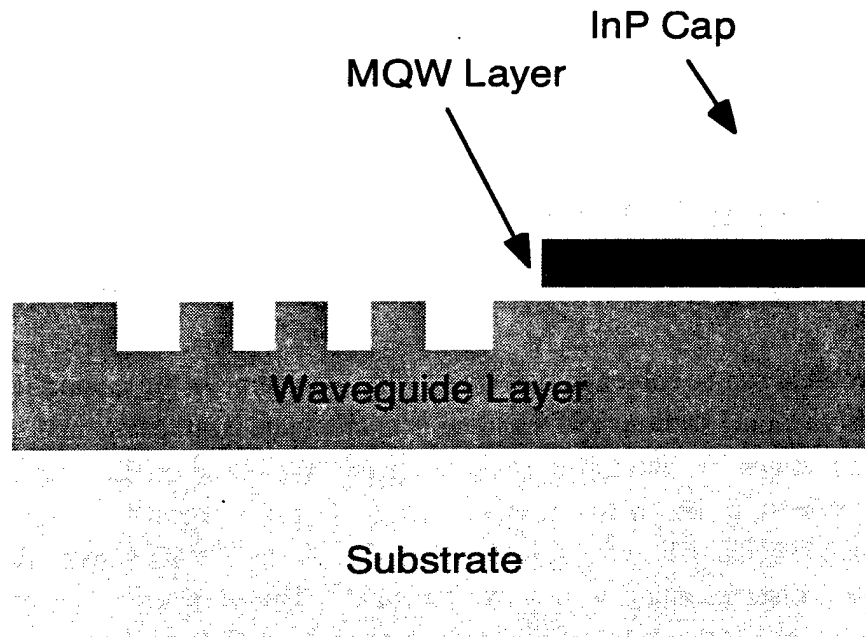


Figure 2-21 Waveguide structure with gratings etched directly into the top of the guide.

This improved tuning in the phase section is important for the SGDBR since 90% of the mirror is passive waveguide and only 10% actually contains gratings. Based on this fill factor we would expect the mirror peaks for the SGDBR to tune with about 90% of the efficiency of the phase section. The index change vs. current density for the SGDBR mirrors is shown in Figure 2-22. The tuning curve is plotted only for the required tuning range for full wavelength coverage in the SGDBR. If we extrapolate based on the phase section results we see that there is now more than double the required index tuning for full wavelength coverage in the ridge SGDBR.

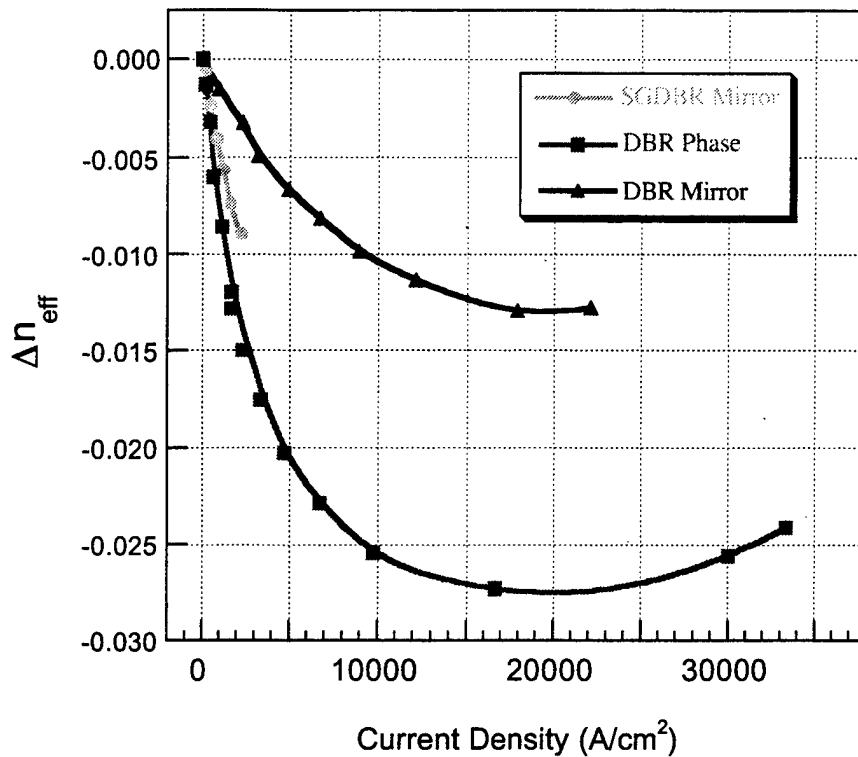


Figure 2-22 Tuning efficiency for ridge waveguide devices without a grating layer.

The DBR mirrors have a much lower tuning efficiency than the phase sections. This is a byproduct of the dry etching process used to form the gratings. Etch damage from the reactive ion etcher creates defects in the surface layers of the grating. These defects act as non-radiative recombination centers that reduce the carrier lifetime in the waveguide. The exposed quaternary material in the gratings during regrowth also leads to defects at the regrowth interface. This reduction in the carrier lifetime in the DBR section reduces the tuning efficiency since increased current density is required to achieve the same carrier density. The additional tuning current increases the device heating which tunes the index in the opposite direction. This thermal effect is particularly important in ridge

waveguide devices that have high thermal impedance. Fortunately the low duty cycle of the grating in the SGDBR allows it to obtain close to the same high tuning efficiency of the passive phase sections.

Effective index shift for ridge and buried waveguides

Buried heterostructure lasers typically have a lower thermal impedance than ridge waveguide devices. They can be fabricated with narrower ridge widths and they have improved lateral carrier confinement. All of these factors should combine to improve their tuning efficiency. The most significant improvement comes from reduced thermal tuning. Studies of the tuning range of ridge waveguide DBR's under pulsed tuning have shown that it can be almost as high as the tuning in buried heterostructure devices. The work by Sundaresan and Henning showed a cw tuning range of only 2.5 nm for a ridge waveguide DBR with a pulsed tuning range of more than 7 nm[22].

To improve the tuning range and overcome the thermal limitations of the ridge structure we fabricated buried heterostructure SGDBR lasers with the same identical transverse structure and 1.8 μm wide waveguides. A comparison between the effective index shift vs. carrier density for the ridge and buried heterostructure SGDBR mirrors is plotted in Figure 2-23. The buried heterostructure device requires approximately 40% lower tuning current than the ridge device up to an effective index shift of about 0.25%. This corresponds to roughly 4 nm of tuning. After this point the tuning in the ridge begins to roll off and the advantage of the buried heterostructure becomes more significant.

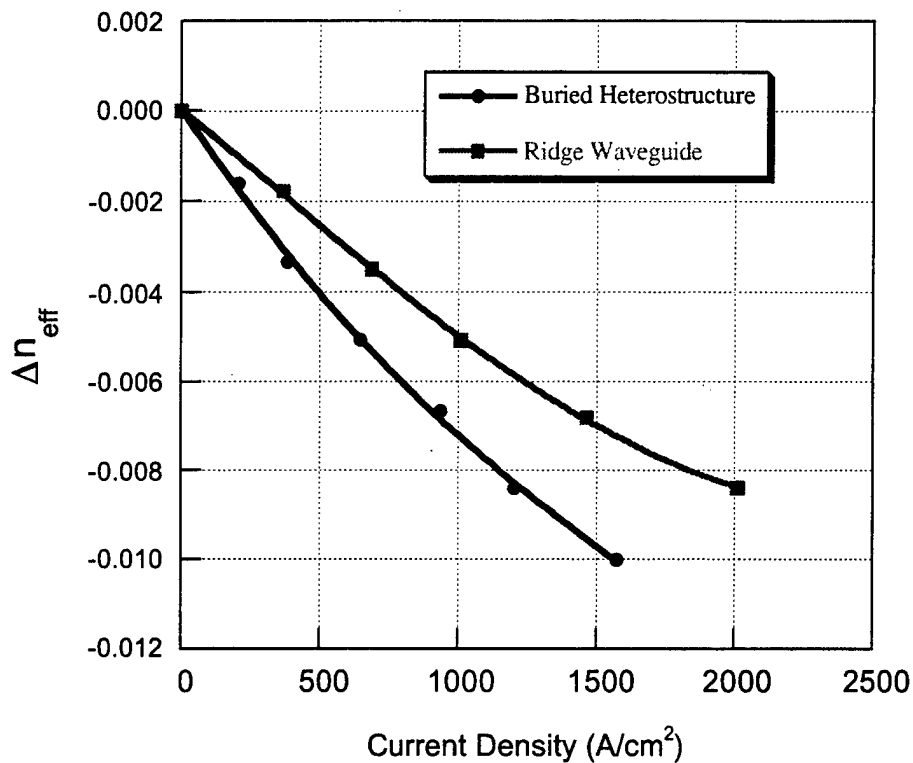


Figure 2-23 Comparison of index change vs. current density for ridge waveguide and buried heterostructure SGDBR mirrors.

2.4 Grating Etching Process

Fabrication of Bragg gratings is one of the critical process steps for the creation of SGDBR lasers. There is a considerable amount of literature devoted to the details of holographic patterning and etching of Bragg gratings which will not be repeated here. This section will include some discussion of the important details of the holographic patterning process but its primary focus will be on a

detailed comparison between wet and dry etching processes for grating formation.

2.4.1 Holographic Patterning

Process review

Gratings are patterned using a holographic exposure technique. In this method a thin photoresist is spun on the sample and then exposed with the interference pattern from a HeCd laser with a wavelength of 325 nm. The preferred photoresist is 1400-5, which is a holographic grating resist. When spun at 6000 RPM the resist is about 700 Å thick. As an alternative 1805 resist can be used if it is diluted to 5% by weight. The holographic exposure setup is shown in Figure 2-24.

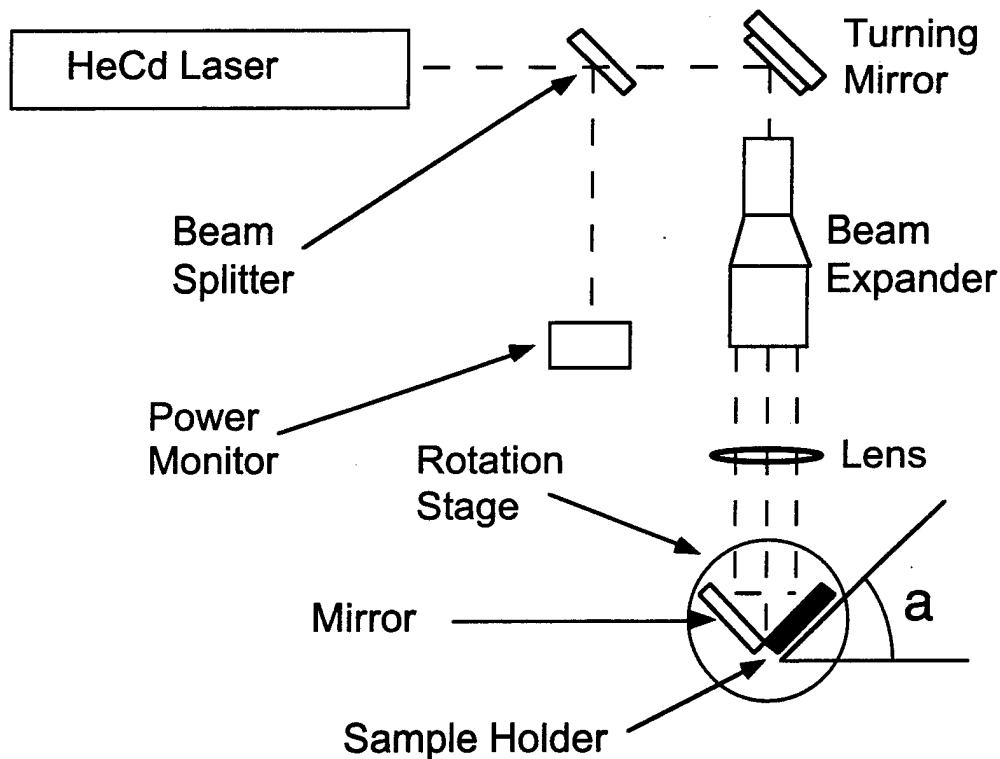


Figure 2-24 Holographic grating patterning system.

Light from the laser is passed through a beam expander and then directed onto the sample stage. The sample stage contains a sample holder and a UV mirror oriented at 90° to one another. One half of the beam is directly incident on the sample and the other half reflects off of the mirror and onto the sample. These two beams create a periodic interference pattern on the surface of the sample that exposes the resist in a grating pattern. The period of the grating Λ can be controlled by varying the incidence angle α of the two beams (2-34). A small portion of the laser light is split off to a power monitor so that the exposure conditions can be monitored.

$$\Lambda = \frac{\lambda}{2 \sin(\alpha)} \quad (2-34)$$

The period of the gratings can be measured very accurately using the setup shown in Figure 2-25. Laser light is directed onto the sample at a 45° angle. The angle is controlled by passing the reflected light through a pair of narrow apertures aligned precisely at 90° to the incident beam. The diffraction angle can then be calculated by measuring the horizontal distance between the incident and diffracted beams at a distance D from the sample.

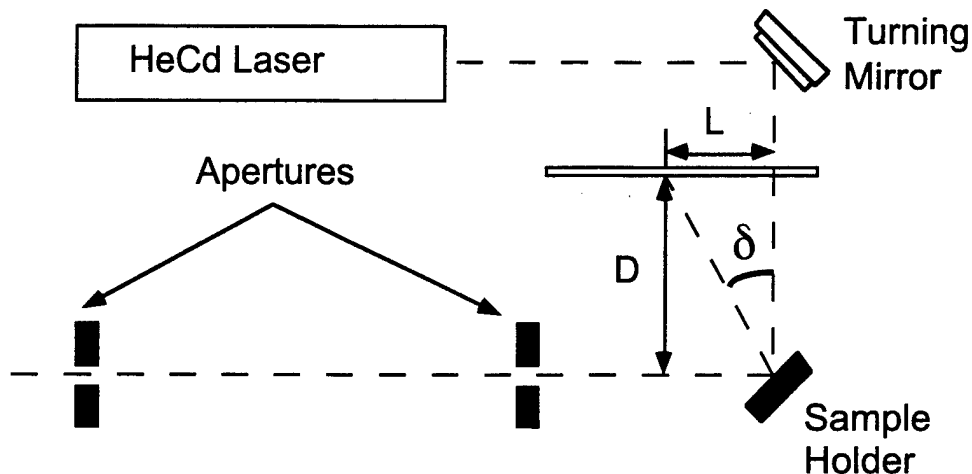


Figure 2-25 Grating period diffraction measurement setup.

The diffraction angle in terms of the distances L and D can be calculated using (2-35).

$$\theta_D = \pi/4 - \tan^{-1}(L/D) \quad (2-35)$$

Then the grating period can be determined using the well know relation for the diffraction angle (2-36).

$$\sin(\theta_D) = \sin(\theta_i) - \frac{\lambda}{\Lambda} \quad (2-36)$$

Taking the incident angle to be 45°, and setting the separation D to 23" these two equations can be combined to give the grating period only as a function of the diffraction distance L (2-37).

$$\Lambda = 325 \cdot \left(\frac{1}{\sqrt{2}} - \sin\left(\frac{\pi}{4} - \tan^{-1}\left(\frac{L}{23}\right)\right) \right)^{-1} \quad (2-37)$$

2.4.2 *Wet etched gratings*

For wet etched sampled gratings the patterning procedure uses a two step exposure that creates the grating bursts and removes the resist everywhere else on the sample. First the resist is exposed with the grating mask in a contact aligner at 7.5 W/cm² for 1 s. Then the holographic exposure is done. After development the gratings remain only in the area covered by the mask.

SBW etchant

Gratings can be wet etched using a saturated bromine water (SBW) based etching solution. The preferred concentration is 2:1:15 SBW:H₃PO₄:H₂O. This etch slows on <111>A planes leaving triangular shaped gratings for ridges oriented in the <011> direction. One nice feature of this etch is that it is self-limiting. The etch rate slows as the time proceeds because the Bromine evaporates from the solution. Unfortunately this also makes it very difficult to

get consistent etching rates so the solution must be calibrated every time it is mixed. Another drawback is that the triangularly shaped gratings have a $2/\pi$ lower kappa than a square wave grating of the same depth.

Etch rate enhancement

The main problem with the wet etching process is the micro-loading effect that occurs around masked areas. The vertical etching rate on the $\langle 100 \rangle$ plane for the SBW based etchant is primarily diffusion limited. This leads to a strong dependence of the etching rate on the mask duty cycle [23]. If the area around the grating bursts is masked off then the etching rate at the edge of the masked area will be significantly enhanced. This can yield etching depths as much as four times greater at the edge of the masked region. To achieve uniform etch depth for the sampled gratings the areas around the grating burst must be left unmasked. This causes the entire surface of the wafer to be etched at about half the rate of the gratings. One advantage of this approach is that the etch rate of the gratings falls off near the edges creating a natural apodization that lowers the side lobes in the reflection spectrum. The negative aspects of this are that the entire surface of the wafer in the passive sections is now left with exposed quaternary material. This complicates the regrowth procedure and lowers the quality of the regrown interface. Another more minor problem is that the active passive junction discontinuity is increased because the passive waveguide is thinned by the grating etch. This slightly increases the coupling loss at these interfaces.

2.4.3 Dry etched gratings

The wet etching technique for fabricating gratings has a number of distinct drawbacks and is fundamentally a difficult process to control. The ideal grating etch process would produce a square etched grating profile to achieve the maximum κ for a given etch depth, and would protect the waveguide sections in between grating bursts. This would improve the active passive junction coupling and maintain an InP surface layer over the majority of the passive

sections. This process requires a non-isotropic etching system with some kind of two step masking technique that will protect the areas outside of the grating bursts. The best method for the etching is a methane-hydrogen-argon based reactive ion etching approach. This can be masked with either silicon nitride or photoresist, which will facilitate a two step masking process.

Two step grating mask technique

For dry etched gratings the two step masking process is more complicated than for the wet etching technique. First a thin SiNx layer is deposited on the surface. This layer is patterned with the grating mask using an image reversal resist, 5214 and dry etched in a CHF₃ RIE process. This process leaves openings in the SiNx mask where the gratings will be formed. Next a holographic resist is spun over the entire surface of the wafer and patterned using the interference technique. It is important to use as thin a layer as possible for the SiNx to avoid perturbing the resist thickness. Initial tests were performed with a 1000 Å thick layer to ensure proper masking for the grating etch. However this thickness significantly perturbed the holographic resist causing it to build up at the edges of the windows. When the gratings were exposed and developed the variation of the resist thickness made some areas overdeveloped while others were underdeveloped. This resulted in considerable non-uniformity for the gratings over the sample and lowered the device yield. Subsequent testing confirmed that a layer of only 300 Å is thick enough to guarantee masking in the dry etch process and thin enough to enable the resist to be spun over it uniformly. Using this thickness for the SiNx gave highly uniform gratings over the entire surface of the wafer.

Grating etching conditions (MHA RIE)

The dry etch process for fabricating gratings is a complicated multi-step procedure. It is highly repeatable if followed exactly however there can be significant variation in the etch rate for samples of different sizes. This makes it important to use a consistent sample size and masking condition to achieve consistent results. The process begins with two steps to prepare the chamber, a twenty minute oxygen clean followed by a ten minute MHA pre-coat step. Omitting either of these steps can dramatically change the etching behavior.

Then the sample is loaded and the chamber pumped down to a pressure of 1×10^{-6} Torr before the etching steps. The etching profile and etch rate is highly dependant on the pressure and bias voltage. The best conditions for forming a square grating profile with good uniformity are to begin with a two minute etch at a pressure of 125 mTorr and a bias of 200V. This low power etch builds a polymer on the surface of the resist which protects it during the subsequent high power etch. The etch rate for a 1 cm^2 test sample under these conditions is approximately 160 \AA per second. The second etch step is performed for 2 minutes at a pressure of 75 mTorr and a bias of 500V. The etch rate for these conditions is approximately 480 \AA per second. These conditions produce a good rectangular grating profile with high κ and good uniformity Figure 2-26.

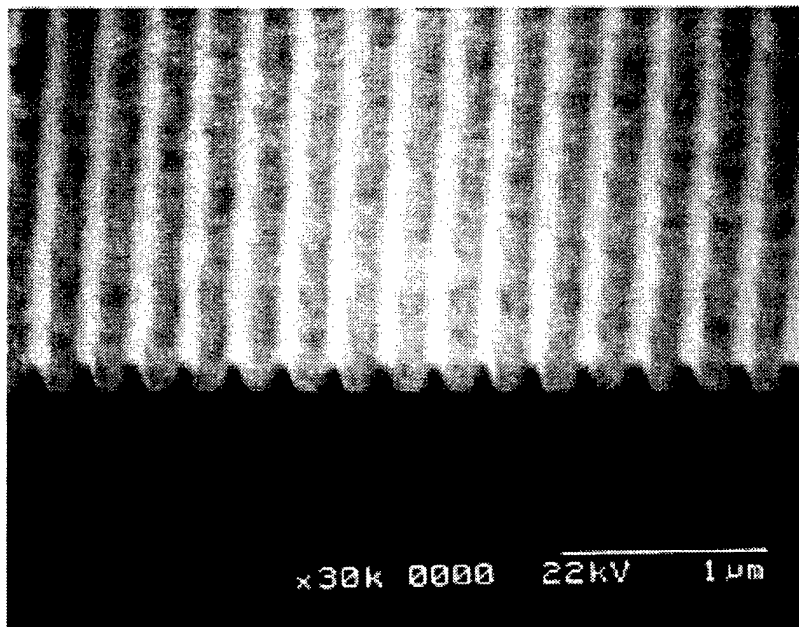


Figure 2-26 SEM Photo of dry etched gratings. Period is 240 nm and the etch depth is approximately 1260 \AA .

A more sinusoidal grating profile can be produced by etching for a longer period of time using the first set of conditions. The higher pressure and lower power produce a more isotropic etch which results in a softer profile. If the first etch

step is omitted then the high-power etch attacks the photoresist resulting in a greater degree of roughness in the grating profile

2.5 Continuously Tunable Ridge SGDBR Lasers.

Ridge waveguide sampled grating DBR lasers have a number of desirable features, which make them attractive for use in photonic integrated circuits. The most significant is that they can be made with a simple low cost fabrication process that can be easily modified to monolithically integrate them with other components. Ridge waveguide structures are not commonly used for tunable lasers since buried heterostructure devices have lower thresholds and more efficient index tuning. However we have shown that by careful design of the waveguide thickness and bandgap it is possible to achieve wide range tuning in ridge waveguide SGDBR's.

2.5.1 Device structure

The waveguide structure for the laser is shown in Figure 2-21 it consists of a 4000 Å thick 1.4Q waveguide with four offset quantum wells separated by a 100Å thick stop etch layer. The barriers in the active region are 80Å thick 1.3Q material with a slight -0.3% tensile strain. The wells are 65Å thick and have a 1% compressive strain. The peak of the photoluminescence spectrum for the quantum wells is at 1550 nm. The upper cladding is 2 μm thick with a 1000Å thick degenerately p-doped InGaAs cap layer. The ridge waveguide is 3 μm wide and is etched down to the top of the waveguide.

The active and phase sections are 450 and 150 μm long respectively. The back mirror has 11 sampling intervals which have a 71 μm period and an 8 μm grating burst this gives it a total length of 789 μm. The front mirror is shorter and has a lower reflectivity, which improves the front differential efficiency. It has 8 sampling intervals with a 64 μm period and 6.5 μm grating bursts for a total length of 518.5 μm. The group index for the waveguide mode is 3.72

which gives the front and back mirrors peaks spaced at 5 and 4.5 nm respectively.

The $L-I$ characteristics for the devices were tested using a broad area detector. The lasers had a threshold current of 20 mA with an output power of 4 mW at a drive current of 100 mA.

2.5.2 *Tuning Characteristics*

Tuning range

In theory the design of the SGDBR is such that if the mirrors can be tuned over the range of their peak spacing the laser can be tuned over the entire tuning range allowed by the repeat mode spacing limit. In practice the mirror reflectivity rolls off at the edge of its spectrum, and the gain rolls off as the wavelength is tuned away from quantum well gain peak. These effects can limit the wavelength range even for devices that have sufficient index tuning to cover their entire mirror spectrum.

The tuning range for the ridge SGDBR lasers was 22 nm which is the widest ever reported for a ridge waveguide laser. The tuning range was limited by gain saturation in the quantum wells and not by the index shift in the mirrors. The superimposed spectra for 27 DWDM channels on the ITU grid with equal output power are shown in Figure 2-27. This required control of all four sections. Without active gain control the power variation for this tuning range was 9.5 dB. This variation was predominantly due to increased loss in the mirrors under high tuning currents. For a constant drive current the variation in the coarse tuned mirror peaks was only 2 dB.

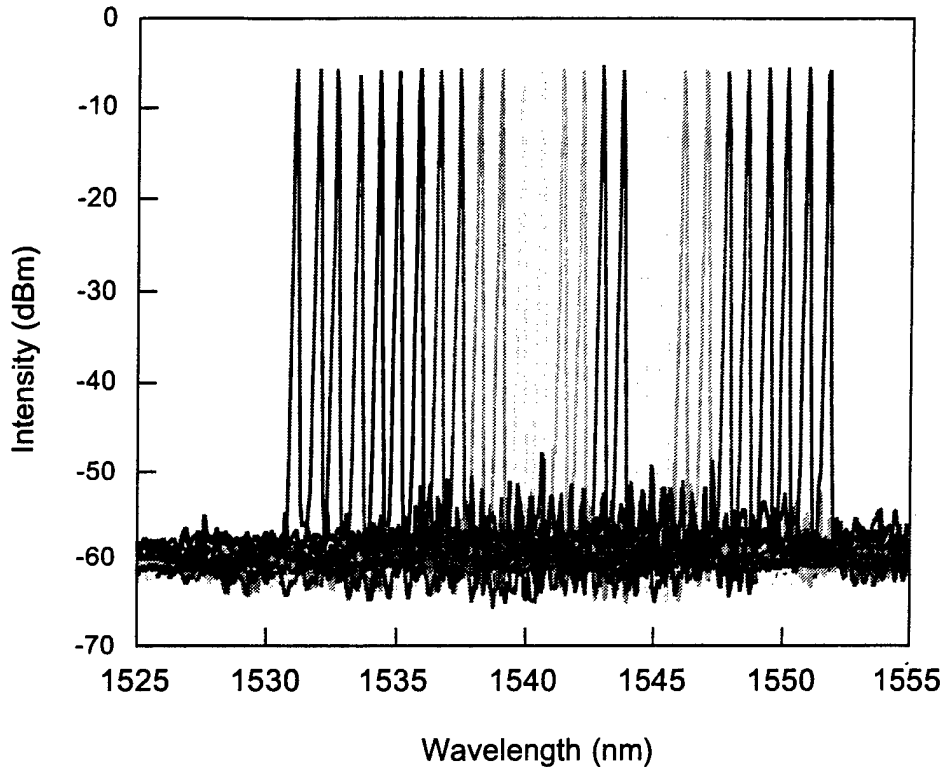


Figure 2-27 Superimposed spectra for ridge waveguide SGDBR showing 27 WDM Channels Spaced at 100 GHz.

The side mode suppression ratio for SGDBR lasers is typically much higher than for DBR lasers. The sampled grating mirrors have a very low effective kappa and a larger mirror penetration depth which gives their reflection peaks a much narrower spectrum. The SGDBR uses two peaks that must be aligned which further increases the loss in the side modes. The 3 dB width of the reflection peaks is generally much narrower than the mode spacing in the laser. Because of this the highest side lobes usually occur at the misaligned adjacent mirror reflection peaks. This is the reason that there is a tradeoff in the mirror design between SMSR and tuning range. As the difference in the peak spacing between the front and back mirrors is decreased the tuning range limited by the repeat mode spacing increases dramatically. However the side mode

suppression ratio decreases because the adjacent mirror peaks are less misaligned. The test results for the ridge waveguide devices indicate that the SMSR is greater than 50 dB for some wavelengths and is more than 45 dB for the entire 22 nm tuning range.

Tuning currents

The tuning currents for the back and front mirror sections are shown in Figure 2-28 and Figure 2-29 respectively. The maximum tuning current in the back mirror was 52 mA. This value could have been reduced to about 40 mA if a more efficient set of mirror peaks were used. One of the drawbacks of the SGDBR's tuning characteristics is that there are typically many different combinations of tuning currents that can be used to reach the same wavelength. These different combinations correspond to the use of different mirror peaks either in the front or the back mirror.

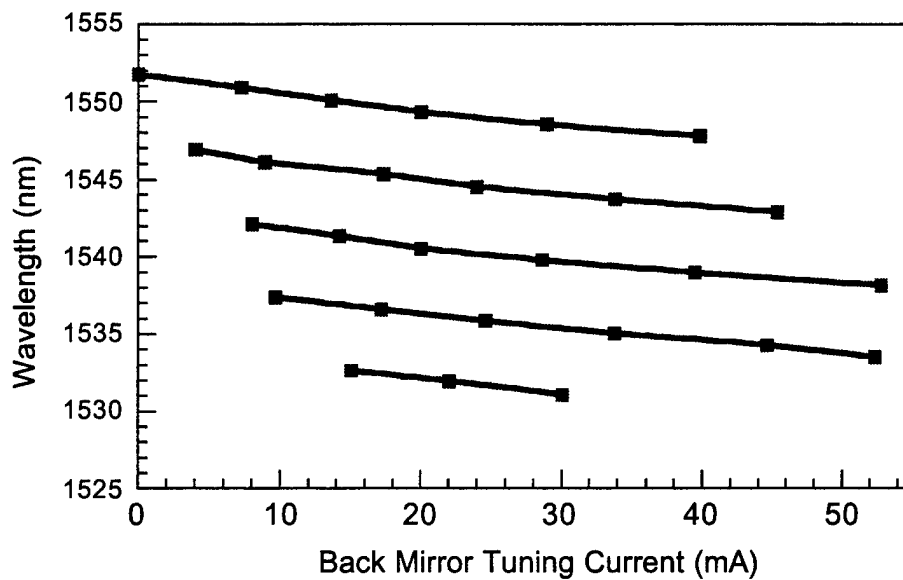


Figure 2-28 Back Mirror Tuning Current For Ridge Waveguide SGDBR

For this particular set of tuning curves the maximum tuning current in the front mirror was 30 mA. The maximum current density in the mirrors was on the order of 2 kA/cm^2 which gave an effective index shift of 0.3%. Five different mirror peaks in the front and back mirror were used to tune over this wavelength range.

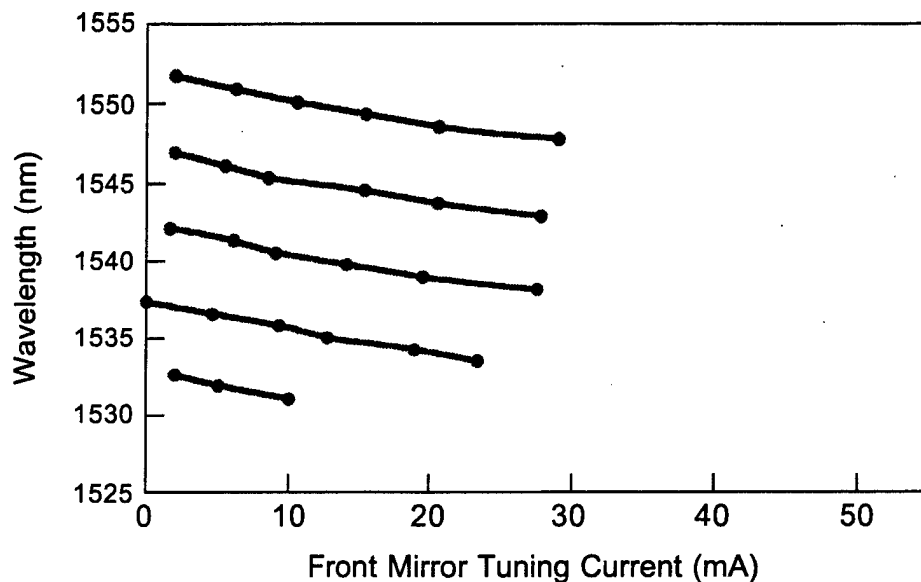


Figure 2-29 Front Mirror Tuning Current For Ridge Waveguide SGDBR

For these tests the phase section was manually adjusted to maintain the maximum side mode suppression ratio and the highest output power at a given wavelength. The phase current required to tune over a single mode spacing, which is about 0.6 nm, was only 2.5 mA.

Linewidth vs. Wavelength

The linewidth for the ridge waveguide SGDBR's was measured using a delayed self homodyne technique. In this approach a Mach-Zehnder interferometer with a path length imbalance that is much greater than the coherence length of

the source is used. The laser is coupled into the interferometer and the optical output is detected by a photodiode and displayed on an electrical spectrum analyzer. For this measurement a fiber-optic Mach-Zehnder was used with a path length imbalance of 3 km. Under these conditions the light from the two paths of the interferometer become statistically uncorrelated and the output is identical to that obtained by mixing two distinct optical sources. However since the line shape of the two sources is identical the power spectrum of the photocurrent is equal to the autocorrelation of the laser line shape. Single mode lasers usually have Lorentzian line shapes which is advantageous since the autocorrelation of a Lorentzian is a Lorentzian of double the width. This makes the half width of the photocurrent spectrum equal to the linewidth of the laser source. We measured the linewidth for a ridge waveguide SGDBR over a range of wavelengths from 1504 nm to 1542 nm. The results are summarized in Table 2-1. There was no observable correlation between the wavelength and the linewidth. The maximum value was 26.2 MHz at 1542 nm and the minimum was 11.3 MHz at 1538.

Table 2-1 SGDBR Laser Linewidth

Wavelength (nm)	1504	1509	1513	1516	1518	1521	1532	1538	1542
Linewidth (MHz)	14.5	12.0	14.9	12.1	12.2	23.9	14.0	11.3	26.2

2.5.3 *Dynamic Characteristics*

Modulation Bandwidth

The modulation bandwidth of a semiconductor laser is determined by its relaxation resonance frequency (ω_R). For small signal modulation the intensity can follow the current modulation up to frequencies near ω_R . Beyond this frequency the response drops off at 10 dB/decade. The 3 dB modulation

bandwidth for a laser can be approximated from the relaxation resonance frequency using (2-38)

$$f_{3dB} = \frac{\sqrt{1 + \sqrt{2}}}{2\pi} \omega_R \quad (2-38)$$

The relaxation resonance frequency for a semiconductor laser can be expanded in terms of the various rate coefficients and written as:

$$\omega_R^2 = \frac{v_g a N_p}{\tau_p} + \left[\frac{\Gamma v_g a N_p}{\tau_{\Delta N}} + \frac{\Gamma R_{sp}^{\circ}}{N_p \tau_{\Delta N}} \right] \left(1 - \frac{\tau_{\Delta N}}{\tau_{\Delta N}^{\circ}} \right) + \frac{1}{\tau_{\Delta N}^{\circ} \tau_p} \quad (2-39)$$

However in practice the first term dominates the response and the others can be neglected giving a more simplified form which can be rewritten in terms of the drive current.

$$\omega_R^2 = \frac{v_g a_0}{q V_p (1 + \epsilon N_p)} \eta_i (I - I_{th}) \quad (2-40)$$

In this equation the differential gain term a has been expanded to include the gain compression factor ϵ which takes into account the reduction in gain at high photon densities. From (2-40) we see that to maximize the bandwidth of the laser it is desirable to maximize the differential gain, minimize the volume of the laser mode, and maximize the current above threshold.

The modulation response for a ridge waveguide SGDBR was tested for four different bias levels from 40 mA to 80 mA. The results which are plotted in Figure 2-30 show a maximum bandwidth of 3.1 GHz at a bias of 80 mA. The threshold current for this device was 36 mA. This bandwidth is sufficient for transmitting under direct modulation at data rates up to OC-48 or 2.488 Gbit/s.

There are several factors which limit the modulation bandwidth for these devices. The most significant is that the SGDBR laser has a large mode volume

typically three to four times larger than a conventional DFB laser. This increases the photon lifetime in the cavity and reduces the modulation bandwidth. Other factors like carrier transport and gain compression which enhances the damping are not significant limitations in this frequency range. It is more important to be concerned with minimizing the parasitic capacitance's of the contacts and increasing the differential gain. The current four quantum well active region is sub-optimal for this device. A higher number of wells will shift the threshold gain to a lower point on the gain curve and enhance the differential gain. This will also improve the DC characteristics for the device at the cost of a small increase in the active passive junction mode mismatch.

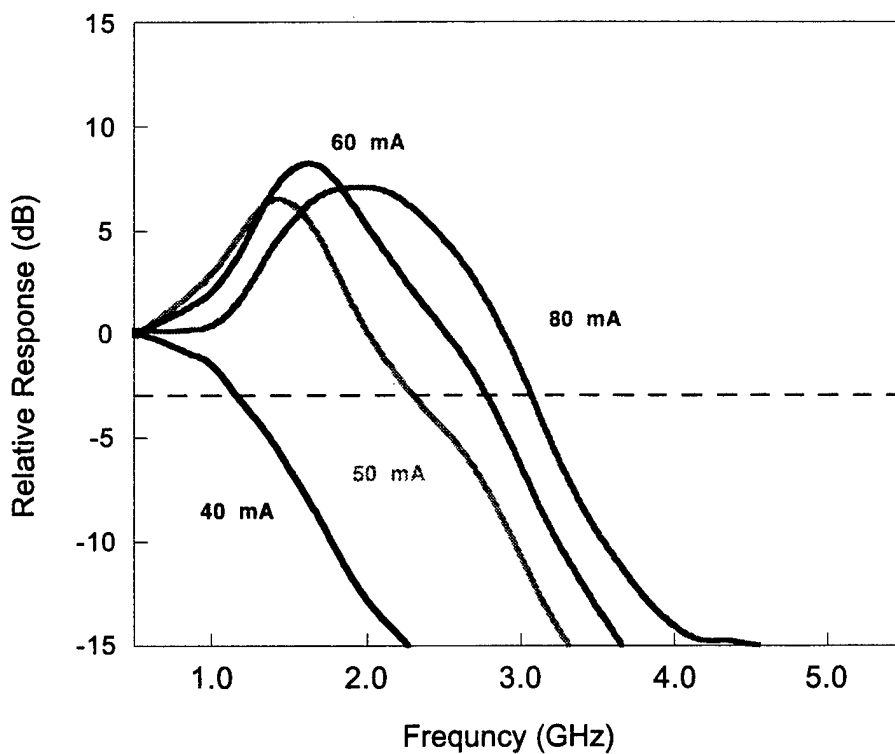


Figure 2-30 Modulation Bandwidth for Ridge Waveguide SGDBR at four different gain current levels.

2.6 Buried Heterostructure Devices.

The buried heterostructure laser has a number of significant advantages over ridge waveguide devices especially for tunable lasers. The buried heterostructure provides lateral current and carrier confinement in addition to improved thermal impedance and lower optical loss. They can be scaled to much smaller waveguide widths than is possible with ridge devices and they have higher tuning efficiencies. These devices are more difficult to fabricate than ridge waveguide lasers but they still have great potential for use in photonic integrated circuits. Ridge waveguide SGDBR lasers have some attractive features but to achieve very wide tuning ranges on the order of 60 nm with continuous wavelength coverage is not possible without the use of a buried heterostructure design.

2.6.1 Device Structure

The simplest form of buried heterostructure laser is the buried ridge stripe. This device can be fabricated with only one regrowth step which makes it almost as easy to make as the ridge waveguide device. More complicated devices such as the planar buried heterostructure laser which use P-N-P junctions for current blocking have lower leakage current and better high temperature performance but are significantly more difficult to produce.

The waveguide structure for the buried laser is identical to the one used for the ridge waveguide device shown in Figure 2-21. It consists of a 4000 Å thick 1.4Q waveguide with four offset quantum wells separated by a 100 Å thick stop etch layer. The barriers in the active region are 80 Å thick 1.3Q material with a slight -0.3% tensile strain. The wells are 65 Å thick and have a 1% compressive strain. The peak of the photoluminescence spectrum for the quantum wells is at 1550 nm. The base structure is capped with a 2600 Å thick layer of InP with a 600 Å doping setback from the top of the quantum wells.

The 1.8 μm wide buried ridge is dry etched through the waveguide with a methane hydrogen argon reactive ion etcher. The regrown cladding layer is 2.5 μm thick with a 1000 \AA InGaAs contact layer. The contact layer is etched off and the cladding is proton implanted on either side of the laser stripe to provide lateral current confinement. A schematic cross section of the active region is shown in Figure 2-31.

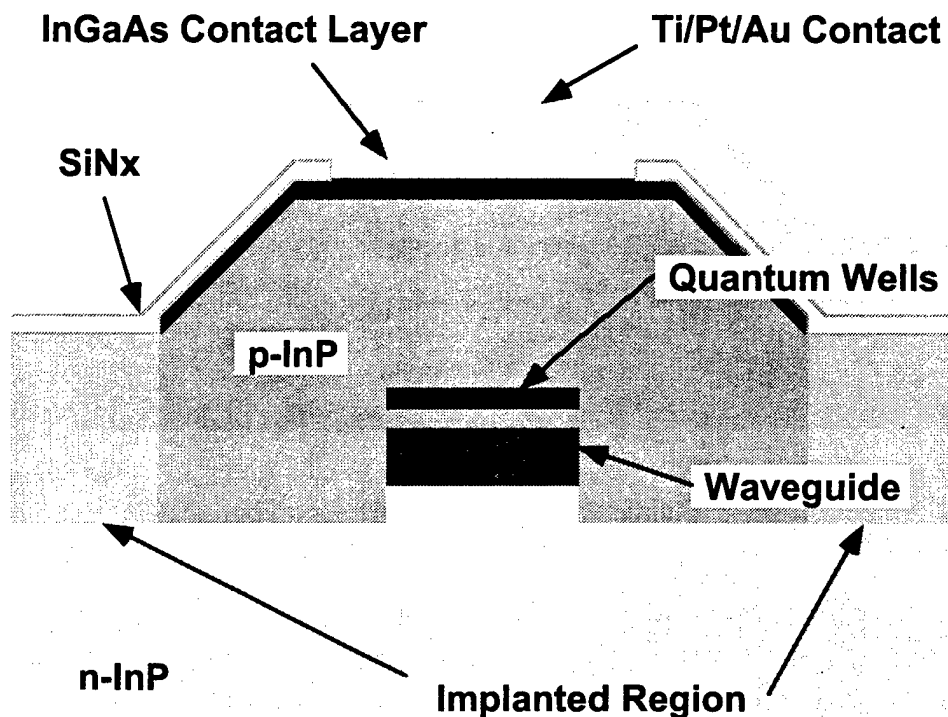


Figure 2-31 Buried Ridge Cross Section With Offset Active Region

A laser was cleaved through the active section and stain etched to reveal the structure Figure 2-32. The waveguide and quantum well active regions are clearly visible separated by a thin InP stop etch layer. The stain etch is dopant

selective so the implanted regions are clearly visible on either side of the buried ridge waveguide.

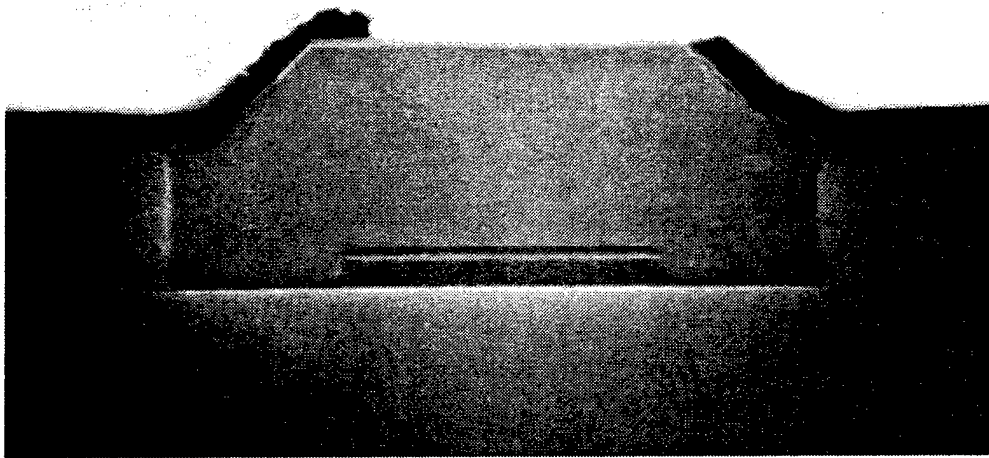


Figure 2-32 Stain etched SEM cross section of buried device.

The active and phase sections are 600 and 150 μm long respectively. The back mirror has 12 sampling intervals which have a 64 μm period and a 6 μm grating burst this gives it a total length of 710 μm . The front mirror is shorter and has a lower reflectivity which improve the front differential efficiency. It has 10 sampling intervals with a 58 μm period and 6 μm grating bursts for a total length of 528 μm . The group index for the waveguide mode is 3.72 which makes the front and back mirrors peak spacing 5.65 and 5.05 nm respectively.

The $L-I$ characteristics for the devices were tested using a broad area detector. The lasers had a threshold current of 15 mA with an output power of 1.2 mW at a drive current of 100 mA. The low output power was caused by high leakage current at the parasitic junction and a low injection efficiency for the quantum wells. The 600 \AA zinc doping setback was insufficient for the 2.5 μm

regrowth thickness. This allowed the zinc dopant to diffuse into the quantum wells shifting the junction below the active region dramatically reducing the injection efficiency and increasing the loss. Keeping the Zn dopant out of the waveguide is critical to achieving low loss in buried heterostructure lasers since inter-valence band absorption is one of the dominant loss mechanism in these devices. A thicker doping set back layer of 1600 Å should be used to prevent this. The leakage current at the parasitic junction can be reduced by increasing the etch depth for the buried ridge to an additional 3000Å past the waveguide into the lower cladding. This will increase the resistance for current leakage around the junction.

2.6.2 *Tuning Characteristics*

Tuning range

A schematic of the buried heterostructure device is shown in Figure 2-33. The continuous coverage tuning range for these lasers was 41 nm. This gave them almost twice the tuning range of the ridge SGDBR's with less than half the tuning current. The device was capable of reaching 51 channels at 100 GHz spacing with equal output power over a range of wavelengths from 1525 to 1565 nm. The superimposed spectra for the DWDM channels are shown in Figure 2-34. Reaching all of these channels required control of all four sections of the laser. Without active gain control the power variation for this tuning range was 14 dB at a constant bias current of 50 mA to the active section. This variation was predominantly due to increased loss in the mirrors under high tuning currents. The laser was designed for a tuning range of 55 nm but could not be tuned over the entire range because the reflectivity of the outer mirror peaks was too low. Lasers were fabricated with four different sets of mirrors each one for a different tuning range. For all of these devices the tuning range was lower than the design value as can be seen in Table 2-2. In each case the outermost mirror peaks for the tuning range could not be reached. For future devices shorter grating bursts should be used to achieve a wider mirror bandwidth.

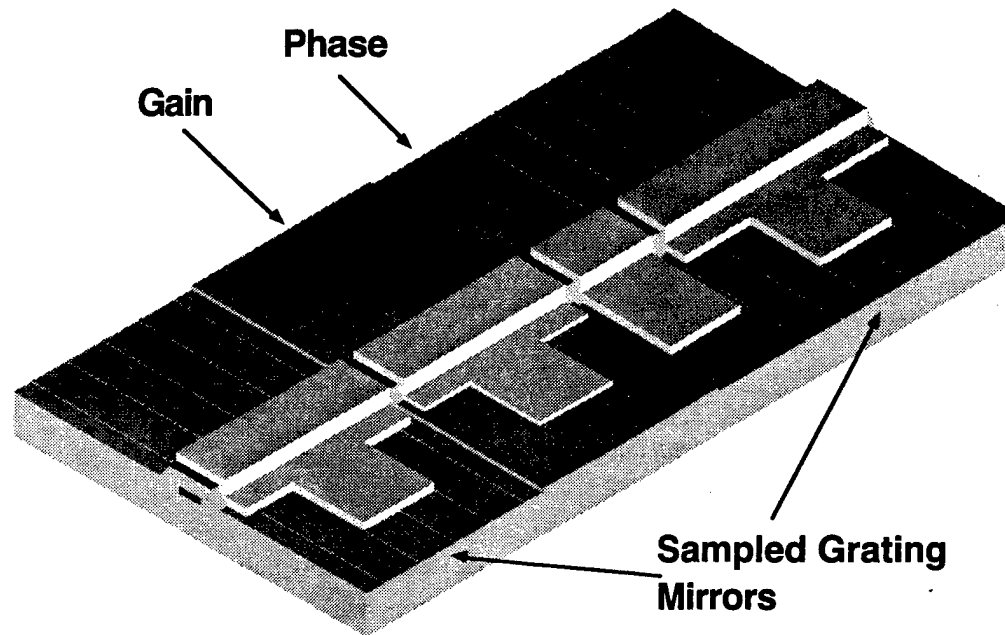


Figure 2-33 Buried heterostructure SGDBR laser schematic

Table 2-2 Summary of Buried Laser Tuning Ranges

Laser #	Designed Tuning Range	Actual Tuning Range
1	36	30
2	45	35
3	55	42
4	66	47

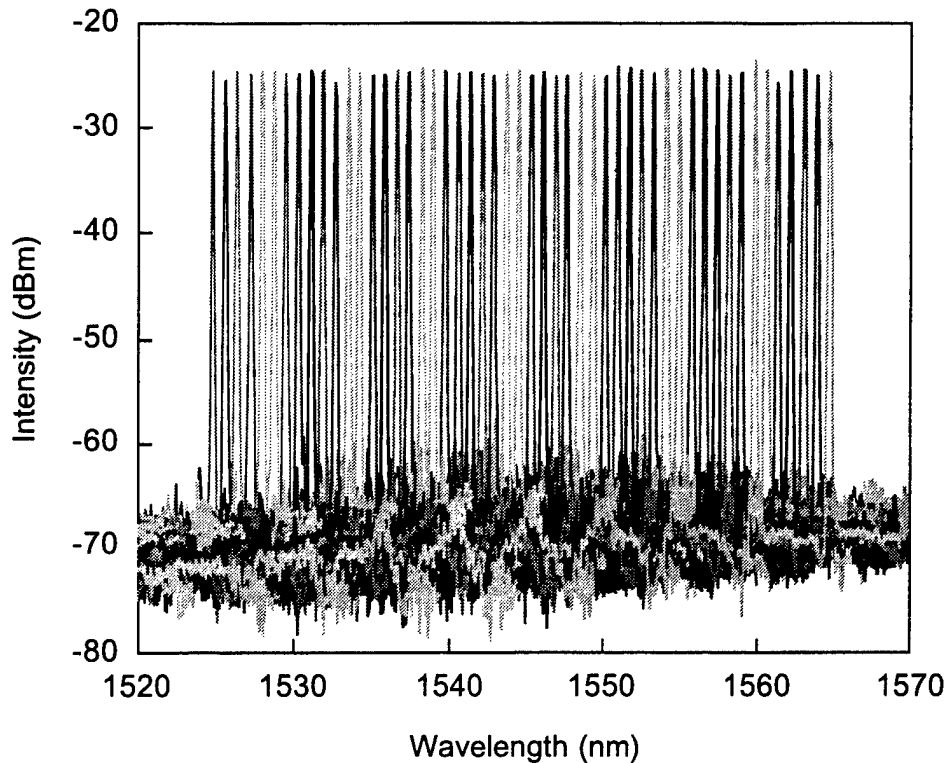


Figure 2-34 Buried heterostructure SGDBR tuning spectra showing 51 channels spaced at 100 GHz over a 40 nm tuning range

The side mode suppression ratio for the buried heterostructure SGDBR lasers was not as good as it was for the ridge devices. This is primarily due to the rollover problem which prevented them from being operated at more than twice the threshold current. The spectra for the laser indicate that the SMSR is greater than 40 dB for some wavelengths and is more than 36 dB over the entire 42 nm tuning range.

Tuning Curves

The tuning currents for the back and front mirror sections are shown in Figure 2-35 and Figure 2-36 respectively. The maximum tuning current in the back mirror was 23.5 mA and the maximum tuning current in the front mirror was

20.5 mA. The maximum current density in the mirrors was on the order of 1.5 kA/cm^2 which gave an effective index shift of 0.32%. The current density is only 75% of the value required for 22 nm of tuning in the ridge device and the total index shift is only slightly higher because a more efficient design was used that took advantage of a greater number of mirror peaks.

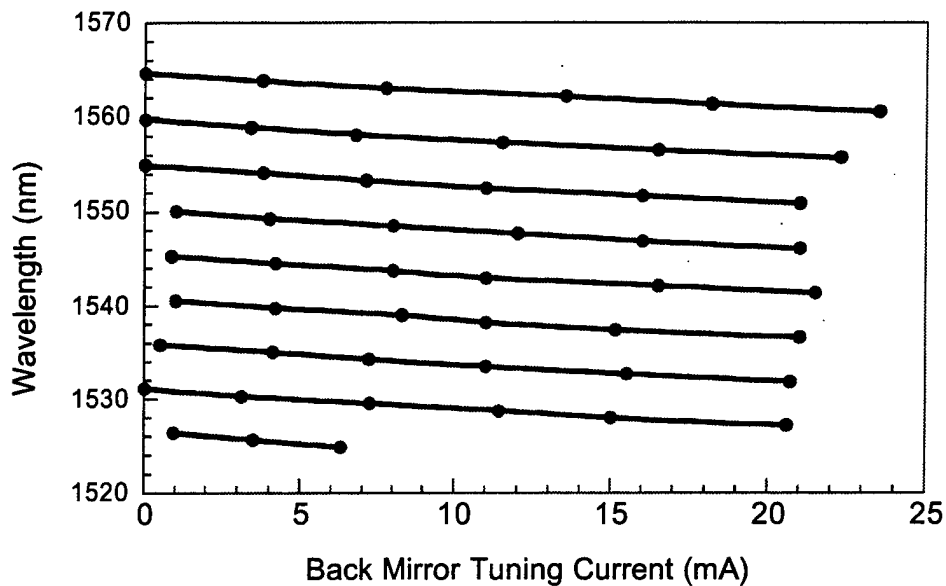


Figure 2-35 Buried Ridge SGDBR Back Mirror Tuning Currents

For these tests the phase section was manually adjusted to maintain the maximum side mode suppression ratio and the highest output power at a given wavelength. The phase current required to tune over a single mode spacing, which is about 0.6 nm, was only 1.2 mA.

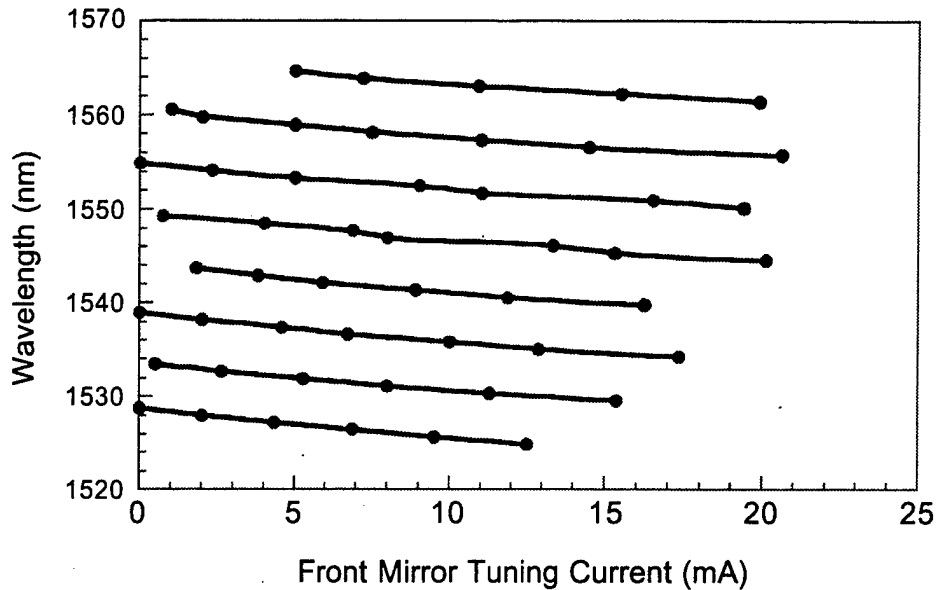


Figure 2-36 Buried Ridge SGDBR Front Mirror Tuning Currents

2.7 Summary

These results clearly demonstrate that practical widely tunable lasers can be made using offset quantum well structures. This is an important development for the development of photonic integrated circuits incorporating tunable lasers. The offset quantum well process for forming active and passive junctions is an extremely efficient high yield process which has been successfully used for large integrated photonic devices like the Lucent Technologies MFL laser. However prior to this work no one had been able to successfully demonstrate a widely tunable laser with an offset quantum well active region. All of the other work to date on tunable lasers has employed butt joint regrowth techniques for fabricating active and passive sections within the same device. This approach is complicated and less suitable for large scale photonic integrated circuits. We have developed a simple low cost process that uses a single regrowth step to

84

fabricate buried heterostructure sampled grating distributed Bragg reflector lasers. This will facilitate the development of future photonic integrated circuits which incorporate these devices.

References

- [1] Frigo, N.J., *et al.*, *A wavelength-division multiplexed passive optical network with cost-shared components*. IEEE Photonics Technology Letters, 1994. 6(11): p. 1365-7.
- [2] Chang, Y., *et al.*, *Optically controlled serially fed phased-array transmitter*. IEEE Microwave and Guided Wave Letters, 1997. 7(3): p. 69-71.
- [3] Forrest, S.R. and R.B. Taylor. *Optically controlled phased array radar*. 1996.
- [4] Ishii, H., *et al.*, *Quasicontinuous Wavelength Tuning in Super-Structure-Grating (Ssg) Dbr Lasers*. Ieee Journal of Quantum Electronics, 1996. 32(3): p. 433-441.
- [5] Oberg, M., *et al.*, *Complete Single Mode Wavelength Coverage Over 40 Nm With a Super Structure Grating Dbr Laser*. Journal of Lightwave Technology, 1995. 13(9): p. 1892-1898.
- [6] Rigole, P.J., *et al.*, *Quasi-continuous tuning range from 1560 to 1520nm in a GCSR laser, with high power and low tuning currents*. Electronics Letters, 1996. 32(25): p. 2352-2354.
- [7] Jayaraman, V., Z.M. Chuang, and L.A. Coldren, *Theory, Design, and Performance of Extended Tuning Range Semiconductor Lasers With Sampled Gratings*. Ieee Journal of Quantum Electronics, 1993. 29(6): p. 1824-1834.
- [8] Delorme, F., *et al.*, *Sampled-grating DBR lasers with 101 wavelengths over 44 nm and optimised power variation for WDM applications*. Electronics Letters, 1998. 34(3): p. 279-81.
- [9] Ougier, C., *et al.*, *Sampled-grating DBR lasers with 80 addressable wavelengths over 33 nm for 2.5 Gbit/s WDM applications*. Electronics Letters, 1996. 32(17): p. 1592-3.
- [10] Saavedra, A.A., *et al.*, *Amplitude and frequency modulation characteristics of widely tunable GCSR lasers*. Ieee Photonics Technology Letters, 1998. 10(10): p. 1383-1385.
- [11] Matthews, P.J., M.Y. Frankel, and R.D. Esman. *Fiber-optic control of a two-dimensional, true time-steered array transmitter*. 1996.
- [12] Delorme, F., *et al.*, *Butt-Jointed Dbr Laser With 15nm Tunability Grown in Three Movpe Steps*. Electronics Letters, 1995. 31(15): p. 1244-1245.

- [13] Jayaraman, V., *et al.*, *Widely tunable continuous-wave InGaAsP/InP sampled grating lasers*. Electronics Letters, 1994. 30(18): p. 1492-4.
- [14] Delorme, F. and G. Alibert, *Reliability study of 1.55 μ m distributed Bragg reflector lasers*. Electronics Letters, 1997. 33(5): p. 394-6.
- [15] Blumenthal, D.J., *et al.* *Experimental demonstration of an all-optical routing node for multihop wavelength routed networks*. 1996.
- [16] Mayweather, D., *et al.*, *Wavelength tracking of a remote WDM router in a passive optical network*. IEEE Photonics Technology Letters, 1996. 8(9): p. 1238-40.
- [17] Doerr, C.R., *et al.*, *Chirped waveguide grating router multifrequency laser with absolute wavelength control*. IEEE Photonics Technology Letters, 1996. 8(12): p. 1606-8.
- [18] Coldren, L.A. and S.W. Corzine, *Diode lasers and photonic integrated circuits*. Wiley series in microwave and optical engineering. 1995, New York: Wiley. xxiii, 594.
- [19] Jayaraman, V., *Extended tuning range semiconductor lasers with sampled gratings*, . 1994. p. xi, 200 , bound.
- [20] Bennett, B.R., R.A. Soref, and J.A. Delalampo, *Carrier-Induced Change in Refractive Index of Inp, Gaas, and Ingaasp*. Ieee Journal of Quantum Electronics, 1990. 26(1): p. 113-122.
- [21] Weber, J.P., *Optimization of the carrier-induced effective index change in InGaAsP waveguides-application to tunable Bragg filters*. IEEE Journal of Quantum Electronics, 1994. 30(8): p. 1801-16.
- [22] Sundaresan, H. and I.D. Henning, *Measurements On Competition Between Carrier-Induced and Thermally-Induced Wavelength Tuning in Ridge Waveguide Dbr Lasers*. Electronics Letters, 1991. 27(21): p. 1897-1899.
- [23] Nishida, T. and T. Tamamura, *Microloading Effect in Inp Wet Etching*. Journal of the Electrochemical Society, 1993. 140(8): p. 2414-2421.

Chapter 3

Wavelength Monitoring

3.1 Introduction

This chapter discusses the design and development of an integrated wavelength monitor for use with tunable semiconductor lasers. Tunable lasers are important components for next generation wavelength division multiplexed fiber optic networks. The wide tuning range, and ability for high speed data transmission under direct modulation, make SGDBR lasers especially attractive for multi-channel dense WDM networks. These lasers tune over wide wavelength ranges by employing Vernier effect tuning. Wavelength control in an SGDBR requires the alignment of reflection peaks from the front and back mirrors with a cavity mode at the desired wavelength. This entails control of four separate currents to achieve complete wavelength coverage over the entire tuning range. The increased complexity of the tuning mechanism in SGDBR lasers and the wider tuning range make them more susceptible to wavelength drift. This drift can be minimized, by operating the device at the optimum mirror alignment for any given wavelength. Using feedback on the output wavelength and intensity, it is possible to lock the device at this operating point. External devices for monitoring the wavelength and output power of the laser can be complicated and expensive. There are a number of significant advantages that can be realized by developing a compact integrated wavelength monitor which can be fabricated on chip with a tunable laser. The monitor must be capable of tracking the laser wavelength over its entire tuning range, which can be greater than 40 nm, and providing sufficient sensitivity to guarantee operation at WDM channels spaced as closely as 50 GHz.

Wavelength control in DWDM systems

Dense wavelength division multiplexing (DWDM) transmission systems are becoming increasingly sophisticated with a wavelength spacing of 100 GHz (0.8 nm) for current systems and less than 50 GHz (0.4 nm) for future systems. This has created a demand for precise and stable wavelength control and monitoring techniques that will ensure long-term reliability. Until recently fixed wavelength distributed feedback lasers (DFB) have been used to provide accurate and stable WDM sources. However as the number of wavelength channels increases and the channel spacing becomes narrower a real-time wavelength control system becomes a necessity to ensure system reliability. The key component in a wavelength control system is the wavelength locker.

Most wavelength lockers use some form of optical filter to lock a source to a fixed center wavelength on the International Telecommunications Union (ITU) grid. Light entering the locker or monitor is split into two paths. The first path sends light directly to a detector which uses the signal to provide a wavelength insensitive reference. The second path directs light through a wavelength dependant filter and then to a second detector. The locker uses the ratio of the two detector outputs to generate an error signal. In a typical module, the error signal is fed to a temperature controller that is adjusted to tune the laser wavelength. Cooling the device shifts the laser output to shorter wavelengths while heating the device shifts it to longer wavelengths. Conventional DFB lasers have a temperature sensitivity of about 0.25 nm/°C or about 30 GHz so a temperature stability of better than 0.17 °C is required for 5 GHz wavelength control [1].

Wavelength drift in Tunable Lasers

Aging of tunable lasers is of considerable importance for wavelength stability in WDM communications systems. The effects of aging on the output wavelength are more significant for tunable lasers than for fixed wavelength DFB lasers. Changes in laser characteristics with aging are the result of increased non-radiative recombination and leakage current [2]. In DFB lasers

the grating which controls the wavelength is in the active section of the device. The carrier density in the active section is clamped once the device reaches threshold. In the tuning section the carrier density is not clamped which enables much higher carrier densities that significantly increase the non-radiative recombination which tends to promote the motion, multiplication and growth of isolated defects into clusters [3]. This causes the tuning section to degrade more rapidly than an active section. In addition to this the effects of aging in an active section have a qualitatively different effect. Since the carrier density in the active region is clamped the effective index in the active region should remain constant as the laser ages even though the threshold current and differential efficiency are changing. This will be true for devices operated at constant drive currents. However for devices which are operated at a constant output power, increased current is required as the laser ages. This leads to increased device heating that can cause a small shift in the laser output wavelength.

There are several ways to combat the aging effects in tunable and fixed wavelength lasers. The primary approach is simply to make better devices which are not as susceptible to aging. For active sections minimizing the leakage paths and reducing the number of defects will increase the device lifetime. For tuning sections it is also desirable to reduce the defects which occur primarily at the regrowth interface and the grating layer. The other key improvement is to optimize the index tuning to reduce the required carrier density. For SGDBR lasers both of these advantages are realized [4]. The sampled grating has a low duty cycle that covers only 10% of the mirror regions. This significantly lowers the defects and the non-radiative recombination rate in the mirrors. The other advantage is the Vernier effect tuning which gives a wider tuning range with a smaller index shift. Using this effect and a low bandgap waveguide enables the maximum carrier density in the tuning regions to be kept to around the same level as the threshold carrier density in the gain section.

3.1.2 *Types of wavelength monitors*

There are a variety of methods which can be used for the optical filtering element in a wavelength monitor. The most common approach is based on an interference filter, however recently devices which have ratiometric filters, or dispersive elements, have become more common. It is important to distinguish between a wavelength locker and a wavelength monitor. The term wavelength locker can refer to the entire system including the temperature controller and wavelength detector, but in general usage it refers specifically to the device. In this section a locker is defined as a wavelength monitor which is capable of providing feedback for control of a laser's wavelength at one or more fixed discrete wavelengths. This is to distinguish it from the more general wavelength monitor which can be used to measure the wavelength of a laser and lock it to any wavelength within its tuning range.

Interference Filters and Etalons

An interference filter design uses a pair of filters to form a notch at the desired wavelength. Instead of using a reference and a filtered signal the light is split into two paths with a different filter in front of each detector. The filters are designed so that the detector response is matched at the desired wavelength. Taking the logarithm of the ratio of the two filter outputs provides an error signal that can be used for tracking the magnitude and direction of the laser wavelength deviation [1]. This type of locker is only good for operation at a single wavelength corresponding to the notch in the filter response. These lockers have a number of advantages including small size and low cost however the filter material is inherently temperature sensitive so the locker must be thermally controlled.

A similar but improved design can be realized with a Fabry-Perot etalon as the filter element. This produces a periodic set of transmission peaks that can be used to lock the laser wavelength to a set of discrete wavelengths. There are a number of significant advantages to this approach. Using an air gap etalon both chromatic dispersion and temperature instability can be eliminated from the system response. The transmission peak spacing is controlled by the length of

the air gap. This can be set to give 100 GHz spacing allowing the device to lock to any ITU grid wavelength channel. The filter can be tuned to set the transmission point for the desired wavelength by simply changing the angle of incidence of the input light. This flexibility and low temperature sensitivity make the etalon locker very attractive for use in controlling fixed wavelength DFB lasers [5]. One significant disadvantage of it is that there is no feedback on the absolute wavelength of the laser which makes it difficult to use with tunable lasers that can cover many ITU grid channels since there is no way of knowing which channel the laser is on. Another drawback is that these devices are only suitable for locking to fixed wavelength channels at a given spacing. This can lead to incompatibility when a system is upgraded from 100 GHz to 50 GHz channel spacing.

Dispersive Wavelength Monitors

Dispersive wavelength monitors or lockers can be based on conventional diffraction gratings, integrated planar waveguide gratings, or arrayed waveguide gratings. These types of monitors are commonly used with an array of detectors to track the output power and wavelength of multiple optical channels in a fiber. They have a considerable advantage over etalon based monitors in that they can be used to simultaneously monitor multiple channels. They are also useful for monitoring a single laser which can tune over multiple channels. An example of an AWG based wavelength monitor in which the filter element and the detectors are all integrated into a single chip is shown in Figure 3-1 this device is from the Opto-electronics Laboratories of NTT [6].

One nice feature of the dispersive WDM monitors is that the device itself can be locked to a reference wavelength. One of the ports of the monitor can be used for this function and the entire device can be temperature tuned to lock it to the reference. This is useful for ensuring that all the lasers in a network are referenced to a common absolute wavelength.

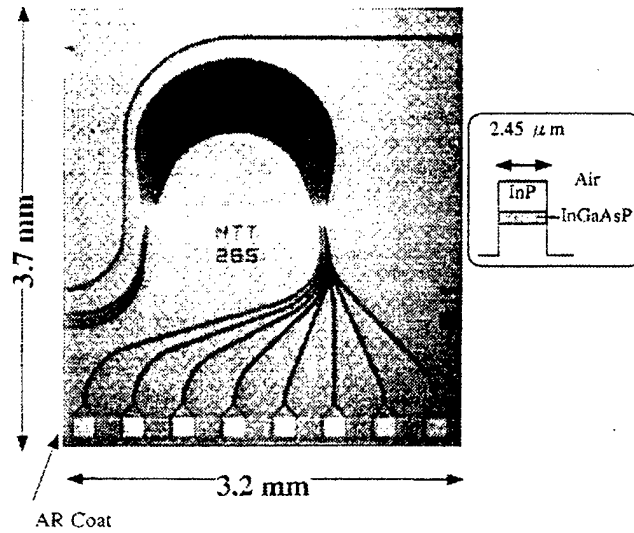


Figure 3-1 NTT Arrayed Waveguide Grating Based Wavelength Monitor

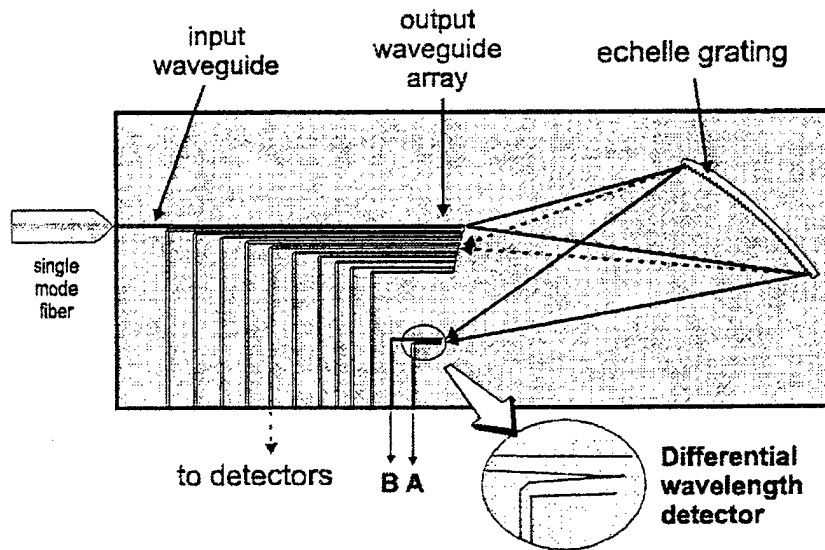


Figure 3-2 Waveguide mux with integrated wavelength locker

In some devices a special differential wavelength locker can be included on a regular waveguide demultiplexer to lock the filter function to the ITU grid [7]. An example of this is shown in Figure 3-2.

Ratiometric Wavelength Monitors

There are two basic methods for implementing ratiometric wavelength monitors. The first is to split the light into two separate paths. One path is detected and used as an intensity reference and the other path is filtered with a wavelength dependant filter function Figure 3-3. The other approach is to use a splitter with a wavelength dependant splitting ratio [8]. In either case the ratio of the two light intensities provides a measure of the laser wavelength. The key difference between this type of monitor and a locker is in the design of the filter. In a ratiometric wavelength monitor a filter function is used which has a monotonic variation with wavelength over the entire range of interest. This allows the absolute wavelength of the laser to be determined from the ratio of the detector signals. A laser can then be locked to any wavelength within the monitors range. This type of monitor is the best suited for use in controlling tunable lasers since it can cover a wide wavelength range unambiguously and lock to any arbitrary wavelength.

A monitor of this type has been demonstrated using a wavelength dependant coupler that had a coupling coefficient that varied from 0 at 1510 nm to 100% at 1590 nm [9]. The logarithm of the ratio of the output signals was used to independently lock 8 different lasers to ITU grid wavelength channels.

3.1.3 Advantages of integrated wavelength monitoring

The design of a proposed system which uses a wavelength monitor with a tunable laser is shown in Figure 3-3. The system includes an optical tap coupler to split off a portion of the laser light to the wavelength monitor, a 3 dB splitter to divide the light into a reference and a filtered path, a wavelength dependant filter, and a pair of detectors. Integrating these components onto a laser card significantly increases the cost and size. The tap coupler can be

eliminated by using light from the back facet of the laser, but this requires an additional fiber pigtail which raises the packaging cost for the laser. A significant reduction in the size and cost of the monitor can be realized by integrating it on chip with the laser. All of the components in the wavelength monitor can be fabricated using semiconductor waveguide technology. Splitters, detectors and even filters can be created using many of the same process steps already involved in the tunable laser fabrication.

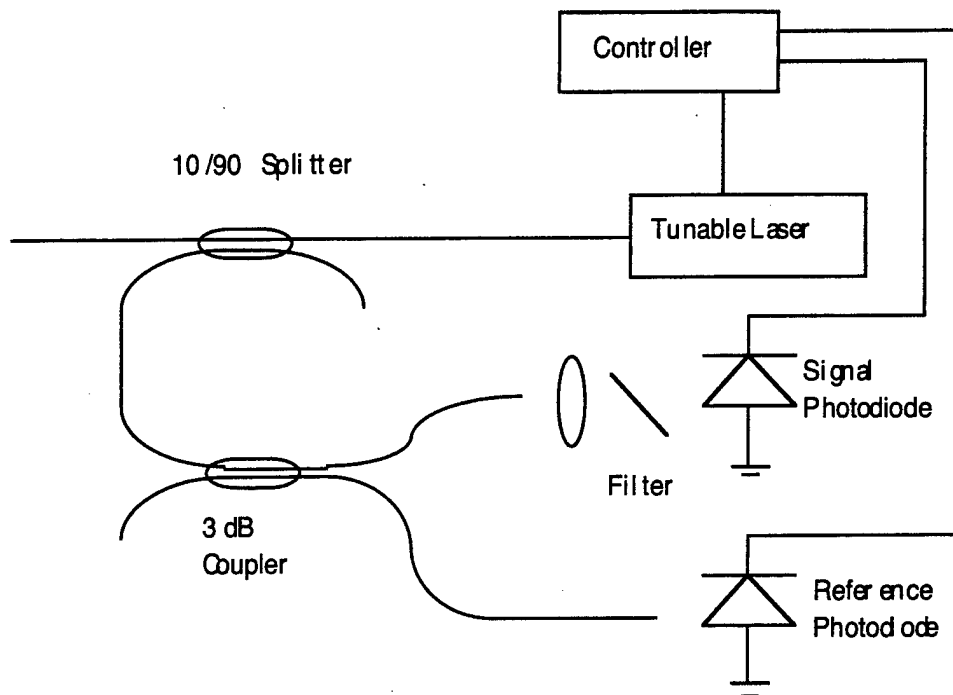


Figure 3-3 Ratiometric Wavelength Monitor and Control System For a Tunable Laser

Significant cost and size reductions have also been shown with hybrid integration of etalon type monitors in thermally tuned DFB laser packages [10]. At the back facet of the laser, a ball lens produces nearly collimated output that passes onto an etalon filter. A pair of closely-spaced photodetectors acting as apertures detect the slightly divergent beam of light transmitted through the solid etalon. A small tilt in the etalon gives each

detector a slightly shifted wavelength response. The detector signals are matched only when the light sits on the center of a wavelength channel. Creating a monitor with a matched response at the correct wavelength requires extremely precise alignment of the etalon filter in the package. Truly monolithic integration eliminates the need for high precision packaging technology.

3.1.4 *Methods for Integrated Wavelength Monitoring*

There are a wide variety of potential methods which can be used for creating an integrated wavelength monitor. It is important to select a method which can provide a robust and highly accurate wavelength signal with the minimum possible complexity. Etalon or differential filter based lockers are unsuitable for this application so they won't be considered here. This leaves dispersive and ratiometric wavelength monitors each of which can be implemented in a number of possible architectures.

For dispersive architectures two possibilities are arrayed waveguide grating (AWG) or planar waveguide grating based devices and surface coupled gratings with flip chip bonded position sensitive detector arrays. The primary problem with these approaches is their large size and high degree of complexity. Fabricating an on chip AWG for a wavelength monitor would be more expensive and more complicated than an external monitor thus eliminating the anticipated benefits of the integration. The surface coupled grating approach would use a second order grating fabricated in the waveguide to couple the light vertically out of the laser at an angle which would be wavelength dependant. The light would be focussed by an integrated microlens fabricated on the backside of a flip chip bonded position sensitive detector Figure 3-4. Unfortunately the dispersion in the grating is not strong enough to achieve an angular shift that would provide a reasonable amount of wavelength sensitivity with the detector mounted only 500 μm above it.

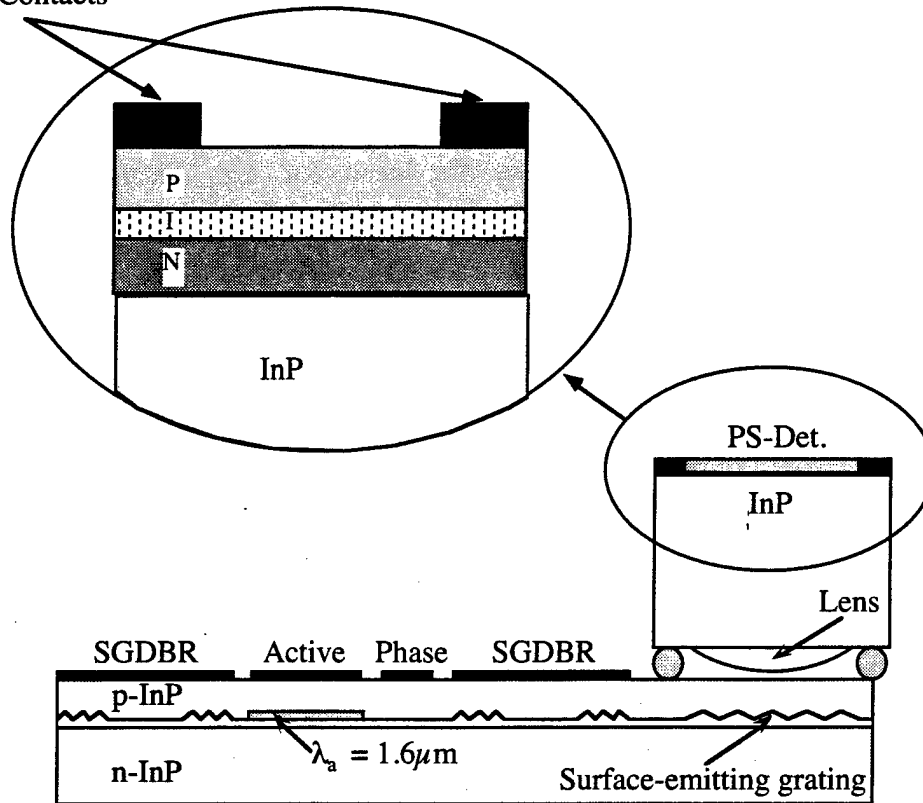


Figure 3-4 Surface Grating Coupled Wavelength Monitor

What is needed is a simple ratiometric monitor design with a wavelength dependant filter or coupler and a pair of detectors. One way to create a wavelength dependant response is to use the absorption difference between two detectors with different bandgaps. The detectors can be coupled in series with the first detector operating in it's band edge region where it is partially absorbing, and the second detector having a much lower band gap so that it absorbs all of the transmitted light Figure 3-5. This design is both compact and highly robust but there is considerable technical difficulty in creating detector regions with different band gaps. This requires either sophisticated selective area growth technology, quantum well disordering or multiple etching and regrowth fabrication steps.

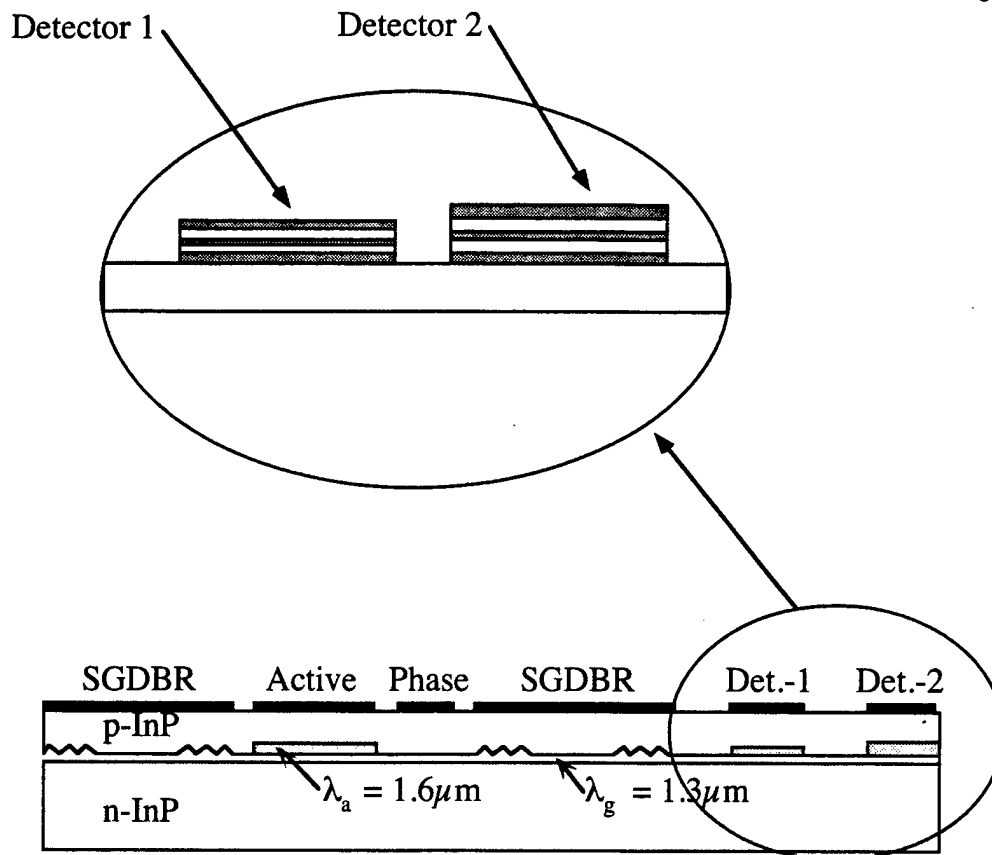


Figure 3-5 Dual Bandgap Detector Wavelength Monitor

The best alternative is to use an approach based on a wavelength dependant splitter with a pair of identical detectors that can use the same active region as the laser for an absorber. In the next section we will discuss how such a splitter can be implemented in a semiconductor waveguide.

3.2 TMI Wavelength Monitors

In strongly coupled semiconductor waveguides an effective way to create a splitter is with a multi-mode (MMI) interference waveguide. The central structure of an MMI device is a waveguide designed to support a large number

of optical modes (typically ≥ 3). Light launched into the guide can be coupled into a set of output guides using the self-imaging principle [11]. There are two different types of MMI 1x2 couplers identified by their waveguide configuration. These are symmetric and asymmetric. Symmetric couplers are not useful for this application since their splitting ratio does not vary with wavelength. Asymmetric couplers which are actually 2x2 couplers do have a wavelength dependent splitting ratio. However the wavelength dependence is typically less than 0.2 dB over a 30 nm range for typical MMI designs. For couplers with wide MMI sections that contain a large number of modes the dispersion is very small and the self imaging length is long. These devices show very little wavelength dependence. As the width of the MMI region is reduced the number of modes decreases and the dispersion between the modes increases. This also shortens the self imaging or beat length for the MMI. Extrapolating this trend it is easy to see that an MMI device with only two modes will have the shortest beat length and the greatest wavelength sensitivity. This device is called a two mode interference splitter and it is equivalent in principle to a zero gap coupler. Using a long interaction length which contains multiple beat periods for the TMI guide further increases the wavelength sensitivity of the device.

3.2.1 *Two mode interference in waveguides*

Two mode interference couplers can be analyzed using a number of different techniques. The limited number of modes makes them especially easy to deal with using modal analysis techniques. This approach is the most useful for generating design parameters and understanding the basic properties. They can also be analyzed using a numerical beam propagation method (BPM) which is more useful for analyzing the sensitivity of the coupler to real world issues like limitations in the lithographic resolution, variations in the waveguide width and surface roughness. For the following analysis we only consider the lateral waveguide modes since all of the waveguides have the same fundamental transverse mode.

TMI theory

The basis for the design of the TMI wavelength monitor is a 2x2 MMI coupler with the extra input guide removed Figure 3-6. At the input waveguide light is coupled off center into a two mode interference (TMI) waveguide. At the end of the TMI section, there is a pair of output guides that divide the light into a pair of detectors. Light coupled from the laser into the TMI section excites the two lowest order lateral modes of the waveguide. These modes propagate with different phase velocities which leads to a characteristic beating in the modal superposition pattern. The beat length is dependent on the difference in the propagation constants for the two modes and on the wavelength of the light. At the end of the TMI section, a y-branch splits the light into a pair of output waveguides with a wavelength dependent splitting ratio. By employing a TMI section that is long enough to contain multiple beat lengths the splitting ratio becomes increasingly sensitive to the wavelength of the light. The total input power can be determined by summing the currents from both detectors. The wavelength dependent signal is normalized to this sum to remove the power dependence. This results in a sinusoidal output signal that varies with wavelength.

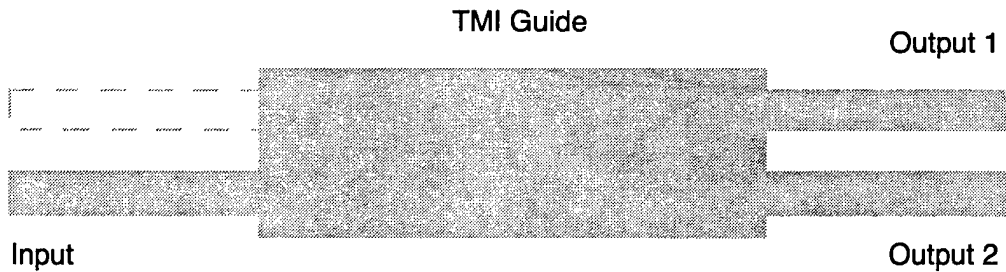


Figure 3-6 Schematic layout of Two Mode Interference splitter

The transfer characteristics of this structure can be derived analytically using coupled mode theory and the expressions for the waveguide modes given by (3-1).

$$\psi_m = E_m U_{mx} U_{my} e^{j(\alpha x - \beta z)} \quad (3-1)$$

Where E_m is the amplitude of the mode and U_{mx} , U_{my} , are the lateral and transverse mode shapes respectively. These are normalized such that $\int(U_m^* \cdot U_m)ds = 1$. If the origin is set at the input to the TMI waveguide then the amplitude of the fields E_1 , E_2 for the TMI waveguide modes can be calculated from the modal overlap of the lateral mode fields using (3-2).

$$\begin{aligned} E_1 &= E_L \int U_{1x}^* \cdot U_{Lx} dx \\ E_2 &= E_L \int U_{2x}^* \cdot U_{Lx} dx \end{aligned} \quad (3-2)$$

Where E_L and U_L are the amplitude and lateral mode shape of the field in the input guide. The lateral mode profiles for the input light and the TMI waveguide are plotted in Figure 3-7 for illustration.

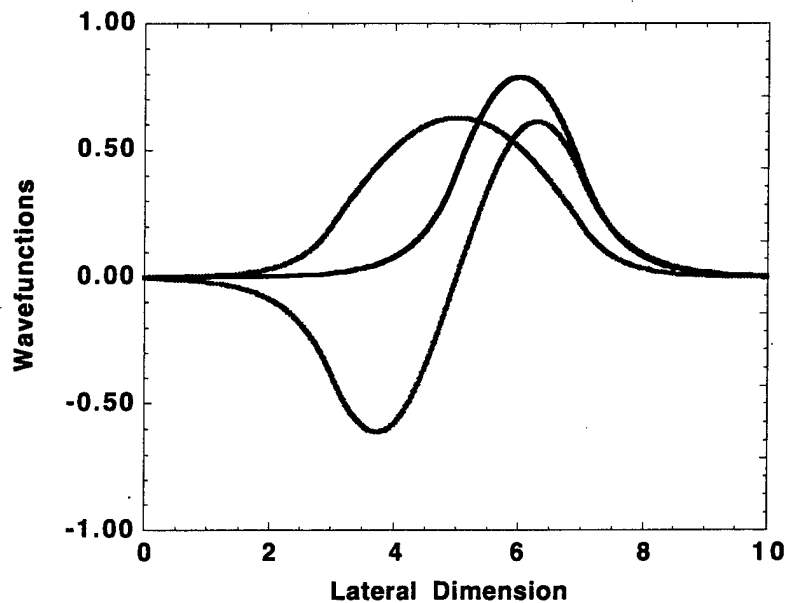


Figure 3-7 Superposition of offset input waveguide mode with the two lowest order TMI waveguide modes

At the output of the TMI section the coupling of the light into the output guides is dependant on the relative phase shift between the TMI waveguide modes. The total electric field will be the superposition of the electric fields for the two waveguide modes (3-3).

$$E_T = E_1 U_{1x} U_{1y} e^{-j\beta_1 z} + E_2 U_{2x} U_{2y} e^{-j\beta_2 z} \quad (3-3)$$

Factoring out the average propagation constant allows this equation to be rewritten in a form which illustrates the periodic dependence of the mode shape on the phase difference (3-4).

$$E_T = U_y \left[(E_1 U_{1x})^2 + (E_2 U_{2x})^2 + 2E_1 U_{1x} E_2 U_{2x} \cos((\beta_1 - \beta_2)z) \right]^{1/2} e^{-j\phi} \quad (3-4)$$

The magnitude of the light coupled into the output waveguides can now be calculated from the modal overlap between the net electric field in the TMI guide and the normalized mode shape of the output waveguide (3-5).

$$E_1 = \int U_{D1}^* \cdot E_T dx \quad (z = L) \quad (3-5)$$

Expanding this integral gives (3-6).

$$E_1 = \int U_D \left[\left(\int U_{1x} U_{Lx} dx \right) U_{1x} \right]^2 + \left(\int U_{2x} U_{Lx} dx \right) U_2(x) \right]^{1/2} + 2 \left(\int U_{1x} U_{Lx} dx \right) U_{1x} \left(\int U_{2x} U_{Lx} dx \right) U_{2x} \cos((\beta_1 - \beta_2)z) \right] dx \quad (3-6)$$

The fraction of the optical power coupled to the output guides is of more interest so we can take the square of the magnitude of the E field after performing the integration to get a simplified form for the coupled power (3-7).

$$P_1 = A + B \cos((\beta_1 - \beta_2)L) \quad (3-7)$$

The magnitude of the coefficients A and B depends on the efficiency of the coupling between the input and output waveguide modes and the TMI modes.

Wavelength sensitivity

The $\Delta\beta L$ phase term, which governs the sinusoidal nature of the splitting ratio in the coupling equation, introduces the wavelength dependence. This property enables the coupler to be used as a wavelength dependent filter or splitter. The value for L at which the phase term equals 2π is known as the beat length. By making the TMI section long enough to include multiple beat lengths the phase becomes increasingly sensitive to the wavelength. For a wavelength monitor a filter function is required which varies monotonically from a minimum at one end of the range to a maximum at the other. This will correspond to a π phase shift of the coupling equation for a wavelength shift of $\Delta\lambda$ corresponding to the monitoring range. Using this we can calculate the length of the TMI section for a given difference in propagation constants (3-8).

$$L = \frac{\lambda_1(\lambda_1 + \Delta\lambda)}{2(\Delta\lambda\Delta\bar{n} - \lambda_1\delta\Delta\bar{n})} \quad (3-8)$$

The $\delta\Delta\bar{n}$ term accounts for the waveguide and material dispersion for the TMI guide. For a filter design with a monitoring range from 1500 nm to 1600 nm and a nominal $\Delta\bar{n}$ of 0.018 which corresponds to a 3 μm wide ridge waveguide the TMI section would be 750 μm long.

Optimizing Dispersion

The length of the TMI coupler section is inversely proportional to the difference in the propagation constants for the two waveguide modes. This difference or modal dispersion increases as the width of the guide is reduced. This shifts the second order mode closer to cutoff in the waveguide. A plot of the effective index for the first two waveguide modes and the resultant dispersion is shown in Figure 3-8 for a ridge waveguide at 1550 nm, with a 3000Å thick 1.3Q waveguide.

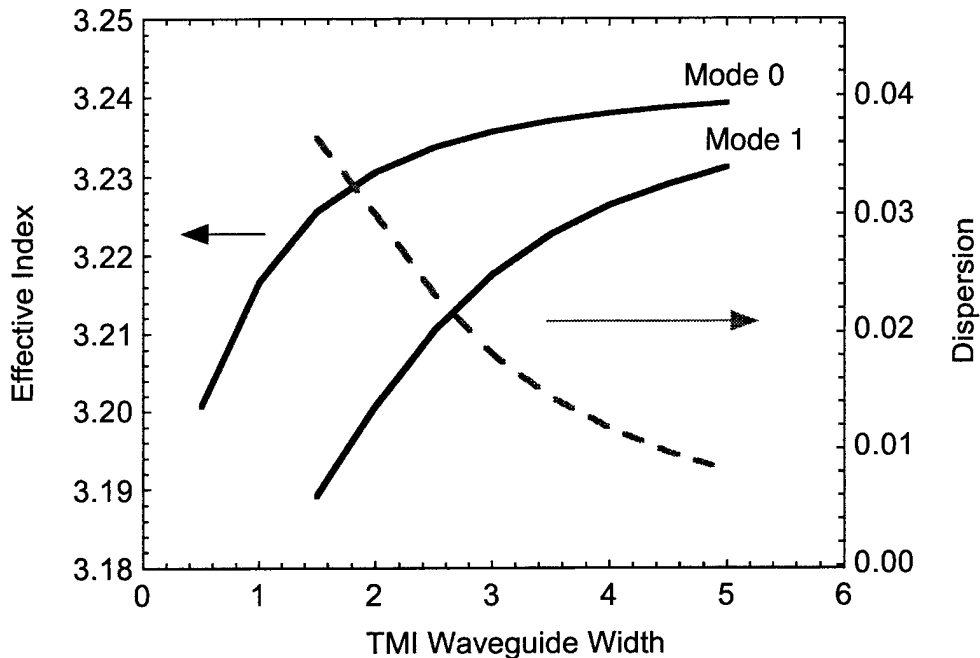


Figure 3-8 TMI Dispersion Plot

As the second mode nears cutoff the dispersion increases dramatically which allows a much shorter TMI section to be used. For higher dispersion TMI sections the width tolerance is correspondingly higher which makes it necessary to actively trim the waveguide index to ensure that the filter passband is correctly aligned with the desired wavelength range. Another drawback associated with using a narrow high dispersion TMI waveguide is the reduced coupling efficiency to the second order mode from the input waveguide.

Tapered TMI design

For a 3 μm wide input waveguide the highest contrast ratio for the splitter is achieved using a 5 μm wide TMI section. However this more than doubles the length which is undesirable. To minimize coupling losses while maximizing

dispersion, the TMI section is tapered in an adiabatic manner from $5\mu\text{m}$, at the ends, to $3\mu\text{m}$ along the central interference section.

In a buried heterostructure design the waveguide is much thinner on the order of $1.8\mu\text{m}$ wide. This allows a thinner TMI section only $3\mu\text{m}$ in width to be used at the input and the output. In this case the guide can be tapered to only $2\mu\text{m}$ which allows it to be considerably shorter than the ridge waveguide monitor.

Y-branch splitter

At the output of the TMI waveguide the ridge waveguide splitter employs a truncated structural y-branch design [12] to lower the splitting loss. The TSYB has a “phase front accelerator” that expands the mode dividing the incoming optical power into the two output branches more smoothly than in a normal y-branch. Achieving low back reflection and high coupling efficiency at the Y-branch junction depends primarily on fabricating a sharp vertex between the two guides. The degree of sharpness is limited however by the resolution of the contact lithography used to define the waveguides. A schematic representation of a TMI wavelength monitor is shown in Figure 3-9 the length scale has been compressed to improve the visibility of the structure..

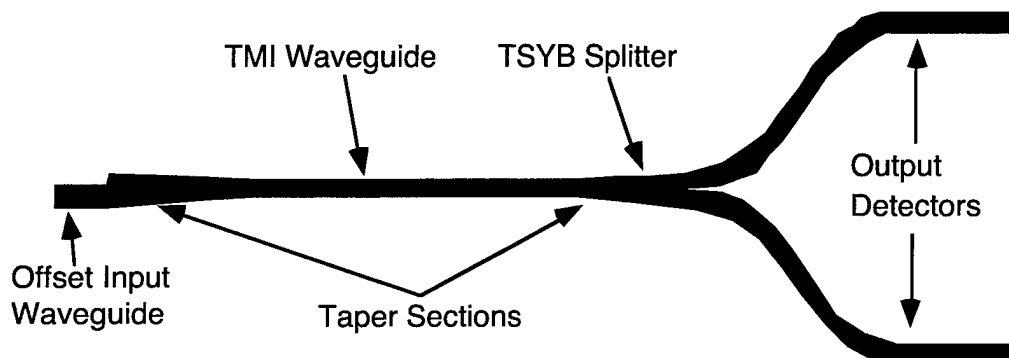


Figure 3-9 Schematic of Two Mode Interference wavelength monitor.

Tapered Mode Expander with Segmented Detectors

For buried heterostructure devices it is difficult to regrow around the sharp junction at the y-branch. This leads to voids at the interface which cause strong reflections that degrade the filter response. To circumvent this problem a tapered mode expander with a segmented detector can be used in place of a true y-branch. In this approach the waveguide is flared out to expand the mode adiabatically and image it onto the detector element. This element is segmented into two sections which capture different portions of the optical mode. The principle of operation is identical to the y-branch but the structure is much easier to fabricate. The detector is segmented by removing the contact layer in a narrow strip between the two halves and then implanting the p-cladding layer for isolation.

3.2.2 BPM simulations of wavelength monitor

Beam Propagation Method (BPM) is a powerful modeling tool which facilitates the analysis of complex waveguide structures. It is particularly useful for visualizing the modal distribution and for simulating the effects of surface roughness, waveguide width variation, and lithographic resolution.

TMI Monitor With TSYB

The coupled mode theory analysis is useful for describing the general characteristics of the TMI wavelength monitor and for generating the initial design parameters. Once these have been selected we can use BPM simulations to optimize the design. Particularly in the input coupling section and the output y-branch splitter. A plot of the distribution in the modal energy for the TMI monitor is shown in Figure 3-10. The beating of the modal superposition is evident in the contour plot. For this particular wavelength (1500 nm) the majority of the light is coupled to the left branch. The dark streaks visible on the left and right side of the start of the TMI section represented radiated light that results from inefficient coupling into the TMI waveguide modes. Note the absence of any radiated light at the y-branch which indicates a good low loss split.

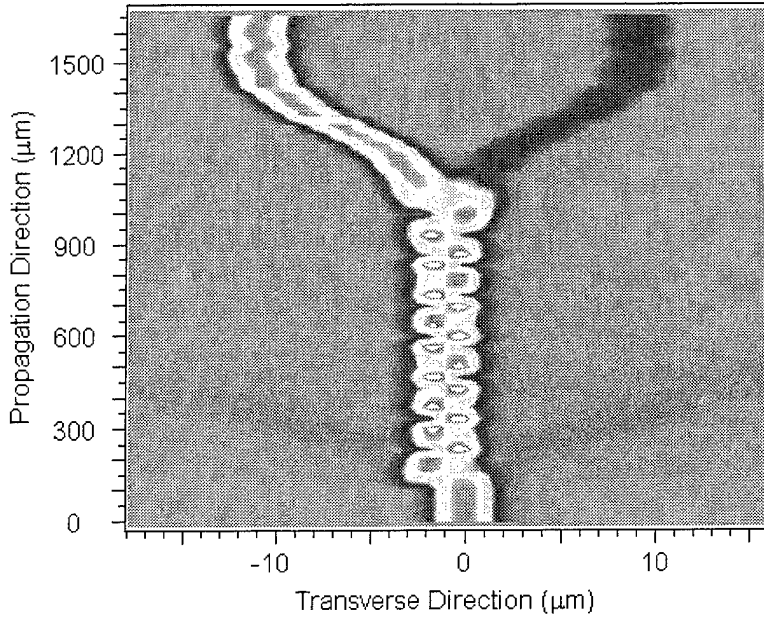


Figure 3-10 Ridge waveguide TMI BPM simulation

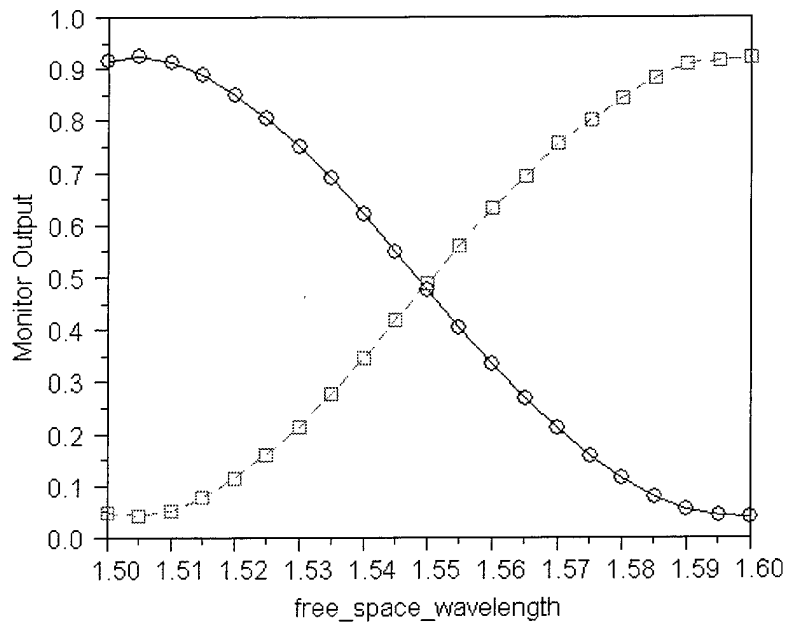


Figure 3-11 BPM simulation of TMI monitor splitting ratio for a wavelength scan from 1500 nm to 1600 nm

Using the BPM simulation we can scan the wavelength of the input light and monitor the power levels in the output waveguides Figure 3-11. This plot shows the wavelength dependence of the splitting ratio and the complementary transfer function for the two detectors.

Device With Tapered Mode Expander

For the buried heterostructure device a flared mode expander with a segmented output detector is used in place of the y-branch splitter. The BPM plot for this structure (Figure 3-11) clearly shows that the mode can be effectively expanded and imaged onto one segment of the detector giving the same characteristics as the y-branch but with a structure that is more robust and has higher fabrication tolerances.

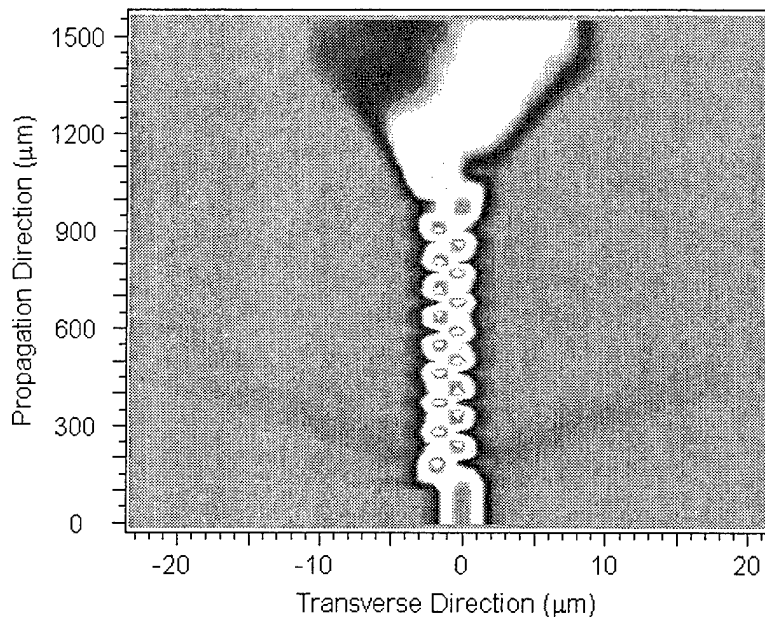


Figure 3-12 Mode beating in wavelength monitor with tapered mode expander and segmented detectors.

The mode beating is easier to visualize if we plot the waveguide power for the right and left hand side of the device Figure 3-12. This plot shows the high

contrast ratio that can be achieved with the segmented detector. It is also helpful in visualizing the beat length for the modal superposition. This beat length changes from about $140\ \mu\text{m}$ at the wide input section to less than $100\ \mu\text{m}$ for the narrow center portion of the TMI waveguide. This illustrates the effectiveness of tapering the TMI waveguide. If a narrow guide was used for the entire length the coupling efficiency would be much lower resulting in increased loss and a reduced extinction ratio. If a wider guide was used for the entire length the device would have to be 40% longer. Using a wide section at the input and tapering the guide which accelerates the mode beating gives the advantage of both structures.

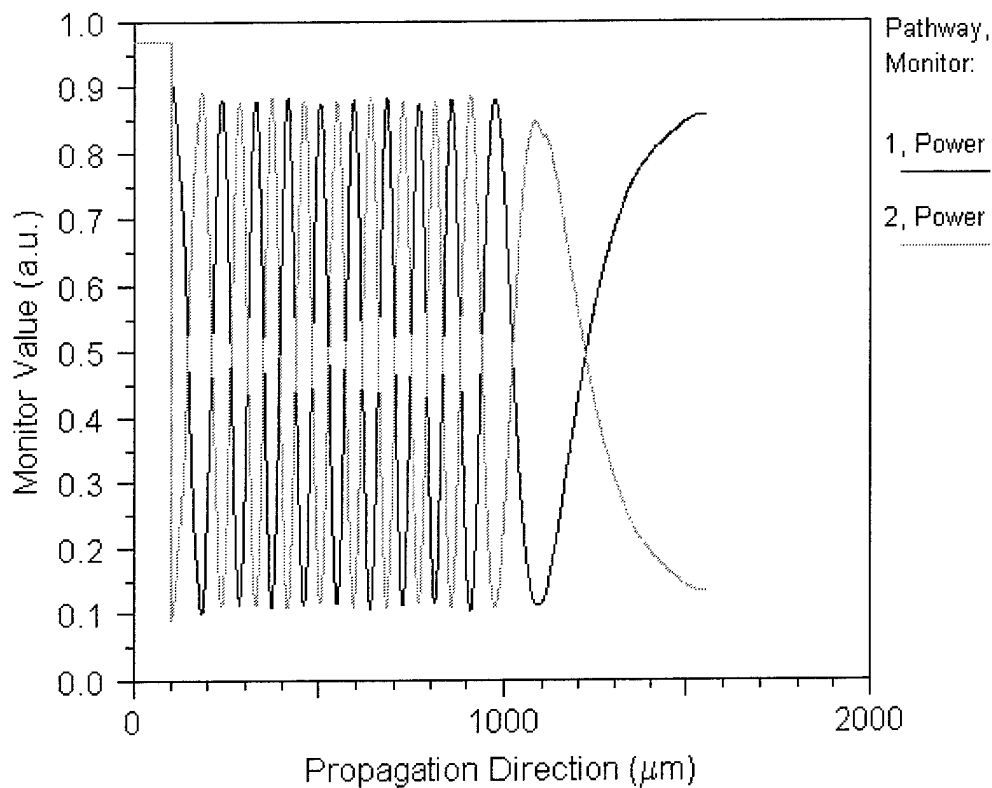


Figure 3-13 Coupled mode power as a function of distance along the TMI waveguide.

3.2.3 Ridge TMI Wavelength Monitor Test Results

Wavelength monitors were fabricated using a ridge waveguide process and the tapered design with y-branch output splitters. The monitors were designed to have a filter bandwidth of 60 nm.

Wavelength Dependence

The wavelength dependence was tested using an external cavity tunable laser source coupled into a short input waveguide with a lensed fiber. The wavelength of the laser was scanned over a range from 1510 nm to 1570 nm at a constant output power and the detector currents were recorded. The response curves for the two detectors are plotted in Figure 3-14.

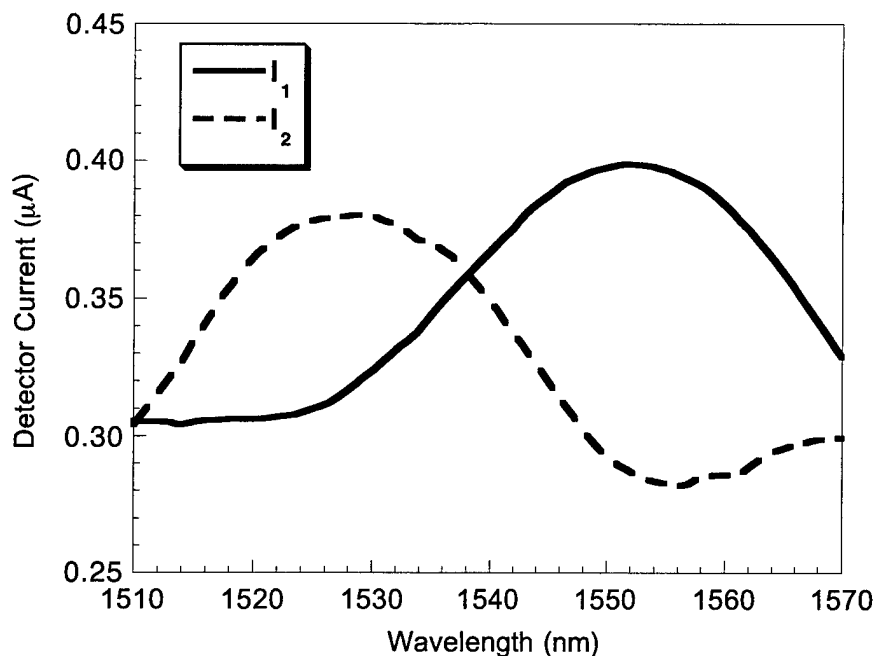


Figure 3-14 Detector response vs. wavelength for ridge waveguide wavelength monitor tested with external cavity tunable laser.

The detector response shows only about a 25% depth of modulation indicating that a significant portion of the light being absorbed is coupled through the

substrate or through other planar waveguide modes. We can normalize these signals to remove some of the spurious signals using (3-9) which takes the ratio of the difference between the detector currents and the sum of the detector currents. This normalized wavelength dependent filter function is plotted in Figure 3-15 with a best fit curve based on (3-7).

$$f(\lambda) = \frac{I_{D1} - I_{D2}}{I_{D1} + I_{D2}} \quad (3-9)$$

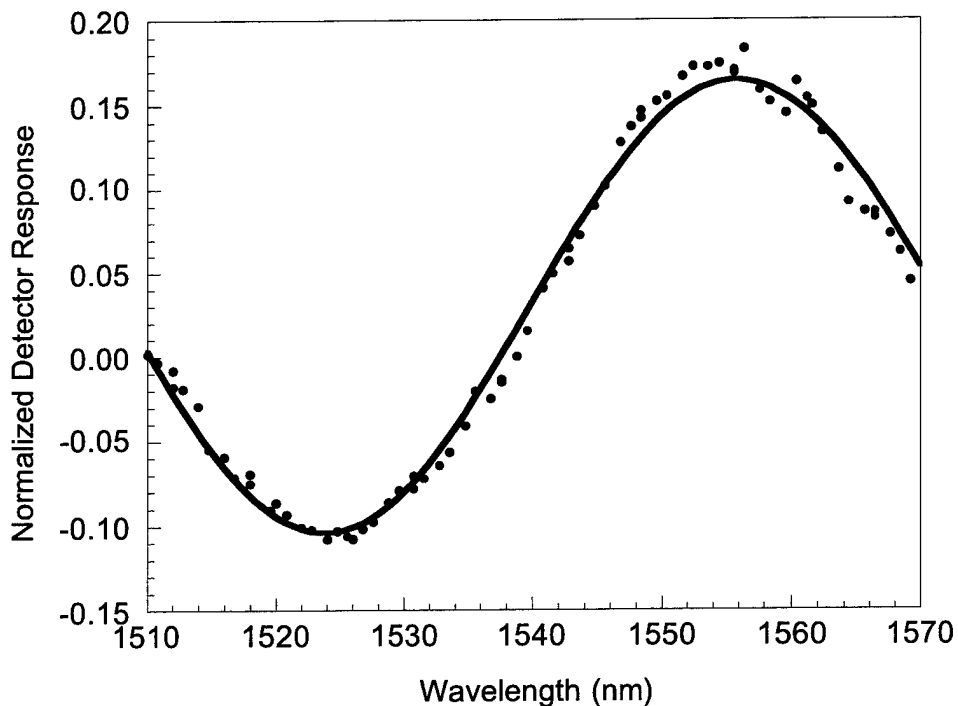


Figure 3-15 Normalized wavelength monitor response.

The monitoring range is from 1535 nm to 1565 nm which is about half of the design range. The reason for this large difference is twofold. The primary cause is a reduction in the waveguide width during processing. The contact exposure and development process typically results in a 0.1 to 0.3 μm

reduction in the width of the stripe when compared to the mask dimension. In addition to this the wet etching step used to form the ridge further reduces the width by an amount between 0.2 and 0.4 μm . This narrower ridge width sharply increases the dispersion in the waveguide resulting in a much narrower filter function.

The wavelength sensitivity for this device was 0.44 nm over a range of 25 nm. At the end points of the monitoring range the slope of the filter function is reduced which reduces the sensitivity. For this measurement instability in the power and wavelength of the external cavity tunable laser when scanning added to the noise in the wavelength measurements. The biggest limitation for the performance results from the low coupling efficiency from the fiber into the wavelength monitor. The excess light is scattered into the substrate and couples to the detectors through a number of different paths introducing a large amount of noise into the experiment.

3.3 Integration of Wavelength Monitors with Tunable Lasers

The purpose of the two mode interference wavelength monitor is to provide a simple compact device that can be monolithically integrated with a widely tunable laser to provide an unambiguous measurement of the laser wavelength. Integrating the wavelength monitor directly onto the rear output waveguide of the tunable laser should significantly improve on the coupling efficiency for the input light since the laser mode is well defined and entirely contained within the input waveguide. Higher power levels and reduced stray light should give the integrated device improved sensitivity. Integration also introduces a number of difficulties into the device design. Isolation both electrical and optical between the devices must be considered. The fabrication process also needs to be adapted to accommodate the various steps required to create the two devices.

Design

The design of the ridge waveguide tunable SGDBR laser with integrated TMI wavelength monitor is shown in Figure 3-16. The device has seven different active elements which require electrical contacts, four in the laser and three in the monitor. The laser consists of a pair of sampled grating mirrors on either end of a cavity which includes both gain and phase control sections. Light from the rear output of the laser is coupled asymmetrically into the two mode waveguide of the wavelength monitor. At the end of the TMI waveguide a y-branch splitter divides the optical power into a pair of output waveguides which contain monitor detectors. An extra contact on top of the two mode section is used to trim the filter response of the monitor to align it with the tuning range of the laser.

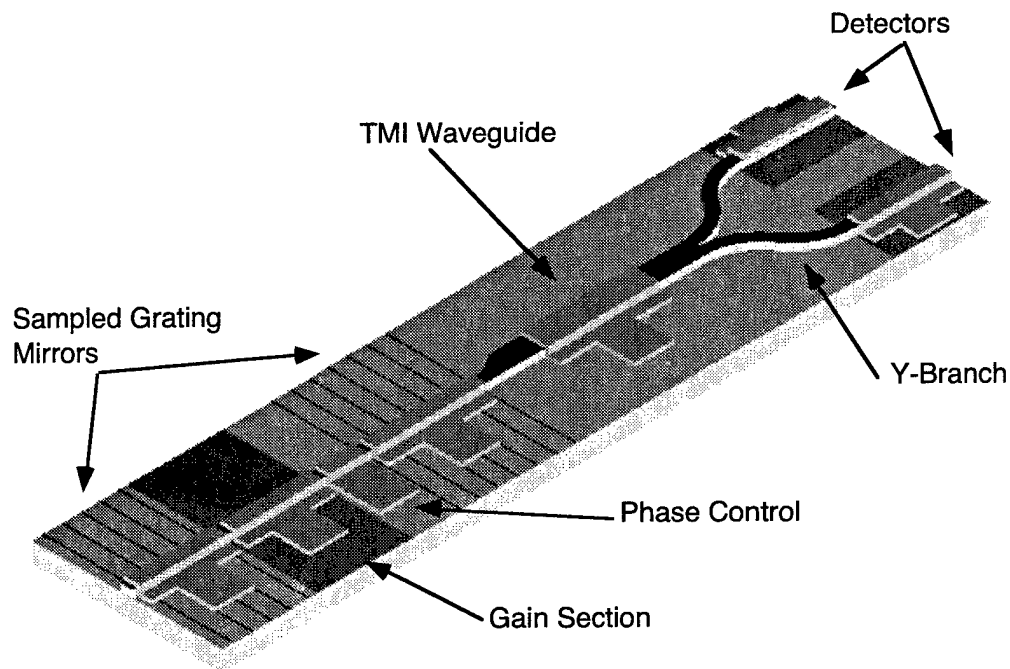


Figure 3-16 Ridge waveguide SGDBR with integrated TMI wavelength monitor.

Fabrication

A key advantage of the TMI wavelength monitor design is that it can be fabricated using many of the steps required for the SGDBR laser. This makes it relatively easy to integrate the two devices using the following fabrication procedure. First, a base structure is grown using near atmospheric MOCVD with tertiarybutylphosphine and tertiarybutylarsine for the group V sources. Passive sections are defined by selectively etching off the cap layer and then the quantum wells. The gratings are then formed for the laser mirrors using a dry etch process. In the second MOCVD step, a 2 μ m InP upper cladding layer and a 100 nm InGaAs contact layer are regrown. The ridge waveguides are etched to within 200 nm of the waveguide layer using a methane-hydrogen-argon (MHA) RIE etch. A selective wet etch (1 HCL:3 H₃PO₄) is then used to remove the last 200 nm and stop on the waveguide. The dry etch is done to maintain the straight side walls in the curved waveguide section, while the final wet etch compensates for the non-uniformity in the MHA RIE and provides for consistent etch depth. A SiN_x layer is used to passivate the surface with self-aligned openings on the ridge tops for the Ti/Au p-contacts. Isolation between the adjacent laser sections and between the detectors is achieved by etching off the contact layer and performing a deep proton implant. This step is essential for providing good isolation between the reversed biased detectors and the forward biased laser sections.

Test Results

The response of the wavelength monitor must be independent of the input power over as wide a range as possible so that a correct measurement of the wavelength can be made independent of the input power levels. This requires the detector response to be as linear as possible with respect to input power. To measure the linearity the integrated device was mounted on a test fixture and light from the laser was coupled into a lensed optical fiber. The fiber coupled power was monitored with a reference photodiode. The two waveguide photodiodes in the wavelength monitor were reverse biased and their photocurrents were recorded and compared to the signal from the reference.

The results are plotted in Figure 3-17 for a range of drive currents from 0 to 120 mA.

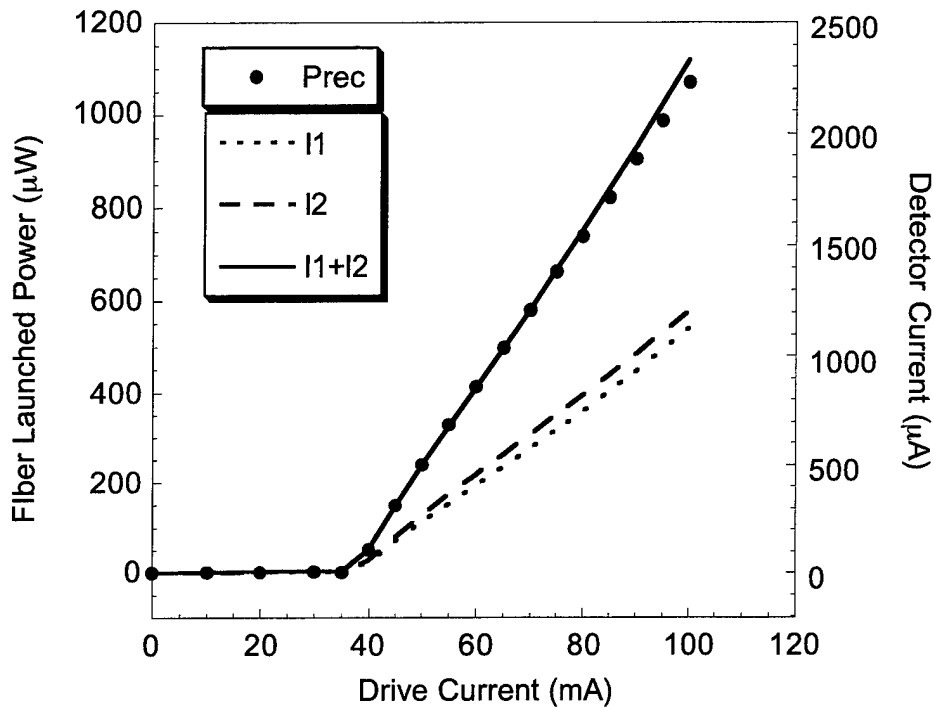


Figure 3-17 Intensity response for wavelength monitor detectors compared with fiber coupled output.

There is little response from the detectors for drive currents below the laser threshold of 35 mA. Above threshold the sum of the detector currents increases linearly with the fiber coupled output power. The ratio of the currents is nearly constant over this entire range. There is a slight drift in the splitting ratio of 1.5% which is caused by thermally induced wavelength drift in the laser as the drive current increases.

The tuning range for this first generation of integrated devices was very small so the wavelength response of the integrated monitor could only be checked at four different wavelengths covering a range from 1534.2 to 1547.3 nm. The

laser was tuned to each one of the accessible wavelengths and the monitor currents were recorded. The normalized detector response for one of the outputs is plotted in Figure 3-18 with the laser spectra shown in the inset. These data points were fit with the response curve for a similar monitor measured using an external cavity tunable laser. This curve is shown as a dotted line in the figure.

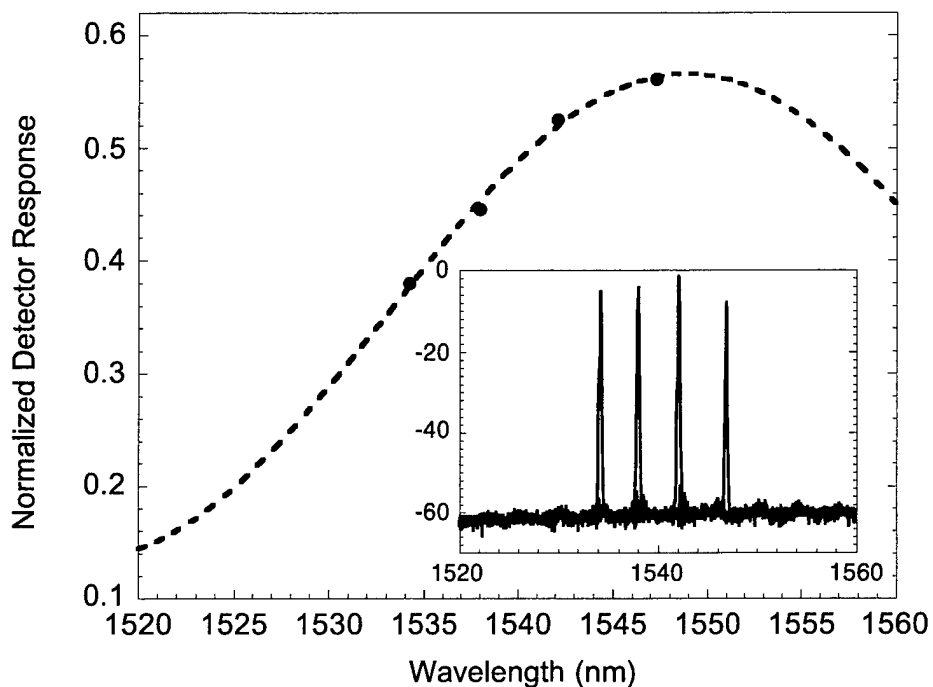


Figure 3-18 Wavelength response for integrated device using calibrated response curve. Laser spectra shown in inset.

3.3.2 *Buried Heterostructure Laser with Integrated Wavelength Monitor*

Design

A schematic of the buried heterostructure tunable SGDBR laser with an integrated TMI wavelength monitor is shown in Figure 3-19. This device has a flared mode expander and a segmented output detector in place of the y-branch

splitter and waveguide detectors used in the ridge device. The buried heterostructure process yields a more tightly confined waveguide with a higher dispersion. This reduces the length of the TMI section. The planar device geometry simplifies bonding and gives the device a lower thermal impedance. The key advantage however is the improved tuning efficiency which is possible with this design.

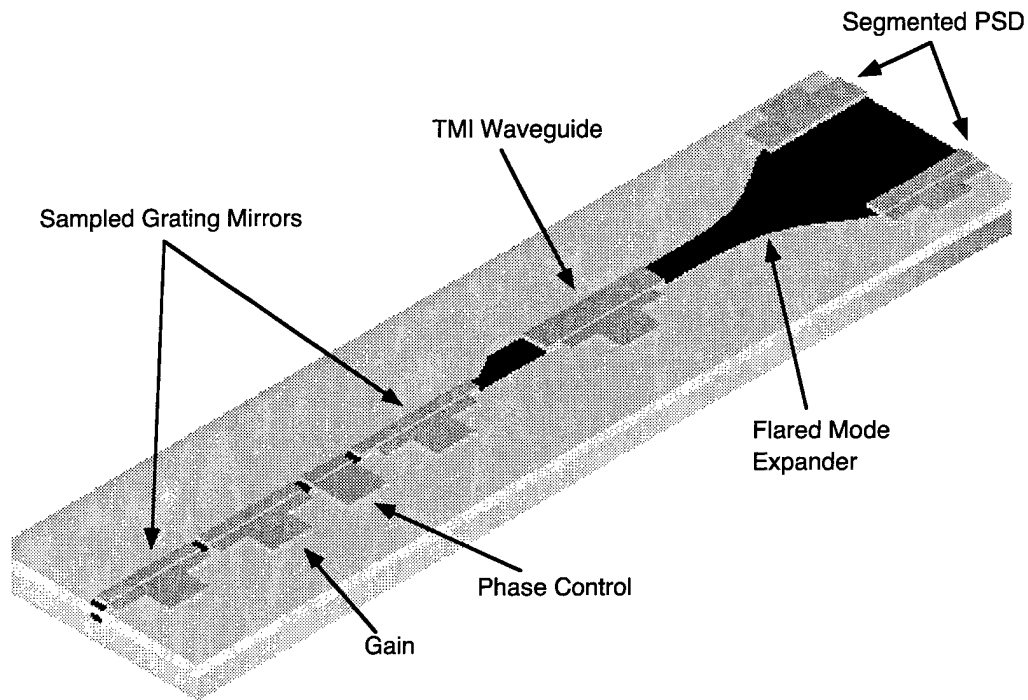


Figure 3-19 Buried SGDBR with integrated wavelength monitor incorporating flared mode expander and segmented detector.

Fabrication

The fabrication process for the buried heterostructure device begins with the same steps as for the ridge waveguide process. The first step is the base structure growth and characterization. A 4000 Å thick waveguide is grown on top of a 1 μm thick n-doped InP buffer. This is followed by a 100 Å thick

undoped InP stop etch layer and then either four 1% compressive strained quantum wells or 6 0.8% wells. The base structure is capped with a 2000 Å thick InP layer to protect the quantum wells during subsequent processing and regrowth steps. The passive sections are defined by selectively etching off the cap layer and then the quantum wells. The gratings are then formed for the laser mirrors using a two step masking technique and a methane hydrogen argon dry etch process. After the gratings have been etched the surface is cleaned and then a 2000 Å thick layer of InP is regrown over the entire surface. After this the ridges are patterned and dry etched through the waveguide layer and into the lower cladding. A Br:HBr:H₂O wet etch is used to clean up the surface damage from the dry etch process. In the final MOCVD growth step, a 2.5 μm InP upper cladding layer and a 100 nm InGaAs contact layer are regrown over the ridge. The regrown samples are implanted to electrically isolate the different device sections and to block lateral current spreading in the p-cladding. A SiN_x layer is deposited to passivate the surface with openings over the buried ridges for the Ti/Au p-contacts. After the p-contacts have been deposited and annealed the sample is thinned to 100 μm and a back side n-contact is deposited. Then the devices are cleaved and AR coated using a single layer SiO_x coating which is deposited in an e-beam evaporator. The coating thickness is about 2100 Å and the index is close to 1.8. For DC testing the devices are soldered onto copper studs which can be mounted on temperature controlled stages to enable electrical and optical probing.

Test Results

The tuning range for the buried heterostructure lasers was significantly larger than for the ridge waveguide devices. Continuous wavelength coverage was achieved over 35, 42, and 47 nm tuning ranges for different device designs. The wavelength response for the monitor was mapped by tuning the laser over a set of discretely spaced wavelengths covering a range from 1530 to 1565 nm. The wavelength monitor was designed for a range of 40 nm. The laser spectra for the test wavelengths are shown in Figure 3-20.

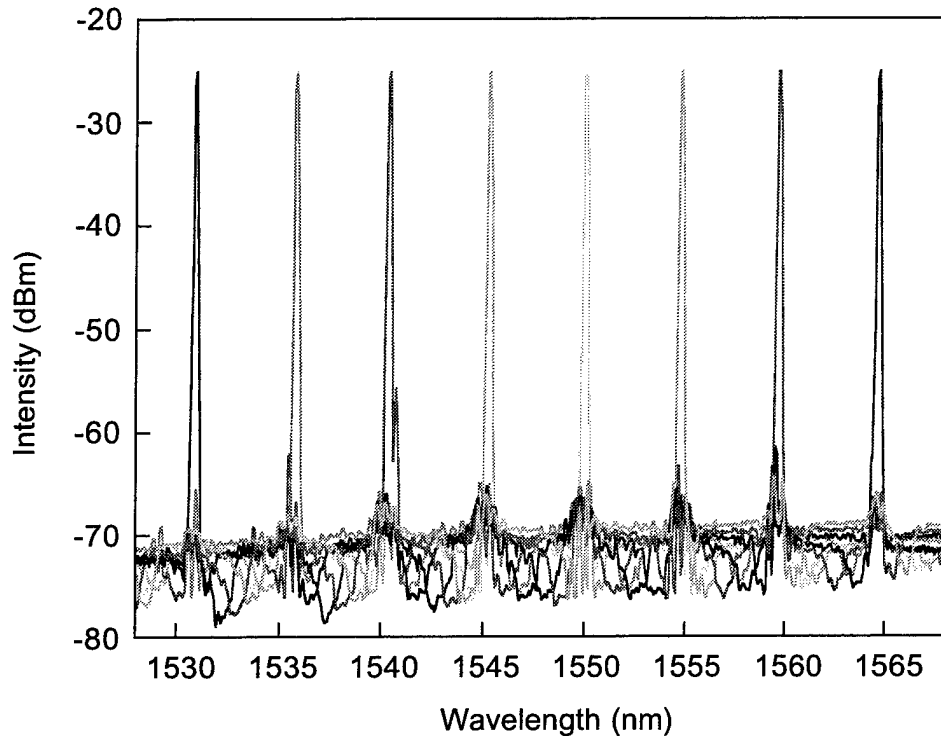


Figure 3-20 Superimposed laser spectra for wide wavelength scan.

The detector currents were measured over the tuning range with the trim electrode left floating. These currents were normalized according to (3-9) and the result is plotted in Figure 3-21. A theoretical response curve was fit to the data to indicate the trends. The result shows that the filter transfer function is once again significantly narrower than the design width of 40 nm. This is due to narrowing of the waveguide during the fabrication process and to higher than expected material dispersion. For this design the half period of the filter response is less than 15 nm. The sinusoidal transfer function for the monitor is preserved with the tapered mode expander and the segmented detector which verifies the BPM model. Some asymmetry in the splitting ratio or the detector response is evident from the offset of the median in the filter function.

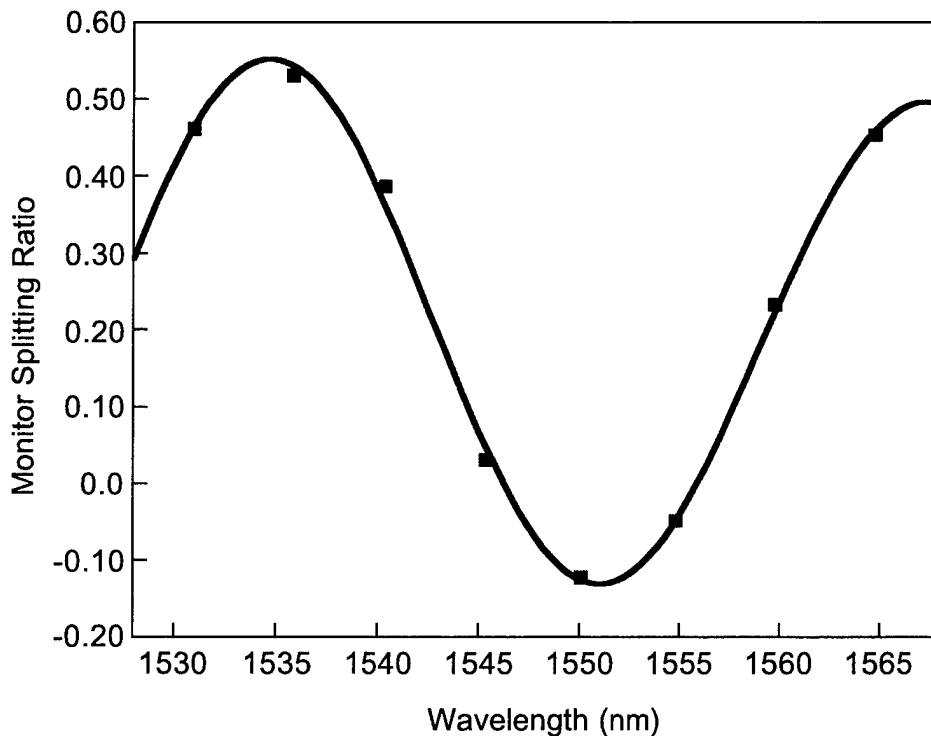


Figure 3-21 Monitor output signal for integrated buried heterostructure device.

To measure the resolution limits for the monitor the laser was tuned over a range of 1 nm in 0.05 nm increments. This test was conducted for wavelengths from 1554 to 1555 nm, at the endpoint of the useful monitoring range where the sensitivity is at a minimum. The wavelength for the laser was measured using an optical spectrum analyzer and the detector currents were monitored with a semiconductor parameter analyzer. The superimposed laser spectra for this test are shown in Figure 3-22. The peaks appear very broad since the highest resolution of the spectrum analyzer is only 80 pm.

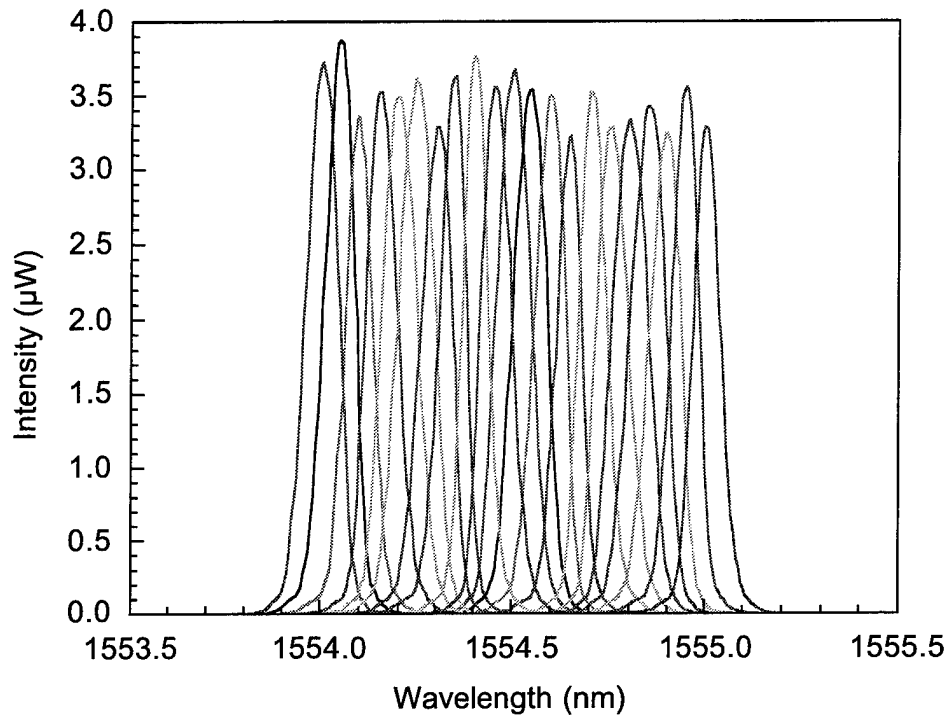


Figure 3-22 Laser spectra for fine wavelength scan in 0.05 nm increments from 1554 nm to 1555 nm..

The normalized detector response is plotted in Figure 3-23 with the square symbols representing measured points. The fitted response from the wide wavelength scan is shown for reference as a smooth solid line. The variation in the monitor response corresponds to a full 1.2 nm of wavelength error for this position on the filter curve. At the mid point where the sensitivity is highest the error would be on the order of 0.1 nm.

The pseudo random nature of the wavelength error in the fine scan test seems to indicate that it is caused by leakage current from the laser drive or some other form of crosstalk. Tuning the wavelength continuously requires the currents in both mirrors and the phase control section to be varied simultaneously. The gain current must also be adjusted to maintain constant

power. All of these changes can couple to the detectors both electrically and optically to perturb the measurement. To improve the performance of the monitor the various sources of crosstalk must be isolated and eliminated from the response.

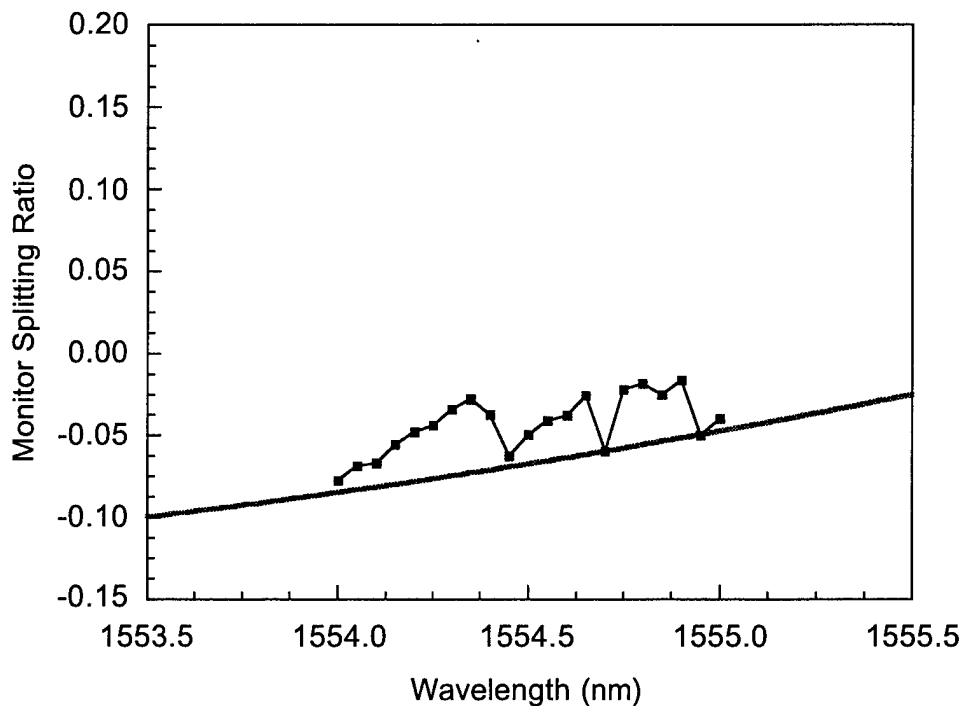


Figure 3-23 Monitor response curve for fine wavelength scan.

Errors in the response can occur both due to electrical crosstalk from tuning and gain currents in the laser and from scattered substrate light and defects in the waveguide structure. Spontaneous emission from the laser can also play a key role at low bias levels. The tapered mode expander eliminates the problems caused by reflections at the splitter in the TMI wavelength monitor but it increases the sensitivity of the device to stray light because of its larger detector sizes.

In the absence of interference the splitting ratio for the monitor should remain constant over a wide range of input optical power levels. To test this we stabilized the laser wavelength with the phase control section and varied the gain current from just below threshold at 24 mA to 65 mA and tracked the monitor response. The lasing wavelength was stable to within 0.01 nm which is the resolution limit for our spectrum analyzer (Figure 3-24).

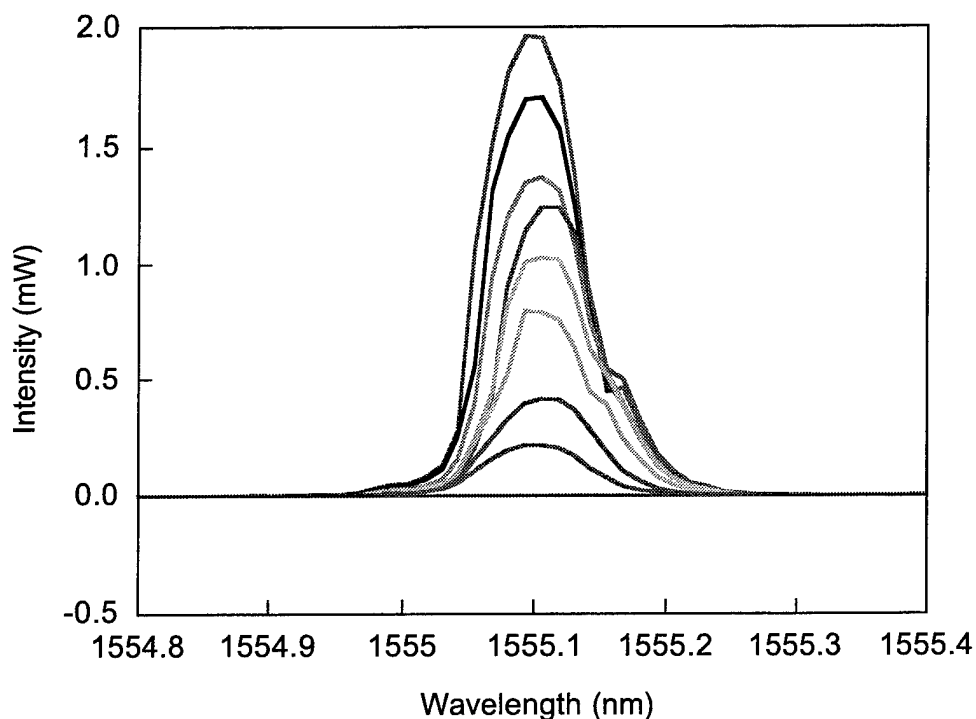


Figure 3-24 Laser spectra for constant wavelength test at 9 different bias levels from threshold to 65 mA.

The monitor signal showed a gradual drift of about 10% as the current increased from 25 mA up to about 40 mA whereupon it stabilized with an oscillation of about 5% of its full scale range. The initial drift can be attributed to an offset in the signal from the spontaneous emission of the laser. The subsequent oscillation is caused by a variation in the mode stability of the laser cavity. As

the gain current is increased the junction temperature of the laser increases in the active region from resistive heating. This temperature rise causes an increase in the index of refraction and a shift of the cavity mode. This is compensated for by the phase section which is tuned to lock the mode on the desired wavelength. Crosstalk or leakage from the gain current or the phase current may be causing the oscillation observed in the filter response.

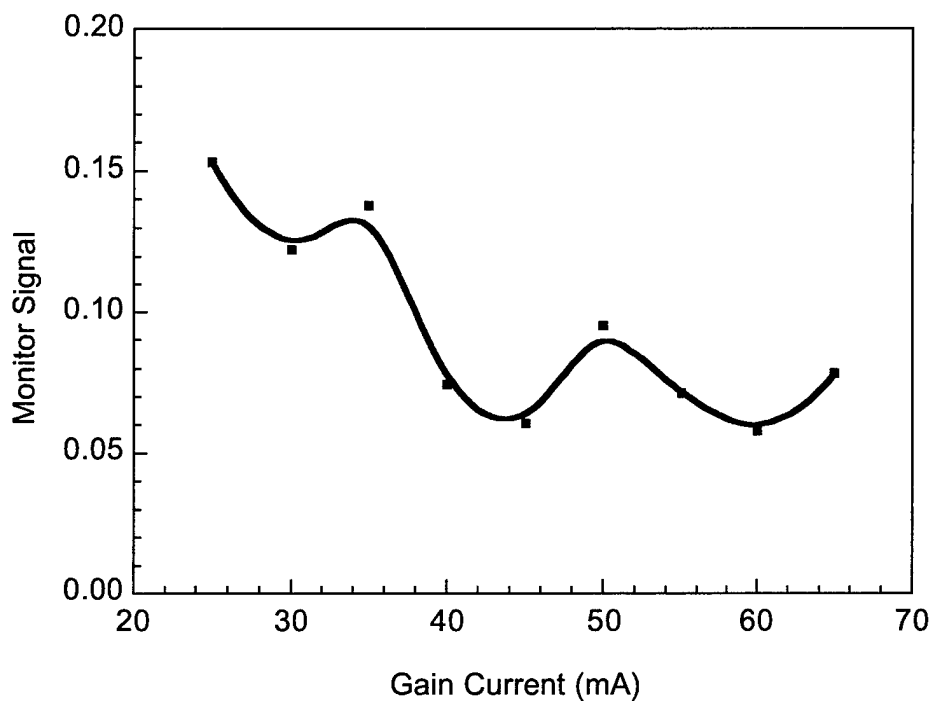


Figure 3-25 Splitting ratio variation with laser gain current for buried wavelength monitor at constant wavelength.

The effect of the spontaneous emission can be monitored by measuring the detector signals for the laser biased below threshold. The photocurrents for the two monitor detectors are plotted in Figure 3-26 for a range of below threshold gain currents from 0 mA to 27 mA. The detector response is matched to

within 1% which should all but eliminate the effects of absorbed spontaneous emission in the normalized measurement.

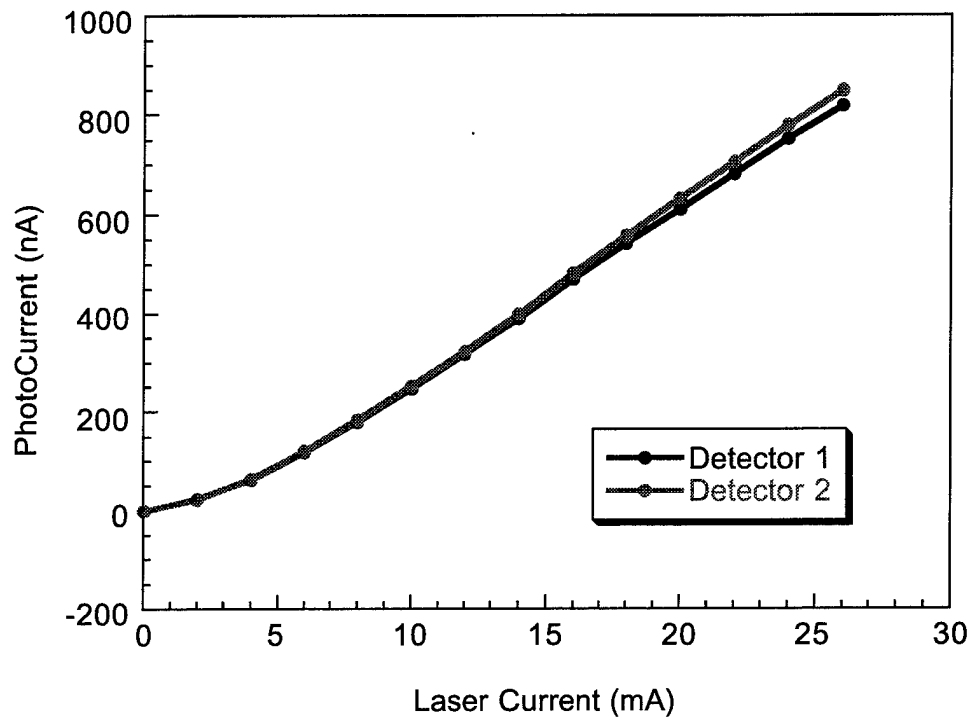


Figure 3-26 Monitor detector response for laser biased below the threshold current of 27 mA.

3.3.3 Sources of Spurious Signals

This section will present a detailed breakdown of the sources of spurious signals which limit the resolution of the current wavelength monitor. It will provide a guideline for eliminating these effects and improving on the device performance. The detector current in the monitors includes signals from a number of different sources. These must be carefully identified and measured

to determine their overall effect on the response. Contributions to the detector current come from both electrical and optical sources. Electrical leakage includes crosstalk from each of the current sources driving the laser plus the intrinsic dark current of the detector itself. The detector dark current can be minimized by operating it with no reverse bias voltage. The optical component of the detector current includes the desired laser signal which is modulated by the filtering function of the TMI waveguide plus spontaneous emission from the laser through the waveguide which is also modulated by the filter function and substrate coupled light. Substrate coupled light can include spontaneous emission both from the laser gain section and from the tuning sections. These effects are difficult to separate so they are typically lumped together with the electrical leakage effects. The detector response for the two monitor photodiodes including all of the different effects is given by (3-10).

$$\begin{aligned}
 I_1 &= i_{D1} + i_{fm1} + i_{bm1} + i_{p1} + \int \eta(\lambda)F(\lambda)P_{sp}(\lambda)d\lambda + \eta(\lambda)F(\lambda_L)P_L \\
 I_2 &= i_{D2} + i_{fm2} + i_{bm2} + i_{p2} + \int \eta(\lambda)(1 - F(\lambda))P_{sp}(\lambda)d\lambda + \eta(\lambda)(1 - F(\lambda_L))P_L
 \end{aligned}
 \tag{3-10}$$

The nominal response i_{D1} and i_{D2} currents represent the signal levels when no current is applied to the laser active sections. They are caused by absorption of background light and not by dark current since the detectors are unbiased. The other leakage terms i_{fm} , i_{bm} , and i_p include both the electrical leakage which is minimal and the optical leakage from substrate or waveguide coupled spontaneous emission which can be fairly significant. The magnitude of these leakage terms for the buried wavelength monitor is given in Table 3-1.

Table 3-1 Detector Leakage Currents.

Detector 1		Detector 2	
i_{D1}	65.0 nA	i_{D2}	328.0 nA
i_{fm1}	0.175 nA/mA	i_{fm2}	0.250 nA/mA
i_{bm1}	2.925 nA/mA	i_{bm2}	2.925 nA/mA
i_{p1}	1.250 nA/mA	i_{p2}	1.240 nA/mA

The response is fairly well matched for the leakage currents except for the front mirror which is negligible. The offset from the background light levels represents the largest contribution to the total however this will be eliminated for packaged devices and can be easily removed in testing by shielding the device from stray light.

The next element in (3-10) represents the contribution from the filtered spontaneous emission which must be integrated over the entire gain spectrum of the active region and convolved with the TMI filter response. This component can not be eliminated from the signal since it is an inherent property of the laser. The spontaneous emission is clamped at threshold for the laser but the threshold varies with the device wavelength resulting in a wavelength dependant spontaneous emission background level. One of the fundamental limits on the wavelength resolution of the monitor will be due to the variation in the ratio of the stimulated to spontaneous emission in the laser output. The results of the below threshold testing on the monitor which are plotted in Figure 3-26 show that the response is at least well matched for the two detectors and the signal level is on the order of a few microamps. Normalizing the detector currents in (3-10) according to (3-9) yields (3-11).

$$S = \frac{\eta[1 - 2F(\lambda)]P_L}{\eta P_L + \eta P_{SP} + I_L} \quad (3-11)$$

This can be simplified by neglecting the leakage contribution and dividing by the optical power in the lasing mode P_L to get (3-12) which describes the fundamental resolution limit for the monitor.

$$S = \frac{1 - 2F(\lambda)}{1 + (P_{SP}/P_L)} \quad (3-12)$$

The error in the wavelength signal S comes from the variation in the spontaneous emission fraction P_{SP}/P_L . For the tunable laser this term can vary by as much as a factor of 2 as the threshold current changes across the tuning

range. For side mode suppression ratios less than 30 dB this can severely degrade the accuracy of the wavelength monitor.

Design for Improved Isolation

Notwithstanding the ultimate limitations on the wavelength monitor sensitivity imposed by the spontaneous emission factor there are several methods which can be used to improve the accuracy by eliminating or reducing electrical and optical crosstalk. The current design employs a common n contact for all of the device sections. Growing the base structure on a semi-insulating substrate and then using a deep He implant will enable the various n-contacts of the device to be segregated which will improve the electrical isolation. A major component of the optical crosstalk comes from light scattered into the substrate. To eliminate this a deep absorber can be grown beneath a thicker n-cladding layer. Using a 1000 Å thick InGaAs layer with a 2 μm thick n-cladding would eliminate up to 95% of the scattered light. The remaining light coupled through the upper cladding or waveguide layers could be blocked by shielding the detectors behind implanted absorber regions so that only light traveling in the TMI waveguide can reach the detectors. Combining these approaches will enable the monitor performance to achieve a resolution which is closer to the theoretical limit.

3.4 Summary

In this chapter we have investigated a promising technique for integrated wavelength monitoring of widely tunable semiconductor lasers. The need for this monitoring has been clearly established on the basis of experimental results that document the wavelength drift in tunable lasers with aging, and on the requirements for current and next generation DWDM communications systems. We have developed and demonstrated a novel design for an integrated wavelength monitor that can be fabricated on chip with a widely tunable sampled grating DBR laser. The technique is based on two mode interference in a semiconductor waveguide which enables it to act as a wavelength

dependent splitter. The design parameters for the monitor were developed using a coupled mode analysis which enabled the filter function to be described in terms of a sinusoidal function with a phase dependence proportional to the difference in the propagation constants for the two TMI waveguide modes. An optimized design which used a tapered TMI waveguide with a wide input for efficient coupling and a narrow central portion with higher dispersion was proposed. This design was simulated using a BPM model and verified experimentally. Wavelength monitors were fabricated in both ridge and buried heterostructure processes. The buried monitors employed a flared adiabatic mode expander with a segmented detector to replace the y-branch splitter used in the ridge waveguide device. This helped to eliminate back-reflections at the y-branch and simplified the fabrication process.

The test results for the buried and ridge waveguide monitors revealed that they are susceptible to cross talk from the drive currents for the laser and from stray light. This cross talk degrades the wavelength sensitivity of the device. It is feasible that future designs could significantly reduce this cross talk and improve the performance of the device. A more fundamental problem however exists in the fabrication for the device. In order to operate correctly the monotonic portion of the filter function must be aligned with the laser tuning range. Unfortunately it is not practically possible to guarantee this alignment with the tolerances inherent in the fabrication process. For initial testing an extra contact was placed on the TMI filter waveguide so that its response could be trimmed to align it with the laser tuning range. This makes the filter an active semiconductor component which is subject to the same aging related drift as the laser. Because of this fundamental limitation the long term potential of two mode interference splitters for wavelength monitoring is questionable.

References

1. Miskovic, E., *Wavelength lockers keep lasers in line*. Photonics Spectra, 1999. **33**(2): p. 104-106,108,110.
2. Delorme, F. and G. Alibert, *Reliability study of 1.55 μ m distributed Bragg reflector lasers*. Electronics Letters, 1997. **33**(5): p. 394-6.
3. Woodward, S.L., P. Parayanthal, and U. Koren, *The Effects of Aging On the Bragg Section of a Dbr Laser*. Ieee Photonics Technology Letters, 1993. **5**(7): p. 750-752.
4. Mason, B., *et al.*, *Ridge waveguide sampled grating DBR lasers with 22-nm quasi-continuous tuning range*. IEEE Photonics Technology Letters, 1998. **10**(9): p. 1211-13.
5. Villeneuve, B., M. Cyr, and H.B. Kim. *High-stability wavelength-controlled DFB laser sources for dense WDM applications*. 1998.
6. Kohtoku, M., *et al.*, *Packaged polarization-insensitive WDM monitor with low loss (7.3 dB) and wide tuning range (4.5 nm)*. IEEE Photonics Technology Letters, 1998. **10**(11): p. 1614-16.
7. Koteles, E.S., *et al.* *An integrated wavelength locker for waveguide DEMUXes*. in *OFC*. 1999.
8. Dimmick, T.E. and J. Weidner, *Simple, inexpensive wavemeter implemented with a fused fiber coupler*. Applied Optics, 1997. **36**(9): p. 1898-901.
9. Lepley, J.J. and A.S. Siddiqui. *A primary-referenced frequency stabilisation technique for use in highly dense wavelength division multiplexing*. in *OFC*. 1999.
10. Villeneuve, B., *et al.* *A compact wavelength stabilization scheme for telecommunication transmitters*. 1997.
11. Soldano, L.B. and E.C.M. Pennings, *Optical multi-mode interference devices based on self-imaging: principles and applications*. Journal of Lightwave Technology, 1995. **13**(4): p. 615-27.
12. Chan, H.P., S.Y. Cheng, and P.S. Chung, *Novel design of low-loss wide-angle symmetric Y-branch waveguides*. Microwave and Optical Technology Letters, 1996. **11**(2): p. 87-9.

Chapter 4

MOCVD Growth for InP PIC's

4.1 Introduction

Growth is the most critical element of the fabrication process for photonic integrated circuits. The quality of the base structure growth and subsequent regrowth steps has a greater impact on the device performance than any other process step. High quality metalorganic chemical vapor deposition (MOCVD) of III-V materials in the InP system is a well developed science which has entered widespread commercial applications. Despite this it is also an area of active research with rapidly developing technology. For photonic integrated circuits MOCVD growth plays a critical role in the fabrication technology. Multiple steps of growth and regrowth are typically required to realize the complex structures used in these devices. Regrowth requires a careful sequence of surface preparation steps followed by a tightly controlled growth process, to achieve desirable results.

4.1.1 MOCVD Growth Fundamentals

Metalorganic chemical vapor deposition is a high quality and efficient technique for the growth of epitaxial thin films on InP substrates. In MOCVD growth metalorganic precursors are used to transport the material components. These precursors are injected into a carrier gas flow that is passed over the surface of a substrate wafer in a reactor cell. The substrate is heated to a temperature which causes the precursors to decompose or pyrolyze in a series of reactions. The decomposition components adsorb on the surface of the wafer and deposit the constituent materials. The high surface temperature enables these elements to diffuse rapidly on the surface and bond to appropriate lattice sites. In the temperature range from 450 to 750°C MOCVD growth is primarily a mass transport limited process where the growth mechanism is dominated by the

diffusion of reactant species to the surface of the wafer. Which means that the composition of the epitaxial material can be controlled by the composition of precursor molecules in the gas stream.

4.1.2 *Source Materials*

For photonic integrated circuits operating in the 1.55 μm wavelength band we are primarily interested in the InGaAsP material system for alloys lattice matched to InP. For dopants we use Si for n-type material and Zn for p-type. The group III precursors are trimethylindium (TMI) and trimethylgallium (TMGa). TMGa is a liquid at room temperature but TMI is a solid which sublimates into the gaseous phase. The sources are held in stainless steel bubblers which sit in temperature controlled baths. Hydrogen gas is bubbled through the container to pick up the source material. The concentration of source in the gas stream is determined by the equilibrium vapor pressure in the bubbler. This can be controlled by changing the bubbler temperature. The output concentration is equal to the ratio of the vapor pressure for the source to the bubbler pressure. The bubbler pressure can be controlled over a limited range and this further enables the output concentration in the gas stream to be adjusted. The bubblers are operated with a stable output concentration and the pure component flow in the reactor is controlled by varying the injection.

TMI has a relatively low vapor pressure (~ 2 Torr at 20°C)[1]so we operate it at a comparatively high temperature and low pressure to achieve a reasonable gas phase concentration. Operating above room temperature can lead to condensation in the lines for liquid sources but this is not as significant a problem for TMI so the bubbler is run at 22°C and a pressure of 900 Torr. One of the key problems with TMI being a solid source is that the output concentration does not always reach equilibrium. Depending on the conditions it can vary with flow rate and with the amount of source left in the bubbler. As the material is used up the surface area decreases and the dynamic equilibrium between the solid and the gas phase becomes more difficult to maintain. There is a great deal of sophisticated proprietary technology which goes into the

design of a TMI bubbler to try and eliminate this problem. We achieved improved stability from TMI by using a pair of bubblers in series to saturate the concentration in the gas stream.

TMGa on the other hand is a liquid source with a very high vapor pressure more than two orders of magnitude greater than TMI. Concentration variation is not a problem for this source. To minimize the vapor pressure we operate TMGa at a temperature of -4°C . This still makes it difficult to achieve the very low gallium concentrations needed for high bandgap quaternary materials so a dilution line is used with this source. The dilution line mixes extra carrier gas with the bubbler flow to dilute the concentration of the source. This enables a much greater range of output concentrations to be reached with improved accuracy.

For the group V sources we use tertiarybutylphosphine (TBP) and tertiarybutylarsine (TBAs). These liquid sources are preferred over the conventional arsine (AsH_3) and (PH_3) gas sources because of their reduced potential for catastrophic release which makes them safer. These sources are not widely used commercially because of their increased cost and because until recently they were not available in the same purity as AsH_3 and PH_3 sources. One significant advantage of these sources is that they have both lower and more similar pyrolysis temperatures which enables lower growth temperature to be used and gives them a smaller segregation coefficient.

The n dopant source is disilane which is a gas. This is the easiest source to use since it only requires an injection and a dilution mass flow controller. The p dopant source diethylzinc DEZn is a liquid which has a very high vapor pressure so it is operated at 0°C and uses a dilution line like TMGa. A schematic of a typical source bubbler configuration is shown in Figure 4-1. Carrier gas from the source manifold is injected into the bubbler through a mass flow controller. This is set up to provide 10% excess flow over what is required for the growth. The excess is vented through the pressure controller. Two separate MFC's are used for the output flow to enable fast switching between different compositions. The MFC flows are switched between

pressure balanced run and vent lines to enable rapid changes in the flow concentration. This is necessary for the growth of very thin layers with abrupt interfaces such as quantum wells.

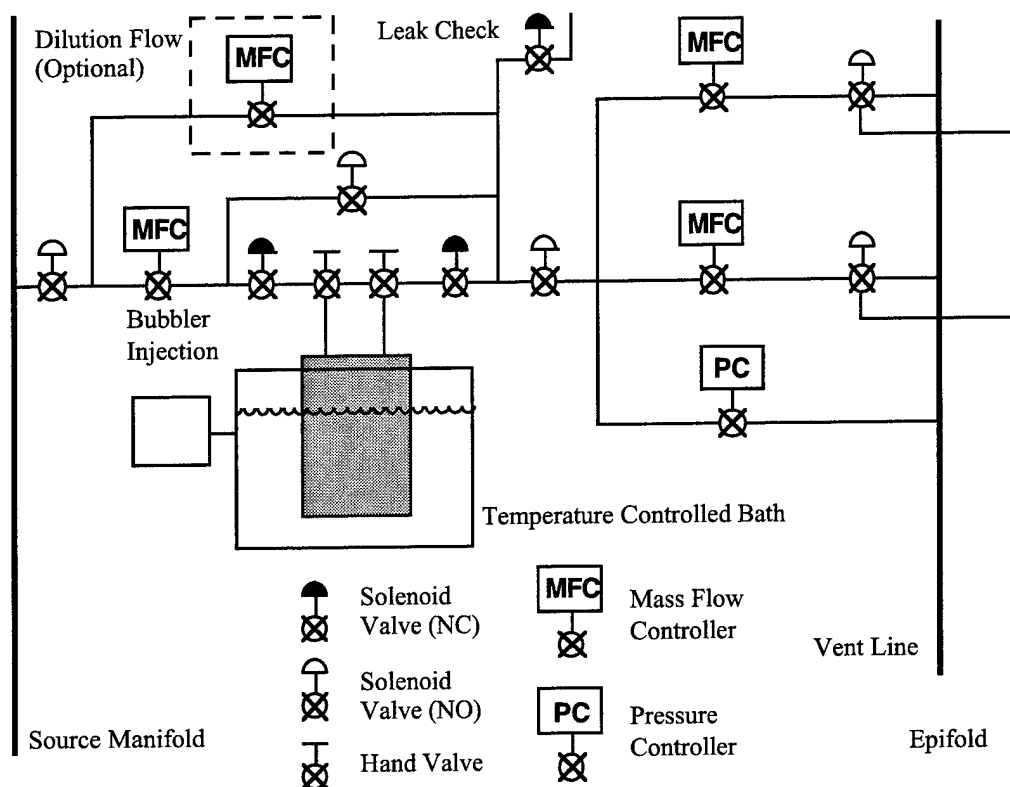


Figure 4-1 Source Bubbler Configuration

The typical source conditions which we use for the reactor are given in Table 4-1. Depending on the type of material being grown these can be modified to enable increased or reduced source concentrations. They are also sometimes changed as a source becomes close to empty to maintain a constant output concentration.

Table 4-1 Source Conditions

Source	Temperature	Pressure	Epison %
TMI	22.0°C	900 Torr	0.140
TMGa	-4.0	1100	2.67
TBP	18.0	1100	18.5
TBA _s	2.0	1250	4.45
DEZn	0.0	1100	~
Si ₂ H ₆	~	~	~

The output concentrations for the sources can be measured accurately using an epison which monitors the speed of sound in an acoustic cell. The gas phase composition can then be controlled by adjusting the flow rates of the mass flow controllers used to inject the source material into the reactor cell. Determining the appropriate gas phase concentration of reactants that is required to achieve a desired solid phase material composition is one of the most difficult aspects of MOCVD growth. This will be discussed in detail in section 4.2.

4.1.3 Reactor Design

The reactor cell consists of a graphite susceptor with a wafer puck inside a specially designed quartz tube. The wafer puck has gas foil rotation which enables it to rotate for improved growth uniformity. The susceptor is 8" long with a 3" entry length before the wafer. This heats up the source materials and causes them to pyrolyze before they reach the wafer. The top wall of the reactor slopes downwards towards the back of the susceptor. This accelerates the flow which reduces the boundary layer thickness. This reduction in the boundary layer is necessary to counteract the depletion of the source material in the gas as it is deposited on the wafer. We operate the reactor at a total carrier gas flow of 16 standard liters per minute (slpm).

Because the mechanical strength of the rectangular reactor quartz is limited it is surrounded by a second tubular quartz liner which equalizes the pressure on

both sides of the reactor. This enables the reactor to be used over a wider range of growth pressures.

4.2 Base Structure Growth and Characterization

The $\text{In}_{1-x}\text{Ga}_x\text{As}_y\text{P}_{1-y}$ material system can be used to create alloys with a wide range of band gaps and lattice constants. Characterization of the band gap, doping levels, and strain in epitaxial grown layer structures is a critical tool in the development of growth processes. X-ray rocking curves are used to measure the lattice constant and thickness of epitaxial layers. The band gap is typically characterized by using the photoluminescence spectrum for the material. Doping concentrations and carrier mobility can be measured using the Hall effect. Background impurity levels, dopant incorporation, and diffusion are accurately determined with secondary ion mass spectroscopy.

4.2.1 Characterization Tools

X-ray Diffraction

Structural information for epitaxial films can be obtained using x-ray diffraction. This section will cover the basic techniques used in our lab to measure x-ray rocking curves for samples grown on [100] oriented InP wafers. In these experiments we use a double crystal diffractometer to obtain high resolution scans Figure 4-2. The double crystal arrangement eliminates the instrument line broadening inherent in single crystal diffractometers. All x-ray sources produce radiation covering a finite wavelength range and with some finite divergence. The divergence is minimized in our system by the use of a channel cut collimator (CCC). The CCC is a Si crystal that is channel cut and oriented for reflection in the [022] direction. The CCC uses four reflections to reduce the angular divergence in the beam to less than 6 arcseconds. After the CCC a Si crystal is used as a monochromator to select out a band of wavelengths from the beam. For high resolution work this can be configured for a symmetric [022] reflection or for increased intensity the [111] reflection can be used[2].

We typically use the [111] reflection to enable faster scans. Our x-ray generator uses a copper anode and produces two peaks $K\alpha_1$ and $K\alpha_2$ at 1.54\AA . For epitaxial layers grown on InP the [400] reflection is convenient since it has a high intensity and the planes are parallel to the surface.

The Bragg angle for the [400] reflection from InP is 31.66° given by Bragg's law (4-1)[3].

$$\lambda = \frac{2a_s \sin(\theta_B)}{\sqrt{h^2 + k^2 + l^2}} \quad (4-1)$$

For single epitaxial layers grown on InP straightforward analysis of the rocking curve data reveals the mismatch in the epitaxial layer. In the absence of tilt the lattice mismatch for a coherent layer is given by (4-2)[3].

$$\left(\frac{\Delta a}{a}\right)_\perp = \frac{a_\perp - a_s}{a_s} = \frac{\sin(\theta_B)}{\sin(\theta_B + \Delta\theta)} - 1 \quad (4-2)$$

A significant improvement in the quality of the epitaxial layers is possible by using substrates that are slightly misoriented. We typically use a [100] oriented wafer with a 0.2° miscut in the [111]A direction. This creates a series of atomic steps on the wafer surface. The step edges act as nucleation sites for growth since it is more energetically favorable to deposit material there. This step flow growth method gives improved uniformity over island growth modes which predominate on non-miscut wafers. This misorientation of the wafer surface creates a tilt in mismatched epitaxial layers. If the epitaxial layer is tilted with respect to the substrate then two rocking curves are needed to obtain $(\Delta a/a)_\perp$ unless the rocking curve is oriented perpendicular to the layer tilt. To achieve this we first perform a scan rotating the wafer in the plane of the surface. This produces a pair of substrate peaks with an angular separation. The angle is then set to the average of the two peak angles which

orients the sample tilt perpendicular to the scan angle. A typical x-ray scan for a 2000Å thick 1.4Q layer is shown in Figure 4-3.

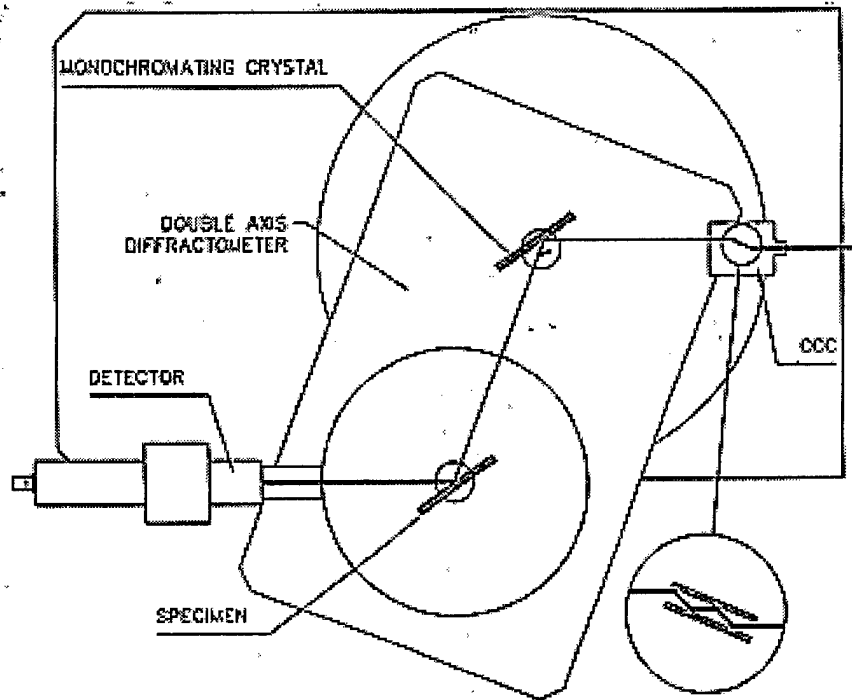


Figure 4-2 Double crystal x-ray diffractometer with channel cut collimator.

The narrow peak at the origin is from the substrate and the broader peak at 130 arcseconds is from the epitaxial layer which has a -0.1% lattice mismatch using (4-2). This is equivalent to a tensile strain of approximately 1000 $\mu\epsilon$.

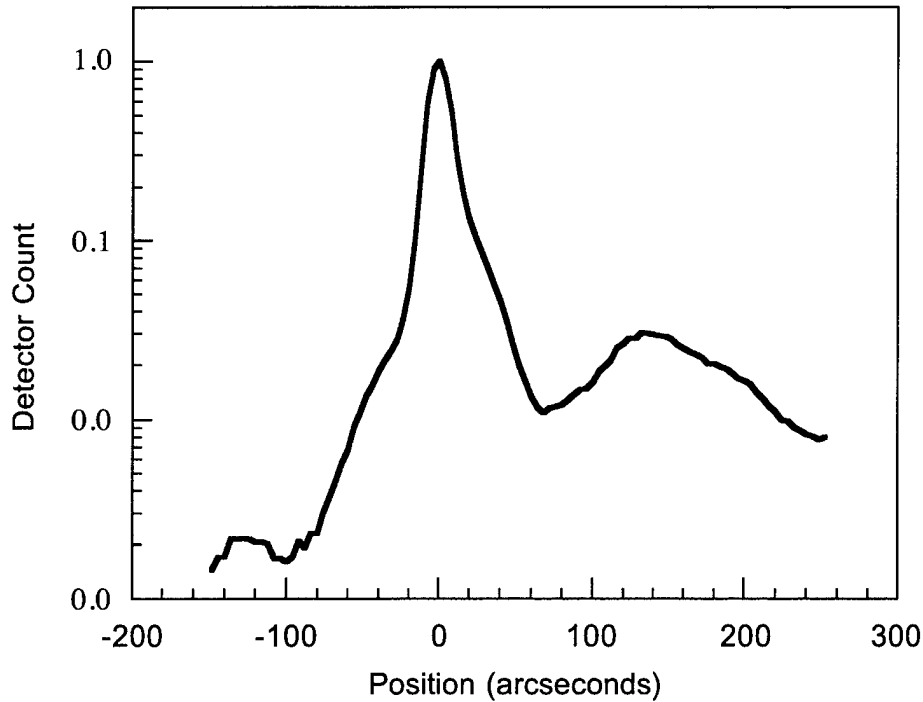


Figure 4-3 X-ray scan for slightly mismatched 1.4Q layer.

Photoluminescence

Room temperature photoluminescence (PL) is a simple and highly effective method for measuring the band gap of epitaxial semiconductor layers. It is also useful for characterizing the transition energies for quantum wells. In this method carriers are generated in the material with a short wavelength laser. The carriers recombine spontaneously in the material giving off light which is characteristic of the band gap of the semiconductor. For pure semiconductors with very low doping the photoluminescence spectrum is characterized by a peak with a sharp cut off at the band edge and a higher energy tail that decays exponentially. For doped semiconductors the spectrum is more symmetrical. For bulk materials grown on InP the bandgap of the material is typically $kT/2$ below the photoluminescence peak and for quantum wells it is usually assumed

to coincide with the peak. A typical PL spectrum from a SGDBR base structure is shown in Figure 4-4.

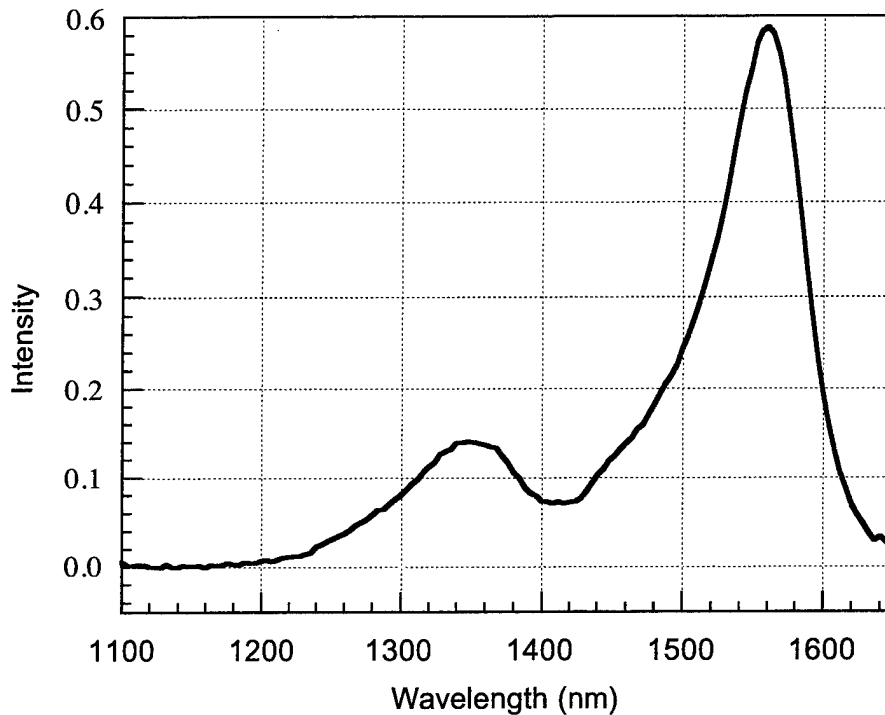


Figure 4-4 Photoluminescence spectrum for SGDBR base structure.

This structure consists of 6 0.8% strained quantum wells with a bandgap of 1560 nm grown on top of a 4000Å thick 1.37Q waveguide layer. For centered quantum well structures the waveguide is typically not visible since the carriers are more efficiently collected into the wells.

The photoluminescence spectrum is a useful tool in characterizing the bandgap and the material quality of MOCVD grown material. The intensity of the PL peak is proportional to the number of carriers that recombine radiatively in the layer. For laser structures this can give a relative measure of the defect density and the collection efficiency for different active regions. It is important to only compare PL from identical structures since different capping layer thickness,

doping levels, or waveguide designs can lead to dramatic differences in the measured intensity.

Hall Measurements

The carrier density and mobility for doped epitaxial layers is another important parameter in MOCVD growth. There is no direct feedback on the effective flow rate for the dopant precursors in the reactor so periodic calibrations must be performed to measure the carrier density and mobility for different effective flows of n and p dopants. These parameters are measured using the Hall effect which can be done by placing contacts on a sample in a classic bridge shape or more conveniently by the Van der Pauw method. This method places four contacts at each of the corners of a square piece of semiconductor material the contacts are labeled around the circumference A,B,C and D. The resistivity for a square sample is then given by (4-3)[3]

$$\rho = \frac{\pi d}{\ln(2)} \frac{(R_{AB,CD} + R_{BC,DA})}{2} \quad (4-3)$$

where $R_{AB,CD}$ is defined as the ratio of the voltage between C and D to the induced current from A to B and $R_{BC,DA}$ is defined in a similar manner. The thickness of the doped layer is represented by d . For our hall measurements we grow 5000 Å thick doped layers of InP on semi-insulating substrates with a 500Å thick InGaAs contact layer. The samples are cleaved into square pieces approximately 5 mm on each side. The corners are covered with photoresist and the contact layer is etched with $H_3PO_4:H_2O_2:H_2O$ at a concentration of 3:1:50 for 30 s. Indium balls are pressed onto the corners and then the samples are annealed at 400°C for 20 s. In the Hall measurement the sample is placed in a strong magnetic field normal to the surface. Then current is applied between two diagonally opposed contacts. This causes a Hall voltage between the two other contacts because the Lorentz force given by (4-4), separates the electrons and holes.

$$q\vec{v} \times \vec{B} \quad (4-4)$$

The Hall mobility can then be calculated from (4-5) where ΔV is the voltage between contacts B and D caused by the current flow j between contacts A and C.

$$\mu_H = \frac{d \Delta V}{B j \rho} \quad (4-5)$$

With the mobility and the resistivity we can quickly determine the carrier density using (4-6) by substituting in the Hall mobility and the resistivity and solving for the electron or hole carrier density assuming that the other component is negligible.

$$\frac{1}{\rho} = \sigma = qn\mu_n + qp\mu_p \quad (4-6)$$

Using this technique we have calibrated the doping density and mobility for n and p type InP grown by MOCVD at several different dopant flow rates. These results are summarized in Table 4-2, which shows the carrier concentration and the mobility for p and n doped layers at a variety of effective flows.

Table 4-2 Doping density and mobility

Zn effective flow	Carrier Density (cm ⁻³)	Mobility (cm ² /V·s)
1.7	1.33E17	
5.0	5.86E17	89.4
15.0	9.59E17	
50	1.58E18	85.1
Si Effective Flow	Carrier Density (cm ⁻³)	Mobility (cm ² /V·s)
2	2.28E17	2813
7	7.65E17	2056
15	1.78E18	1716

The n type mobility is typically 20 to 30 times higher than the p type. This is partly due to the increased effective mass for holes versus electrons in InP. Both n and p type mobilities decrease with increased doping concentration. This effect occurs because the dopant ions act as scattering centers for the carriers. The greater the dopant level the higher the probability that a carrier will undergo a scattering event. This lowers the mean free path in the semiconductor and reduces the mobility. For p type doping with Zn the activation of the dopant decreases as the doping density increases. The Zn atoms start to incorporate in interstitial sites where they do not behave as donors. This causes the p-type doping in InP to saturate at a carrier concentration of about 2×10^{18} . For lower bandgap materials like $\text{In}_{0.53}\text{Ga}_{0.47}\text{As}$ much higher doping levels can be achieved which enables us to grow degenerately doped contact layers for low p-contact resistance.

4.2.2 Determination of Material Parameters

Lattice Matched Materials

For lattice matched alloys of $\text{In}_{1-x}\text{Ga}_x\text{As}_y\text{P}_{1-y}$ the Ga mole fraction x is related to the As mole fraction by (4-7)[3].

$$x = \frac{0.4541}{1 - .029y} \quad (4-7)$$

Using this relation the band gap for the material can now be expressed only as a function of the As mole fraction y using Vegard's law (4-8).

$$E_g = 1.35 - 0.72y + 0.12y^2 \quad (4-8)$$

To determine the composition of a lattice matched epitaxial layer we can solve (4-8) for the As mole fraction y using the bandgap determined from photoluminescence measurements. Then for lattice matched materials we can solve (4-7) for the Ga mole fraction x . This gives us a simple and

straightforward method for correlating the solid composition of an epilayer to the gas phase concentration of reactants.

Strained Materials

The more general problem of determining the exact composition of strained layers from x-ray and photoluminescence data is much more difficult. This is because the deformation of the strained epitaxial layer affects the electronic properties of the material. To obtain the composition we must assume a material composition based on a As y and Ga x mole fraction and then solve for the correct values using an iterative approach. For the more general case of non-lattice matched materials the expression for the bandgap energy (4-8) can be replaced by the more complicated expression in (4-9)[4].

$$E_o = 1.35 + 1.42x - y - 0.33xy - (0.73 - 0.28y)x(1 - x) - (0.101 + 0.109x)y(1 - y) + 0.05\sqrt{xy(1 - x)(1 - y)} \quad (4-9)$$

Here the square root term has been introduced empirically to account for the reduced bowing in quaternary materials. Using this expression enables us to calculate the unstrained band-gap for any composition of $\text{In}_{1-x}\text{Ga}_x\text{As}_y\text{P}_{1-y}$. The optically measured bandgap for the epitaxial layer differs from the calculated value because of strain induced splitting of the valence band degeneracy and shifting in the direct band gap energy. The heavy hole and light hole strained band gap energies for the material can be expressed in terms of the unstrained bandgap E_o and shifts due to hydrostatic and shear deformation[4].

$$\begin{aligned} E_{lh} &= E_o + \Delta E_H + \Delta E_S \\ E_{hh} &= E_o + \Delta E_H - \Delta E_S \end{aligned} \quad (4-10)$$

The values for the energy shifts can be calculated in terms of the strain in the epitaxial layer ϵ_z and the hydrostatic a and shear b deformation potentials for the material. The C_{ij} terms are the elements of the elastic stiffness matrix.

These can be interpolated from the binary values given in Table 4-3 along with the deformation potentials.

$$\begin{aligned}\Delta E_H &= -2a[(C_{11} - C_{12})/C_{11}]\epsilon_z \\ \Delta E_S &= -b[(C_{11} + 2C_{12})/C_{11}]\epsilon_z\end{aligned}\quad (4-11)$$

We can also calculate the unstrained or relaxed lattice constant for this material by interpolating from the binary values using (4-12).

$$a(x, y) = 5.8687 + 0.1896y - 0.4175x + 0.0124xy \quad (4-12)$$

Table 4-3 Binary Compound Properties[4]

Compound	a_0 (Å)	C_{11} (10^{12} dyn/cm 2)	C_{12} (10^{12} dyn/cm 2)	A (eV)	B (eV)
GaAs	5.6533	1.188	0.532	-9.8	-1.76
GaP	5.4512	1.412	0.625	-9.5	-1.3
InP	5.8686	1.022	0.576	-8.0	-1.55
InAs	6.0584	0.833	0.453	-5.8	-1.8

The relaxed lattice mismatch $(\Delta a./a)_o$ is related to the measured perpendicular $(\Delta a./a)_\perp$ strain determined from x-ray rocking curves by (4-13) assuming that $\Delta a_{||}=0$.

$$\left(\frac{\Delta a}{a}\right)_o = \frac{1-\nu}{1+\nu} \left(\frac{\Delta a}{a}\right)_\perp \quad (4-13)$$

Where Poisson's ratio ν for the material can be calculated from the elastic stiffness constants (4-14).

$$\nu = \frac{C_{12}}{(C_{11} + C_{12})} \quad (4-14)$$

The exact composition of an epitaxial layer can be determined from the x-ray and PL data using the following procedure. The initial composition is estimated from the bandgap using the formulas for an unstrained epilayer (4-8) and (4-7). Then using these values for x and y and the strain determined from the x-ray rocking curve the lattice constant is calculated from (4-13). We then use the strain and the measured bandgap to solve for the unstrained bandgap using (4-10). The composition is now determined by simultaneously solving (4-9) and (4-12) using the unstrained bandgap and the relaxed lattice constant. The resulting x and y values can now be used as the initial guess for a subsequent iteration. This method converges rapidly to the correct value for the material composition.

Kseg and Keff

The relationship between the gas phase and the solid phase composition is dominated by the segregation coefficients for the group III and group V materials. Once the coefficients are known for a given material we can quickly calculate the required pure component flows to achieve the desired composition. The segregation coefficients are determined by taking the ratio of the solid phase composition calculated from the x-ray and PL data to the gas phase concentration determined by the epison values for the source concentration and the effective flow rates from the growth program. The segregation coefficient for the group III components referred to as K_{eff} is calculated from (4-15)[1].

$$x = \left(\frac{F_{TMGa}}{F_{TMGa} + F_{TMI}/K_{eff}} \right) \quad (4-15)$$

For group V components K_{seg} is calculated from (4-16)

$$y = \left(\frac{F_{TBAs}}{F_{TBAs} + F_{TBP}/K_{seg}} \right) \quad (4-16)$$

Index of Refraction

The index of refraction is an important material parameter especially for the design of semiconductor lasers and photonic integrated circuits. For quaternary $\text{In}_{1-x}\text{Ga}_x\text{As}_y\text{P}_{1-y}$ alloys lattice matched to InP the index of refraction can be easily determined for a wide range of optical wavelengths. There are a number of different models which can be used most of which are based on a simple double harmonic oscillator model. The model given by Adachi[5] which can be fit to the experimental data from Chandra, Coldren and Streege[6] is given in (4-17).

$$n^2 = A(y) \left[f(\chi) + \frac{1}{2} \left(\frac{E_g}{E_g + \Delta} \right)^{3/2} f(\chi_o) \right] + B(y) \quad (4-17)$$

and

$$\begin{aligned} f(\chi) &= (2 - \sqrt{1 + \chi} - \sqrt{1 - \chi}) / \chi^2 \\ \chi &= E_p / E_g \\ \chi_o &= E_p / (E_g + \Delta) \end{aligned}$$

All of the parameters in equation (4-17) can be expressed in terms of the A_s mole fraction y for the material. The split-off valence band energy gap Δ at 300K is given by (4-18).

$$\Delta = 0.118 + 0.225y \quad (4-18)$$

The A and B coefficients are given by (4-19)

$$\begin{aligned} A(y) &= 8.616 - 3.886y \\ B(y) &= 6.621 + 3.461y \end{aligned} \quad (4-19)$$

and the band gap can be calculated from (4-7). The photon energy in eV can be found quickly using the simple relation in (4-20).

$$E_p = \frac{hc}{\lambda} \approx \frac{1.24}{\lambda} \text{ eV} \cdot \mu\text{m} \quad (4-20)$$

Other Material Parameters

Using the composition parameters x and y we can calculate the conduction, heavy hole, light hole and split off band effective masses (4-21)[7].

$$\begin{aligned} m_c &= (0.08 - 0.039y)m_o \\ m_{hh} &= (0.56 - 0.22y + 0.11y^2)m_o \\ m_{lh} &= (0.12 - 0.092y + 0.024y^2)m_o \\ m_{so} &= (0.12 + 0.074y - 0.05y^2)m_o \end{aligned} \quad (4-21)$$

For tuning efficiency the thermal resistivity can be an important parameter and this depends on the alloy composition according to (4-22).

$$\rho_T = 1.47 + 59.78y - 39.42y^2 \quad [K \cdot \text{cm}/W] \quad (4-22)$$

4.2.3 MOCVD Growth Conditions

Growth rate conditions are highly machine and source material dependent. The results presented here are for growth at 615°C and 350 Torr in a Thomas Swan reactor with a 2" rotating susceptor. In order to achieve consistent results a fixed pure component flow is used for the indium (TMI) and phosphorous (TBP) sources for all of the quaternary materials. The composition is controlled by varying the arsenic (TBAs) and gallium (TMGa) flows taking into account the relations in equations (4-15) and (4-16). The pure component flow is calculated by multiplying the output concentration by the effective flow for the source.. Since we are operating in the mass transport limited regime the growth rate is governed by the total group III flux. The growth rate as a function of group III pure component flow is plotted in Figure 4-5.

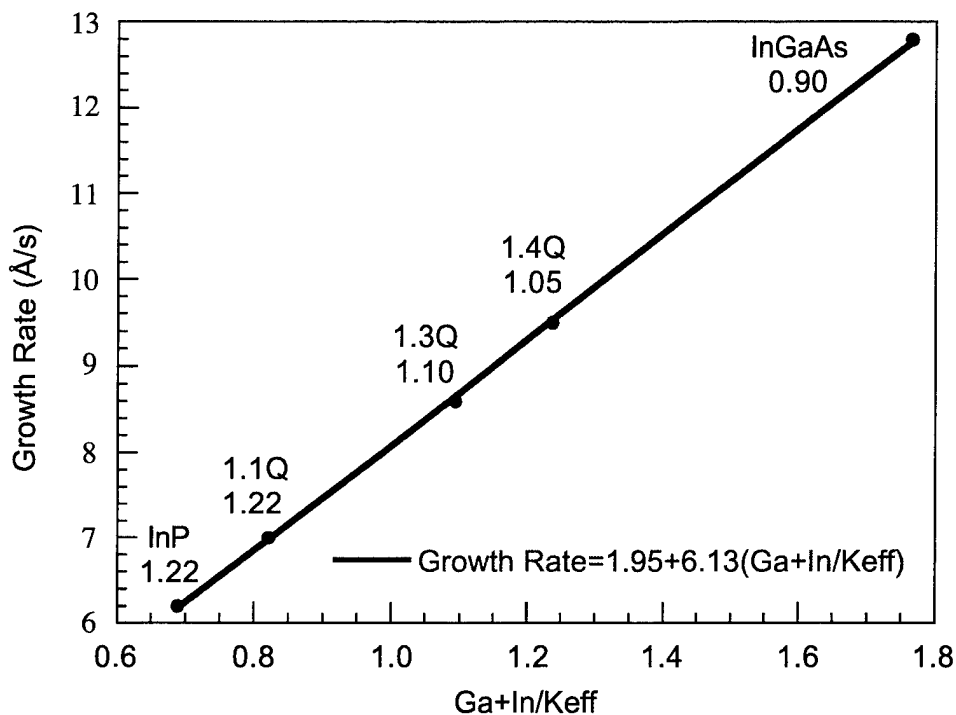


Figure 4-5 Growth rate vs. group III pure component flow for various materials from InP to InGaAs

The growth rate increases linearly from 6.2 for InP to 12.8 for $In_{0.53}Ga_{0.47}As$. The non zero intercept of the fit suggests that for lower carrier concentrations the growth rate dependence will become nonlinear. This suggests that there is a pre-reaction occurring when the group III component concentration exceeds some critical value.

In contrast to the well behaved linear dependence of the growth rate on the pure component flow (PCF) the segregation coefficients that determine the solid phase composition vary significantly depending on the relative component flows. The K_{seg} and K_{eff} for four common materials are plotted in Figure 4-6. K_{eff} is very nearly unity for all compositions which is the ideal case. It decreases almost linearly from 1.2 for 1.1Q material to 0.95 for the

quantum wells. K_{seg} on the other hand is nearly constant for materials up to 1.3Q and then falls off rapidly with decreasing bandgap. This means that as we increase the TBAs flow the efficiency of arsenic incorporation goes down. This happens because the decomposition components of TBAs catalyze the pyrolysis of TBP making it more readily available.

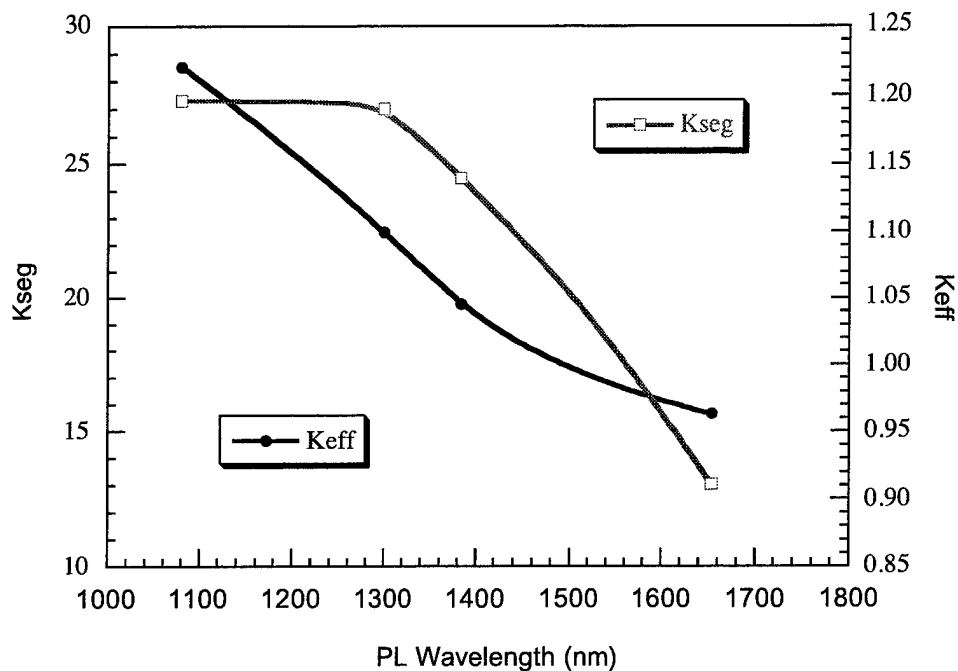


Figure 4-6 Plot of K_{seg} and K_{eff} vs. peak PL wavelength

4.2.4 Quantum Well Design

The design of the quantum well active region is the most complex element of the laser base structure. There are many degrees of freedom and choosing an optimum structure can be difficult. The basic parameters that must be selected are the bandgap and strain in the barrier, the bandgap and strain in the well, the well width and the barrier width. Quaternary wells with quaternary barriers are

of greatest interest since they allow the most degrees of freedom in the design. The strained band gap energy as a function of the x and y composition for InGaAsP is plotted in Figure 4-7. It is evident from this that for tensile strained wells the only practical material choice is InGaAs. Using strained quantum wells is an important improvement since the lower valence band density of states leads to lower threshold currents and higher differential gain and output power [8]. For InGaAs with a tensile strain of 1% the band gap of the well material would be 0.797 meV which is already the desired quantum confined energy. So for InGaAs strained wells we are limited to about 0.8% tensile strain but this requires a 200Å wide well. As the well width increases the energy separation of the quantum confined subbands decreases, resulting in a larger density of states near the valence band maximum. This increases the carrier density required for inversion which correspondingly increases the laser threshold current. For a narrower 100Å wide well with 1.3Q lattice matched barriers the maximum tensile strain is only 0.28% and the degeneracy between the light hole and heavy hole bands is almost completely eliminated. This makes it preferable to use compressively strained quaternary quantum wells. One possible advantage of the wide shallow tensile wells is that they have a broader gain spectrum which could allow a wider tuning range. However the photoluminescence from most compressively strained quantum well active regions shows a 3 dB bandwidth in excess of 70 nm which is more than adequate for most tunable lasers. This bandwidth can be further increased using techniques which we will discuss later in this section.

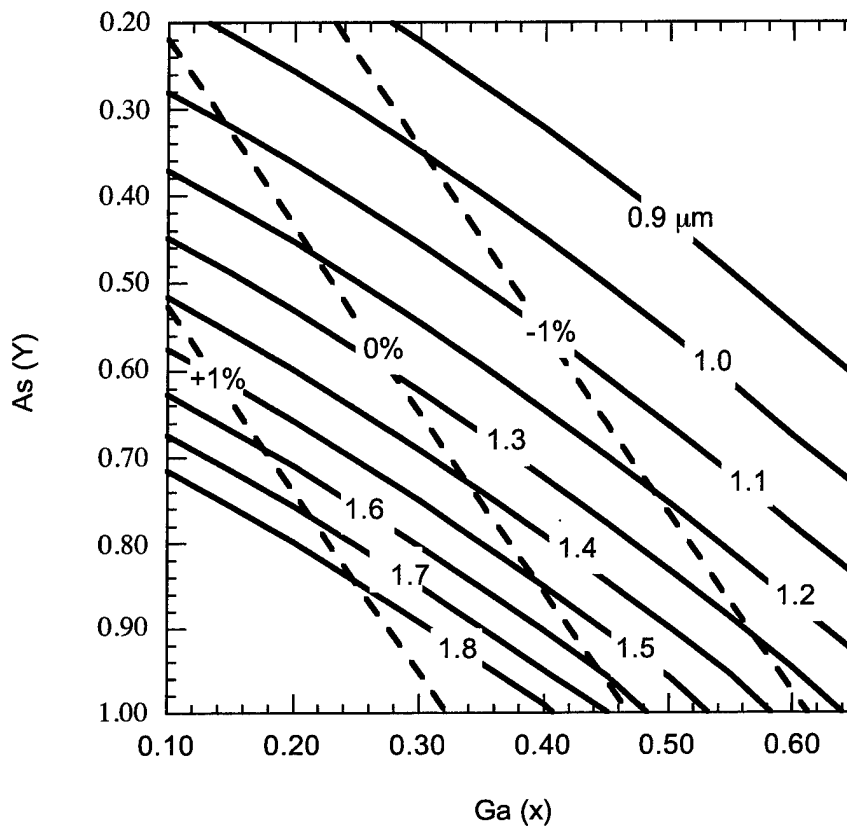


Figure 4-7 Bandgap and strain for $\text{In}_{1-x}\text{Ga}_x\text{As}_y\text{P}_{1-y}$ quaternary material. Energy contours are plotted in wavelength.

Compressively Strained Wells

For compressively strained quantum wells in $\text{In}_{1-x}\text{Ga}_x\text{As}_y\text{P}_{1-y}$ there are two main types that are of significant interest. These are the constant x (CX) and the constant y (CY) structures in which either the group III or group V composition are identical for the wells and barriers. In the constant x structure it is easy to grow lasers which have strained wells and unstrained barriers. As the strain in the well is increased the laser characteristics improve. The threshold current density decreases and the differential gain increases up to a

lattice mismatch of about 1.0% where it begins to saturate. Beyond 1.2% there is no significant improvement in device characteristics and in fact there is little benefit in exceeding 1% compressive strain [8]. For devices with 1% compressive wells we are able to grow up to four 65Å wide wells with lattice matched barriers before reaching the critical thickness. The wells were $\text{In}_{0.78}\text{Ga}_{0.22}\text{As}_{0.78}\text{P}_{0.22}$ and the barriers were $\text{In}_{0.72}\text{Ga}_{0.28}\text{As}_{0.6}\text{P}_{0.4}$. Other researchers have demonstrated up to 8 wells at 1% with lattice matched barriers using different growth conditions [9]. For increased numbers of wells we have grown up to 6 at 0.8% compressive strain with a constant x structure and lattice matched barriers. The wells were $\text{In}_{0.73}\text{Ga}_{0.27}\text{As}_{0.82}\text{P}_{0.18}$ and the barriers were $\text{In}_{0.73}\text{Ga}_{0.27}\text{As}_{0.82}\text{P}_{0.18}$. Using this structure we should be able to grow up to 8 wells in our conditions without reaching the critical thickness.

Much larger numbers of highly strained wells can be grown using strain compensation in the barriers to create a zero net strain structure [9]. This can be accomplished with a constant y structure but only with a significant reduction in the barrier height. For a typical well with a bandgap of 0.75 eV and a strain of 1% the arsenic mole fraction is about 0.83. If the barrier is strained at -1% the maximum bandgap energy is only 0.89 eV. This low barrier can result in significant carrier leakage. For a zero net strain structure with a barrier bandgap of 1.3 eV the material composition required for the barriers is in the miscibility gap making it extremely difficult to grow [1].

Gain Flattening

For tunable lasers a broad flat gain spectrum is preferred. For most cases the multiple quantum well active regions which are typically achievable on InP have a broad enough gain spectrum. However for really wide range tuning over up to 100 nm it is possible to increase the width of the gain spectrum by chirping the well bandwidth throughout the growth. This can be done by changing the well thickness or by changing the well composition. The best method is of course to change the well thickness. A comparison of the PL spectrum for a chirped and unchirped quantum well active region is shown in Figure 4-8. The chirped structure has a wider bandwidth but at the cost of reduced peak gain. Despite the reduction in peak gain it will be advantageous

to use the flattened structure since the tuning performance will be more consistent.

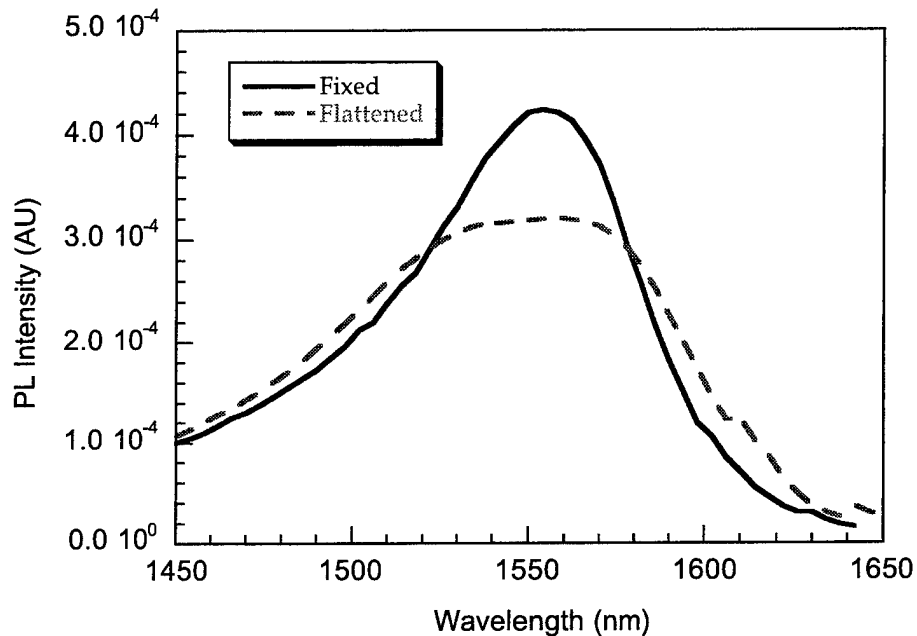


Figure 4-8 Comparison of PL spectrum from standard MQW structure and chirped structure for flattened gain.

4.2.5 Growth Structure and Doping

The base structure for the SGDBR laser is grown on an n-type substrate which is doped with either sulfur or zinc. The first layer is an n-type buffer 1 μm thick. Using a thick buffer layer lowers the loss by decreasing the modal overlap with the substrate which has higher loss than the MOCVD grown layers. The increased loss is a result of the higher doping levels and increased defect density in the substrate. The next layer is a 3500 \AA thick 1.4Q

waveguide. The waveguide is doped lightly n type to increase the carrier injection efficiency into the quantum wells. A 100 Å thick stop etch layer separates the waveguide from the quantum wells. The stop etch is left undoped so that it can be converted to p-type in the tuning sections during the regrowth. Six quantum wells are grown using a constant x structure with 65 Å thick 0.8% wells and 1.3Q lattice matched barriers 80 Å thick. A 300 Å thick 1.3Q cap layer is grown on top of the wells. This layer helps to prevent zinc diffusion into the wells by pinning it at the InP interface. A 200 Å thick InP cap layer is grown on top of the structure to protect the quantum wells during the subsequent regrowth steps. The p doping in the cap layer is set back 1600 Å from the quaternary layers to account for the zinc diffusion during the regrowth.

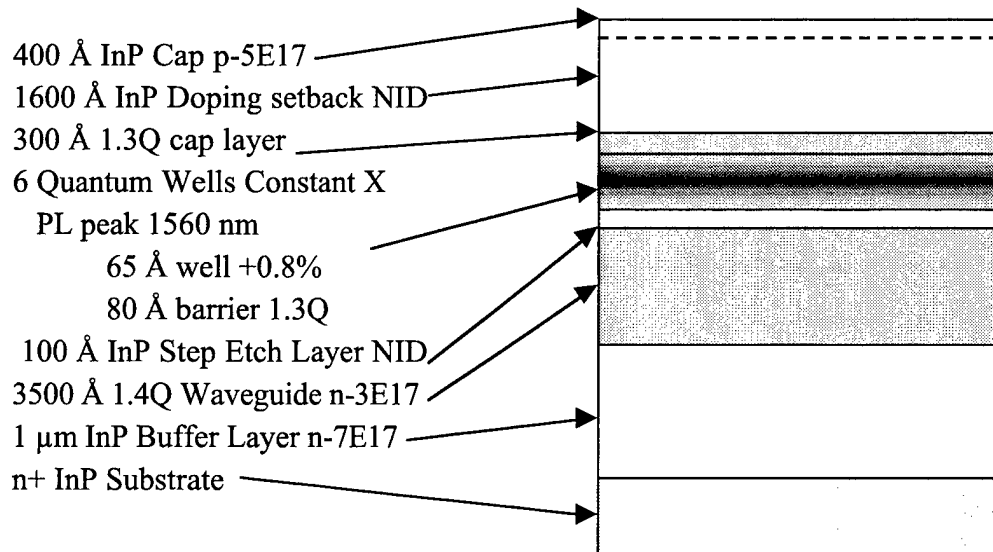


Figure 4-9 SGDBR base structure layer composition and doping

4.3 Grating Regrowth

4.3.1 Surface Preparation

Regrowth is an essential step in the fabrication of both ridge and buried heterostructure lasers. It is also one of the most difficult and yield limiting steps in the process. Good surface preparation is essential to achieving high quality regrowth interfaces. The regrowth preparation begins with a thorough surface cleaning in a series of solvents. The sample is immersed in 1165 photoresist stripper at 80°C for one hour. Then it is rinsed in acetone, followed by isopropanol and then deionized (DI) water. After this the sample is oven baked at 120°C for twenty minutes. Early preparation methods included an oxygen plasma treatment to descum the wafer of photoresist residue. This step was eliminated after studies revealed a 20 to 30% decrease in the PL intensity for regrown structures with the O₂ plasma treatment versus layers without the treatment. This reduction in PL intensity is caused by the creation of defects within the sample during the oxygen plasma treatment and the incorporation of extra oxygen at the regrowth interface. After the sample has been cleaned and baked it is placed in a UV-Ozone oven for one hour. This creates a thin oxide layer on the surface of the wafer that is removed just before the sample is inserted into the reactor. The final step in the preparation is a buffered HF etch followed by a water rinse. This is a critical element in the procedure since the BHF dip removes the oxide layer leaving a clean surface with low contamination. Tests on regrowth using other etchants for the final surface cleaning gave extremely poor results. The water rinse is also critical. The sample must be rinsed in flowing DI water for a minimum of 3 minutes. After this the sample is removed and blown dry with a N₂ gun. If the water rinse is sufficient the sample will be hydrophilic and water will cover the entire surface evenly. If the surface is hydrophobic then the rinse wasn't long enough and the regrowth will be poor. In this case the preparation steps should be repeated from the bake step. The difference between a good and a bad preparation can determine whether the sample looks like sandpaper or has a mirror smooth surface finish.

After the rinse the sample is loaded into the nitrogen filled glove box immediately. This prevents the surface from re-oxidizing. Before the regrowth the sample is baked at 150°C for 15 minutes under a hydrogen ambient at atmospheric pressure with a 20 sccm flow of H₂ carrier gas.

4.3.2 *Regrowth Interface*

Carrier lifetime and tuning efficiency in the mirror sections of SGDBR lasers depends strongly on the quality of the regrowth interface which is in close proximity to the waveguide layer. Defects at this interface can cause a significant increase in nonradiative recombination which reduces the carrier lifetime and limits the tuning range. At the beginning of the regrowth the temperature of the wafer is ramped to the growth temperature and stabilized. The wafer is then baked at this temperature for 3 minutes to desorb surface contaminants. During this time the reactor is purged with hydrogen carrier gas and an appropriate mixture of the group V sources. The group V source flow is required to create an overpressure of reactants in the gas stream that effectively balances the vapor pressure of the group V material in the wafer.

In the standard fabrication process for the SGDBR laser the cap layer and quantum wells are removed from on top of the waveguide in the passive tuning sections. Then the gratings are patterned and etched into the waveguide with a SBW based etchant. This etchant is strongly diffusion limited which gives it a large etch rate enhancement near the edge of any masked region. This makes it necessary to limit the masked area of the sample to just the grating burst section which allows the entire surface of the wafer to be etched to the same depth as the grating bursts Figure 4-10.

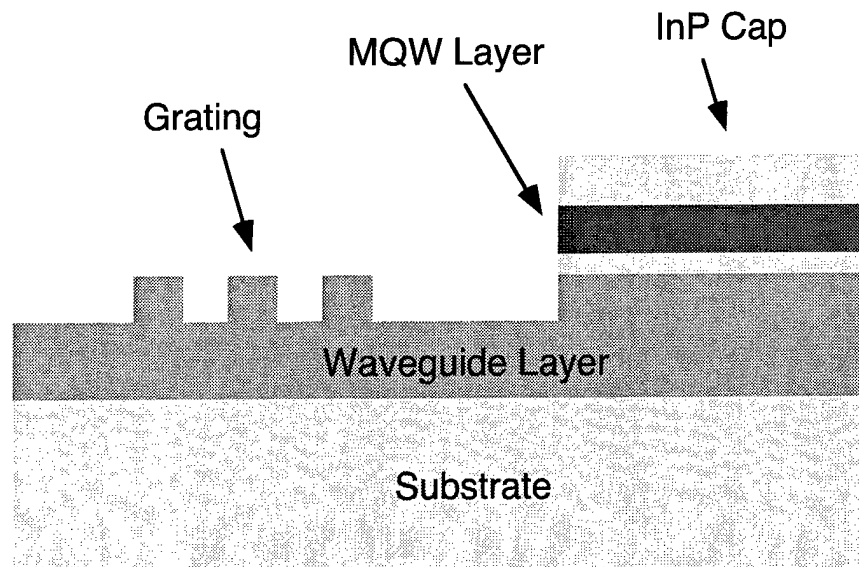


Figure 4-10 Base structure with wet etched gratings.

The problem with this approach is that it leaves about two thirds of the surface terminated in quaternary material and one third covered with InP. During the heat up and bake cycle if the wafer is purged with TBP then arsenic on the surface of the quaternary layer will desorb and be replaced with phosphorous. This substitutional exchange of As and P on the surface of the quaternary layer leads to a highly strained and defected interface. If instead we purge with a mixture of TBAs and TBP which is balanced to the group V composition of the quaternary we get the opposite effect happening in the InP covered areas. To minimize this problem a very short purge cycle on the order of 15 s is used with only TBP overpressure. Unfortunately this procedure does not allow sufficient time for proper surface reconstruction and significantly reduces the quality of the regrowth Figure 4-11.

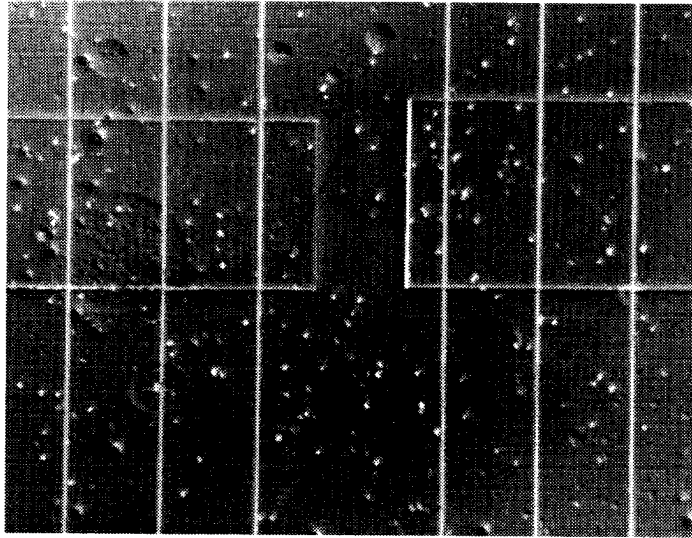


Figure 4-11 Surface of wet etched sample after grating regrowth.

To improve the regrowth, the grating fabrication process must be modified so that the entire surface of the sample is left covered with InP after the etch. This can not be achieved with a wet etching process so a dry etching technique must be used for the gratings. In this new process the quantum well active layer and the InP cap are removed with a selective wet etchant that stops on a thin InP layer covering the waveguide. The sample is then blanketed with a 300Å thick SiN_x masking layer and windows are opened in this mask for the grating bursts. Following this a 1400-5 resist layer is spun on top of the mask and patterned with a holographic exposure. The gratings are dry etched in a methane/hydrogen/argon (MHA) reactive ion etcher (RIE). The SiN_x mask protects the sample so it is only etched in the grating burst area. This leaves more than 95% of the sample covered in InP with exposed quaternary material only in the etched portion of the grating Figure 4-12.

The pre-growth bake time can now be increased and the sample protected with an overpressure of TBP only. With this method the regrowth quality is dramatically improved with a significant reduction in surface defects Figure 4-13.

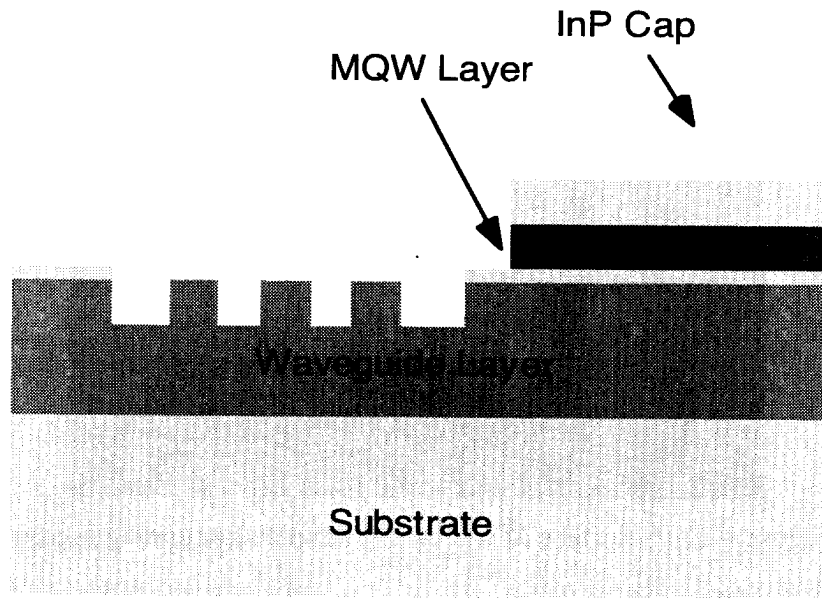


Figure 4-12 Base structure with dry etched gratings

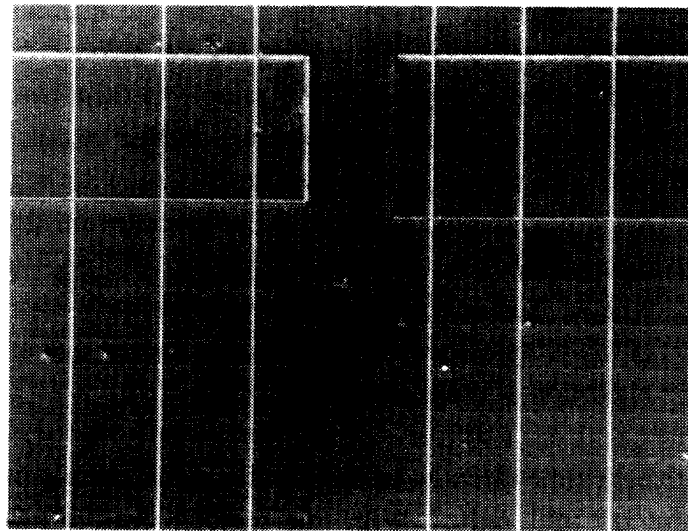


Figure 4-13 Surface of dry etched sample after grating regrowth.

This improved interface quality correlates with increased carrier lifetime in the waveguide layer giving the dry etched gratings a higher tuning efficiency. Ridge waveguide DBR lasers fabricated with wet etched gratings could be tuned over 2.6 nm with 110 mA of DBR current Figure 4-14. Lasers fabricated from the same waveguide structure with dry etched gratings could be tuned over 5.8 nm with 110 mA which is more than twice the range of the wet etched sample Figure 4-15. Tuning ranges of up to 6.5 nm were obtained with an optimized waveguide design. This is significantly greater than the best previously reported result for a ridge waveguide laser of 2.5 nm.

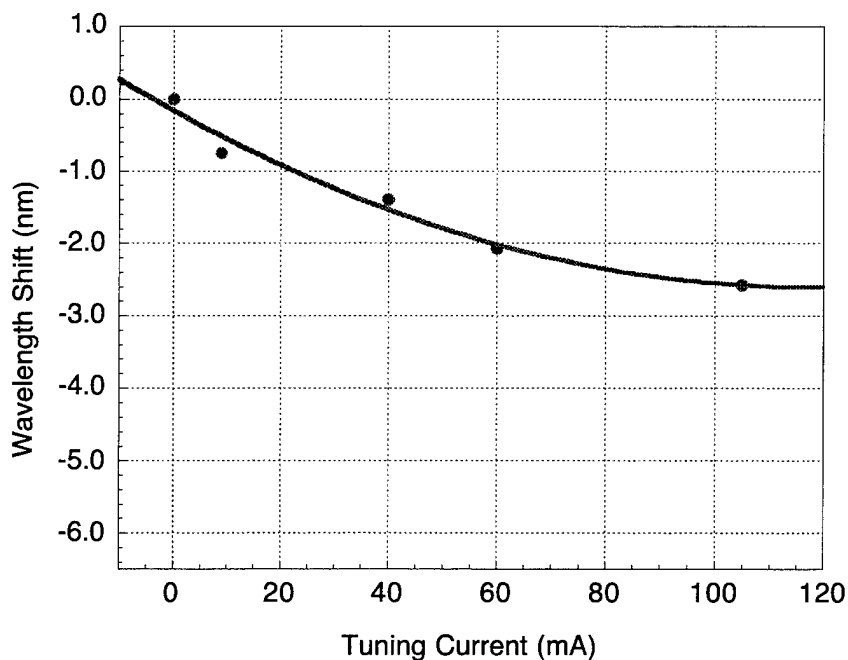


Figure 4-14 Wet etched DBR with 2.8 nm tuning range.

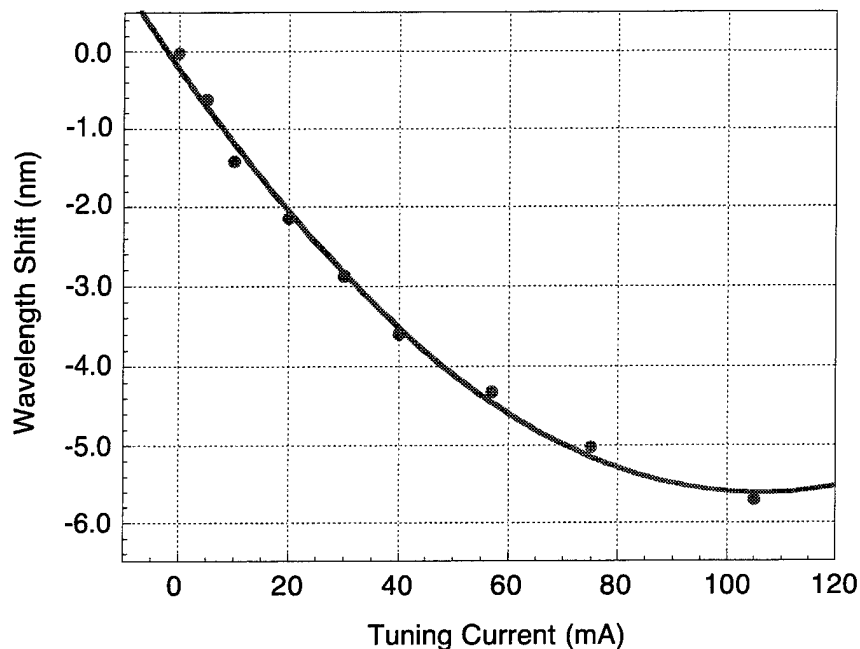


Figure 4-15 Dry etched DBR with 5.8 nm tuning range.

The tuning range for the ridge waveguide devices is primarily limited by two factors carrier leakage and joule heating. Using a buried laser structure rather than a ridge waveguide design can give significant improvement in both these areas. The buried heterostructure provides lateral carrier confinement, which a ridge structure doesn't, and it has a lower thermal impedance.

4.4 Buried Heterostructure Laser Regrowth

The three most common types of buried heterostructure lasers are the simple buried ridge stripe (BRS), the blocking junction planar buried heterostructure (BJ-PBH) and the semi-insulating buried ridge stripe (SI-BRS). A schematic cross section of a simple BRS structure is shown in Figure 4-16. This device is fabricated by etching a narrow ridge through the quantum wells and the waveguide and then regrowing a p-type InP cap layer over the entire structure.

Lateral current confinement can be obtained by either implanting the upper cladding on either side of the stripe or etching isolation trenches. This is the simplest structure and the easiest to fabricate since it does not require any patterned regrowth.

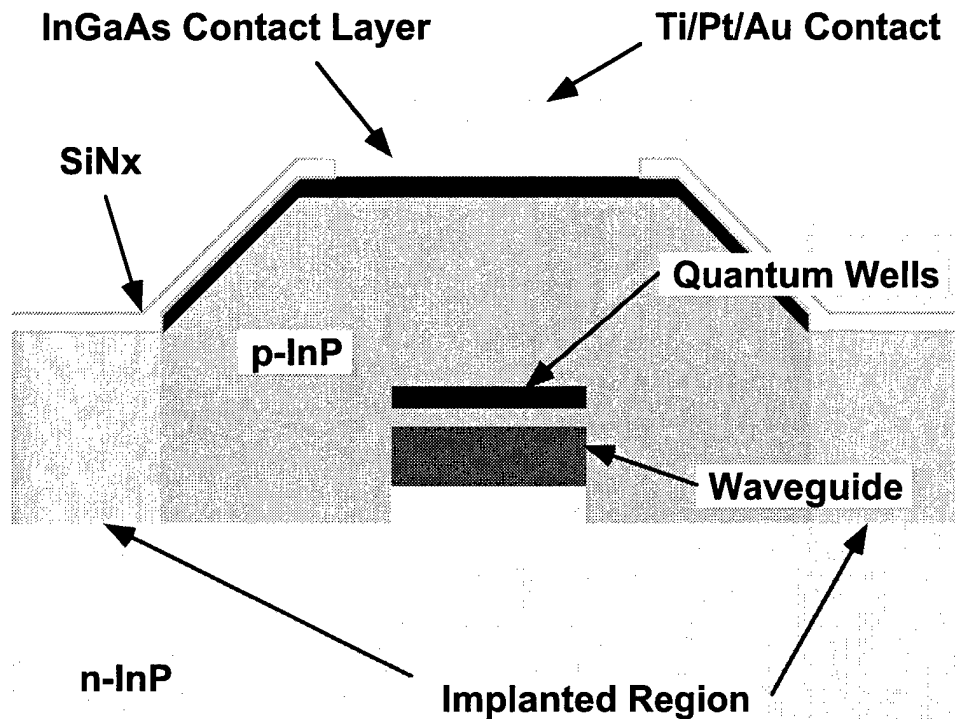


Figure 4-16 Cross section of buried ridge stripe laser.

In a BJ-PBH design two separate regrowth steps are required to bury the ridge. In the first regrowth the ridge top is covered with a dielectric mask and a p-n blocking junction is grown around the ridge. After this growth the mask is removed and a p-type contact layer is grown. A cross section of a stain etched BJ-PBH SGDBR laser is shown in Figure 4-17. The stain etch reveals the contrast between the n and p-type layers. This particular device had very high leakage current because the n blocking layer was too thin. However in general the BJ-PBH lasers have lower leakage. This typically gives them lower

threshold currents and higher differential efficiency. The simple BRS lasers depend on the laser having a lower turn on voltage than the parasitic p-n junction. As the bias is increased in these devices the leakage increases and the L-I curve tends to roll over. In contrast to this the BJ devices use a reverse biased p-n junction to eliminate the leakage path. This gives them a more linear L-I curve and better high temperature performance.

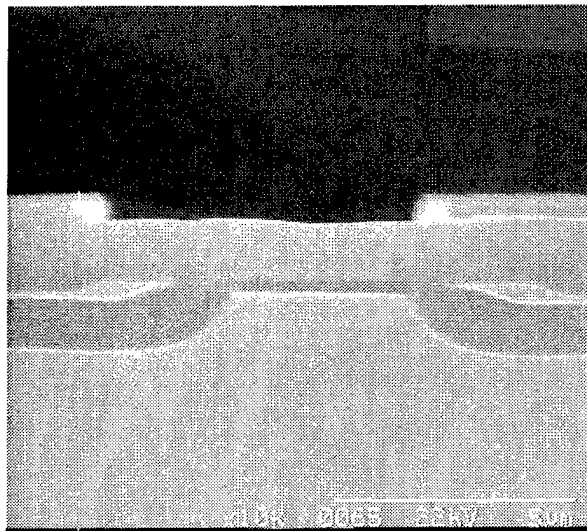


Figure 4-17 Buried heterostructure laser with blocking junction.

One problem that exists with both the BJ-PBH and the BRS structures is that they have a fairly low modulation bandwidth. The primary reason for this is the large parasitic junction in these devices[10]. This junction is typically on the order of $10\ \mu\text{m}$ wide even though the active section is only 1.5 to $2\ \mu\text{m}$ in width. This junction has a large capacitance that limits the modulation bandwidth. The third type of buried laser the SI-BRS is particularly attractive because it eliminates this parasitic capacitance. In this method a deep ridge is etched through the waveguide layer then an Fe-doped semi-insulating InP layer is grown around the ridge which is covered with a dielectric cap. A thin n-type layer is grown on top of the Fe layer to block inter-diffusion of Fe and Zn in

the subsequent capping regrowth. After this growth the dielectric cap is removed and a p-type contact layer is grown on the whole surface of the device. The semi-insulating layer is typically greater than $1\ \mu\text{m}$ in thickness which enables it to act as an effective current blocking layer and also dramatically reduces the parasitic junction capacitance. This gives these types of devices a much greater modulation bandwidth. The principle disadvantage of both the SI-BRS and the BJ-PBH is that they require an extra selective area regrowth step. For this reason we primarily pursued the simple BRS structure for the buried SGDBR lasers.

Buried Ridge Stripe Lasers

Buried ridge stripe lasers can be fabricated with either wet etched or dry etched ridges. Wet etching the ridges gives smoother side walls which taper out at the base. A stain etched cross section from a wet etched buried heterostructure SGDBR is shown in Figure 4-18. The p and n type InP are clearly delineated along with the waveguide and the offset active region. The wet etched ridges are fabricated with a saturated bromine water based etchant (SBW:H₃PO₄:H₂O 4:0.8:15). This etch is isotropic and undercuts the mask on either side of the ridge by an amount equal to the etch depth. To compensate for this the mask ridges are patterned at a width equal to twice the depth plus the intended final ridge width. So for a $1.5\ \mu\text{m}$ etch depth and a $2\ \mu\text{m}$ final ridge width a $5\ \mu\text{m}$ wide mask is required. The etch rate can vary significantly depending on the size of the sample and the volume of etchant. It is also highly prone to localized etch rate enhancement in areas where the mask coverage is more dense. This can lead to significant nonuniformity in both the etch depth and the ridge width across a sample.

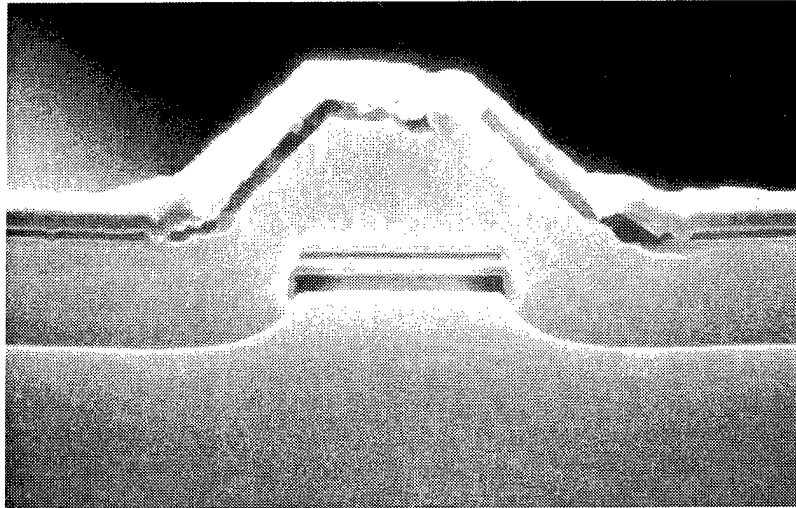


Figure 4-18 Wet etched buried ridge stripe laser.

The dry etch process leaves a sharp corner at the base of the ridge, and tends to have rougher side walls. Dry etching also creates damage at the surface in the form of defects. These defects can act as non-radiative recombination centers in the intrinsic layers. The principle advantage of the dry etching technique is enhanced uniformity. The amount of undercut in the etch is generally less than $0.05\ \mu\text{m}$ for a $1\ \mu\text{m}$ etch depth. Also the etch rate is consistently accurate to within 5% over a quarter wafer. Dry etching can be more precisely controlled with the use of a laser monitor. The laser monitor reflects a 980 nm laser beam off of the surface of the sample and looks at the interference between the surface reflection and the reflection at the epilayer interfaces. Using this technique we can monitor the etch depth accurately and determine exactly when the etch penetrates the waveguide layer. This enables a precise etch depth to be reached consistently even if the sample size or the etching conditions vary. A stain etched cross section for a dry etched ridge is shown in Figure 4-19. In this structure the cap layer thickness has been increased and an isolation implant has been performed for lateral current confinement. The surface damage inherent in the dry etching process is typically only a few

hundred angstroms in depth and can be removed by performing a brief wet etching step after the dry etch.

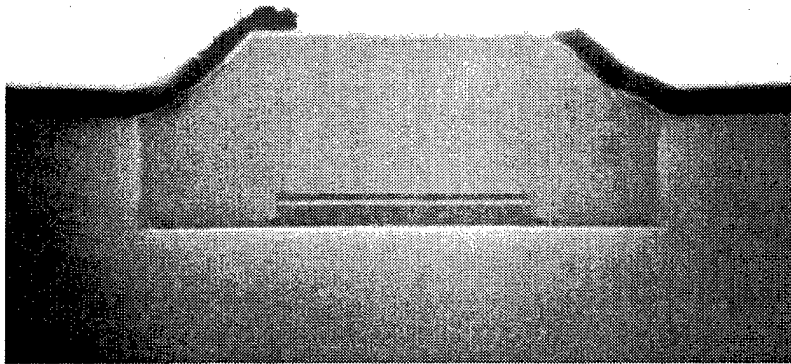


Figure 4-19 Dry etched buried ridge stripe laser.

In both the cross sections it is evident that the growth rate in the vertical or [100] direction is much higher than the growth rate in the lateral direction. The general shape of the sidewall is close to a [111] plane. However the side walls for these devices show a great deal of roughness which indicates that there is competition between growth planes. After 2 μm of growth the top of the ridge is only 20% wider than the etched width. This corresponds to only 0.2 μm of lateral growth or about 10% of the vertical growth rate. This rough sidewall which is clearly evident in Figure 4-20 and Figure 4-21 can cause significant optical scattering loss in the waveguide. To achieve a smoother regrowth profile the growth conditions must be selected so that surface migration of the reactants relative to the growth rate is enhanced. This can be done by increasing the temperature and reducing the pressure. These structures were grown at the standard conditions of 615°C and 350 Torr. There is some concern that raising the growth temperature will lead to increased thermal diffusion of dopant atoms that would deteriorate the device characteristics.

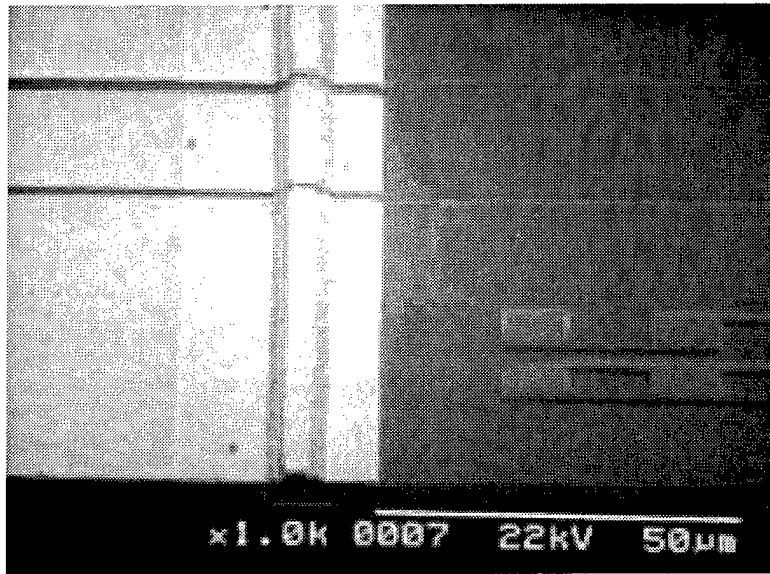


Figure 4-20 SEM of buried heterostructure DBR laser showing sidewall roughness

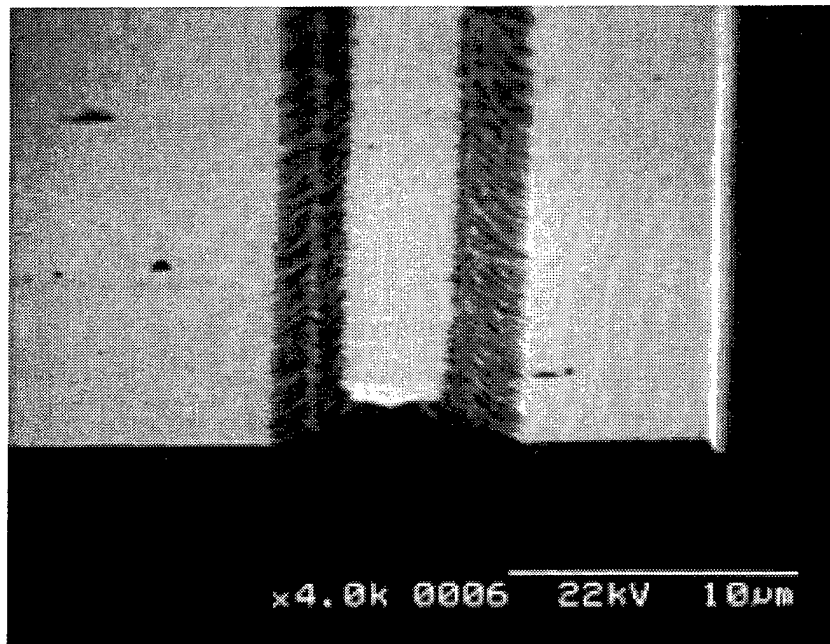


Figure 4-21 Close up of buried ridge with rough side walls.

The other alternative approach is to lower the effective V to III ratio at the surface. Normally it is not possible to do this when using a phosphine source since a minimum partial pressure of phosphorous must be maintained in the gas stream to prevent desorption from the surface. However with TBP as a phosphorous source the V to III ratio can be much lower due to its increased cracking efficiency at lower temperatures. It is thus possible to operate at a lower growth temperature. Using a lower growth temperature reduces the cracking efficiency for the TBP which increases the surface mobility of the group III compounds. For a temperature of 585°C we get significantly smoother side walls and increased lateral growth rate Figure 4-22.



Figure 4-22 SEM of low temperature regrown buried heterostructure laser with smooth side walls.

The enhanced lateral growth rate is visible in the cross section shown in Figure 4-23. It is significant that this large difference in the regrowth characteristics occurs for only a 30°C difference in growth temperature. All other factors were kept constant. It is apparent that the lower temperature reduced the

decomposition rate of the TBP effectively lowering the surface V to III ratio. This increased the surface mobility of the group III compounds giving a dramatic improvement in the growth structure. Lowering the temperature also increases the Zn dopant incorporation for p-type material so the Zn dopant flow must be recalibrated for the new conditions.

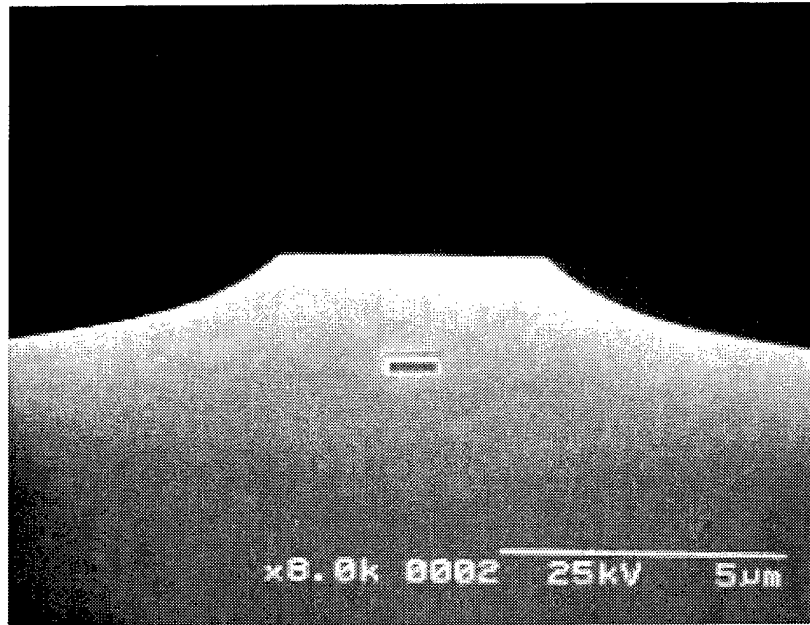


Figure 4-23 SEM cross section of low temperature regrowth showing enhanced lateral growth rate.

4.5 Summary

The techniques for growth and regrowth that have been developed in this chapter enable the fabrication of devices with both active and passive sections that have high tuning efficiency and low threshold currents. These are applicable to a wide variety of photonic integrated circuits. Future work

should focus on addressing the current weaknesses in the buried heterostructure design while still maintaining the generality of the process.

Future Work

In order to address the fundamental bandwidth limitations of the buried ridge stripe design and to develop SGDBR lasers with improved linearity and high temperature performance we need to develop the semi-insulating buried ridge stripe design. This will require a selective area regrowth step to planarize a tall dry etched ridge. The principle difficulty is suppressing growth over the dielectric mask. Researchers using phosphine as a group V source have been required to resort to the addition of Cl compounds, high speed rotating susceptors[11], or high regrowth temperatures[12] to achieve this. For our system however it should be possible to use the same low temperature conditions developed for the smooth side walls on the buried ridge stripe laser. These conditions give high group III surface mobility and a long diffusion length which will prevent mask overgrowth. With this approach it should be possible to create p-n-Fe blocking junctions that will eliminate lateral leakage current and lower the parasitic capacitance of buried SGDBR lasers. This will enable devices with increased output power, higher efficiency, and greater modulation bandwidth.

References

1. Stringfellow, G.B., *Organometallic vapor phase epitaxy : theory and practice*. 1989, Boston: Academic Press. xviii, 398.
2. Loxley, N., D.K. Bowen, and B.K. Tanner. *The performance of channel cut collimators for precision X-ray diffraction studies of epitaxial layers*. 1991.
3. Swaminathan, V. and A.T. Macrander, *Materials aspects of GaAs and InP based structures*. Prentice Hall advanced references series. Engineering. 1991, Englewood Cliffs, N.J.: Prentice Hall. xvii, 606.
4. Flemish, J.R., *et al.*, *Determination of the Composition of Strained InGaAsP Layers On InP Substrates Using Photoreflectance and Double-Crystal X-Ray Diffractometry*. *Journal of Applied Physics*, 1991. **70**(4): p. 2152-2155.
5. Adachi, S., *Refractive indices of III-V compounds: key properties of InGaAsP relevant to device design*. *Journal of Applied Physics*, 1982. **53**(8): p. 5863-9.
6. Chandra, P., L.A. Coldren, and K.E. Strege, *Refractive index data from Ga/sub x/In/sub 1-x/As/sub y/P/sub 1-y/ films*. *Electronics Letters*, 1981. **17**(1): p. 6-7.
7. Krijn, M., *Heterojunction Band Offsets and Effective Masses in Iii-V Quaternary Alloys*. *Semiconductor Science and Technology*, 1991. **6**(1): p. 27-31.
8. Silver, M. and E.P. Oreilly, *Optimization of Long Wavelength InGaAsP Strained Quantum-Well Lasers*. *Ieee Journal of Quantum Electronics*, 1995. **31**(7): p. 1193-1200.
9. Streubel, K., *et al.*, *Importance of Metalorganic Vapor Phase Epitaxy Growth Conditions For the Fabrication of InGaAsP Strained Quantum Well Lasers*. *Journal of Crystal Growth*, 1994. **143**(1-2): p. 7-14.
10. Bertone, D., *et al.*, *MOCVD regrowth of semi-insulating InP and p-n junction blocking layers around laser active stripes*. *Journal of Crystal Growth*, 1997. **170**(1-4): p. 715-718.
11. Takemi, M., *et al.*, *Improved selective growth of InP around dry-etched mesas by metalorganic chemical vapor deposition at low growth temperature*. *Journal of Electronic Materials*, 1996. **25**(3): p. 369-74.

12. Nordell, N., *et al.*, *MOVPE regrowth of semi-insulating InP around reactive ion etched laser mesas*. Electronics Letters, 1991. **27**(11): p. 926-7.

Chapter 5

Device Packaging and System Testing

5.1 Introduction

Packaging is one of the most critical issues for photonic devices. It can represent 80% of the cost for a laser source and results in more than 90% of the failures for long wavelength lasers. The most critical aspect of laser packaging is the fiber pigtailling procedure. Fiber pigtailling or coupling is the process of aligning an optical fiber to the device and fixing it in place so that the light is efficiently launched into the fiber. This process is critical because of the extremely tight mechanical tolerances which must be achieved and maintained over long periods of time. Laser packaging also includes both electrical and thermal issues. For directly modulated devices high speed electrical connections must be provided. For long wavelength and particularly WDM applications a thermoelectric cooler must be included in the package along with a sensor so that the laser can be maintained at a constant temperature. This helps to ensure stable output power and wavelength at a fixed drive current.

Device packaging represents such a large segment of the cost of a laser because all of the operations involved in the packaging process must be performed individually for each device. Growth and processing steps for the laser are performed simultaneously on many thousands of devices. Even though the equipment and facilities required for these steps are much more expensive than for packaging the economies of scale make this a lower cost operation.

5.2 Device Packaging

5.2.1 SGDBR Laser Butterfly Package Design

A standard package type for long wavelength semiconductor lasers is the 14 pin butterfly. We have designed a modified version of this package for the SGDBR laser. An SMA connector has been added to the back side of the package to enable high speed drive signals to be efficiently coupled into the device. The SMA is rated for frequencies up to 18 GHz which is far beyond the bandwidth of the laser response. For most applications the regular input pins which are rated to 3 GHz have sufficient bandwidth. However for laboratory applications the SMA is a convenient way to interface the device to external instruments. The detailed mechanical design drawings for the butterfly package can be found in Appendix C.

The assembly of the laser package is a multi step process which uses soldering as the primary assembly technique. This provides a stable long term bonding method which is more consistent than epoxy techniques. To assemble the different elements a technique called step soldering is used. In this method a number of different solders are used with progressively lower melting temperatures. Components are mounted using the highest temperature solders first this prevents previously attached components from shifting during subsequent soldering steps. The lowest temperature solder is used to mount the TEC to the package and to mount the laser submount to it. This is because the TEC is internally soldered together using a low temperature BiSn solder that melts at 138°C. The laser package has 14 different components which are all shown in Figure 5-1 except for the lid.

The first step in the packaging process is to mount the support block to the butterfly package using a 179°C SnPb solder. Then the TEC is mounted into the package using a low temperature 118°C InSnPb solder. The TEC connections are hand soldered to two of the package leads. The laser is first mounted on a 125 μm thick AlN submount using a AuSn solder that melts at 221°C. Then the laser mount, the heater blocks and the thermistor are all

mounted on the main AlN submount using the 179°C solder. At this point the laser is wire bonded to the submount with a wedge bonder and tested to ensure that it has not been damaged in the soldering procedure. The main AlN submount is now ready to be mounted into the laser package. It is soldered to the top of the TEC cooler using a 118°C solder. The SMA connector is next inserted into the back of the package and epoxied in place using conductive epoxy. The center pin on the SMA contacts a microstrip line on the main AlN submount. The last step before pigtailing is to wire bond the package pins to the submount using a deep access ball bonder.

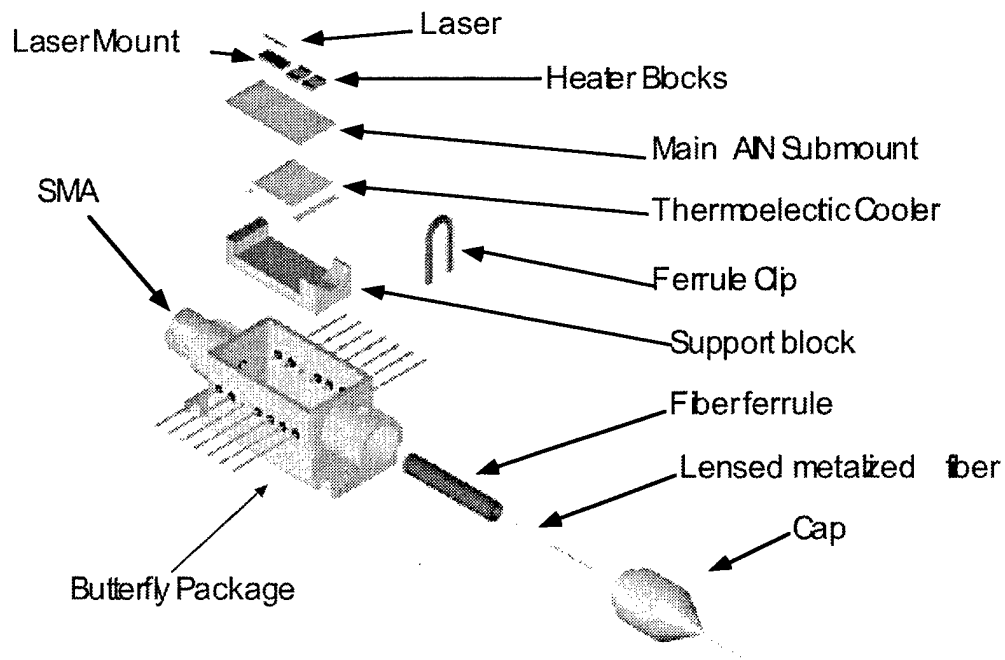


Figure 5-1 Laser package components.

5.2.2 Fiber attachment

For fiber pigtailing the assembled package is mounted on a support stage which enables electrical connection to be made to the laser and the thermoelectric

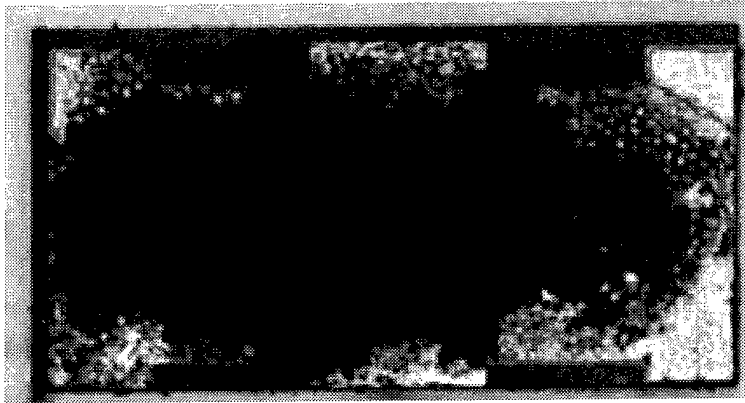
cooler (Figure 5-2). A fiber with a lens ground onto the end is used to increase the output coupling efficiency and reduce the backreflection into the laser cavity. There are a number of different fiber lens designs. Some use gradual tapers with a rounded tip, others employ graded index multimode fibers as lenses and some simply form a ball on the end of the fiber. We tested several different designs and got the highest coupling efficiency and the lowest backreflection with a simple design that uses a cone ground on the end of the fiber with a half angle of 70° . This has very low backreflection and less than 4 dB of coupling loss.



Figure 5-2 Close up of laser pigtailed procedure.

The fiber is mounted in a metal ferrule which enables it to be held rigidly from outside the package. The end of the fiber is metallized so that it can be soldered in place once it is aligned with the laser. The pigtailed procedure uses

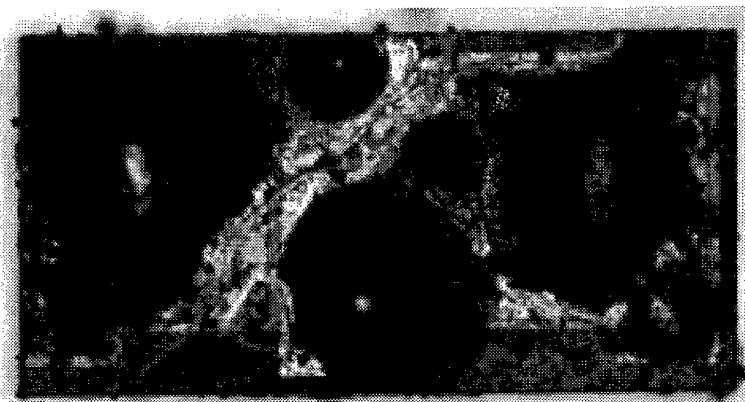
an active alignment in which the laser is driven above threshold and the fiber is positioned to maximize the coupled power. The fiber lays across a pair of heater blocks in front of the laser (Figure 5-2). The heater blocks have thin film resistive heaters patterned on their surface. On top of the heater is an insulating layer of SiNx and then a metal bonding pad. Once the fiber is in place a small amount of solder paste is applied to this bonding pad. Current is passed through the heater which heats up the block and melts the solder attaching the fiber to the submount. The solder paste has a BiSn eutectic which melts at 138°C. The paste contains the solder in small balls suspended in a flux solution. The fiber attachment process requires a precise amount of solder paste to be applied to the block. Successful fiber attachment also depends on the heating cycle for the block. Applying current too slowly reduces the viscosity of the solder flux enabling the paste to spread over the entire surface of the block before the solder melts. Then when it melts it shorts out the heater preventing full melting of the solder Figure 5-3A. If too much solder paste is used when it melts the surface tension is not high enough to contain it to the center of the block and it doesn't give a uniform mound in the center which can hold the fiber Figure 5-3B. When the block is heated up to too high a temperature then the solder tends to splatter and distribute itself in a non-uniform manner across the surface of the block leaching up the gold from the contacts and shorting out the heater Figure 5-3. For the correct amount of solder and the appropriate soldering temperature cycle a smooth uniform mound of solder confined to the central contact pad results in good fiber adhesion Figure 5-3D. As the solder solidifies there is some shrinkage which tends to pull the fiber downward towards the submount. This can reduce the coupling efficiency for the device. To eliminate this the fiber position can be precompensated so that it sits slightly above the optimum coupling point. When the solder solidifies it then pulls the fiber into the correct alignment. In practice this is difficult to achieve and typically several attempts involving remelting of the solder and repositioning of the fiber are required.



(A)



(B)



(C)



(D)

Figure 5-3 Heater blocks for various soldering conditions (A) Heat up rate too slow, (B) Too much solder, (C) Temperature too high, (D) Correct temperature, time and solder levels

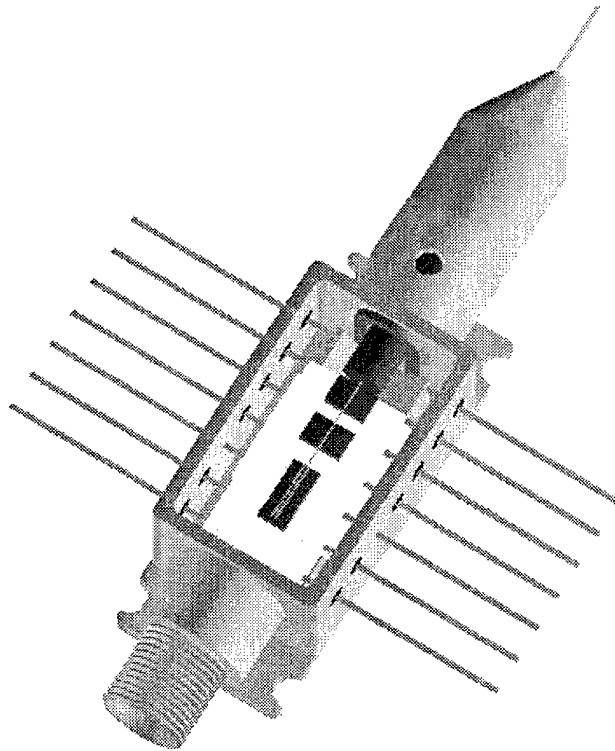


Figure 5-4 Rendering of assembled butterfly package

Once the fiber has been attached a metal clip is inserted around the ferrule and epoxied into place. This provides strain relief for the fiber attachment and gives the assembly improved mechanical stability. The ferrule is then released from its fixture and the front cap is slid over the ferrule and attached to the package. The outer jacket of the fiber is bonded to the cap for additional strain relief. A schematic rendering of the completed package with the cap removed is shown in Figure 5-4. A photograph of the same view is shown in Figure 5-5. The gold electrical interconnects on the surface of the main AlN submount are visible along with the laser and the metalized fiber..

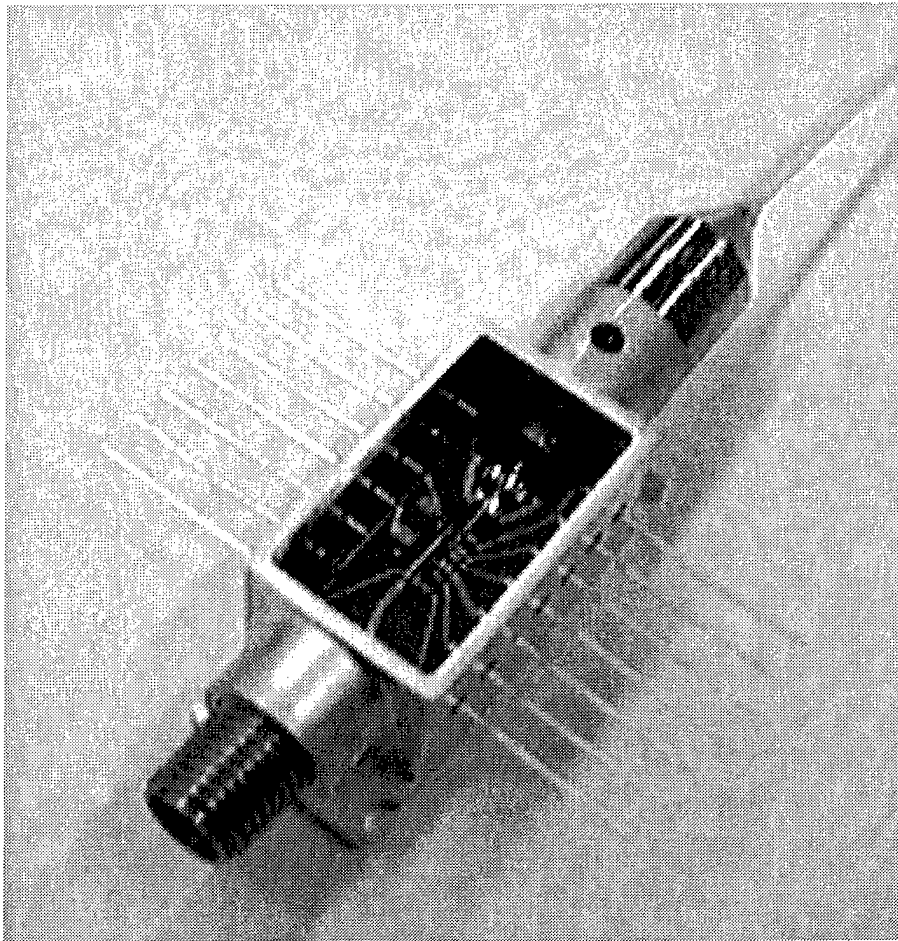


Figure 5-5 Photograph of finished laser package.

5.3 Device Characterization and System Testing

In Chapter 2 we discussed the intensity modulation characteristics for the SGDBR laser. It was found that the devices had a typical bandwidth on the order of 3 GHz. This is sufficient for direct modulation data transmission at 2.488 Gbit/s. In this section we demonstrate the performance of the SGDBR for data transmission applications. We also investigate the tuning speed for the device. One key advantage of integrated tunable semiconductor lasers is their potential for extremely fast tuning.

5.3.1 Dynamic Tuning Characteristics

The dynamic tuning response for the device is limited by the carrier dynamics in the tuning sections which are dominated by the spontaneous emission rate. This limits the bandwidth of the tuning section to less than 1 GHz. To confirm this we measured the wavelength switching speed between two adjacent coarse tuned channels using a tunable filter and a high speed receiver .

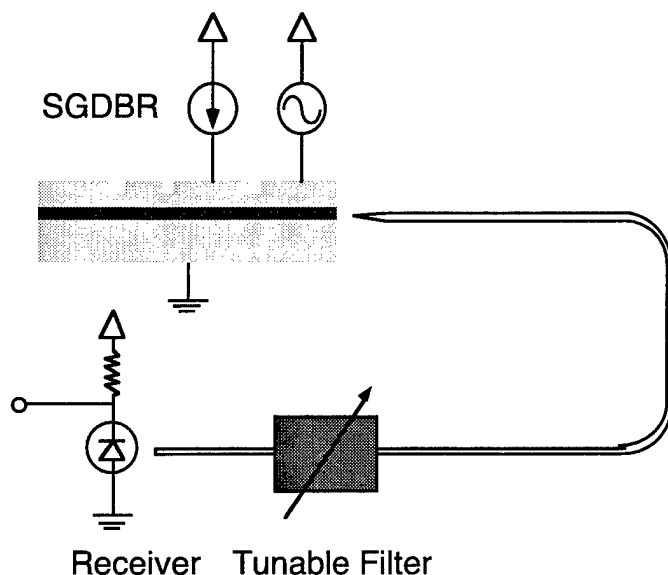


Figure 5-6 Experimental apparatus for wavelength switching tests.

A 100 MHz square wave modulation signal with a very fast rise time was applied to one of the laser mirrors. The output light was filtered through a 0.8 nm wide passband filter to select out a single wavelength channel. The signal from the high speed receiver was captured using a sampling oscilloscope Figure 5-7. The wavelength switching time for the device shows a fast transition of 1.5 ns with a subsequent settling time of 3 ns to within 5% of the final value. This shows the capability for very fast stable wavelength switching.

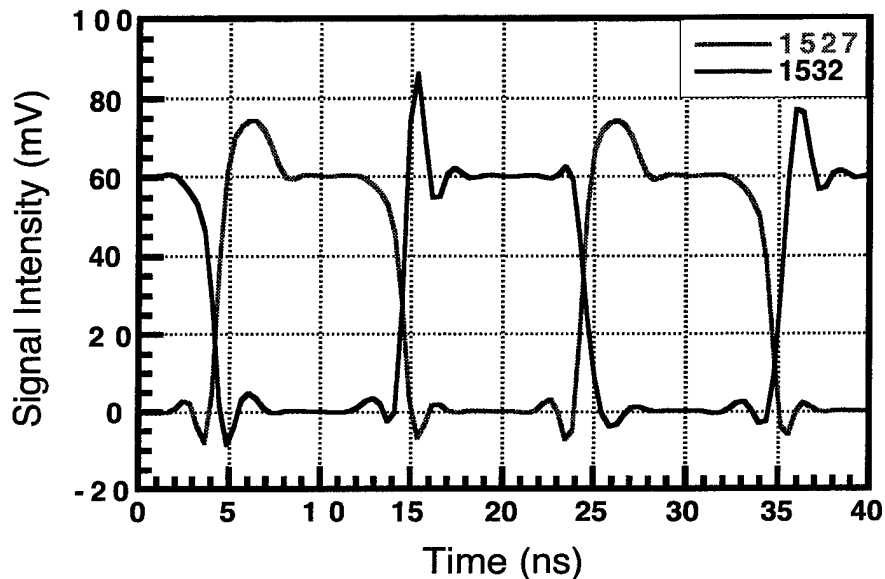


Figure 5-7 High speed wavelength switching waveforms

The spectrum of the light under continuous switching operation is shown in Figure 5-8. For this test the switching was between two adjacent coarse mirror peak alignments separated by 5 nm. Light in the side modes is still greater than 45 dB below the level of the two wavelength peaks.

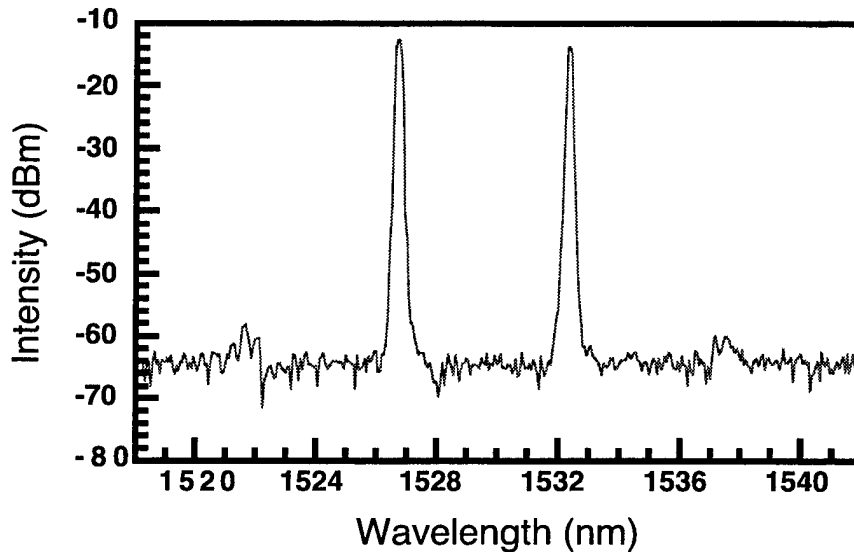


Figure 5-8 Spectrum under periodic wavelength switching

5.3.2 *BERT results and analysis*

Broadly tunable semiconductor lasers, have a number of potential applications, in wavelength division multiplexed communications [1]. The low-chirp and high modulation bandwidth of sampled grating DBR lasers make them well suited for directly modulated data transmission applications. SGDBR lasers have been fabricated with wide cw tuning ranges, narrow linewidths, and high side mode suppression ratios [2]. The enhanced tuning range of SGDBR lasers would tend to indicate that they would also have enhanced chirp characteristics, however measurements of these lasers using the gated delayed self-heterodyne technique have shown linewidth enhancement factors of less than 4 [3]. This compares favorably with results for standard DFB lasers that are generally between 5 and 8 at 1.55 μm [4]. In this section we demonstrate 1.244 GBit/s data transmission on four separate wavelength channels, covering

a range of 45 nm, with less than 0.6 dB of dispersion penalty over a transmission distance of 50 km.

The four-section SGDBR laser requires three bias currents to operate. One for each of the mirrors, one for the active region, and one for the phase control section. Data modulation was supplied by a 3 GBit/s pattern generator coupled to the device through a bias-T. The laser was packaged and mounted on a thermoelectric cooler to stabilize the temperature. All transmission tests were carried out at 20°C. Light was launched into single mode fiber using a pigtailed lensed fiber with an integrated optical isolator. Two 25 km spools of conventional single mode fiber, having a dispersion constant of 17 ps/nm-km and a loss of 0.21 dB/km, were inserted for the transmission tests. After the fiber, a variable optical attenuator was used to control the signal level to the receiver. The receiver is an AT&T Microelectronics APD with an impedance matched preamplifier. The received signal was split by a 3 dB coupler between the error detector and a sampling oscilloscope which captured the eye diagrams. The transmission wavelength was tracked by an optical spectrum analyzer which was also used to determine the side-mode suppression ratio for the various channels.

The superposition of the laser spectra for the four different wavelength channels is shown in Figure 5-9. More than 42 dB of side mode suppression is measured for all four channels under modulation. The transmission wavelengths are equally spaced approximately 15 nm apart and cover a range of wavelengths from 1524 to 1570 nm. The nominal operating wavelength channel for the laser with no mirror current was 1553.9 nm. The other channels were reached by differentially tuning the mirrors to align the nearest adjacent reflection peaks. This kept the tuning current low and provided equally spaced transmission channels. Tuning the phase section allowed the cavity mode to be aligned with the mirror reflection peaks. This ensured that the lasing wavelength remained stable and singlemode under modulation. Injecting tuning current into the mirror increased the loss within the laser cavity. This caused the laser threshold to vary across the four channels. The threshold currents for channels 1 to 4 were 86, 63, 58, and 89 mA respectively.

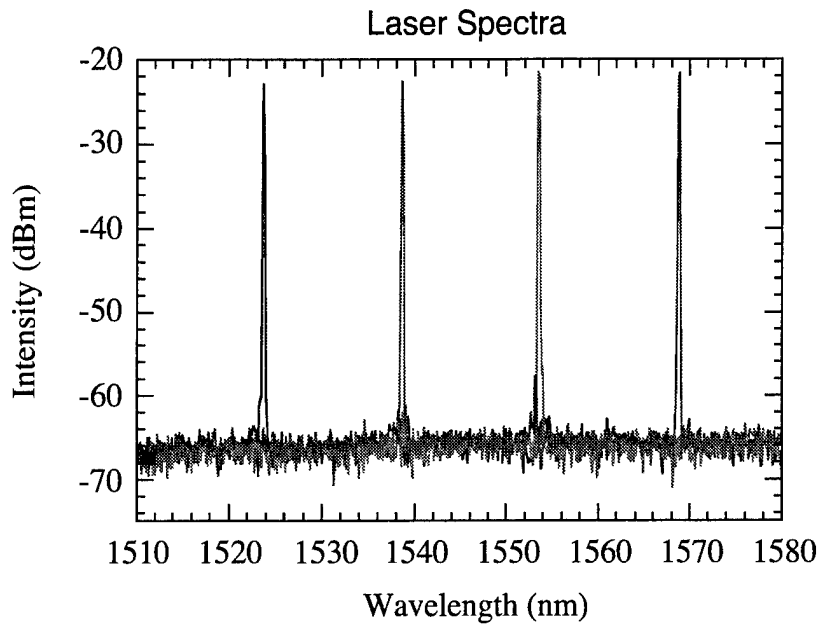


Figure 5-9 Superimposed laser spectra for the four transmission channels which are equally spaced 15 nm apart.

The transmission tests were carried out with a pattern length of $2^{15}-1$ and a modulation current of 16 mA peak-to-peak. Initial tests conducted at a bias of 10 mA above threshold showed good receiver sensitivities for the back-to-back measurements. However, after 50 km, channel 2 showed an error floor at 10^{-5} BER resulting from mode partition noise. To eliminate this problem all four channels were operated at a bias current of 20 mA above threshold. This ensured that at least a 40 dB side mode suppression ratio was maintained under modulation and that the lasing wavelength was insensitive to slight variations in the temperature or tuning currents. The tradeoff for this approach was that the modulation depth was reduced to 4 dB which resulted in an estimated 3.7 dB extinction ratio penalty [5]. This tradeoff between increased chirp at higher extinction and reduced signal-to-background ratio at low extinction has been examined previously. In a typical weakly guided DFB ridge laser structure the

optimum extinction ratio was found to be less than 4 dB for a 4 Gbit/s 100 km transmission system [6].

The bit error rate vs. received power for the back-to-back and 50 km tests are plotted in Figure 5-10. The receiver sensitivities that were measured at a bit error rate of 10^{-9} for channels 1 through 4 are all less than -29.5 dBm. The dispersion penalties for the 50 km distance were 0.4, 0.5, 0.3, and 0.6 dB, for channels 1 to 4 respectively. The maximum dispersion penalty of 0.6 dB was measured on channel 4 which was the longest wavelength channel. No error floor was observed on any of the channels down to a BER of 10^{-11} at the chosen bias conditions. This indicates that the RIN is less than -125 dB/Hz [7].

The side mode suppression is greater than 40 dB of on all four wavelengths at the chosen operating conditions so we can employ a simple model for the chirp-induced power penalty [5]. The effective chirp parameters and the dispersion limit for this device can be determined from (5-1).

$$\delta_c = 5 \log_{10} \left[(1 + 8\alpha\beta_2 B^2 L)^2 + (8\beta_2 B^2 L)^2 \right] \quad (5-1)$$

Where α is the chirp parameter, δ_c is the associated power penalty, B is the bit rate, L is the fiber length, and β_2 is the group velocity dispersion parameter. To a first order approximation this formula is independent of the extinction ratio. The effective chirp parameters for this device at the four different wavelengths are 6.3, 7.7, 4.1 and 9.5 respectively. For high modulation frequencies the effective chirp parameter is equal to the linewidth enhancement factor [3]. For SGDBR lasers, this is typically true for modulation frequencies above 1 GHz. The chirp parameters calculated from the dispersion penalties are higher for wavelengths on the long side of the gain peak. This result is in agreement with previous measurements on SGDBR's that indicated an increase in the linewidth enhancement factor from 3 to 8 as the devices were tuned to longer wavelengths [3]. The exception to this is channel 3 which shows the lowest chirp parameter. This channel is the operating wavelength for the laser with no tuning current.

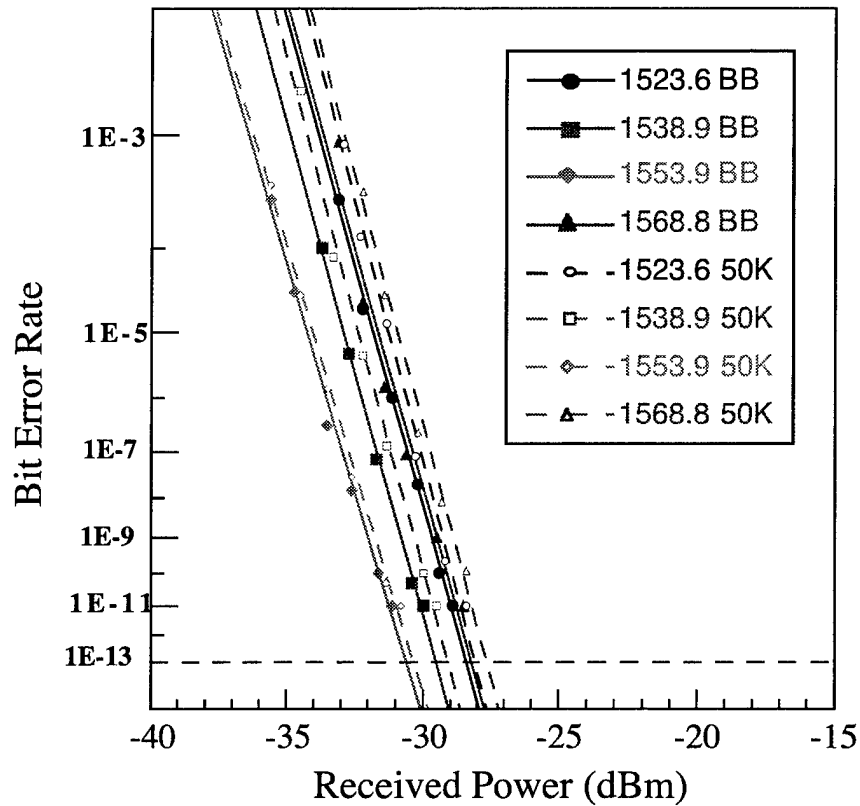


Figure 5-10 Bit error rate curves for back to back and 50 km transmission over standard single mode fiber at four widely spaced wavelengths.

The chirp parameters are enhanced on all channels where current is being injected into at least one of the mirrors. This effect can be attributed to the low isolation (less than 1 k Ω) that was achieved between the different sections. Modulating the active region current results in a small amount of modulation of the mirrors. When the mirrors are not forward biased, they have a very high impedance so this modulation is negligible. However, when a mirror is forward biased for tuning it has a much lower impedance, and the modulation results in

significant index changes. More than 40% of the measured wavelength chirping can be attributed to this effect. From this we can expect that if the electrical isolation between sections is improved it will result in a reduction of the lasers chirp characteristics. Using the worst case chirp parameter, the dispersion penalty for this device is calculated to be 3 dB for transmission over 200 km of standard single mode fiber.

5.4 Summary

In this chapter we have discussed some of the important technologies in the packaging and pigtailling of long wavelength semiconductor lasers. A viable packaging technique was developed which is based on step soldering for assembly and fiber attachment. The fiber pigtailling method used an active alignment technique with integrated micro-heaters for soldering the fiber in place. This is an attractive low cost alternative to laser welding. The principle problem with this method is the contraction when the solder cools. This tends to misalign the fiber and reduce the coupling efficiency. Pre-compensating for this by shifting the fiber in the opposite direction before soldering is one possible solution. A better approach would be to hold the fiber more rigidly at a point that is closer to the attachment.

In the testing we investigated the dynamic tuning performance of the SGDBR laser and showed that it is capable of stable wavelength switching with less than 4 ns transition times. The wavelength channel switching times are dominated by the settling time for the laser and not by the rise time. For communications applications we have demonstrated data transmission over 50 km of single mode fiber at 1.244 GBit/s on four equally spaced wavelength channels covering a range of 45 nm. We measured less than 0.6 dB of dispersion penalty for all four channels. The maximum transmission distance for a 3 dB dispersion penalty was estimated to be ~200 km. These results are consistent with previously published data on the wavelength dependence of the linewidth enhancement factor for SGDBR lasers.

References

1. Koch, T.L. *Laser sources for wavelength-division multiplexing*. 1995.
2. Mason, B., et al., *Ridge waveguide sampled grating DBR lasers with 22-nm quasi-continuous tuning range*. IEEE Photonics Technology Letters, 1998. 10(9): p. 1211-13.
3. San-Liang, L., et al., *Dynamic responses of widely tunable sampled grating DBR lasers*. IEEE Photonics Technology Letters, 1996. 8(12): p. 1597-9.
4. Kruger, U. and K. Kruger, *Simultaneous measurement of the linewidth, linewidth enhancement factor α , and FM and AM response of a semiconductor laser*. Journal of Lightwave Technology, 1995. 13(4): p. 592-7.
5. Agrawal, G.P., *Fiber-optic communication systems*. Wiley series in microwave and optical engineering. 1992, New York: Wiley. xv, 445.
6. Corvini, P.J. and T.L. Koch, *Computer simulation of high-bit-rate optical fiber transmission using single-frequency lasers*. Journal of Lightwave Technology, 1987. LT-5(11): p. 1591-5.
7. Coldren, L.A., et al. *Properties of widely-tunable integrated WDM sources and receivers*. 1996.

Chapter 6

Summary and Suggestions for Future Work

6.1 *Summary of Thesis*

This work has primarily focused on developing a design and fabrication process for a widely tunable sampled grating distributed Bragg reflector laser with an integrated wavelength monitor. The basic technology developed for this has the potential for widespread application in the development of photonic integrated circuits. The key to PIC technology is having an established set of building block elements and the appropriate fabrication technology to integrate them together on a common substrate. In this thesis we have developed growth, and processing techniques for creating and integrating these basic building blocks into more complex integrated devices. Significant improvements have been made in the design and fabrication process for the tunable laser. These have resulted in a dramatic improvement in the tuning efficiency and wavelength range for this device. To compliment this work a novel wavelength monitor has been developed and integrated monolithically with the tunable laser. These developments have been founded on consistent improvements in the growth processes that have resulted in better uniformity, increased quantum well gain, and reduced recombination at the regrowth interface.

6.1.1 *Tunable Lasers*

Significant improvements have been made in the performance of both the ridge and the buried heterostructure sampled grating DBR lasers. By employing a thick low bandgap waveguide the tuning efficiency has been increased allowing the ridge waveguide devices to tune continuously over more than 22 nm with

better than 45 dB side mode suppression ratio over this entire range. The maximum tuning current density in the mirrors was only 2200 A/cm^2 and the nominal threshold current for the device was 23 mA. The buried heterostructure devices had a simple buried ridge stripe design which provided better carrier confinement and reduced thermal impedance. This gave them a continuous tuning range of 49 nm with a maximum current density of only 1700 A/cm^2 in the mirrors. The changes that led to the improvement in the laser tuning performance are primarily related to the growth and processing procedure. The waveguide bandgap was reduced to 0.88 eV to increase the index tuning efficiency. Higher performance compressive strained quantum wells were used for the active region with six wells instead of two. In the fabrication steps a new dry etched grating process was developed that enabled better regrowth interfaces and more controllable grating kappa. Future work in this area should concentrate on reducing the leakage current in the buried heterostructure design and finding new ways to create active passive junctions.

In the testing we investigated the dynamic tuning performance of the SGDBR laser and showed that it is capable of stable wavelength switching with less than 4 ns transition times. The wavelength channel switching times are dominated by the settling time for the laser and not by the rise time. For communications applications we have demonstrated data transmission over 50 km of single mode fiber at 1.244 GBit/s on four equally spaced wavelength channels covering a range of 45 nm. Direct modulated data transmission was demonstrated at rates up to 2.488 Gbit/s.

6.1.2 *Wavelength Monitoring*

The need for wavelength monitoring in tunable lasers has been clearly established on the basis of experimental results, which document the wavelength drift in tunable lasers with aging. We have investigated a promising technique for wavelength monitoring of widely tunable semiconductor lasers. This technique is based on a novel design for an integrated wavelength monitor that can be fabricated on chip with a tunable SGDBR laser. The monitor uses

two-mode interference in a semiconductor waveguide to create a wavelength dependent splitter. A model for the wavelength response was developed using coupled mode analysis. This model was used to design a tapered TMI waveguide with a wide input for efficient coupling and a narrow central portion with higher dispersion. This design was simulated using a BPM model and verified experimentally. Wavelength monitors were fabricated in both ridge and buried heterostructure processes. The buried monitors employed a flared adiabatic mode expander with a segmented detector to replace the y-branch splitter used in the ridge waveguide device. This helped to eliminate back-reflections at the y-branch and simplified the fabrication process.

The test results for the buried and ridge waveguide monitors revealed that they are susceptible to cross talk from the drive currents for the laser and from stray light. This cross talk degrades the wavelength sensitivity of the device. It is feasible that future designs could significantly reduce this cross talk and improve the performance of the device. A more fundamental problem however exists in the fabrication tolerances. In order to operate correctly the monotonic portion of the filter function must be aligned with the laser tuning range. Unfortunately it is not practically possible to guarantee this alignment with the tolerances inherent in the fabrication process. For initial testing an extra contact was placed on the TMI filter waveguide so that its response could be trimmed to align it with the laser tuning range. This makes the filter an active semiconductor component, which is subject to the same aging related drift as the laser. Because of this fundamental limitation the long term potential of two mode interference splitters for wavelength monitoring is uncertain.

6.1.3 *Growth and Fabrication*

The techniques for growth and regrowth that have been developed in this thesis enable the fabrication of devices with both active and passive sections that have high tuning efficiency and low threshold currents. They are applicable to a wide variety of photonic integrated circuits. Future work should focus on

addressing the weaknesses in the current buried heterostructure process. To increase the bandwidth of the buried ridge stripe design and to develop SGDBR lasers with improved linearity and high temperature performance we need to develop a semi-insulating buried ridge stripe process. This will require a selective area regrowth step to planarize a tall dry etched ridge. The principle difficulty is in suppressing growth over the dielectric mask. For our growth system it should be possible to use the same low temperature conditions developed for the smooth side walls on the buried ridge stripe laser to achieve this. These conditions give high group III surface mobility and a long diffusion length, which help to prevent mask overgrowth. With this approach it should be possible to create p-n-Fe blocking junctions that will eliminate lateral leakage current and lower the parasitic capacitance of buried SGDBR lasers.

6.1.4 *Packaging*

The packaging and pigtailling of long wavelength semiconductor lasers is the most cost intensive step in commercial production of devices. A viable packaging technique was developed which is based on step soldering for assembly and fiber attachment with integrated micro-heaters. The fiber pigtailling method used an active alignment technique to position the fiber prior to soldering it in place. This is an attractive low cost alternative to laser welding. The principle problem with this method is the contraction when the solder cools which can misalign the fiber and reduce the coupling efficiency. A better approach needs to be developed that enables the fiber to be held more rigidly at a point that is closer to the attachment. This should reduce the pulling effect and improve the fiber coupling.

6.2 *Suggestions for Future Work*

Opportunities for future work exist both in the development of more complicated photonic integrated circuits based on the growth and processing techniques that have been developed for the tunable laser and in investigating new more sophisticated fabrication techniques. For the tunable laser a promising area for new research is in quantum well disordering for the creation of active and passive sections. The use of ion implantation damage to create selectively disordered regions with different bandgap shifts is a promising new technique. In PIC research two important opportunities that merit further investigation are all optical wavelength converters and tunable laser with integrated electro-absorption modulators.

6.2.1 *Tunable Laser with Integrated Modulator*

SGDBR lasers and other widely tunable designs have direct modulation bandwidths between 3 and 4 GHz. This enables them to be used in OC-48 data transmission systems under direct modulation if some wavelength chirping can be tolerated. However this bandwidth is insufficient for use in most phased array radar systems or in OC-192 data transmission networks operating at 10 GBit/s. In these applications external modulators are frequently used to apply the r.f. signal or data to the optical carrier. Even for OC-48 systems external modulators are sometimes used to minimize the chirp over longer transmission spans. External modulators add significant cost and complexity to the optical assembly, which can be prohibitive in systems that require a large number of sources. For this reason it is desirable to monolithically integrate a high-speed modulator on chip with the tunable laser.

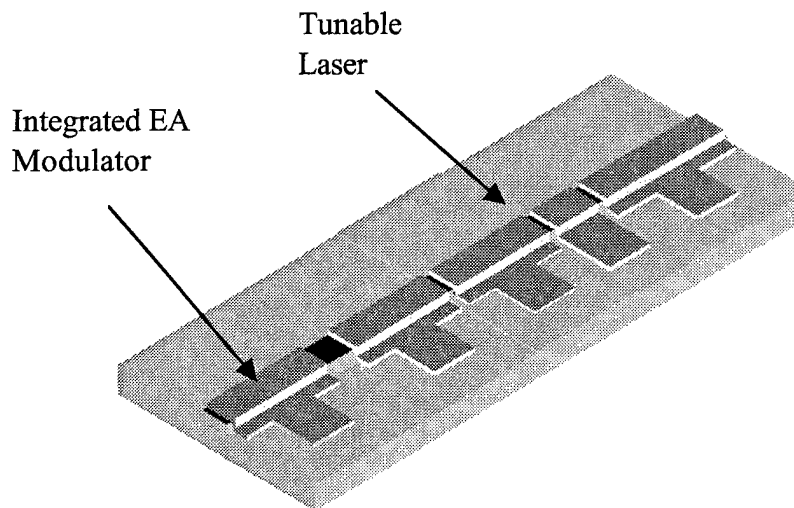


Figure 6-1 Tunable SGDBR laser with integrated modulator.

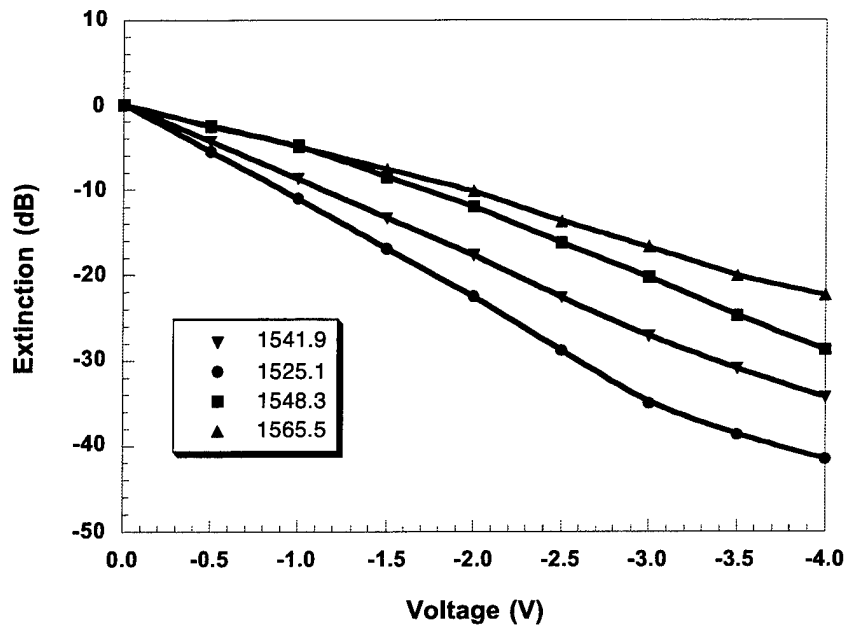


Figure 6-2 Modulator response curves for four wavelengths spanning more than 40 nm.

Electro-absorption (EA) modulators have already been successfully integrated with fixed wavelength DFB lasers to provide high-speed low chirp modulation for data transmission at rates of 10 GBit/s and higher. The simple structure and small size of these EA modulators make them ideal for monolithic integration with fixed and tunable semiconductor lasers. Preliminary work has demonstrated an EA modulator integrated with a SGDBR laser Figure 6-1 that can achieve more than 22 dB of extinction over a 40 nm tuning range Figure 6-2.

6.2.2 *Integrated wavelength converters*

One of the most important applications for tunable lasers and photonic integrated circuits in general is in all optical networking. Switching and routing data using only photonic components is an extremely attractive alternative to conventional electrical cross connects. Tunable lasers and wavelength converters are key components for some next generation optical cross connect designs. Achieving high bandwidth operation with Mach-Zehnder based interferometric wavelength converters (Figure 6-3) requires high optical power densities. Fabricating the pump laser on chip with the wavelength converter Figure 6-4 can eliminate coupling losses from the pump laser to the fiber, and from the fiber to the converter. This will enable higher bandwidth operation from the wavelength converter and will reduce the overall cost of the optical assembly.

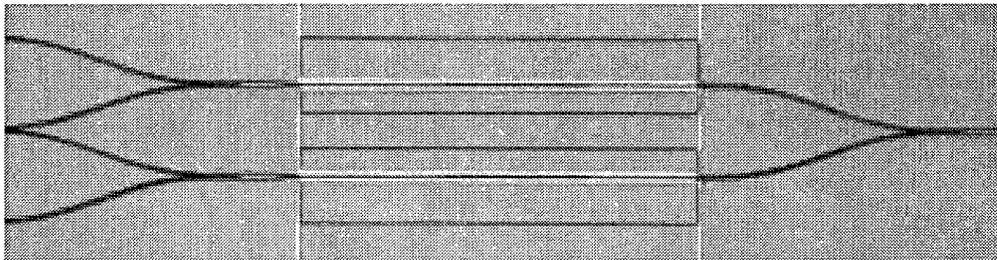


Figure 6-3 Die shot of interferometric wavelength converter with multi-mode interference splitters.

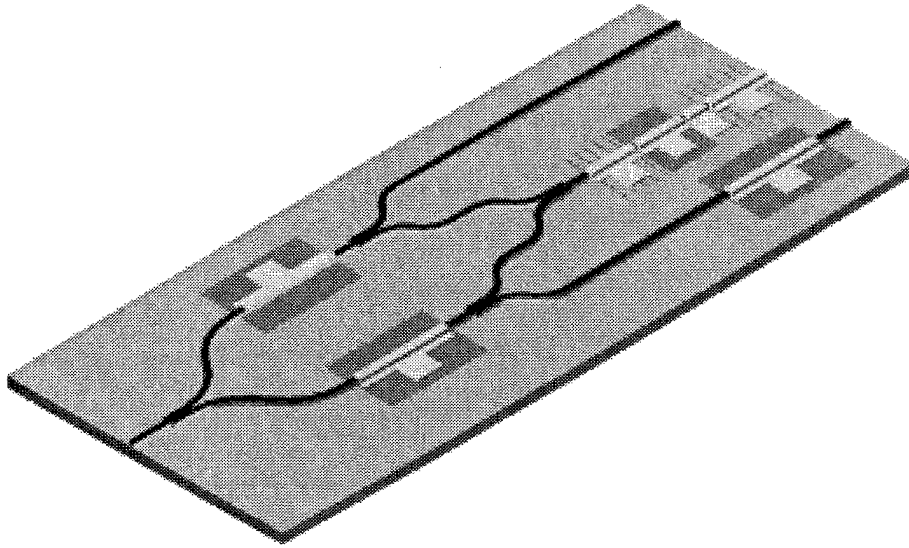


Figure 6-4 Proposed interferometric wavelength converter with integrated tunable laser source.

Appendix A

Buried Ridge SGDBR Fabrication Process

1. Base structure Growth

MOCVD Growth Program SGDBR Base

Substrate is 2" 0.2° misoriented Sulfur (S) doped InP wafer

Growth layers

10000 Å InP buffer Layer n doped 1E18

3500 Å 1.4Q waveguide layer n doped 5E17

100 Å InP layer undoped n doped 3E17

6 0.8% Offset quantum wells NID

300 Å 1.3Q capping layer NID

1600 Å InP doping setback layer NID

200 Å InP cladding layer p-doped 5E17

2. Active Passive Junction Etch

Clean sample

- Acetone Spray Rinse

- Isopropanol Spray Rinse

- Blow dry with dry N₂

- Bake on hot plate at 105°C for 2'

Spin on HMDS at 6000 RPM for 1'

Spin on 4110 at 6000 RPM for 1'

Bake on hot plate at 95°C for 1'

Expose edge bead removal mask 1' at 7.5 W/cm²

Develop 40" in AZ400K:H₂O 1:4

Expose Active/Passive Junction pattern 7.5" at 7.5 W/cm²

Develop 1' 20" in AZ400K:H₂O 1:4

Post bake sample for 2' at 105°C on hot plate

Etch InP cap layer for 25" in H₃PO₄:HCL 3:1

Check for uniform surface color, and dektak to confirm etch depth.

202

Mix $\text{H}_2\text{SO}_4:\text{H}_2\text{O}_2:\text{H}_2\text{O}$ 1:1:10 and allow to cool to room temperature
(Approximately five minutes for 50 ml)
Etch 35" to remove quantum well active region
Check for uniform surface color, and dektak to confirm etch depth.

Strip Resist from Sample

- Acetone Spray Rinse
- Isopropanol Spray Rinse
- Blow dry with dry N_2
- Bake on hot plate at 105°C for 2'

O_2 Plasma descum for 30" at 100 Watts 300 mTorr (300/100/L)
Dektak to confirm correct etch depth

3. Grating Etch Mask

Pre-Clean PECVD 30' SiN_x clean and pre-deposition cycle
Load Sample
Deposit 300A of SiN_x in PECVD
Check thickness and index of refraction

Spin on HMDS at 6000 RPM for 1'
Spin on 5214 at 6000 RPM for 1'
Bake on hot plate at 95°C for 1'
Expose edge bead removal mask 1' at 7.5 W/cm^2
Develop 40" in $\text{AZ400K}:\text{H}_2\text{O}$ 1:4
Expose Sampled Grating pattern 15" at 7.5 W/cm^2
Reversal bake the sample for 2' at 105°C
Flood expose the sample for 1' at 7.5 W/cm^2
Develop 1' in $\text{AZ400K}:\text{H}_2\text{O}$ 1:5.5

Etch SiN_x in DE100 for 30" at 300/100/L
Post etch O_2 plasma for 30" at 300/100/L
Remove sample and do a 10' O_2 clean at 300/300/L for chamber
BHF dip 5" to clean surface
Rinse in DI H_2O for 3'

Strip Resist from Sample

- Acetone Spray Rinse
- Isopropanol Spray Rinse
- Blow dry with dry N₂
- Bake on hot plate at 105°C for 2'

4. Grating Etch

Turn on laser and allow to warm up for at least one hour. Verify that the beam profile is correct and the intensity level at the shutter is around 40 nA on the power meter. Prepare a test sample to check the grating period.

Spin on HMDS at 6000 RPM for 1'

Spin on 1400-5 holographic grating resist at 6000 RPM for 1'
(Alternative resist is 1805 5% by weight.)

Bake on hot plate at 95°C for 1'

Load test sample on the vacuum holder

Adjust angular alignment of the holder

Expose for 45" at 40 nA

Develop in AZ400K 1:4 for 12s

Check the grating period using the diffraction set up.

Mount sample on test stage

Place turning mirror in laser path

Align reflection to pass through both slits

Read L from ruler distance between incident and diffracted beams

Calculate the grating period Λ from the following formula

$$\Lambda = \frac{\lambda}{\sin(\theta_i) + \sin(\theta_d)} = \frac{325}{1/\sqrt{2} + \sin(45 - \tan^{-1}(L/23))}$$

Load the sample on the vacuum holder

Adjust angular alignment of the holder

Expose for 45" at 40 nA

Develop in AZ400K 1:4 for 12s

Load sample in PEII

O₂ Plasma Descum 300 mTorr/ 100 Watts / 10 Seconds

Dry Etch Gratings in RIE II

Clean with O₂ 20 sccm, 125 mTorr, 500V for 20'

PreCoat with MHA 4/20/10 sccm, 75 mTorr, 500V for 10'

Load Sample

Etch with MHA 4/20/10 sccm, 125 mTorr, 200V for 2'

Etch with MHA 4/20/10 sccm, 75 mTorr, 500V for 1'30"

Polymer Removal O₂ 20 sccm, 125 mTorr, 300V for 4'

Clean Sample

- Acetone Spray Rinse

- Isopropanol Spray Rinse

- Blow dry with dry N₂

- Bake on hot plate at 105°C for 2'

Remove SiN_x with a 2' dip in buffered hydrofluoric acid (BHF)
Rinse in flowing DI H₂O for 3'

5. Ridge Etch

Pre-Clean PECVD 30' SiN_x clean and pre-deposition cycle

Load Sample

Deposit 1000Å of SiN_x in PECVD

Check thickness and index of refraction

Spin on HMDS at 6000 RPM for 1'

Spin on 4110 at 6000 RPM for 1'

Bake on hot plate at 95°C for 1'

Expose edge bead removal mask 1' at 7.5 W/cm²

Develop 40" in AZ400K:H₂O 1:4

Expose Buried Ridge pattern 7.5" at 7.5 W/cm²

Develop 1' 20" in AZ400K:H₂O 1:4

Load sample in PEII

O₂ Plasma Descum 300 mTorr/ 100 Watts / 30 Seconds

Etch SiN_x in RIE III

PreClean Chamber O₂ 25 sccm, 50 mTorr, 500V, 10'
Load sample and align laser monitor
Etch CHF₃ 20 sccm, 5 mTorr, 500V, ~5' (Use monitor)
Descum O₂ 25 sccm, 100 mTorr, 200V, 3'

Clean Sample

- Acetone Spray Rinse
- Isopropanol Spray Rinse
- Blow dry with dry N₂
- Bake on hot plate at 105°C for 2'

Dry Etch Ridge in RIE II

Clean with O₂ 20 sccm, 125 mTorr, 500V for 20'
PreCoat with MHA 4/20/10 sccm, 75 mTorr, 500V for 10'
Load Sample
Align laser monitor
Etch with MHA 4/20/10 sccm, 125 mTorr, 200V for 2'
Etch with MHA 4/20/10 sccm, 75 mTorr, 500V for ~ 45'
(Use monitor go through the waveguide and an additional 2000Å of depth in the active section.)
Polymer Removal O₂ 20 sccm, 125 mTorr, 300V for 12'

Dektak to confirm etch depth

Clean up etch in (Br:HBR 1:17):H₂O 1:10 for 10"

Rinse in DI H₂O

Dektak to confirm etch depth

6. Regrowth

Clean Sample

- Acetone Spray Rinse
- Isopropanol Spray Rinse
- Blow dry with dry N₂
- Bake on hot plate at 105°C for 2'

Warm up UV Ozone oven for 30'

UV Ozone Bake for 1 hour

Dip in BHF for 1'
 Rinse in flowing DI H₂O for 3' minimum
 (Surface should be hydrophilic)
 N₂ Blow Dry
 Transfer to glove box immediately
 Load reactor
 Bake at 150°C for 15' in reactor before regrowth.

Regrow SGDBR Buried Ridge Program (Appendix B.)
 Regrowth temperature 585°C
 5000 Å InP doping setback layer NID
 2 µm InP upper cladding p-doped 5E17
 5000 Å InP upper cladding p-doped 1E18
 1000 Å InGaAs contact layer p-doped 1E19

7. Implant

Pre-Clean PECVD 30' SiN_x clean and pre-deposition cycle
 Load Sample
 Deposit 3000Å of SiN_x in PECVD
 Check thickness and index of refraction

Spin on HMDS at 4000 RPM for 1'
 Spin on 4330 at 4000 RPM for 1'
 Bake on hot plate at 95°C for 1'
 Spin on 4330 at 4000 RPM for 1'
 Bake on hot plate at 95°C for 1'
 Expose edge bead removal mask 2' at 7.5 W/cm²
 Develop 60" in AZ400K:H₂O 1:4
 Expose edge bead removal mask 1' at 7.5 W/cm²
 Develop 60" in AZ400K:H₂O 1:4

Expose implant pattern 60" at 7.5 W/cm²
 Develop 1' 20" in AZ400K:H₂O 1:4
 Post bake sample for 2' at 105°C on hot plate

Load sample in PEII
 O₂ Plasma Descum 300 mTorr / 100 Watts / 30 Seconds
 Etch SiN_x in DE100 etch gas 300 mTorr / 100 Watts / 3'

Etch InGaAs Contact Layer in $\text{H}_3\text{PO}_4:\text{H}_2\text{O}_2:\text{H}_2\text{O}$ 3:1:50 for 1'

Mount on Si wafer with Kapton tape

Implant with Hydrogen using the following energy and dose

20 keV	$4 \times 10^{13} \text{ cm}^{-2}$
55 keV	$5 \times 10^{13} \text{ cm}^{-2}$
110 keV	$7 \times 10^{13} \text{ cm}^{-2}$
175 keV	$9 \times 10^{13} \text{ cm}^{-2}$
240 keV	$1 \times 10^{14} \text{ cm}^{-2}$
300 keV	$1.2 \times 10^{14} \text{ cm}^{-2}$

Unmount sample clean off photoresist

Acetone rinse and cue-tip scrub

Isopropanol rinse

N_2 blow dry

Remove remaining SiN_x with Buffered HF 3'

Rinse in DI H_2O

N_2 blow dry

8. Dielectric Cap Layer

Pre-Clean PECVD 30' SiN_x clean and pre-deposition cycle

Load Sample

Deposit 5000Å of SiN_x in PECVD

Check thickness and index of refraction

Spin on HMDS at 6000 RPM for 1'

Spin on 5214 at 6000 RPM for 1'

Bake on hot plate at 95°C for 1'

Expose edge bead removal mask 1' at 7.5 W/cm^2

Develop 40" in AZ400K: H_2O 1:4

Expose Sampled Grating pattern 15" at 7.5 W/cm^2

Reversal bake the sample for 2' at 105°C

Flood expose the sample for 1' at 7.5 W/cm^2

Develop 1' in AZ400K: H_2O 1:5.5

Etch SiN_x in CF_4 for 5' at 300/100/L

Post etch O_2 plasma for 30" at 300/100/L

Remove sample and do a 10' O_2 clean at 300/300/L for chamber

BHF dip 5" to clean surface
Rinse in DI H₂O for 3'

Clean Resist off Sample

- Acetone Spray Rinse
- Isopropanol Spray Rinse
- Blow dry with dry N₂
- Bake on hot plate at 105°C for 2'

9. Top Side Metal

Spin on HMDS at 6000 RPM for 1'
Spin on 825 at 4000 RPM for 1'
Bake on hot plate at 95°C for 1'
Flood Expose for 30" at 7.5 W/cm²
Spin on 4110 at 6000 RPM for 1'
Bake on hot plate at 95°C for 1'
Expose edge bead removal mask 1' at 7.5 W/cm²
Develop 60" in AZ400K:H₂O 1:4
Rinse in DI H₂O
N₂ Blow Dry
Expose Top Side Metal Mask for 7.5" at 7.5 W/cm²
Develop 1'30" in AZ400K:H₂O 1:4

Load sample in E-Beam number 1
Evaporate Ti/Pt/Au 300/500/10000 using lowered angled spinning evaporation.
Soak in acetone and spray rinse to lift off metal
Rinse in Isopropanol
N₂ blow dry
Anneal at 400 °C for 30 seconds using strip annealer

10. Lapping

Mount sample upside down on Si wafer using high temperature crystal wax.
Mount Si wafer onto the lapping chuck using low temperature paraffin wax

Lap sample to 100 um thickness using blue 9 μm grit lapping paper and a figure 8 motion.
Dismount Si wafer from chuck clean in acetone and Isopropanol

11. Back Side Metal

Mount sample in E-Beam evaporator
Deposit Ti/Pt/Au 300/500/5000 back side contact

12. Cleaving

Dismount sample from Si wafer
Heat wafer to 130°C
Gently slide sample off of Si wafer
Clean in acetone and Isopropanol
Rinse sample in funnel until clean
Scribe and cleave into laser bars.

13. AR Coating

Evaporate test sample of SiOx in e-beam 2 to check index and thickness
Scan for minimum in lambda 9 and scale thickness from minimum
Load sample in evaporation fixture
Evaporate SiOx index ~ 1.8 thickness ~ 2150A

14. Mounting

Apply small amount of blue flux to submount
Place SnPb solder preforms on submount.
Place sample on submount
Heat submount to 180 °C and allow solder to melt and reflow
Remove submount from heater and rinse in DI water.
Test.

Appendix B

Submount Fabrication Processes

Main Submount

1. Layer Structure

2.5 μm Au Metal Layer
TiW Interface Layer
TaN Resistor Layer 70 ohms/square
AlN Submount 635 μm thick
TiW Sticking Layer
2.5 μm Au Metal Layer

2. Protect Back Side

Clean sample

- Acetone Spray Rinse
- Isopropanol Spray Rinse
- Blow dry with dry N_2
- Bake on hot plate at 105°C for 2'

Pre-Clean PECVD 10' SiN_x clean and pre-deposition cycle

Load Sample

Deposit 1000Å of SiN_x in PECVD on back side of sample

Check thickness and index of refraction using a Si sample

3. Pattern Interconnect Metal

Spin on HMDS at 6000 RPM for 1'

Spin on 4110 at 6000 RPM for 1'

Bake on hot plate at 95°C for 1'

Expose Interconnect Metal pattern 7.5" at 7.5 W/cm^2

Develop 1' 20" in AZ400K: H_2O 1:4

Post bake sample for 2' at 105°C on hot plate

212

Etch sample for 30' in Iodine based Au Etchant
Rinse in DI H₂O
N₂ blow dry

Etch TiW and TaN layers in HF:HNO₃ 1:3 for 10"
Rinse in DI H₂O
N₂ blow dry

Etch off backside SiN_x protection layer in BHF for 1'
Rinse in DI H₂O
N₂ blow dry

Strip Photoresist

- Acetone Spray Rinse
- Isopropanol Spray Rinse
- Blow dry with dry N₂
- Bake on hot plate at 105°C for 2'

4. Dice Sample

Mount sample on 4" Si wafer with high temperature crystal wax
Dice sample using DISCO DADI into individual submounts
Use the blade designed for ceramic submounts
After dicing remove sample using hot plate at 130°C
Rinse submounts in Methylene Chloride
Rinse in acetone
Rinse in isopropanol
Blow dry with N₂

Laser Mount and Thin Film Heaters

1. Layer Structure

- 2.5 μm Au Metal Layer
- TiW Interface Layer
- TaN Resistor Layer 70 ohms/square
- AlN Submount 254 μm thick
- TiW Sticking Layer
- 2.5 μm Au Metal Layer

2. Protect Back Side

Clean sample

- Acetone Spray Rinse
- Isopropanol Spray Rinse
- Blow dry with dry N_2
- Bake on hot plate at 105°C for 2'

Pre-Clean PECVD 10' SiNx clean and pre-deposition cycle

Load Sample

Deposit 1000Å of SiNx in PECVD on back side of sample

Check thickness and index of refraction using a Si sample

3. Pattern Interconnect Metal

Spin on HMDS at 6000 RPM for 1'

Spin on 4110 at 6000 RPM for 1'

Bake on hot plate at 95°C for 1'

Expose Interconnect Metal pattern 7.5" at 7.5 W/cm²

Develop 1' 20" in AZ400K:H₂O 1:4

Post bake sample for 2' at 105°C on hot plate

Etch sample for 30' in Iodine based Au Etchant

Rinse in DI H₂O

N₂ blow dry

Strip Photoresist

- Acetone Spray Rinse
- Isopropanol Spray Rinse
- Blow dry with dry N₂
- Bake on hot plate at 105°C for 2'

4. Pattern Thin Film Resistors

- Spin on HMDS at 6000 RPM for 1'
- Spin on 4110 at 6000 RPM for 1'
- Bake on hot plate at 95°C for 1'
- Expose Resistor pattern 7.5" at 7.5 W/cm²
- Develop 1' 20" in AZ400K:H₂O 1:4
- Post bake sample for 2' at 105°C on hot plate

- Etch sample for 10" in HF:HNO₃ 1:3
- Rinse in DI H₂O
- N₂ blow dry

Strip Photoresist

- Acetone Spray Rinse
- Isopropanol Spray Rinse
- Blow dry with dry N₂
- Bake on hot plate at 105°C for 2'

5. Etch TiW Interconnect layer from on top of resistors

- Etch for 3' in H₂O₂
- Check resistance using probe station
- Continue etching until resistance reaches desired value

6. Deposit SiNx Layer For Solder Pad

- Pre-Clean PECVD 10' SiNx clean and pre-deposition cycle
- Load Sample
- Deposit 1000A of SiNx in PECVD
- Check thickness and index of refraction using a Si sample

7. Pattern Solder Pads

- Spin on HMDS at 6000 RPM for 1'
- Spin on 825 at 4000 RPM for 1'

Bake on hot plate at 95°C for 1'
Flood Expose for 30" at 7.5 W/cm²
Spin on 4110 at 6000 RPM for 1'
Bake on hot plate at 95°C for 1'
Expose edge bead removal mask 1' at 7.5 W/cm²
Develop 60" in AZ400K:H₂O 1:4
Rinse in DI H₂O
N₂ Blow Dry
Expose Top Side Metal Mask for 7.5" at 7.5 W/cm²
Develop 1'30" in AZ400K:H₂O 1:4

Load sample in E-Beam number 1
Evaporate Ti/Pt/Au 300/500/5000
Soak in acetone and spray rinse to lift off metal
Rinse in Isopropanol
N₂ blow dry
Anneal at 400 °C for 30 seconds using strip annealer

8. Dice Sample

Mount sample on 4" Si wafer with high temperature crystal wax
Dice sample using DISCO DADI into individual submounts
Use the blade designed for ceramic submounts

Appendix C

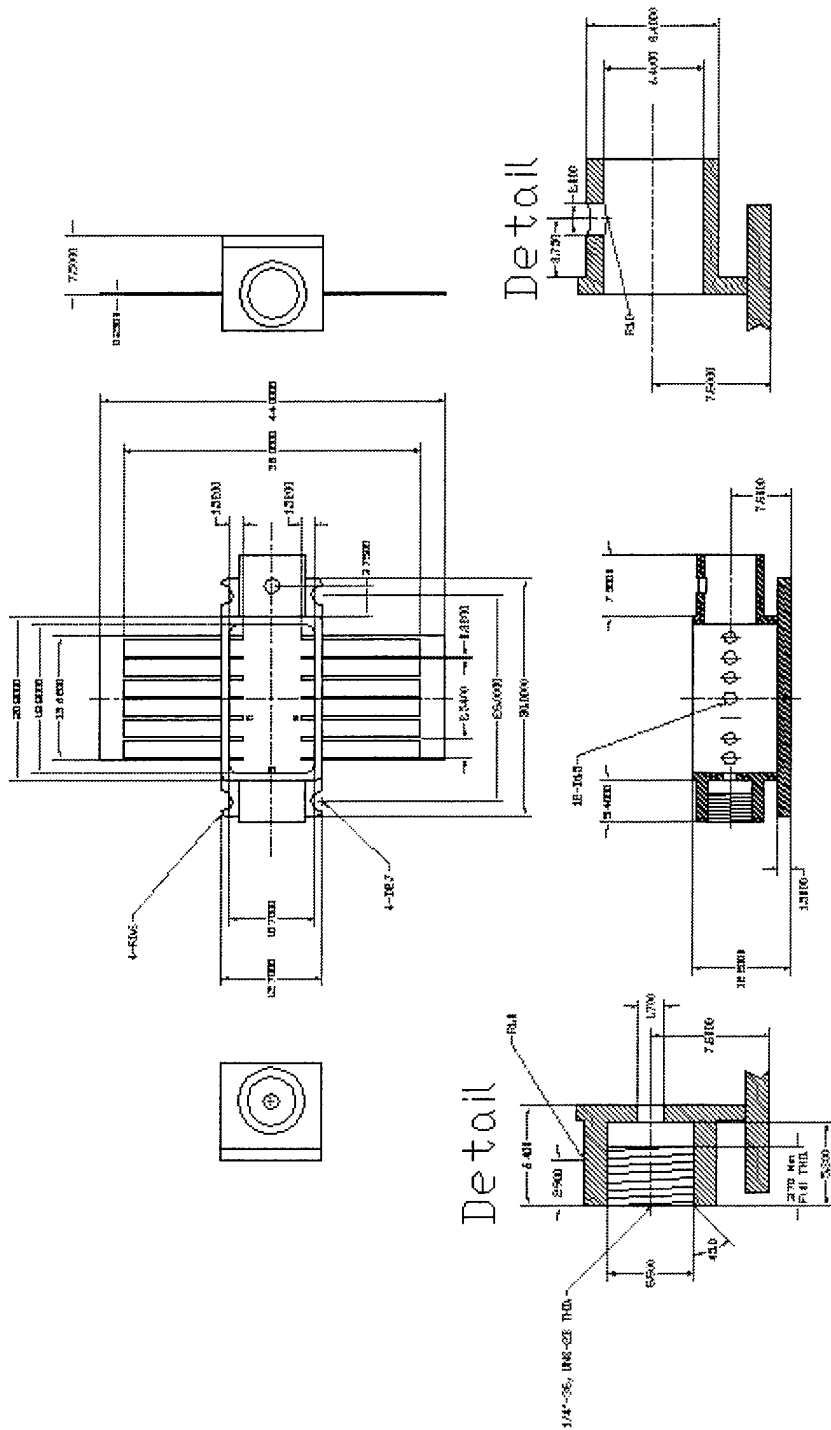
Device Packaging Process

Laser Package Assembly

1. Mount Laser to Submount #1
2. Mount Heaters to Submount #2
3. Mount Thermistor to Submount #2
4. Mount Submount #1 to Submount #2
5. Wire Bond Laser to submount #1 and submount #1 to submount #2
6. Solder Support Structure to Butterfly Package
7. Mount TEC in Butterfly Package
8. Mount Submount #2 into Butterfly Package
9. Mount SMA Connector to Butterfly Package
10. Connect SMA to Submount
11. Wire Bond Submount #2 to package

Pigtailing

1. Mount laser in pigtailling fixture
2. Thread Cap Onto Lensed Metalized Fiber
3. Attach Ferrule to Lensed Fiber
 - Use two part 5' epoxy
 - Leave 6 mm of fiber exposed from the end of the ferrule
4. Mount Ferrule in Holder
5. Perform test alignment and check laser operation
 - Pull fiber up and back afterwards
6. Deposit solder paste onto thin film heater
7. Probe the heater pads and check for continuity
8. Align fiber to laser
 - After alignment precompensate by moving the fiber up 1 μm vertically
9. Apply heater current to solder fiber in place
10. Slide clip over ferrule and epoxy it in place
11. Release ferrule holder and move it to support the cap
12. Slide cap onto package and epoxy in place
13. Fill cap tube with epoxy
14. Test laser
15. Epoxy lid in place



This page intentionally left blank.

REPORT DOCUMENTATION PAGEForm Approved
OMB No. 0704-0188

Public reporting burden for this collection of information is estimated to average 1 hour per response, including the time for reviewing instructions, searching existing data sources, gathering and maintaining the data needed, and completing and reviewing the collection of information. Send comments regarding this burden estimate or any other aspect of this collection of information, including suggestions for reducing this burden, to Washington Headquarters Services, Directorate for Information Operations and Reports, 1215 Jefferson Davis Highway, Suite 1204, Arlington, VA 22202-4302, and to the Office of Management and Budget, Paperwork Reduction Project (0704-0188), Washington, DC 20503.

1. AGENCY USE ONLY (Leave blank)		2. REPORT DATE 6 March 2000	3. REPORT TYPE AND DATES COVERED Final Report, 9/20/96 – 2/29/2000	
4. TITLE AND SUBTITLE Improved Sampled Grating DBR Widely-Tunable 1.55 μ m Lasers			5. FUNDING NUMBERS N00014-96-1-G014	
6. AUTHORS Larry A. Coldren, Beck Mason, and Jonathon Barton				
7. PERFORMING ORGANIZATION NAME(S) AND ADDRESS(ES) University of California Department of Electrical & Computer Engineering Santa Barbara, CA 93106			8. PERFORMING ORGANIZATION REPORT NUMBER	
9. SPONSORING/MONITORING AGENCY NAME(S) AND ADDRESS(ES) Department of the Navy Naval Research Laboratory 4555 Overlook Avenue, SW Washington, D.C. 20375-536			10. SPONSORING/MONITORING AGENCY REPORT NUMBER	
11. SUPPLEMENTARY NOTES				
12a. DISTRIBUTION/AVAILABILITY STATEMENT Approved for public release; distribution unlimited.			12b. DISTRIBUTION CODE	
13. ABSTRACT (Maximum 200 words) Over the last three years, a number of improvements have been made in the design of SGDBR lasers with integrated componentry. Device design has improved the output power and tuning range due to an increase in the number of quantum wells in the active region from four to six. Devices with up to 8 mW of output power with integrated amplifiers and buried heterostructure devices with 72 nm tuning ranges were realized. Current laser results indicate that leakage current in buried heterostructure lasers is a major factor in limiting the device performance. To eliminate the parasitic leakage paths we have begun to investigate Fe doped blocking junctions for the device. Work on the wavelength monitor has focused on an external approach, which uses a wavelength dependent coupler in conjunction with a pair of photodetectors. Initial results show better than 1 nm sensitivity over a 30 nm range. The most recent work on the laser has focussed on integrating additional components for increased functionality. We have developed a curved waveguide semiconductor optical amplifier that can be integrated with the laser to increase the output power to greater than 6 mW. We have also investigated SGDBR lasers with integrated electro-absorption modulators. Using a 300 μ m long bulk EA modulator we have demonstrated error free data transmission at 2.5 GBit/s with a 2 ³¹ -1 pattern length at received powers of -32.5 dBm.				
14. SUBJECT TERMS Semiconductor lasers, photonic integrated circuits, wavelength monitors, WDM devices, semiconductor optical amplifiers, electro-absorption modulators			15. NUMBER OF PAGES 247	
			16. PRICE CODE	
17. SECURITY CLASSIFICATION OF REPORT Unclassified	18. SECURITY CLASSIFICATION OF THIS PAGE Unclassified	19. SECURITY CLASSIFICATION OF ABSTRACT Unclassified	20. LIMITATION OF ABSTRACT UL	